Multi-Eigenmode Control for Improved Tracking Speed in Multifrequency Atomic Force Microscopy

Andreas Schuh

Submitted to the Department of Electrical Engineering
in partial fulfillment of the requirements for the degree of

Doctor of Philosophy (Doktoringenieur) in Electrical Engineering

at the

ILMENAU UNIVERSITY OF TECHNOLOGY

July 2014

urn:nbn:de:gbv:ilm1-2015000566

Multi-Eigenmode Control for Improved Tracking Speed in Multifrequency Atomic Force Microscopy

---

Dissertation

zur Erlangung des akademischen Grades
Doktoringenieur (Dr.-Ing.)

vorgelegt der
Fakultät für Elektrotechnik und Informationstechnik
der Technischen Universität Ilmenau

von
M.Sc. Andreas Schuh

Erstbetreuer/Supervisor: Herr Univ.-Prof. Dr.-Ing. habil. I. W. Rangelow
Technische Universität Ilmenau, Fakultät für Elektrotechnik und Informationstechnik

Zweitbetreuer/Co-Supervisor: Herr Prof. Kamal Youcef-Toumi, ScD.
Massachusetts Institute of Technology, Department of Mechanical Engineering

vorgelegt am / submitted on: 01. Juli 2014

urn:nbn:de:gbv:ilm1-2015000566

Gutachter/Reviewers:

1. Herr Univ.-Prof. Dr.-Ing. habil. I. W. Rangelow
   Technische Universität Ilmenau, Fakultät für Elektrotechnik und Informationstechnik
2. Herr Prof. Kamal Youcef-Toumi, ScD.
   Massachusetts Institute of Technology, Department of Mechanical Engineering
3. Herr Prof. Dr. Ulrich Köhler
   Ruhr-Universität Bochum, Fakultät für Physik und Astronomie

Verteidigung am / Defense on: 08. Mai 2015

Verf.-Nr.: EI

Eine elektronische Version (PDF) dieser Dissertation ist auf http://www.db-thueringen.de/ verfügbar.
An electronic version (PDF) of this dissertation is available online at http://www.db-thueringen.de/.

Abstract

Atomic Force Microscope probes are mechanical beams that can be used to simultaneously map topography and material properties. In particular the imaging speed and force sensitivity are major concerns that often require a trade-off approach. In this work, a novel estimator based multi-eigenmode compensator is introduced to modify the dynamics of each resonance independently. Modeling, compensator design, implementation strategy in a digital system and validation in experiments will be presented. A single-eigenmode version of the compensator is used to modify the Q factor of the first three eigenmodes separately. Using higher eigenmodes in combination with a modified Q factor leads to a 20-fold increase in image acquisition rates. The modification of the natural frequency (F control) allows imaging at resonance frequencies that are not natural to the cantilever. The emerging multifrequency Atomic Force Microscopy utilizes higher eigenmodes to improve imaging speed and force sensitivity concurrently. One method actuates the first eigenmode for topography imaging and records the excited higher harmonics to map a sample's nanomechanical properties. To enhance the higher frequencies' response two or more eigenmodes are actuated simultaneously, where the higher eigenmodes are used to quantify the nanomechanics. In experiments, the compensator is used to specifically modify the Q factors of the cantilever's first two transversal eigenmodes concurrently in both imaging schemes. The experiments indicate most enhanced material contrast and imaging rate with low Q factors in the first eigenmode and high Q factors in the higher eigenmode. An extension of the compensator allows for a high speed Lock-in amplifier free amplitude demodulation, which is used for topography imaging with the first resonance. A different technique for improving material property sensitivity is presented based on structural modifications of the cantilever. Focused Ion Beam milling is used to remove mass from specific areas in the cantilever such that the first and higher eigenmodes are tuned towards each other. The shape and location of mass removal is determined either by simulation beforehand or through an in-situ approach. Higher harmonics of the harmonic active cantilevers indicate a significant response of up to 10 % in respect to the first resonance/harmonic.

Zusammenfassung

Die Sensoren von Rasterkraftmikroskopen sind mechanische Schwinger, die zur zeitgleichen Aufnahme von Topographie und Materialeigenschaften genutzt werden können. Besonders wichtig sind die Bildrastergeschwindigkeit und Kraftsensitivität, die oft einen Kompromiss benötigen. In dieser Arbeit wird ein neuartiger Multi-Eigenmode Kompensator basierend auf einem Zustandsschätzer vorgestellt, der die dynamischen Eigenschaften jeder Cantilever-Resonanz unabhängig voneinander modifizieren kann. Dargelegt wird die Modellierung, Kompensator-Design und Implementierungsstrategie in ein digitales System. Als Erstes wird der Kompensator zur Modifikation des Q Faktors einzelner Eigenmoden genutzt. Somit kann die Abbildungsrate um das 20-fache erhöht werden. Die Modifikation der natürlichen Frequenz erlaubt die Abbildung von Proben mit vollständig verschobenen Resonanzen. Moderne Mehrfachfrequenz-Abbildungsverfahren nutzen höheren Eigenmoden, um bessere Abbildungsraten und Materialsensitivitäten zu erreichen. Bei einer Methode werden die angeregten höheren Harmonischen extrahiert, die beim Rastern einer Oberfläche im Fourier-Spektrum entstehen. Eine andere Methode regt die erste und höhere Eigenmoden gleichzeitig an. In Experimenten wird der Kompensator in Kombination mit beiden Abbildungsverfahren genutzt, um speziell den Q Faktor der ersten beiden transversalen Eigenmoden gleichzeitig zu beeinflussen. Experimente zeigen, dass beste Abbildungsraten und Materialkontraste mit geringen Q Faktoren in der ersten und hohen Q Faktoren in der zweiten Eigenmode erreicht werden. Eine Erweiterung des Kompensators erlaubt die Hochgeschwindigkeits-Demodulation von Cantilever-Amplituden ohne Einsatz eines Lock-in Verstärkers, was anhand von Abbildungen mit der ersten Eigenmode gezeigt wird. Eine weitere Möglichkeit zur Verbesserung des Materialkontrastes basiert auf der strukturellen Modifikation des Cantilevers. Mit Hilfe einer Ionenfeinstrahlanlage wird Material an bestimmten Bereichen des Cantilevers entfernt, so dass die erste und höheren Eigenmoden aufeinander abgestimmt werden. Die Bestimmung von Form und Ort der Materialentfernung wird entweder durch Simulationen im Voraus oder mit einem in situ Ansatz erreicht. Die extrahierten höheren harmonischen Signale des harmonischen Cantilevers zeigen ein deutlich verstärktes Signal von bis zu 10 % im Vergleich zur ersten Resonanz.

Contents

1 Introduction

This Chapter gives a brief motivation and indicates the state of the art of high speed Atomic Force Microscopes (AFMs) and material property mapping. A more rigorous overview of past research efforts is presented in Chapter 2: *Fundamentals*. There, it is embedded within the proper context with other fundamental concepts needed throughout this work. The last Section of this Chapter lists the aims and outline of the presented thesis.

1.1 Motivation

The contact mode AFM is a developmental response to the Scanning Tunneling Microscope (STM) that could only be used on conductive samples, often in vacuum [1]. Since then, the instrument has been tremendously improved. Dynamic modes, such as the non-contact [2] and tapping (also called intermittent) [3] modes, have been introduced to reduce forces exerted onto the sample by the cantilever tip. The AFM imaging speeds has been highly increased by enhancing all the components evolved [4–10]. The cantilever itself has also involved from simple beams to fully integrated Microelectromechanical Systems (MEMS) incorporating actuation and sensing [11–15].

The AFM has become an essential instrument in the areas of nanotechnology, life sciences, chemistry, MEMS and semiconductors [16–19]. Its ability to obtain atomic resolution in vacuum, liquid and even air is unprecedented by other types of microscopes. Compared to Scanning Electron Microscopes (SEMs), its potential resolution is higher without the need for the conductive sample. Functionalization of cantilever tips has broadened its application spectrum to detect, e.g., magnetic forces, heat and capacitance. In particular molecular forces have been an extensive research area [20–22]. The cantilever has also been discovered as pressure, gas and mass sensors [23, 24]. However, its versatility is limited by its maximum imaging rates. Biological and chemical processes are often on a time scale much faster than the AFM's capabilities, making its nanoscale real-time observations impossible [25, 26]. Metrology of semiconductor wafers is a different example, where large static samples need to be imaged. Here, the AFM is limited in its scan range that makes a combination with other kinds of long range scanners necessary.

Increasing the AFM's acquisition rate is essential for future nanoscale discoveries and as a test tool, e.g. in process control, with a resolution that cannot be achieved by other instruments. This is useful for the investigation of chemical compounds and biological processes, such as diagnosing diseases based on protein folding mechanisms [27] and capturing antibiotic actions [28]. The cantilever is also able to locally probe material properties [29]. Hence, a high speed tool with nanometer resolution, the possibility to capture fast dynamics and the ability to locally map material properties is vital for future discoveries. This can ultimately lead to a better understanding of underlying processes and, for example, can help to discover new cures and medications to diseases.

1.2 State of the Art

A indicated earlier, a major and inherent limitation of the AFM is its low acquisition rate. Responsible are the different components of the AFM that have been addressed in the past [4, 6, 7]. The lateral scanner directions follow a triangular actuation signal and stiff scanners are required to not excite its resonances [30, 31]. Resonance suppression can be achieved by control means [32–35]. The scan pattern can also be changed from a triangular to a sinusoidal signal and operating [36, 37].

The vertical out of plane z-axis follows the topography of the sample and has a limited bandwidth as well. Approaches have been developed to tackle this problem, like the dual actuator principle [38–40], using piezo-stacks instead of a tube scanner [41, 42], counter z balancing [43, 44] or an H^∞ controller instead of a Proportional Integral Differential (PID) controller [45]. Structures with high aspect ratios are harder to follow than small ones. The resulting saturation problem of the error signal is tackled by an adaptive Q controller [46] and dynamic PID [47]. These utilize adaptive adjustments on the control signal depending on the feedback error signal.

The intermmittent mode imaging bandwidth of a cantilever eigenmode depends on its effective Q-factor and resonance frequency. The cantilever has a time constant $\tau = 2Q_{eff,i}/\omega_{n,i}$, where ω_n is the natural angular frequency of eigenmode i. Variations in the sample structure are slowly picked up by high Q factored cantilevers that are typical in AFMs [48]. Hence, even with all other components in the feedback loop being fast enough, the Q factor remains as a bottleneck in the system. This is particularly the case in vacuum, where the cantilever can reach extremely high Q factors due to low external damping. In contrast, high Q factors are reported to enhance the sensitivity of the measurement due to the decreased forces applied to the sample. These are two contradicting behaviors, which both are desirable simultaneously [49, 50]. Faster cantilever dynamics have been achieved by structural modifications [15,51] or by control means [46,48,50,52,53]. In the latter case electronic active resonant control is an approach, where the damping of the cantilever is modified in a feedback fashion, either through an added analog or digital circuit. Q control for higher Q factors has been applied in various applications for cantilevers in the first eigenmode, mainly for increased imaging sensitivity. It also increases the sensitivity of the phase information that is correlated to dissipative tip-sample interactions. Phase imaging has been extensively used for nanomechanical property mapping in the first eigenmode [54–56]. In contrast, the damping can be increased to receive lower Q factors for high speed imaging [48]. Using higher cantilever eigenmodes can increase both the imaging rate and material sensitivity [13, 57, 58].

Recent imaging methods involve two or more cantilever frequencies in a multi-frequency approach [59]. In one method, the first eigenmode is used for topography imaging and the material dependent excitations of higher harmonics are mapped. The higher frequencies appear due the tip periodically and intermittently touching the sample surface [60–64]. Based on the periodicity of the tip-sample force, it can be expanded into a Fourier series [65,66]. The distribution of the harmonic magnitudes depends on the tip-sample contact time of each cantilever vibration cycle. Mapped with the cantilever transfer function, the response is more or less attenuated depending on the vicinity of nearby eigenmodes. In order to enhance the Signal-to-Noise Ratio (SNR) of higher frequencies, another method uses several concurrently actuated eigenmodes. The first eigenmode maps the topography and the higher eigenmodes are used to map the nanomechanical properties [67–71]. The amplitude and phase of the of the higher eigenmodes can be used to e.g. quantify the sample's Young's modulus. In bimodal actuation (first and second actuated eigenmode), the phase shift of the second eigenmode is one order of magnitude more sensitive to compositional variations than the first one [72]. In both methods, a reference material with known properties is often measured and compared with the sample under investigation to gain quantitative information.

1.3 Aims and Outline of this Work

In this Section, the aims and an outline of the presented work are given. Parts of this work are also published in [73–75].

Aims

In a brief manner, the aims can be formulated as:

- The dynamics of the active cantilever can be modified by a compensator, both in Q factor and natural frequency.
- The compensator can be formed by a full order estimator with full state feedback control. The estimator allows the estimation of unmeasured sensor signals.
- Each modeled eigenmode can be modified independently and concurrently, such as setting a low Q factor in a lower eigenmode and a higher factor in the higher eigenmode or modifying the natural frequency.
- The greatly noise-reduced estimated cantilever sensor signal can be used for an alternative estimator based amplitude demodulator.
- Structural modification of the cantilever can be carried out to influence its dynamics and receive similar benefits compared to the compensator approach.
- With the help of the developed methodologies the material contrast and tracking speed of the AFM can be considerably enhanced, enabling the measurement of small material differences. This can be tremendously useful in the fields of material and life sciences, for example enabling the observation of fast nanoscale biological processes.

Outline

It is intended to give the reader an overview of the work and help to match specific Chapters with its content. Hence, the outline is:

- **Chapter 2** will start with general fundamental aspects that give the reader the necessary background to understand all consecutive Chapters.

- **Chapter 3** introduces experimental setups, such as the AFMs, interferometer, Focused Ion Beam (FIB) and Field Programmable Gate Array (FPGA) platforms utilized throughout the work.
- **Chapter 4** carries out initial imaging, control and characterization experiments, such as Q control on the first resonance, mode shapes measurements of active cantilevers and imaging under various settings.
- **Chapter 5** introduces the novel discrete estimator based compensator design that is able to simultaneously and independently modify the dynamics of several eigenmodes.
- **Chapter 6** uses the derived compensator of Chapter 5 in a single-eigenmode control fashion to modify the first and higher resonances' Q-factor and natural frequency. Imaging results indicate increased tracking speeds when scanning a sample.
- **Chapter 7** uses the compensator of Chapter 5 in a multi-eigenmode approach of higher order. It controls two individual eigenmodes concurrently and each dynamics independently. Improved material sensitivity is demonstrated on a two-polymer sample with different elasticities.
- **Chapter 8** extends the compensator to perform an amplitude demodulation to potentially replace a Lock-in amplifier.
- **Chapter 9** introduces the design of fully integrated active harmonic cantilevers. Here, material sensitivity is enhanced by a completely different approach in contrast to the compensator of Chapter 5. The cantilever is structurally modified to specifically change and match different eigenmodes by an integer multiple.
- **Chapter 10** concludes the presented work. In addition, ideas are outlined how this work could be extended and improved in the future.

2 Fundamentals

The scope of this Chapter is the introduction of widely known fundamental theories, concepts and techniques as well as recent research efforts to help understanding the consecutive Chapters. Section 2.1 gives an introduction into the AFM and Section 2.2 specifically covers the cantilever theory. Its modeling and control are covered in Sections 2.3 and 2.4, respectively. Section 2.5 introduces the state-space based compensator design and Section 2.6 the signal processing aspect. At last, Section 2.7 discusses the potential of AFMs to image material properties.

2.1 Atomic Force Microscopy

After its invention in 1986 by Binnig *et al.* [1] as a successor to the STM, the AFM has gone through many evolutions since then. First, the less complex contact mode is mainly used to obtain the topography of a sample. Forces measured are in the repulsive regime and the tip is dragged along the surface, producing high friction that could destroy softer samples [76]. To minimize these impact forces two dynamic modes, namely tapping and non-contact modes, have been invented. In both modes, the amplitude and natural frequency of the cantilever is modulated in the vicinity of a sample surface. This is used for feedback purposes, e.g. keeping the distance between the tip and sample constant. The tapping mode penetrates the repulsive forces, whereas the non-contact mode stays within the attractive force's dominant range. Figure 2.1 shows a model of the Lennard Jones potential $w(x)$ and force $P(x)$ with the different force regimes. The contact mode and non-contact mode work in the repulsive and attractive force regime only, respectively, whereas the tapping mode covers the repulsive and attractive forces due to its large oscillating amplitude. The force $P(x)$ is proportional to the derivative of $w(x)$. For example, the force is zero when the energy is at its minimum. Detailed introductions to the AFM can be found in [77, 78].

Cantilever vibrations can be sensed by different techniques. Optical readout is the most popular and least noisy method, but requires bulky equipment around the AFM. In this case, a laser is

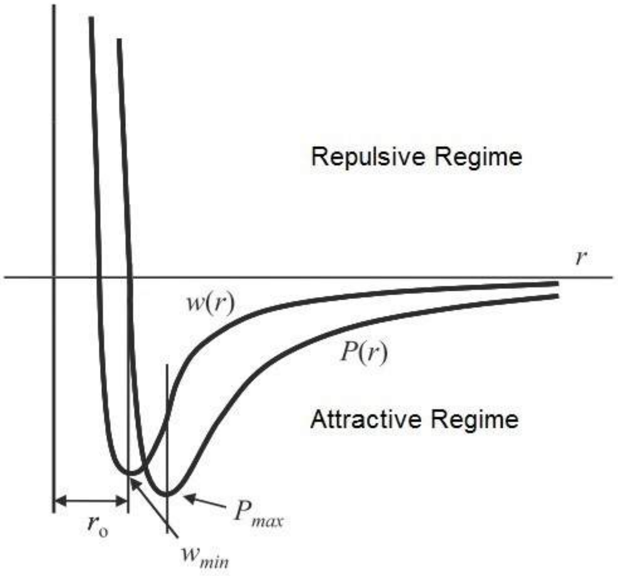

Figure 2.1: Lennard Jones potential and its derivate proportional force, adapted from [79].

focused onto the free end of the cantilever, which has the greatest slope along the beam upon bending, which is also valid in higher eigenmodes. The reflected beam hits a multiple segment photodiode for deflection sensing. For a more compact setup, the sensing can be integrated into the cantilever as piezo-resistive sensors. These sensors are sensitive to stress and are therefor located close to the support of the beam, where the highest stress due to bending occurs. Independent of the used sensors, it is important not to place/focus them onto vibrational nodes when imaging with higher eigenmodes. For example, focusing the laser or placing the piezo-resistive sensors onto slope or strain nodes, respectively. In contrast, if an eigenmode is to be excluded explicitly from the detection, the corresponding eigenmode's node can be targeted.

A general optical sensor and piezo shaker based AFM setup that can be switched between static and dynamic modes is shown in Figure 2.2. The scan pattern of the x and y directions is indicated that is generated by the function generators. The actuation signal of the cantilever can be provided externally to both the cantilever and Lock-in amplifier, where a Phase Locked Loop (PLL) locks onto it to provide proper phase and frequency values. Alternatively, the signal can be generated directly within the Lock-in amplifier.

In this work, concentration will be on cantilever beams with an almost rectangular cross section. In contrast, the widely available and often in water used triangular shaped cantilevers have the advantage of less torsional displacement (twist) while scanning compared to the rectangular beams.

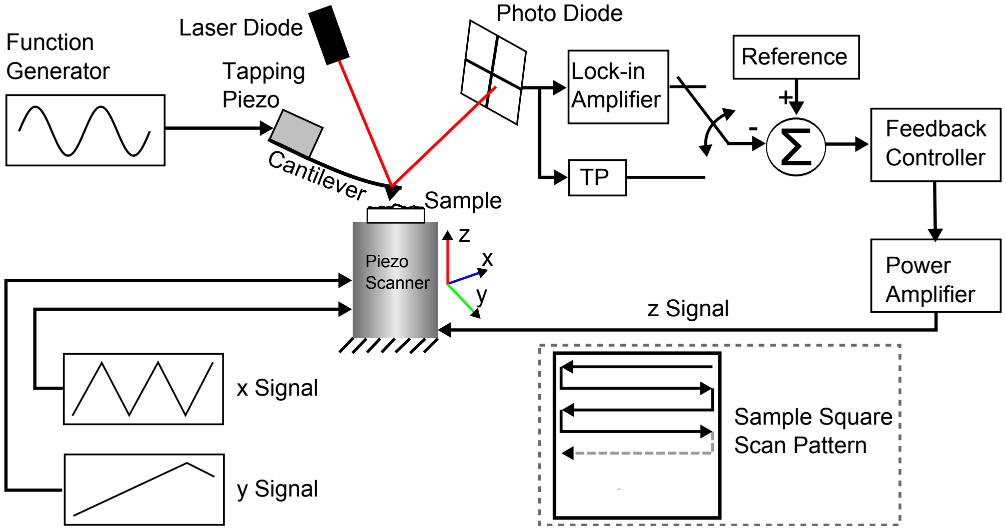

Figure 2.2: General optical sensor and piezo shaker based AFM setup that can be switched between static and dynamic modes. The scan pattern of the x and y coordinates is indicated.

But as fabricated cantilever dimensions are continuously shrunk, rectangular beams become stiffer and hence less prone to torsion. Thus, the need for triangular levers shrinks with the use of higher frequency cantilevers.

In the following, the dynamic modes, closed loop feedback, resolution, imaging speed and imaging environments are discussed in more detail.

2.1.1 Dynamic Modes of AFMs

The non-contact mode attempts to minimize the tip forces on the sample by not touching (repulsive force regime) the surface. This is achieved by keeping the tip within the short range of the attractive forces, like the van der Waals forces. It requires small tip amplitudes of 0.1-1 nm [2,80–84]. Although the disturbance of the sample is very small, the tip has a high risk of being trapped in a liquid layer on the sample surface that is often adsorbed in air. The non-contact mode is often called Frequency Modulation (FM) AFM due to the usually utilized modulation effect of the surface forces onto the frequency and therefor required demodulation technique. Hence, in contrast to the tapping mode, the frequency is used as a feedback parameter to keep the tip-sample distance constant.

The tapping mode (initially named by Veeco Instruments, Inc.) is also widely known as intermittent mode or Amplitude Modulation (AM) mode [3,80,85]. The latter one is called after the modulating effect - the damping of the amplitude due to surface forces - and the generally utilized amplitude demodulation technique in this mode. It operates with relatively high amplitudes >10-20 nm at the cantilever tip. The amplitude is beyond the dominant effect of the short range attractive forces of the surface. Each cycle, the tip experiences the repulsive forces during a short time and, hence, is in contact with the sample. On impact, the tip is creating a peak force, which can be too high for soft samples, although the average impact force appears to be small. This can be especially problematic for biological samples that can collapse and buckle upon a threshold force being applied. However, the tapping mode is very popular for biological samples and can even reach atomic resolution. The transition between attractive and repulsive forces upon the distance of the tip to the sample can create discontinues regimes and results in jumps in the amplitude [86–88]. The tapping mode is often used in commercial AFMs, whereas the non-contact mode is of higher interest in research and Ultra High Vacuum (UHV) applications.

Modern dynamic techniques involve higher eigenmodes and harmonics of the cantilever vibrations to retrieve additional information about the sample under investigation other than the topography [59, 61, 66]. Imaging in higher eigenmodes and fully objecting the first one is a different approach to increase the scanning speed due to the higher resonance frequency used [57, 58, 89]. Hence, even cantilevers with a low first resonance frequency in the range of 10^4 to 10^5 Hz can be challenging for the controlling electronics, since the higher eigenmodes can reach frequencies well into the MHz range. The second characteristic parameter is the Q factor [90, 91]. A low Q factor is associated with a fast energy loss and fast tracking ability of the sample surface, to the cost of increased forces exerted on it. In contrast, high Q factors indicate lower forces with a decreased bandwidth, potentially decreasing the overall imaging speed.

2.1.2 Closed Loop Feedback Components and Image Resolution

Whether the AFM is used in a static or dynamic mode, the information retrieved from the cantilever is usually used within a feedback loop. The vicinity of the sample with its potentially various different materials cause the amplitude and phase/frequency to be modulated. For example, a feedback loop can be used to keep the cantilever's amplitude constant and hence distance to the sample surface. Presence of different materials can be monitored by the frequency/phase shift and kept constant by adjusting the distance to the sample.

The static mode provides the amplitude for the feedback directly, possibly filtered by a low pass filter to reduce high frequency noise. In the dynamic modes the demodulation of the amplitude, phase and frequency became a necessity for forming control signals and images. As a result, the feedback loop is extended by a demodulator, most often a Lock-in amplifier [92]. Other less popular methods are based on Root Mean Square (RMS) or Direct Current (DC) converters. The Lock-in amplifier is a powerful tool to retrieve signals covered in noise. However, the demodulator is also an additional component in the feedback loop that further decreases the imaging bandwidth. Its filter time constant plays a crucial role in the two opposing measures feedback bandwidth and rejection of sensor noise. High feedback bandwidths require low filter time constants, whereas a good noise rejection needs higher constants. Usually, a trade-off between the two has to be found depending on the application and noise characteristic of the sensors. The cantilever sensor signal is recovered in respect to a reference signal. The reference signal is often similar to the signal used for the cantilever actuation. Consecutive filtering and additional operations result in the estimated amplitude. Figure 2.3 is a block diagram of the Lock-in's functionality indicating the different steps involved.

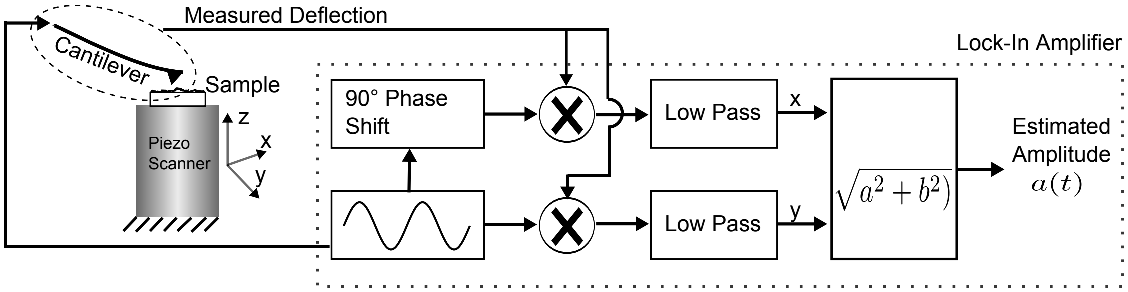

Figure 2.3: Principle of a regular Lock-in amplifier connected to an active cantilever and delivering the estimated amplitude.

Often, a PI controller is used to regulate the control variable according to a set-point, for example, keeping the amplitude of the cantilever constant at a specific value by varying the distance to the sample [93]. As in any regulation, the controller parameters are subject to a proper tuning that determines the speed, overshoot, error, stability, etc. of the feedback controller. Higher imaging rates and/or step-shaped structures on the sample require more aggressive controller parameters to properly track the sample. In turn, this can introduce a higher degree of overshoot that is visible in the resulting image as ringing lines perpendicular to the fast scan direction. For topography imaging, gentle penetration of the sample is desired, resulting in set-points often to be around 85%-95% of the free amplitude. In contrast, for material properties mapping, a strong interaction with the sample is desired to receive good contrast in the properties of the material.

The resolution of the resulting images is determined by different factors. First, a major limitation is random noise in the system. It causes uncertainties in the positioning of the scanner and detection/demodulation of sensor signals. Second, digital controllers are often used for generating various control signals including the feedback loop. Analog-to-Digital Converters (ADCs) and Digital-to-Analog Converters (DACs) have limited resolution and hence signals can only be detected and created in specific step sizes. In particular small signals can then incorporate great uncertainties. For example, the scanner axis can only be positioned according to the least significant bit in the DACs' resolution, which often requires a trade-off in scan size when trying to image nanometer sized objects. The problem of limited ADC resolution can partially be solved by oversampling that increases the effective resolution after decimation/down-sampling. Third, the forces during imaging let the tip penetrate the sample depending on its elasticity. Hence, gentle imaging conditions are required to not influence the sample surface by the tip and acquire the true force information of the sample. Scanner related non-linearities such as creep and hysteresis do not influence the resolution, but distort the images.

2.1.3 Limitations Regarding the Imaging Speed

A major and inherent limitation of the AFM is its low acquisition rate. Beside the limitations already mentioned in the previous Section, further responsible components are scanners, electronics, high voltage amplifiers, feedback control loop and the cantilever probe in the dynamic modes [4–10]. Ultimately, a High Speed AFM is a great tool for observing biological processes that cannot be achieved by other instruments [28, 94]. Many individual components have been addressed in the past to increase the overall speed of the AFM. In the following, each paragraph explains a limiting component.

Lateral Scanner Directions. Usually, the lateral scanner directions follow a triangular actuation signal. Hence, stiff scanner structures are required, so that the very same are not excited at higher scan speeds. Different designs have been proposed before, as in [26, 30–32, 95]. Also, resonance suppression can be achieved by control means [32–35, 96, 97] and an adaptive scan speed control [98] has been proposed. A different approach is changing the scan pattern from a triangular to a sinusoid and operating the scanner in resonance (tuning-fork), such as in [36, 37].

Vertical Scanner Direction. The vertical out of plane z-axis follows the topography of the sample. In this case, the shape of the sample directly influences the quality of the scan and its maximum allowable scan speed. For example, step-shaped structures contain high frequency components. Different approaches have been developed to tackle this problem, like the dual actuator principle [38–40], using piezo-stacks instead of a tube scanner [41, 42], counter z balancing [43, 44] or an H^∞ controller instead of a PID controller [45]. All methods aim to increase the tracking speed of the vertical z-axis by different means, such as suppressing imposed vibrations due to the controller gains or dividing tasks between actuators of different bandwidths.

Sample Structure Aspect Ratios. Also, structures with high variations in their heights (high aspect ratios) are harder to follow than small ones. This is mainly due to the saturation problem of the error signal. If the cantilever is scanning above a steep downward step, the cantilever becomes free from the sample [99]. The amplitude of the cantilever will approach the free amplitude, where no damping through the surface is present. At this point, the amplitude stops increasing and the error will be constant, no matter how far the cantilever is away from the surface. Equipped with a regular PID controller, the cantilever takes prolonged times to get back to the surface. A similar problem appears, when the cantilever is hitting an upward step and the amplitude becomes completely suppressed by the surface. Approaches to tackle this problem are the adaptive Q control [46] and dynamic PID control [47]. These utilize adaptive adjustments on the control signal depending on the feedback error signal.

High Voltage Amplifiers. Piezoelectric actuators require voltages of 100 V or more to be operated in their full range. In addition, the actuators impose a large load on the amplifier with up to several nano-Farad, to be driven as fast as possible. Hence, the amplifier needs to supply high currents well into the range of Amperes and specialized high power amplifiers can be used for this purpose. The capacitive load causes the phase and gain margin to drop, and a resonance can appear below the amplifier's cutoff frequency. A low pass filter can prevent this by limiting the bandwidth of the amplifier, for the price of tracking speed.

Cantilever Q Factor. The tapping mode imaging bandwidth of the i^{th} cantilever eigenmode depends on its effective $Q_{eff,i}$ factor and natural frequency $\omega_{n,eff,i}$. This is in the presence of a sample surface with a corresponding time constant $\tau_{eff,i} = 2Q_{eff,i}/\omega_{n,eff,i}$. The Q factor can be understood as a reciprocal rate of energy dissipation to its environment. Variations in the sample structure are slowly picked up by high Q_i factored cantilevers that are typical in AFMs [48]. Hence, even with fast demodulators, scanners and feedback controllers available, in particular the Q factor remains a bottleneck in the system. This is particularly true in vacuum, where the cantilever can reach extremely high Q factors due to the absence of external damping. In contrast, high Q factors are reported to enhance the sensitivity of a measurement, based on the decreased forces applied onto the sample. Thus, the different Q factors form two contradicting behaviors, which would be both desirable simultaneously [49].

Cantilever Modifications. A faster cantilever dynamic behavior can be achieved by structural modifications [15,51]. It requires a modification in the fabrication process, which is expensive, time consuming and subject to parameter spread. Active Q control is an alternative approach, where the damping of the cantilever is varied by control means [46,50,52,53,100]. Q control can be easily incorporated into an existing system, either through an analog or digital circuit. Further, with existing AFMs using FPGAs, Q control is simply a configuration update. In the past, Q control has been applied in various applications for cantilevers in the first eigenmode, mainly for increased imaging sensitivity. However, Ashby [101] shows that using small amplitudes rather than active Q control can be more beneficial. In contrast, the damping can be increased to receive lower Q factors for high speed imaging, provided the sensor noise permits this [48]. Different approaches directly regulate the interaction force of tip and sample [102].

2.1.4 Imaging Environments and its Influence on the Cantilever

The dynamic modes can be used in different environments, like vacuum, ambient air and fluids. The Q-factor is very different in all these environments. In vacuum with a gas pressure <100 Pa, Q factors become very high. This is due to the absence of viscous damping and hence dominance of internal losses [103,104]. Internal damping is very small in silicon cantilevers with its (nearly) perfect lattice structure. In contrast, Q factors in air and fluid are much smaller due to the dominance of the viscous damping [103,105–109]. In addition, if the cantilever is close to a surface a 'squeezing' effect takes place. This is additional damping due to the gas/fluid between the surface of the sample and the cantilever. Also, water layers on the surfaces in air can cause the tip of the cantilever to stick to the sample due to capillary forces. This often happens during imaging in air, in particular with small tip amplitudes. However, this effect is absent during imaging in vacuum and fluid. A damping model approach is outlined in [110] and a multi-mode air damping analysis can be found in [111]. For rectangular cantilevers with a tip, the modal stiffnesses and mode shapes in higher eigenmodes are found to be different in air and water [112].

2.2 Cantilever Theory

2.2.1 Beam Theories

The choice of an appropriate model depends on the requirement on its accuracy to represent the cantilevers' behavior. Dynamic and static beam equations exist, where the former one differs by additional time dependent terms. In the following, only the dynamic beam equations are discussed.

The dynamic Euler-Bernoulli beam theory models the effect of translational inertia and bending strain [113]. It is known to be accurate for slender beams, where the slenderness ratio is defined as the ratio of width to thickness. The literature gives different definitions of non-slender beams, whose values range from <100 to <10. The Euler Bernoulli beam including internal and external damping as well as actuation and surface forces can be represented as [87]

$$EI\frac{\partial^4}{\partial x^4}\left(z(x,t)+\alpha_1\frac{\partial z(x,t)}{\partial t}\right)+\rho A\frac{\partial^2 z(x,t)}{\partial t^2}+\alpha_0\frac{\partial z(x,t)}{\partial t}=\delta(x-L)\left(F_{act}(t)+F_{ts}(d)\right), \tag{2.1}$$

where $z(x,t)$ is the beam displacement, E the modulus of elasticity, I the area moment of inertia, ρ is the mass density, A the rectangular cross section. x is the coordinate along the beam, t the time variable and L the length of the cantilever. a_0 and a_1 represent the external and internal damping, respectively [103, 104]. $F_{act}(t)$ and $F_{ts}(d)$ are the actuation force and tip-sample interaction, respectively. The first term $EI\frac{\partial^4}{\partial x^4}(\dots)$ only applies in the case of a homogeneous beam with rectangular cross section. For a non-homogeneous beam, this term expands to $\frac{\partial^2}{\partial x^2}EI\frac{\partial^2}{\partial x^2}(\dots)$.

For higher accuracy, the Rayleigh beam adds rotational inertia to the Euler-Bernoulli beam. AFM cantilevers are continuously scaled down to supply higher first resonances. This also makes cantilevers less slender, since thickness and length do not scale by the same factor, with the thickness shrinking less. The Euler-Bernoulli and Rayleigh beams give similar errors in predicting the behavior of such beams. They appear stiffer and therefor tend to overestimate the frequency response, in particular at higher eigenmodes.

A different model, the shear model, adds the shear strain to the Euler-Bernoulli beam. Although now lacking the rotational inertia, it has a higher accuracy towards non-slender beams. Finally, the Timoshenko beam model combines all effects and reaches the highest accuracy [114–122]. In terms of non-slender, rectangular beams, the shear force and Timoshenko model give similar results, meaning the effect of the rotational inertia is small. The model uses two dependent variables, the transverse bending and the bending angle of the cross section for incorporating the shear strain. The result is a coupled partial differential equation. In case of a homogeneous beam, the equation can be reduced to a uncoupled equation, where the angle of displacement disappears. The velocity proportional viscous damping has been considered in the last term on the left side of the equation [118, 123]:

$$\frac{EI}{\rho A}\frac{\partial^4 z(x,t)}{\partial x^4} - R_g^2\left(1+\frac{E}{KG_s}\right)\frac{\partial^4 z(x,t)}{\partial x^2 \partial t^2} + R_g^2\frac{\rho}{KG_s}\frac{\partial^4 z(x,t)}{\partial t^4} + \frac{\partial^2 z(x,t)}{\partial t^2} + c\frac{\partial z(x,t)}{\partial t} = 0. \tag{2.2}$$

κ is the shear coefficient, G_s the shear modulus and $R_g = \sqrt{(I/A)}$ the radius of gyration. For rectangular beams, κ can be calculated as [118, 123]:

$$\kappa = \frac{5+5v}{6+5v}, \tag{2.3}$$

where v is the Poisson ratio of the fabricated material, which within the frame of this work is a dominant mono-crystalline silicon layer. Here, v is 0.22-0.28 depending on the orientation. The shear modulus can be calculated as $\frac{E}{2(1+v)}$.

Han *et al.* have compared non slender beams and obtained the errors between calculation and experiment [113]. The Euler-Bernoulli beam shows an error of +14% to +26% in the first eigenmode and +78% to +133% in the second eigenmode. In contrast, the Timoshenko beam presents errors of −1% to +2% and −1% to +6% in the first and second eigenmode, respectively.

2.2.2 Beam Discretization

The method of assumed modes separates the spatial dependent mode shape (eigenfunction) from the time dependent deflection of each point along the beam,

$$z(x,t) = \sum_{i=1}^{J} \Phi_i(x) y_i(t), \tag{2.4}$$

where J is the number of eigenmodes counted in and i the eigenmode index. All eigenmodes are considered linearly independent and therefore treated as a superposition, based on the orthogonality condition and the assumption of small amplitudes. Plugging 2.4 into the original beam equation, the separated spatial and temporal functions for each eigenmode are obtained. $\Phi_i(x)$ can be seen as a weighting factor normalized to 1, multiplied with the resonating second order system $y_i(t)$. By setting $x = L$ the deflection of the cantilever at the tip is addressed, resulting in $\Phi_i(L) = 1$.

Spatial Function

The general solution of the spatial function includes four terms with four unknowns C_1 to C_4. Applying the following boundary conditions of a cantilever beam

$$\begin{aligned} \text{Displacement at } x = 0\text{:} \quad & \Phi_i(0) = 0, & (2.5)\\ \text{Slope at } x = 0\text{:} \quad & \Phi_i(0)' = 0, & (2.6)\\ \text{Moment at } x = L\text{:} \quad & \Phi_i(L)'' = 0, & (2.7)\\ \text{Shear Force at } x = L\text{:} \quad & \Phi_i(L)''' = 0 & (2.8) \end{aligned}$$

to the set of general solutions, the characteristic equation

$$cos(\alpha_i L) + cosh(\alpha_i L) = -1 \tag{2.9}$$

can be found. The solution to the characteristic equation is dimensionless and can be obtained numerically or approximated by the Rayleigh-Ritz method. The solutions for the first three eigenmodes are: $\alpha_1 = 1.875$, $\alpha_2 = 4.694$ and $\alpha_3 = 7.855$. Using the dispersion relationship

$$\omega_{n,i} = \alpha_i^2 \sqrt{\frac{EI}{\rho A}}, \tag{2.10}$$

the natural frequency of each eigenmode with the relationship 1 : 6.28 : 17.86 : etc. can be retrieved. Further, applying the boundary conditions (Equations (2.5) to (2.8)) and results of the characteristic equation (Equation (2.9)) to the general solution, it leads to an equation describing the displacement mode shape of the beam:

$$\Phi_i(x) = \frac{1}{2}\left[cos(\alpha_i x) - cosh(\alpha_i x) - \frac{cos(\alpha_i L) + cosh(\alpha_i L)}{sin(\alpha_i L) + sinh(\alpha_i L)}(sin(\alpha_i x) - sinh(\alpha_i x))\right] \tag{2.11}$$

The corresponding normalized displacement of the cantilever for the first three transversal mode shapes is graphically shown in Figure 2.4.

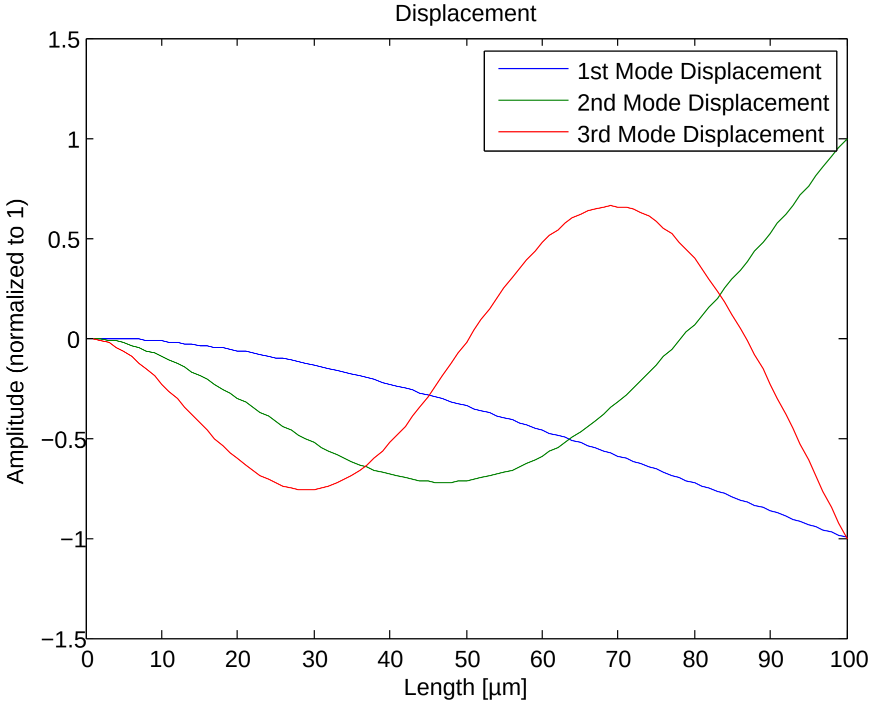

Figure 2.4: Normalized displacement of the cantilever for the first four transversal mode shapes based on the Euler Bernoulli beam theory. The plot is according to equation (2.11).

Temporal function

With the presence of damping, the second order temporal function can be written as

$$\frac{d^2 y_i(t)}{dt^2} + \frac{\omega_{n,i}}{Q_i}\frac{dy_i(t)}{dt} + \omega_{n,i}^2 y_i(t) = \frac{F_{act}(t)}{m_{eq,i}}, \tag{2.12}$$

where $\frac{\omega_{n,i}}{Q_i} = c$ is the damping term, Q_i the Q factor and $m_{eq,i}$ the equivalent mass of each eigenmode, and F_{act} the actuation force. The solution is in the form of $y_i(t) = A_i cos(\omega_i t)$. The Q factor is also often expressed in the form of a damping ratio $\xi_i = 1/2Q_i$.

Combination of Spatial and Temporal Functions into a Time-Dependent Solution

The combined solution at the tip of the cantilever can be described by the solution of the spatial function at the tip position $x = L$, multiplied by the temporal solution:

$$z(L,t) = \frac{1}{2}\sum_{i=1}^{J} A_i cos(\omega_i t)\times \times \left[cos(\alpha_i L) - cosh(\alpha_i L) - \frac{cos(\alpha_i L) + cosh(\alpha_i L)}{sin(\alpha_i L) + sinh(\alpha_i L)}(sin(\alpha_i L) - sinh(\alpha_i L))\right], \tag{2.13}$$

$$z(L,t) = \sum_{i=1}^{J} A_i cos(\omega_i t)\Phi(L)_i, \tag{2.14}$$

and since $\Phi(L)_i = 1$ due to normalization:

$$z(L,t) = \sum_{i=1}^{J} A_i cos(\omega_i t) \tag{2.15}$$

2.2.3 Cantilever as Harmonic Oscillators

In the following, the time dependent part of the beam model is further addressed. Based on equation (2.12), the frequency dependent amplitude of each eigenmode can be determined to

$$A_i(\omega) = \frac{F_0/m_i}{\sqrt{(\omega_{eff,i}^2 - \omega^2)^2 + (\omega\omega_{eff,i}/Q_{eff,i})^2}} \tag{2.16}$$

and the phase shift to

$$\tan\varphi_i(\omega) = \frac{\omega\omega_{eff,i}/Q_{eff,i}}{\omega_{eff,i}^2 - \omega^2}. \tag{2.17}$$

The coefficients $\omega_{eff,i}$ and $Q_{eff,i}$ are the effective natural frequency and Q factor, respectively. They depend on whether the cantilever is free in air or in the proximity of a sample surface [87,124]. For example, $\omega_{eff,i}$ can be calculated through $\sqrt{k_{eff,i}/m_i}$, where $k_{eff,i}$ is the effective spring constant under the influence of the sample surface forces. Here, $k_{eff,i} = k_{eq,i} + k_{ts}$, where $k_{eq,i}$ is the equivalent dynamic spring constant in the i$^{\text{th}}$ eigenmode and k_{ts} the equivalent spring constant of the tip-sample interaction. In the absence of a sample, $\omega_{eff,i} = \omega_{n,i}$ and $Q_{eff,i} = Q_i$.

Hence, the influence of the sample's force gradient on the canitlever's natural frequency is a combination of conservative and dissipative forces. Attractive forces lead to a decrease in frequency, whereas repulsive forces cause a frequency increase. This results in the overall frequency change and amplitude drop of the AM-Signal during tapping mode imaging [87].

Residual or added stress on the cantilever surface can additionally influence its natural coefficients [125–129]. The throughout this work used bimorph cantilever is fabricated of different materials that can have residual stresses within the layers. Also, the actuator is based on an electrical current induced heat expansion that introduces additional stresses [130]. The tip at the free end of the cantilever has an influence on the dynamics as well, particularly in a combination of small cantilever and comparably large tip [131].

The maximum amplitude appears at the cantilever's resonance frequencies. It is very close to the natural frequency for high Q factored cantilevers. However, for low Q factors the resonance frequency can be substantially lower than the natural frequency. The relationship based on the damping is

$$\omega_{r,i} = \omega_{n,i}\sqrt{1 - \frac{1}{2Q_i^2}}. \tag{2.18}$$

The damped frequency $\omega_{d,i}$ is slightly different with $\omega_{d,i} = \omega_{n,i}\sqrt{1 - 1/(4Q_i^2)}$. The phase will always coincide with the natural frequency at a phase lag of 90 degrees, although its shape is greatly influenced. The cantilever, as any resonating system, requires a Q factor of >1/2 to show oscillations (underdamped system).

The poles of each eigenmode modeled as separate second order systems can be determined to

$$p_{i1,2} = -\frac{\omega_{n,i}}{2Q_i} \pm \sqrt{\left(\frac{\omega_{n,i}}{2Q_i}\right)^2 - \omega_{n,i}^2} = \omega_{n,i}\left(-\frac{1}{2Q_i} \pm \sqrt{\frac{1}{4Q_i^2} - 1}\right). \tag{2.19}$$

The Q factors are a measure of the energy dissipation relative to the cantilever's oscillation frequency in a specific eigenmode. The dissipation rate can be expressed as an exponential time constant τ_i, as in

$$\tau_i = \frac{2Q_i}{\omega_{n,i}} = \frac{1}{\xi\omega_{n,i}}. \tag{2.20}$$

Hence, the Q factor can be determined by the oscillatory decay proportional to $e^{-t/\tau}$. Alternatively, the center frequency of the resonance peak in the frequency domain is divided by its bandwidth, evaluated at its half-power points (70.7% of peak amplitude) on both sides of the curve. The zeros of the system depend on, for example, the position of the sensors and actuators along the cantilever beam [132]. Further modeling aspects as well as comparisons of point-mass and continues models can be found in [133–140]. Non-linear modeling and analysis are outlined in [88, 141]. It allows for the consideration of effects such as discontinuities of the cantilever amplitude during the approach in the tapping mode. Gauthier *et al.* treat a case for the non-contact mode in [142].

2.2.4 Cantilever Sensors

Often, cantilever sensors do not measure its displacement directly, but a quantity that is proportional to it. For example, a laser preferably focused on the end of the beam measures the slope, which is the first derivative of the displacement. In contrast, a piezo-resistive sensor located at the base of the beam measures the moment proportional strain/stress. The latter one is of special interest as the cantilevers throughout this work are equipped with piezo-resistive sensors.

Laser Sensor

The laser is reflected from the backside of the cantilever and the response is proportional to the slope of the beam ($\frac{d\Phi_i(x)}{dx} = \Phi_i(x)^{'}$)

$$\Gamma_i(x) = \Phi_i(x)^{'}. \tag{2.21}$$

Figure 2.5 is the slope of the first three transversal mode shapes according to the Euler Bernoulli beam theory. As indicated earlier, the best location for the reflecting laser spot is at the free end of the lever at $x = L$. However, different locations result in different sensitivities and slope nodes can be utilized to mask out specific eigenmodes.

A simple photo-diode sensor for the detection of transversal bending is horizontally split in 2 halves. Due to the vibrations hence varying slope at the end of the beam the laser will periodically move over the diode's upper and lower half. The output signal is

$$V_{out} = GH\frac{Z_u - Z_l}{Z_u + Z_l}\sum_{i=1}^{J}\Gamma_i(x), \tag{2.22}$$

where Z_u is the upper half, Z_l the lower half, G a gain through signal amplification and H a gain that depends on the laser diode, sensor configuration and its alignment.

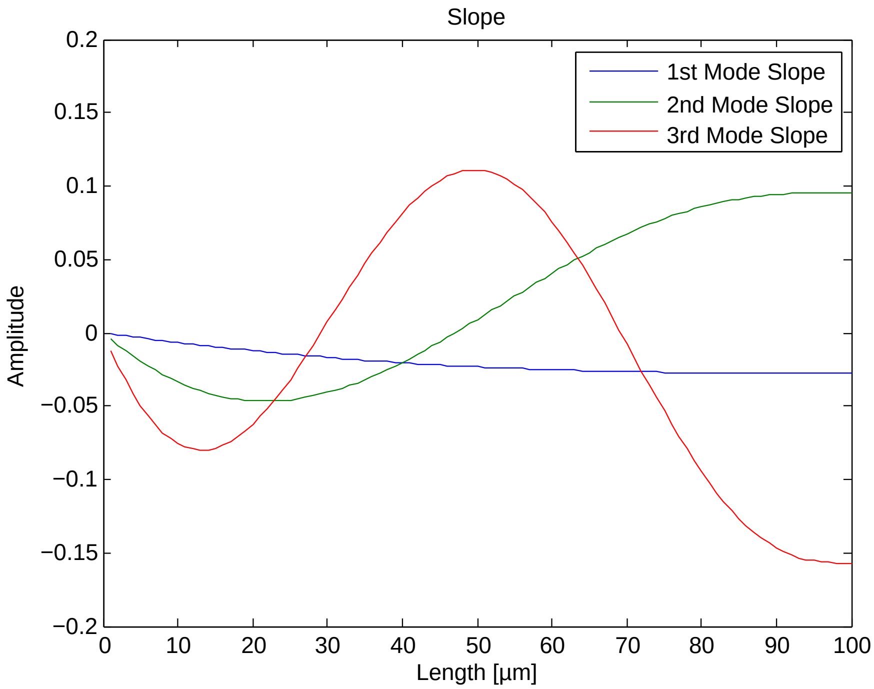

Figure 2.5: Slope of the beam calculated from normalized displacement for the first four transversal mode shapes according to the Euler Bernoulli beam theory.

Piezo-Resistive Sensor

Resistors based on the piezo-resistive effect change their resistance based to applied stress. Bending of the beam results in material independent strain, which further leads to material dependent stress. For every eigenmode to be detected, the potential sensors need to be located away from the corresponding strain nodes. Strain eigenmodes are proportional to the second spatial derivative of the cantilever's displacement (moment in the cantilever):

$$\Psi_i(x) = \Phi_i(x)''. \tag{2.23}$$

The function is linear throughout the thickness of the cantilever and either of stretching or compressing nature, where the neutral/central plane is strain free. Figure 2.6 indicates the strain mode shapes for the first three transversal eigenmodes according to the Euler Bernoulli beam theory.

The moment in a lever is defined as

$$M_i(x) = EI\Psi_i(x), \tag{2.24}$$

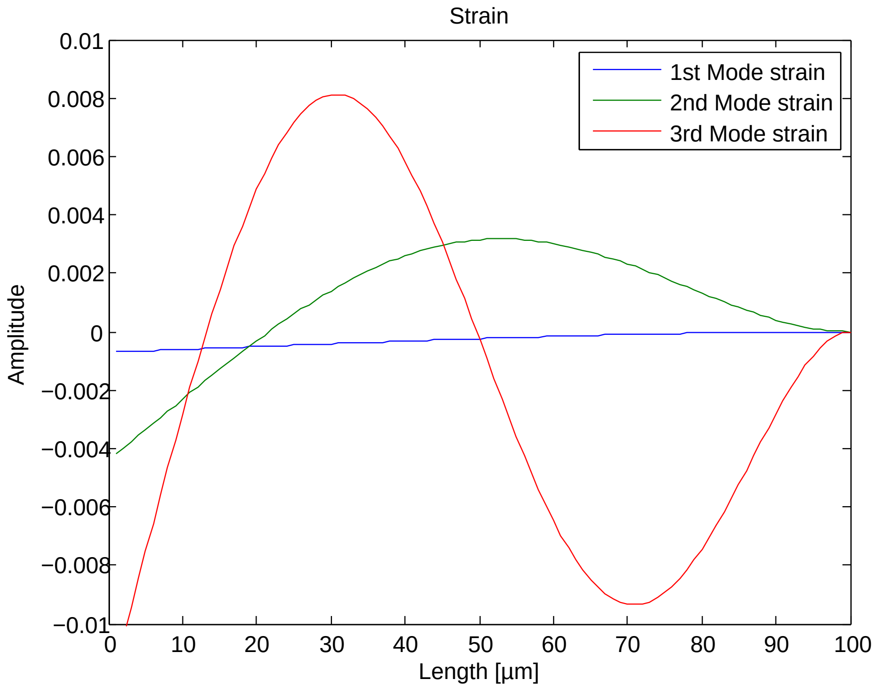

Figure 2.6: Strain of the beam calculated from normalized displacement for the first four transversal mode shapes according to the Euler Bernoulli beam theory.

and the stress as

$$\sigma_i(x) = \frac{T}{2}\frac{M_i(x)}{I}, \tag{2.25}$$

where T is the thickness of the cantilever. The highest stretching/compression occurs on the surfaces of the beam. Thus, the thickness from the neutral axis to the surface ($\frac{T}{2}$) is to be taken into account. Since the sensor has a length l_p, which is covering a part of the cantilever surface, an average stress based on its length is

$$\bar{\sigma}_i = \frac{\int_0^{l_p} \sigma_i(x)dx}{l_p}. \tag{2.26}$$

Superposition of the average stresses of all considered eigenmodes combined with the proper piezoresistive coefficient results in a resistance variation

$$\Delta R = R \sum_{i=1}^{J} \bar{\sigma}_i \pi_l. \tag{2.27}$$

Here, ΔR and R is the variable resistance and nominal resistance of the piezo-resistors, respectively. The best location for stress sensors is therefore at the base and surface of the beam. The stress sensor can be placed in a Wheatstone bridge configuration. Different possibilities exist to configure the bridge, such as forming two of the four resistors as a stress sensor, as in Figure 2.7. The remaining resistors could be placed away from the base of the cantilever. If all resistors match, the output of the Wheatstone bridge is then

$$V_{out} = V_s G \left(\frac{R}{2R + \Delta R} - \frac{R + \Delta R}{2R + \Delta R} \right), \tag{2.28}$$

where V_{out} is the bridge output voltage and V_s its supply voltage. The bridge output voltage is possibly amplified, which results in an additional gain G. However, it is beneficial to match the resistances closely and introduce a second variable resistor in the bridge to increase sensitivity. Thus, all resistors can be fabricated close to each other onto the cantilever and with a similar fabrication technique/step, e.g. as implanted semiconductors. Piezo-resistive sensors have been previously used to achieve atomic resolution in AFMs [143].

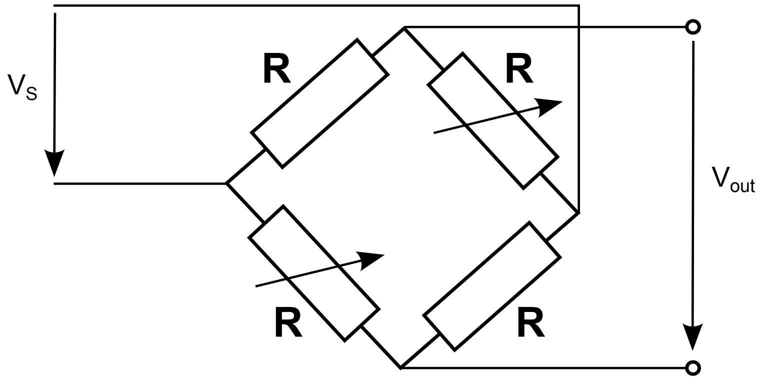

Figure 2.7: Piezo-resistive Wheatstone bridge with two out of four stress-sensitive resistors.

2.2.5 Noise Spectrum

Cantilevers are subject to various different noise sources. They determine the minimal detectable signal. Hence, imaging nanometer sized object requires probes with very low noise characteristics. Figure 2.8 indicates the different noise spectra. The Johnson noise is associated with electrical circuits and based on thermal excitation of charge carriers. This applies to electrical circuits sensing and amplifying the cantilever sensor signals. The thermo-mechanical noise, e.g., is created by molecular movement [144, 145]. It depends on coefficients such as mass, resonance frequency, temperature and acceleration. It also depends on the Q factor of the sensor, with higher factors reducing the noise power. A multi-mode noise analysis is given in [146] and a discussion in respect to active Q control in [101].

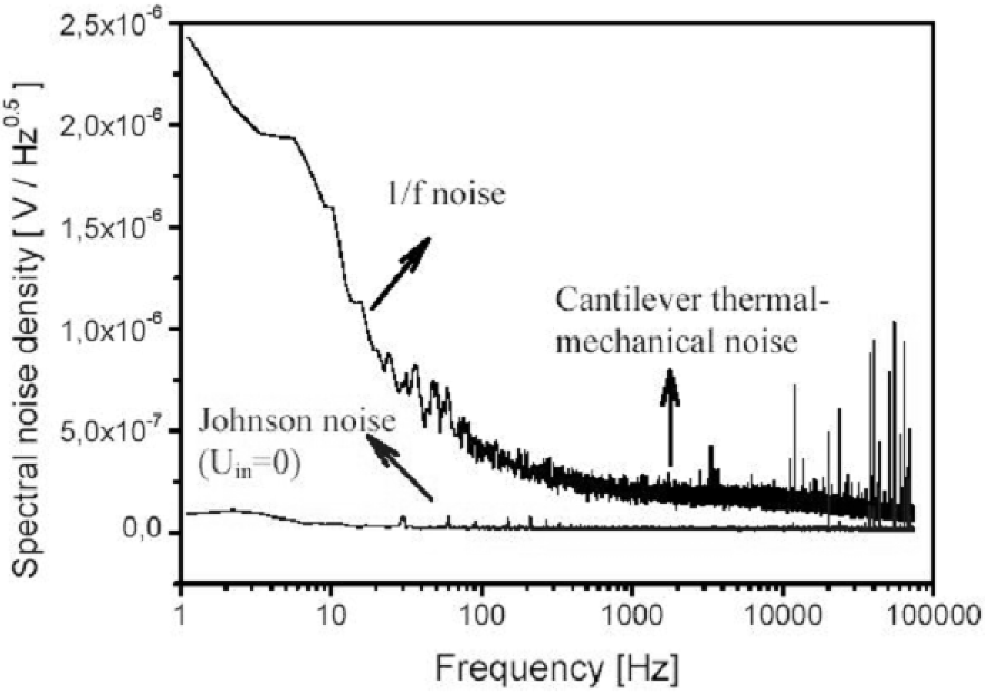

Figure 2.8: Cantilever subject to various noise source with the indicated spectra [144].

2.3 Obtaining a Proper Cantilever Model

The importance of an accurate model has various reasons. First, with a mathematical representation it is possible to analyze the system and predict its output on specific inputs, without the need to carry out the experiments on the physical AFM system. Further, the model can be used to design and simulate a compensator for achieving a desired behavior in the physical system such as, e.g., an increased imaging rate or minimal tracking error. In addition, the model can be actively used in model-based control approaches, such as the Kalman filter [147]. Here, the states of a physical system with a noisy sensor are estimated in a trade-off between cantilever dynamics and model dynamics. A model of the cantilever can be obtained by various methods, as described below. Previous work in estimating the transfer function and state-space model of AFM cantilevers are e.g. presented in [148, 149].

2.3.1 System Identification based on Time Domain Responses

By exciting a system with a known signal pattern, such as an Random Binary Signal (RBS), it can be combined with the response to compute the transfer function. System Identification models such as the ARX, ARMAX and State-Space Methods can be used for an estimation [150,151]. The success of the model identification depends, among others, on the set model order. Generally, a minimum order model is desired that still sufficiently describes the system.

2.3.2 System Identification based on Frequency Domain Responses

This method is similar to the Time Domain identification with similar models that can be used to estimate the system in the frequency domain [150,151]. The difference is the frequency dependency rather than the time dependency. In later chapters, this method is a preferred choice as the frequency domain signal is commonly obtained by AFMs frequency sweeps. However, in particular for the design of model based compensators, one needs to be cautious to obtain the model properly. The frequency sweep from the AFM software might have different components in the loop that results in an improper model. Ideally, the identification step uses the same hardware loop as the compensator implementation to ensure matching magnitudes and phases.

2.3.3 Observing the Resonances

The resonance sweep can also be observed and its coefficients extracted. Resonance frequency, damping, gain (peak of the resonance dependent on the Q factor) and phase of each eigenmode can be determined and matched with a second order transfer function. The natural frequency and Q factor, for example, could be calculated based on the frequency sweep obtained either with the AFM software or compensator hardware. In contrast, the gain and phase obtained by a frequency sweep might be incorrect. Here, a sinusoidal excitation from within the compensator hardware can lead to proper loop phases and gains.

In case of a frequency sweep from within the compensator hardware, the gain can be obtained by using the second order transfer function. Here, the equation is solved by plugging in the known coefficients and solving for the unknown gain K at the natural frequency ω_n, based on the measured magnification g:

$$\frac{Y(j\omega_n)}{U(j\omega_n)} = g = \frac{K\omega_n^2}{(j\omega_n)^2 + j\frac{\omega_n^2}{Q} + \omega_n^2} => K = \frac{g}{Q}, \tag{2.29}$$

Also, the specific phase of each resonance can be calculated. However, it will be difficult to relate the phase shift to the zeros in the transfer function. As a remedy, a transfer function with the proper natural frequency, Q factor and gain can be converted into frequency domain data consisting of magnitude and phase. The phase can then be artificially modified to match the true phase of the system. Consecutive frequency domain system identification incorporates the true zeros in the resulting transfer function.

Alternatively, by using sinusoidal actuation signals at the resonances, a cross-correlation can be formed of both the actuation and sensor signals. Thus, this allows the computation of the phase and gain at the cantilever's resonances. A relatively long excitation signal of more than 10 ms is beneficial to suppress the random noise of the sensor signal. As with the frequency sweep case, the zeros can be added to the transfer function by a phase matching and consecutive frequency domain system identification.

Different methods for obtaining the cantilever coefficients, mainly for the spring constant k, are often based on the observed resonance frequency and explained in [152–159].

2.3.4 Equivalent Point Mass Models

Theoretical derivations and Finite Element Method (FEM) simulations have led to equivalent spring constants and masses for first and higher resonances, leading to point mass models representing each eigenmode. For example, Melcher *et al.* have derived analytical expressions based on the Euler Bernoulli beam and validated the results with simulations [160]. Here, the equivalent mass is determined by $m_{eq,i} = m_r/4$, where m_r is the total mass of the cantilever. The equivalent spring constant of each eigenmode can be determined by $k_{eq,i} = k_s\alpha_i^4/12$, where $k_s = 3EI/L^3$ is the static spring constant and α_i the i^{th} solution of Equation (2.9) on page 17. For the first three eigenmodes, this results in the spring constants of $k_{eq,1} = 1.03 \times k_s$, $k_{eq,2} = 40.5 \times k_s$ and $k_{eq,3} = 317 \times k_s$. Hence, the equivalent spring constant increases with higher eigenmodes, making the cantilever to appear stiffer. Additional methods are introduced in [161–163]. The Q factor based on damping models and beam theories is theoretically derived in [104]. Although the above methods are very useful for theoretical studies involving cantilevers, they are hard to be used in modeling the behavior of practical applications. For example, it does not consider additional influences from electronics and mechanics around the cantilever and the resulting and phase modifications. In addition, the analytical expression can only be derived for relatively simple beams.

2.4 Control of Resonant Dynamic Systems

The dynamics of a resonant system can be modified by changing the Q factor, the natural frequency or both simultaneously. Here, an added feedback of the sensor output to the cantilever input is necessary to modify the internal coefficients [164]. The following example is based on a cantilever modeled as a resonating second order system, however, it is valid for a system of any order. Figure 2.9 indicates two feedback possibilities, taken from the sensor output and fed back to the cantilever input.

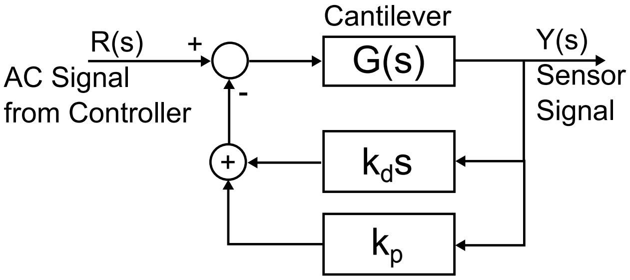

Figure 2.9: Feedback control on a resonating system.

The reference is a force proportional signal, that results in a displacement proportional signal after the double integration of the second order cantilever system. In the following two subsections, two types are evaluated for the case of a single eigenmode.

2.4.1 Q Factor Control

The Q factor can only be influenced by feeding back the derivative of the displacement proportional sensor signal, because the velocity is not measured directly. This is equivalent to feeding back the signal with a 90 degrees phase lead. The Laplace transformation of Equation (2.12) on page 18 for one particular eigenmode results in:

$$G(s) = \frac{Y(s)}{U(s)} = \frac{K\omega_n^2}{s^2 + \frac{\omega_n}{Q}s + \omega_n^2}, \tag{2.30}$$

with $U(s)$ and $Y(s)$ the Laplace transform of the input and output, respectively. According to Figure 2.9, the velocity feedback term is taken into account by

$$(R(s) - bsY(s))G(s) = Y(s). \tag{2.31}$$

After rearranging the equation and plugging in the expression for G(s), it results in

$$G(s) = \frac{K\omega_n^2}{s^2 + (\frac{\omega_n}{Q} + bK\omega_n^2)s + \omega_n^2}. \tag{2.32}$$

Figure 2.10(a) and (b) indicate the effect of the modified Q factor on the cantilever bandwidth. For example, by starting with a high Q factor, it can be lowered to achieve a faster response and thus tracking ability of topographical variations. Figure 2.10(c) indicates the result of above equations to achieve a desired Q factor. Further previous approaches can be found in [48, 165–169].

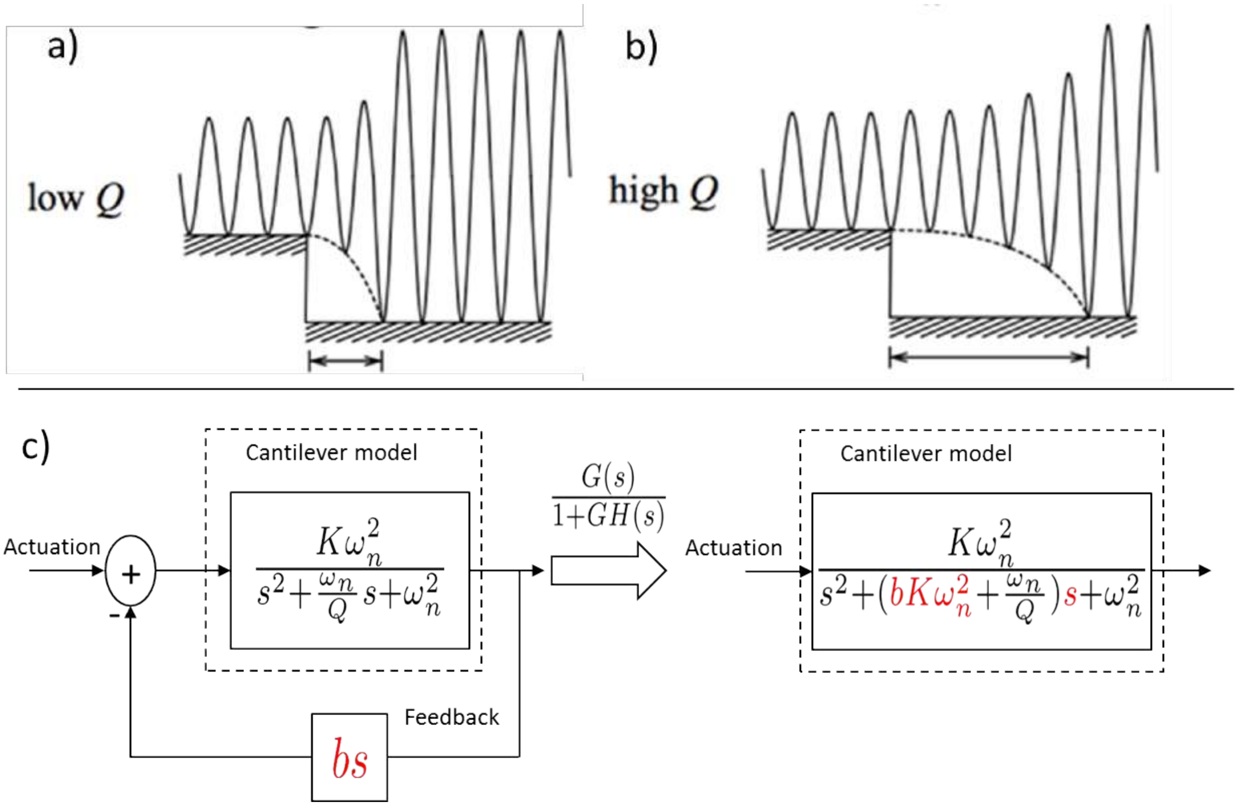

Figure 2.10: Q Control on a resonating system. a) and b) indicate the effect of different Q factors and thus bandwidths on the tracking ability during topography imaging. c) visualizes the the effect of the feedback on the system dynamics.

2.4.2 Frequency (F) Control

By only taking the displacement proportional signal into account and applying the same procedure as before, the transfer function

$$G(s) = \frac{K\omega_n^2}{s^2 + \frac{\omega_n}{Q}s + (1 + aK)\omega_n^2} \tag{2.33}$$

is obtained. According to Figure 2.9, a combination of both frequency and Q control can be implemented simultaneously, influencing both respective terms in the transfer function denominator simultaneously. The simultaneous modification of cantilever coefficients is particularly important for Chapter 5 that introduces a compensator design with such properties.

2.5 Compensator, Estimator and Full-State Feedback Control

In contrast to transfer functions, the state space modeling takes place in the time domain [164,170]. In addition, internal states are accessible, whereas this is not possible with transfer functions. The estimator is used to retrieve internal states of a system that are not measured through a sensor. In addition, measured states can be estimated as well to reduce the sensor noise. Full-state feedback control is based on the availability of all states and allows the arbitrary placement of poles within the complex plane, provided the actuator has the capability. The Separation Principle allows to separately design the estimator and controller, and combine the two to form the compensator. Here, the poles of the compensator are the combined poles of estimator and controller. The poles of the estimator should be at least two to five times faster than the controller poles. Otherwise, they might impact the dynamics of the controller and physical system.

2.5.1 Conversion between Transfer Function and State-Space Model

Transfer functions and state space representations can be converted into each other. State space representations are a system of first order differential equations that are not unique. They can be transformed into an indefinite count of different representations. In matrix form, a physical system can be represented as:

$$\dot{\mathbf{q}}(t) = \mathbf{A}\mathbf{q}(\mathbf{t}) + \mathbf{B}u(t), \tag{2.34}$$

$$y(t) = \mathbf{C}\mathbf{q}(\mathbf{t}) + Du(t), \tag{2.35}$$

where **A** is the state transition matrix containing the system dynamics and **B** is the input vector/matrix. Vector **q** contains the states and u the input. The output y is formed with the use of the output vector/matrix **C**. The term Du is a direct feed-through and is used to model inputs that have an direct influence on the output. As an example, the first eigenmode of Equation (2.12) on page 18 is converted into a state space representation. First, the second order system is represented as first order equations resulting in a total of two states (e.g. q_1 for the position and q_2 for the velocity):

$$\dot{q}_1(t) = q_2(t), \tag{2.36}$$

$$\dot{q}_2(t) = \ddot{y} = F(t)/m - \frac{\omega_n}{Q} q_2(t) - \omega_n^2 q_1(t), \tag{2.37}$$

where the notation $\frac{d^2q(t)}{dt^2}$ is equal to $\dot{q}(t)$. The state space representation in matrix form is then:

$$\underbrace{\begin{bmatrix} \dot{q}_1(t) \\ \dot{q}_2(t) \end{bmatrix}}_{\dot{\mathbf{q}}} = \underbrace{\begin{bmatrix} 0 & 1 \\ -\omega_n^2 & -\frac{\omega_n}{Q} \end{bmatrix}}_{\mathbf{A}} \underbrace{\begin{bmatrix} q_1(t) \\ q_2(t) \end{bmatrix}}_{\mathbf{q}} + \underbrace{\begin{bmatrix} 0 \\ \frac{1}{m} \end{bmatrix}}_{\mathbf{B}} \underbrace{F(t)}_{u} \tag{2.38}$$

$$y(t) = \underbrace{\begin{bmatrix} 1 & 0 \end{bmatrix}}_{\dot{\mathbf{C}}} \underbrace{\begin{bmatrix} q_1(t) \\ q_2(t) \end{bmatrix}}_{\mathbf{q}} \tag{2.39}$$

The above representation can be converted in any other representation. Common forms are the controller and observer canonical forms as well as the modal form. The former two are direct representations of the transfer function and easier to convert. However, they can have high conditioning numbers, called ill-conditioned. The internal states could experience high values which can be difficult to incorporate in a physical implementation. To keep internal voltages (analog system) or numerical values (discrete system) as balanced as possible, a well-conditioned state transfer matrix **A** and all other vectors is desired. The characteristic polynomial of the system is the determinant

$$\lambda(s) = \left| s\mathbf{I} - \mathbf{A} \right|, \tag{2.40}$$

whose roots are the eigenvalues (poles). **I** is the identity matrix. The state space system can be converted back to a transfer function by

$$G(s) = \mathbf{C}(s\mathbf{I} - \mathbf{A})^{-1}\mathbf{B} + D. \tag{2.41}$$

2.5.2 Optimal and Current/Predictive Compensator

An optimal compensator, or Linear Quadratic Gaussian (LQG), can be formed from a Linear Quadratic Estimator (LQE) and Linear Quadratic Regulator (LQR). The LQE can be a steady state Kalman filter, which design coefficients resemble the sensor and process noise [147, 171]. The relationship between the two values determines whether the trust is higher in the sensor measurement or in the model. They can be retrieved based on actual noise behavior or be seen as design parameters to find the best trade-off. The continues time Kalman filter is

$$\dot{\hat{\mathbf{q}}}(\mathbf{t}) = \bar{\mathbf{A}}\hat{\mathbf{q}}(\mathbf{t}) + \bar{\mathbf{B}}u(t) + \mathbf{L}(y(t) - \hat{y}(t)), \tag{2.42}$$

where $\hat{\mathbf{q}}$ and $\hat{y} = \bar{\mathbf{C}}\hat{\mathbf{q}}$ are estimated states and system output, respectively. $\bar{\mathbf{A}}$, $\bar{\mathbf{B}}$ and $\bar{\mathbf{C}}$ are the modeled system matrices. The LQR, similarly, tries to find the best compromise between a control action and cost. It can be incorporated as

$$u(t) = -\mathbf{K}\mathbf{q}(\mathbf{t}). \tag{2.43}$$

Both techniques are based on quadratic cost functions. However, the poles can also be directly set to desired specific values.

Depending on the relationship of compensator loop rate to sampling rate in a discrete system, either a predictive or current estimator can be implemented. The current estimator computation includes measurements up to the ones obtained during the current sampling iteration. It requires additional computational effort and is usually used in situations, where the compensator loop processing time is much lower than the sampling time. In contrast, the predictive estimator is lacking behind one sample. Hence its calculation is based on the samples of the previous iteration.

The current estimator including control law has the form

$$\begin{bmatrix} \mathbf{q}_k \\ \hat{\mathbf{q}}_k \end{bmatrix} = \begin{bmatrix} \mathbf{A} & -\mathbf{BK} \\ \mathbf{L}\bar{\mathbf{C}}\bar{\mathbf{A}} & \bar{\mathbf{A}} - \bar{\mathbf{B}}\mathbf{K} - \mathbf{L}\bar{\mathbf{C}}\bar{\mathbf{A}} \end{bmatrix} \begin{bmatrix} \mathbf{q}_{k-1} \\ \hat{\mathbf{q}}_{k-1} \end{bmatrix}. \tag{2.44}$$

In contrast, the predictive estimator including the control has the form

$$\begin{bmatrix} \mathbf{q}_k \\ \hat{\mathbf{q}}_k \end{bmatrix} = \begin{bmatrix} \mathbf{A} & -\mathbf{BK} \\ \mathbf{L}\bar{\mathbf{C}} & \bar{\mathbf{A}} - \bar{\mathbf{B}}\mathbf{K} - \mathbf{L}\bar{\mathbf{C}} \end{bmatrix} \begin{bmatrix} \mathbf{q}_{k-1} \\ \hat{\mathbf{q}}_{k-1} \end{bmatrix}. \tag{2.45}$$

The characteristic equation of the combined estimator and controller is

$$\lambda(s) = \left| z\mathbf{I} - \bar{\mathbf{A}} + \mathbf{L}\bar{\mathbf{C}} \right| \left| z\mathbf{I} - \mathbf{A} + \mathbf{BK} \right|, \tag{2.46}$$

which allows the separate design of estimator and controller, hence the separation principle.

2.5.3 State Controllability and Observability

Controllability means that the states of a system can be transferred from some initial state to any desired final state by the input in a finite time [172,173]. Thus, the actuator must be located away from the nodes of vibration. A placement at the node would mean a mode shape factor of zero, resulting in non-controllability of that eigenmode. The following test determines whether all modes can be controlled. A system is controllable if and only if

$$rank \begin{bmatrix} B & AB & A^2B & ... & A^{i-1}B \end{bmatrix} = i \tag{2.47}$$

has full rank.

A system is observable, if and only if

$$rank \begin{bmatrix} C & CA & CA^2 & ... & CA^{i-1} \end{bmatrix}^T = i \tag{2.48}$$

has full rank. It means that any initial state can be determined by a finite record of the output. If certain states are not controllable, but the uncontrollable part is stable, the system is stabilizable. Similarly, if certain states are not observable, but the unobservable part is stable, the system is detectable. In addition, the degree of controllability and observability can be important as well as the actuator capability. Actuators with saturation could mean that a specific state, starting from an initial state, can never be reached. If a system is weakly controllable, meaning a strong input is necessary to reach final states, the problem becomes even larger. All physical actuators and sensors do have limits and cannot be infinitively fast with infinite power, etc.

2.6 Signal Processing Aspects in Field Programmable Gate Arrays (FPGAs)

The FPGA is a powerful reconfigurable platform to integrate signal processing and control techniques with true parallel computation e.g. that is useful for filters. Large advances and cost reduction have made them a strong competitor to Central Processing Units (CPUs) with a variety of hardware description languages that can be used. In the following, two signal processing concepts are introduced that are used throughout this work, in particular in Chapter 5 for the compensator design.

2.6.1 Sample Rate Change

The sample rate in digital systems is often lowered to reduce the data rate and lower the computational effort. That is necessary, because often fast ADCs sample much faster than the algorithm loop rate. Hence, after incoming samples the sampling rate is reduced. After computation, the sampling rate is again increased again to meet the sampling rate of the DACs [174].

For a simple downsampling after the Analog-to-Digital (AD) conversion, one could simply take every M sample and use it for further processing:

$$y[n] = x[nM], \tag{2.49}$$

where n is the current sample and $x[n]$ the input data stream. However, aliasing can potentially be a problem. Usually, the ADC with its original sample rate has analog anti-aliasing filters that meet the Nyquist rate. By simply reducing the sample rate by taking every M sample, the frequency content in the signal is not reduced. It can be well above the Nyquist rate of the new sampling rate. This can be prevented by either an appropriate analog filter before the conversion or by a digital filter before the downsampling. Both reduce the bandwidth of the signal by a factor M to meet the new Nyquist rate. For example,the digital filter can be implemented as an Finite Impulse Response (FIR) filter. The new procedure including the filter is called decimation and is

$$y[n] = \sum_{k=0}^{K-1} h[k]x[nM-k], \tag{2.50}$$

where h[k] is the impulse response of the filter. The downsampling comes with an increased effective bit-width and improved SNR, which is due to the filtering. Each additional bit requires an oversampling factor of 4. Relating this to the downsampling factor M leads to $B = log_4(M)$, where B is the additional increase in resolution. The improvement of the SNR in dB due to total number of effective bits $B_{eff} = B_{ADC} + B$ is SNR $= 6.02 \times B_{eff} + 1.76$.

The interpolation inserts zeros between the samples in the reduced sampling domain to meet the sampling rate of the faster domain. Consecutive low-pass filtering smooths the results, recreating a proper signal:

$$y[n] = \sum_{k=0}^{K-1} h[n-kL]x[k], \tag{2.51}$$

where L is the integer factor for the sampling rate increase. M and L do not need to be the same factor and can be used to create non-integer factored sample rate conversions. A simpler version of the interpolation could store the sample of the lower sampling rate in a buffer. The sample will then be repeatedly read out by the faster sampling rate, until new sample is put into the buffer. This would resemble a upsampling technique, which is without filtering.

2.6.2 Floating Point Arithmetic

Floating point arithmetic is easily available on FPGAs and many Intellectual Property (IP) modules are developed for its usage in the different languages. A floating point number has a much higher dynamic range than a fixed point number of same bit size. Instead of incorporating the number at the given resolution, it is divided into a fractional and exponential part. However, rounding errors are still present. An example of implementing Floating-Point operations in FPGAs can be found in [175].

Single-precision Floating point arithmetic is of highest interest in the following work. It consists of a total of 32 bits, divided into 23 fractional bits for the significant precision, 8 bits exponent and 1 sign bit. The smallest and largest number that can be represented is approximately 1.2×10^{-38}

and 3.4×10^{38}, respectively. Thus, compared to a 32 bit fixed point number with a maximum range of around 4.3×10^{9}, the single precision floating point number has a much greater dynamic range. This is helpful to implement any algorithm in discrete systems, as saturation is less likely to occur. The precision of a 32 bits fixed point number can be higher or lower than a floating point number of same bit size, depending on the number stored.

2.7 Material Sensitive Imaging

Traditional material property mapping has focused on phase detection of the first transverse resonance. The phase sensitivity to compositional variations of the sample is generally accounted to non-conservative/dissipative tip-sample interactions [54–56, 176–179]. The Q factor has a great influence on the phase change at resonance and, hence, can improve the sensitivity in phase images. Monitoring the phase of higher cantilever eigenmodes has improved the cantilever's material sensitivity [57] [58]. In material contrast mapping, the tapping mode is usually used. This is since the non-contact mode is based on the attractive forces only that are not dependent on the elastic properties of the sample.

Modern methods of mapping material properties involve two or more cantilever eigenmodes at a time. Two major methods exist, where the first resonance obtains the topography of a sample surface and the response of the higher eigenmodes is used to obtain material specific information. The scheme is based on the assumption of small cantilever amplitudes, which can be treated as a superposition of its individual components. The first method worth mentioning is the excitation of the cantilever in the first eigenmode and extraction of the excited harmonics during imaging [61–64,66,180–182]. The second method is the actuation of the cantilever in two or more eigenmodes simultaneously by a superposition of the individual actuation signals (Bimodal AFM) [59, 67–72, 183–185]. The two methods are further introduced in more detail in the following subsections.

In both cases, the material properties, such as the Young's modulus, cannot easily be obtained quantitatively. Often, a reference material with known properties is measured and then compared to the sample under investigation. However, by detailed knowledge of all the cantilever and setup parameters, such as spring constants, tip shape and phase interpretation, the material property could be calculated.

One more promising method, but not further discussed, uses two actuation signals, both close to the first resonance of the cantilever [186, 187]. The intermodulation approach indicates sensitivity to material properties.

2.7.1 Higher Harmonic Imaging

In the regular tapping mode, the periodic impact of the tip onto the sample results in a non-linear tip-sample force function F_{ts}:

$$F_{ts}(r) = \frac{HR}{6\sigma^2}\left(-\left(\frac{\sigma}{r}\right)^2 + \frac{1}{30}\left(\frac{\sigma}{r}\right)^8\right), \tag{2.52}$$

$$F_{ts}(d) = \frac{4}{3}E\sqrt{R}d^{3/2}. \tag{2.53}$$

H, R, σ, r and d are the Hamaker constant, tip radius, atomic tip-sample distance, tip-sample separation and sample indentation, respectively [65]. Equation (2.52) is the tip far away from the sample and Equation (2.53) when indenting the sample. The resulting contact time mainly depends on the Young's modulus [182, 188]. It determines the magnitudes of the higher harmonics that are then excited in the cantilever. The harmonics appear in integer multiplies of the first eigenmode's actuation frequency. The higher eigenmodes directly influence the response of the cantilever, such that the harmonics in the vicinity of the eigenfrequencies are amplified. [66, 133, 189, 190]. In contrast, the first harmonic represents the average tapping force and depends on the cantilever and its actuation/set-point. Hence, it has a constant magnitude across different materials [65].

The periodic tip-sample force F_{ts} can be expanded into a Fourier series [65, 66]

$$F_{ts}(t) = \sum_{n=0}^{\infty} \alpha_n cos(n\omega_1 t) + \beta_n sin(n\omega_1 t). \tag{2.54}$$

The n^{th} harmonic force is determined by

$$F_{ts_n} cos(n\omega_1 t + \Theta_n) = \alpha_n cos(n\omega_1 t) + \beta_n sin(n\omega_1 t), \tag{2.55}$$

where α_n, β_n are the Fourier coefficients, ω_1 the driving frequency and Θ_n the harmonic phase. The magnitude of a specific harmonic force is

$$F_{ts_n} = \sqrt{\alpha_n^2 + \beta_n^2}. \tag{2.56}$$

The Total Harmonic Distortion (THD), a measurement of such coupling, is typically in the range of a few percent [190, 191].

Sahin *et al.* have numerically compared the amplitudes of excited harmonics on stiff, medium stiff and soft samples [65], where short contact times generate increased magnitudes at higher frequencies and vice versa. Here, the magnitudes of the harmonics are not yet mapped with the cantilever that experiences the contact with the sample. Hence, it is not yet accounted for the influence of the higher eigenmodes of the cantilever. Imaging in liquid rather than air indicates a higher harmonic response that can be useful for the investigation of biological samples [61,192]. It is desirable to quantitatively retrieve a sample's material properties from the higher harmonics, such as its stiffness [188]. However, this requires detailed knowledge of the overall AFM system. Hence, the cantilever's response is generally compared to a reference sample obtained beforehand.

2.7.2 Bimodal Imaging

The cantilever is actuated with an amplitude of several nanometers in the fundamental eigenmode and keeps a specific setpoint to intermittently contact the sample. Concurrently, the higher eigenmode oscillates with an amplitude of only a fraction of that. It probes the instantaneous effective frequency and amplitude, which is affected by the local tip-sample force gradient [70, 184]. The amplitude and phase of the higher eigenmode can be used to quantify, e.g., the Young's modulus based on the experienced forces of the sample. In particular the phase shift of the second eigenmode is one order of magnitude more sensitive to compositional variations of the sample than the first eigenmode [72]. Mostly, only one higher eigenmode is actuated simultaneously with the first one. Hence, it is called bimodal AFM.

The frequency shift and the tip-sample force gradient are, at a first approximation, related by

$$\delta v_2 = v_2 - v_{2-o} = \frac{k_{ts}}{2k_2} v_{2-o}, \tag{2.57}$$

where δv_2 is the frequency shift of the higher eigenmode response, v_2 is its instantaneous frequency, v_{2-o} is its free resonance frequency, k_2 is its harmonic force constant and k_{ts} is the local tip-sample stiffness, equal to the negative of the tip-sample force gradient.

For example, the effective frequency of the oscillating higher eigenmode in the vicinity of a sample surface is outlined in [70]. The reader can imagine a complete oscillation cycle of the first eigenmode. Then, the higher eigenmode's frequency is unperturbed when the tip is farthest away from the sample. It remains unperturbed until the tip begins to experience the attractive interactions towards the sample, which cause the higher eigenmode's frequency to decrease. At some point, the tip begins to experience repulsive interactions (negative force gradient) and the higher frequency increases up to the point of maximum tip penetration. This is also the closest point to the sample in the trajectory of the first eigenmode's vibration. While the first eigenmode's trajectory starts moving away from the sample the higher eigenmode's behavior is almost a mirrored compared to the preceding trajectory. From that, the tip-sample force gradients can be calculated and the force curve obtained through numerical integration.

More recent publications have started with trimodal actuations (three eigenmodes simultaneously). Here, the dissipation is much higher than in the bimodal oder single mode operation, compared at equal amplitude set-points in AM-AFM operation. This is accounted to the increased tip velocity and effective cantilever stiffness at the higher frequency [68, 184]. Solares *et al.* also outline the conservative and total force trajectories for single-mode, bimodal and trimodal operation in [68].

3 Experimental Setup

In this chapter, the experimental tools are introduced that are used for a variety of tasks throughout the following Chapters 4 to 9. They include two different AFM setups used for imaging and characterization, an interferometer for eigenmode shape and absolute amplitude measurements, a FIB for structural modifications of active cantilevers and two FPGA platforms to implement digital compensators.

3.1 Atomic Force Microscope

In this work, two different AFM setups are used. In both cases, the AFM consists of generators for the scanner's and cantilever's excitation signals as well as a feedback controller for keeping a specified distance between the sample and tip. High voltage amplifiers are needed for the piezo actuators and a computer software is used for parameter settings and plotting. Both AFMs use open loop scanners that need to be linearized before imaging. In this procedure, the hysteresis is determined and compensated for through parameters that change the excitation signal appropriately. Figure 3.1 shows the basic setup with its components that is valid for both AFMs. The following two subsections indicate the differences between the two systems.

AFM I

This AFM is a custom development, created by the scientists and engineers in our department in Ilmenau as well as by collaborators outside the university. The only exception is the commercial scanner with a range of $9\,\mu$m, namely 'microTRITOR' of Piezosystem Jena GmbH, Germany. Figure 3.2 is a photograph of the setup. This AFM is later used in Chapter 6 for the control of first and higher cantilever eigenmodes for imaging rate improvements.

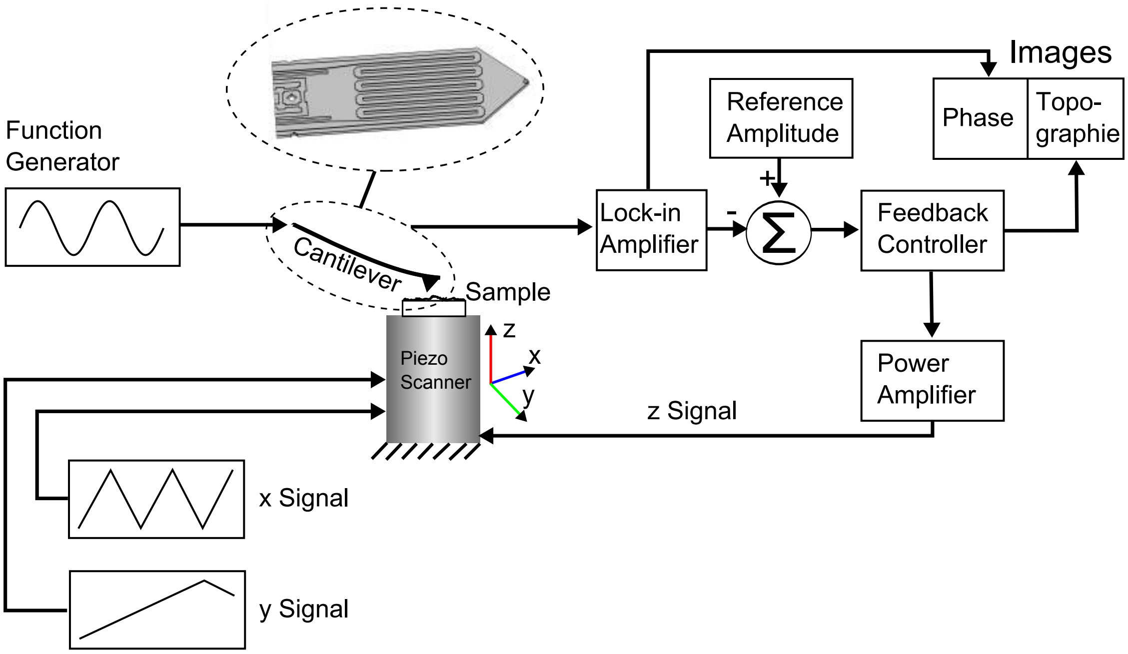

Figure 3.1: Experimental AFM setup with its basic components applying to the two different setups, in combination with fully integrated active cantilevers.

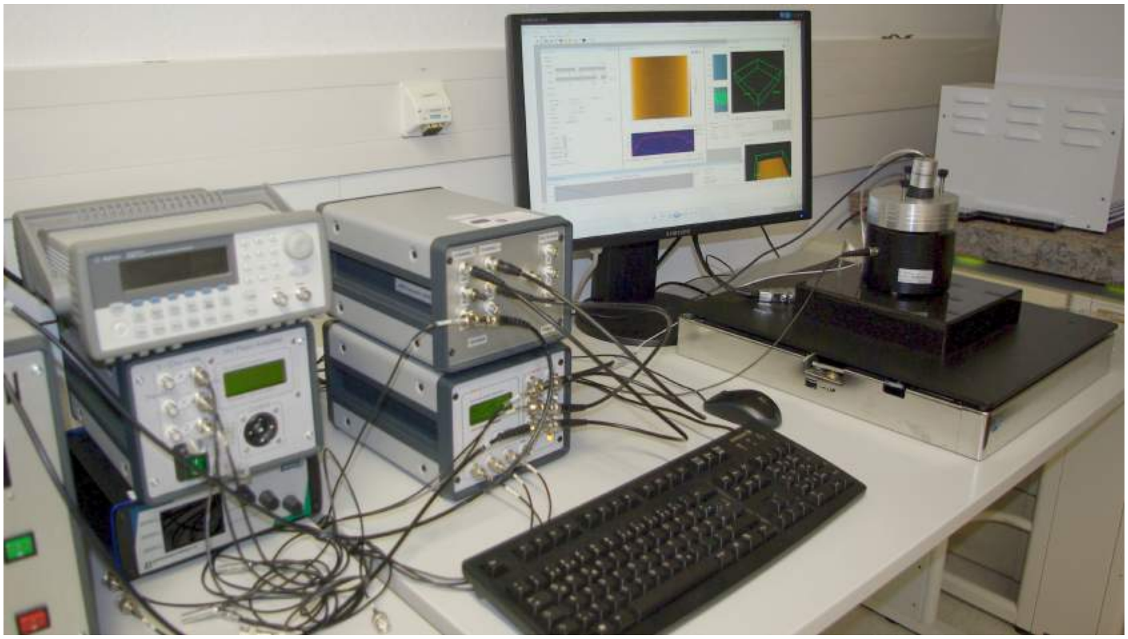

Figure 3.2: AFM I setup, with its different components such as controller, scanner, high voltage amplifier and control software.

AFM II

The second used AFM is a commercial microscope from Anfatec GmbH, Germany, in a custom setup combined with active cantilevers and an own developed pre-amplifier as well as a homemade scanner. The commercial part consists of the controller, high voltage amplifier and a computer containing additional hardware and control software. The custom scanner has a range of 30 μm. Figure 3.3 shows a photograph of the Anfatec AFM and some additional components attached to it. Figure 3.4 is the AFM scanning head with a mounted active cantilever and a sample attached to the scanner below. The scanner mounted to the cantilever head is not used here and since it is fixed during the experiments, its mass does not cause an influence on scanning speed. This AFM is used for the Multi-Eigenmode Control, Amplitude Demodulation and Harmonic Cantilever work in chapters 7, 8 and 9, respectively.

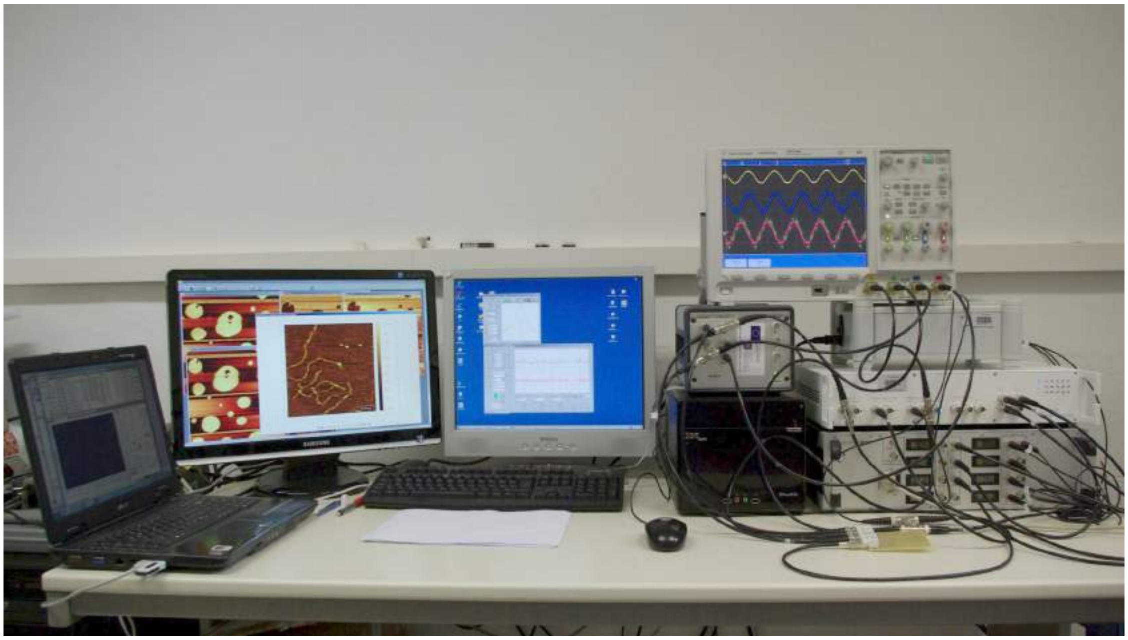

Figure 3.3: AFM II setup, a mix of custom made and commercial parts.

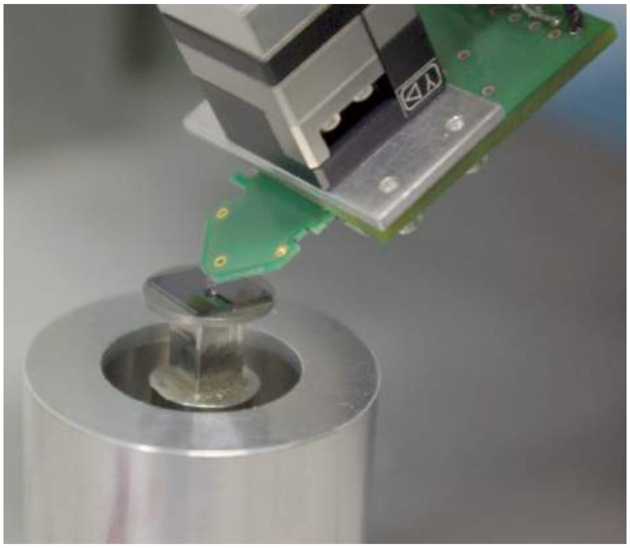

Figure 3.4: AFM II scanner and cantilever head. Only the bottom scanner is used in this work.

3.2 Active Microcantilevers

The active cantilevers used throughout the following Chapter have integrated actuation and sensing and are developed in our department in Ilmenau [11–15, 193]. Characterization and imaging performance in air and liquid are laid out in [39, 194], and compared to other types of cantilever sensors/actuators. The piezo-resistive stress sensors are located near the cantilever base and sense a tip displacement proportional signal, as outlined in Subsection 2.2.4. By organizing the sensors in a Wheatstone bridge formation a significant improvement in the deflection sensitivity is achieved [195]. The surface at the base of the cantilever represents the location with the maximum stress upon a given static bending or oscillation, compared to any other location along the beam. In addition, the Wheatstone bridge is formed around a fabricated hole in the cantilever that enhances the stress distribution in that area. The relation of static displacement at the tip (x=L) to output voltage can be stated as

$$V_{out}(t) = \frac{3\pi t_b E V_s}{L^2} z(L,t), \tag{3.1}$$

where t_b is the thickness and L the length of the cantilever.

The bimorph effect based actuation is achieved by a combination of materials with different heat expansion coefficients. A meander shaped layer effectively dissipates an applied current into heat. This forces the cantilever layers to expand and then bend vertically towards the material with the lower coefficient. By using a sinusoidal input Alternating Current (AC) voltage V_{ac} the cantilever's mechanical transverse oscillations peak at its first and higher resonances. The power dissipation is maximized by considering still acceptable drift in the measurements. The actuation is different from common piezo-stack actuation, because of the square dependency of the generated heat on the current. This generates additional frequencies beside the applied actuation. In most cases, a static DC voltage V_{dc} is added for proper operation, as it follows the relationship [11]:

$$P_{heater} = \frac{1}{R_{heater}}(V_{dc}^2 + 2V_{dc}V_{ac}sin\omega t + V_{ac}^2 sin^2\omega t). \tag{3.2}$$

Without a DC voltage, only the last term inside the parentheses remains in Equation (3.2), which is twice the actuation frequency. This would be difficult to implement with standard Lock-in amplifiers. The actuation and locked frequency differ that also prohibits a proper phase interpretation. However, this approach can be beneficial to prevent cross-talk between the neighboring actuator and sensor, as described in [11]. The actuation and sensing are explained in more detail in [144].

A major point is the noise power spectrum of the piezoresistive sensors. As the piezoresistive effect depends on the temperature [196], the resulting fluctuations on the cantilever sensor signal are of special concern. Two measures can be used to counteract this behavior. First, a temperature drift compensation has been introduced [195]. Second, piezoresistivity is significantly larger for low dopant concentrations. However, a high concentration can be used to achieve a low temperature dependence [197]. Also, the sensors are electrically isolated from the actuator and designed for minimum capacitive and thermal crosstalk. A thorough investigation is also done in [198]. Low noise is important for high resolution measurements and minimum detectable forces. Also, low noise requires less aggressive filtering, such as by the Lock-in amplifier, allowing higher filter bandwidths and thus faster feedback loops. The piezo-resistive sensor has to compete with other types of displacement sensors, most popular the laser deflection technique measuring the displacement proportional slope at the end of the cantilever. As a reference, the laser based sensing is also discussed in Subsection 2.2.4.

Figure 3.5 shows a typical active cantilever, where sub-figure 3.5(a) is a schematic of the cantilever that serves as a model for the simulations in Chapter 9. Figure 3.5(b) is an image obtained by an optical microscope, showing the entire silicon chip that is glued onto a Printed Circuit Board (PCB). An area indicated in Figure 3.5(b) is magnified in Subfigure 3.5(c), where the cantilever itself is seen in an SEM image. Visible are the tip, heating meander towards the free end, structures for crosstalk prevention between actuation and sensors, and the Wheatstone Bridge at the base.

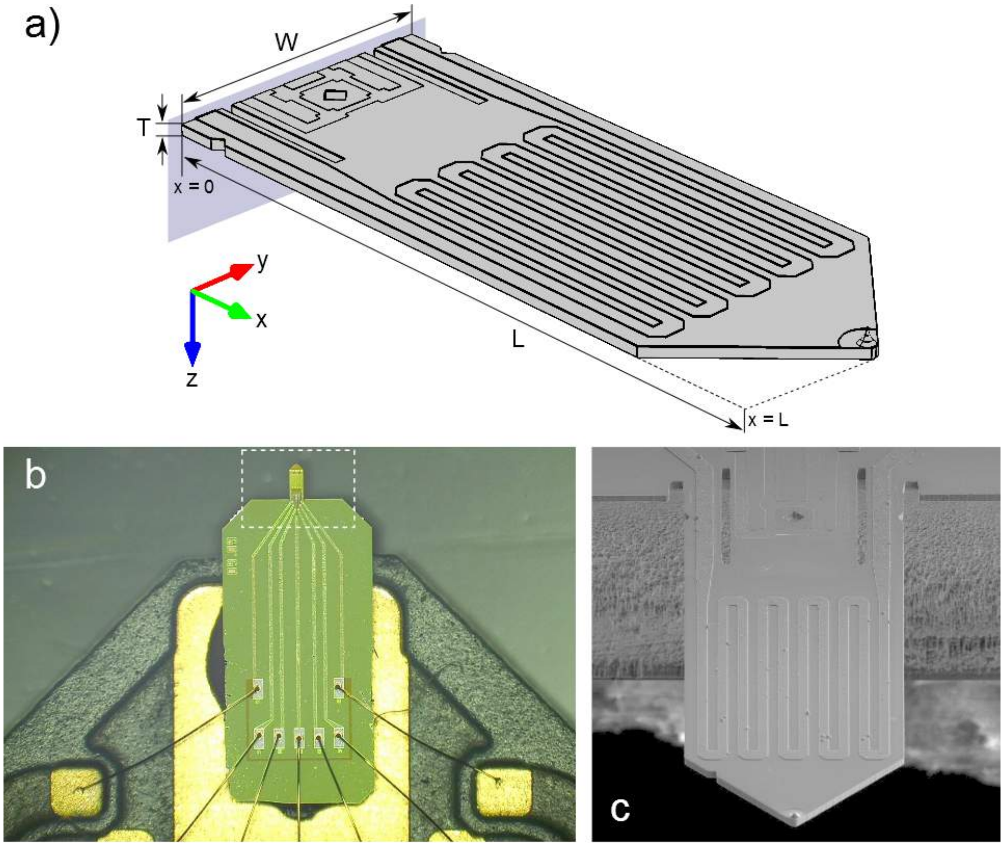

Figure 3.5: (a) is a model of the cantilever created in Autodesk Inventor, (b) an optical image and (c) an SEM magnification of the indicated area in (b).

The cantilevers are fabricated through a series of micromachining processes involving consecutive steps of deposition, lithography, ion implantation and etching. Advantages are gained from recent high performance cantilever bulk fabrication technologies [14, 199]. After formation of the tip by reactive ion etching the electrical shielding to prevent crosstalk is implanted. The piezoresistors are defined by a standard CMOS doping procedure, followed by a thermal annealing step. Then, a low stress silicon nitride layer is formed by Plasma-Enhanced Chemical Vapor Deposition (PECVD) for electrical passivation. The meander shaped metal actuator is placed on top of the passivation layer. The contact pads are realized thereafter. The cantilever thickness is defined by a backside anisotropic etching step. Finally, the cantilever's lateral dimensions are defined by a gas chopping etch process [200, 201]. The fabrication is outlined in more detail in [15, 193]. In the end the fabricated cantilever's layers consist of single-crystalline silicon with a thickness of about 5 μm, 700 nm thick SiO_2, a 500 nm thick Al meander and a final 200 nm Si_3N_4 passivation on top. Nominal lateral dimensions are 360 μm in length and 140 μm in width with a sharp tip of 8 μm high. Ideally, the tip has atomic sharpness.

Figure 3.6 shows the active cantilever connected to electronic components required for actuation and sensor post-processing. The *Direct Digital Synthesis (DDS)* excites the cantilever at its resonances. The *Bridge Supply* is a static voltage resulting in a deflection signal at the inputs of the differential amplifier G with superimposed resonant signals. After amplification, the signal is processed through other components, such as the demodulator.

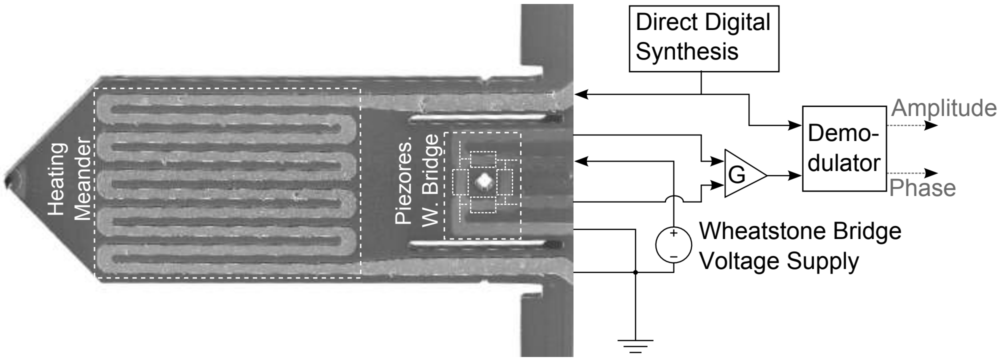

Figure 3.6: Active cantilever (SEM image) and its connections to electronic components for actuation and sensor post-processing.

3.3 Interferometer

An interferometer is used to measure the mode shapes of different cantilevers in Section 4.3 and the FIB modified cantilevers in Chapter 9. In addition, it is used to measure the amplitude at the tip of the cantilever to determine imaging conditions and the relationship to the actuation signal (Section 4.3). The particular device is a SIOS GmbH, Germany, interferometer (Nano Vibration Analyzer) with a <0.1 nm resolution that is mounted on an anti-vibration table. The laser can be focused onto the cantilever, which in turn is mounted on a stage adjustable by three micrometer screws, as shown in Figure 3.7. The inlet of Figure 3.7 indicates the mounted cantilever in front of the interferometer optics with the focused laser on its tip.

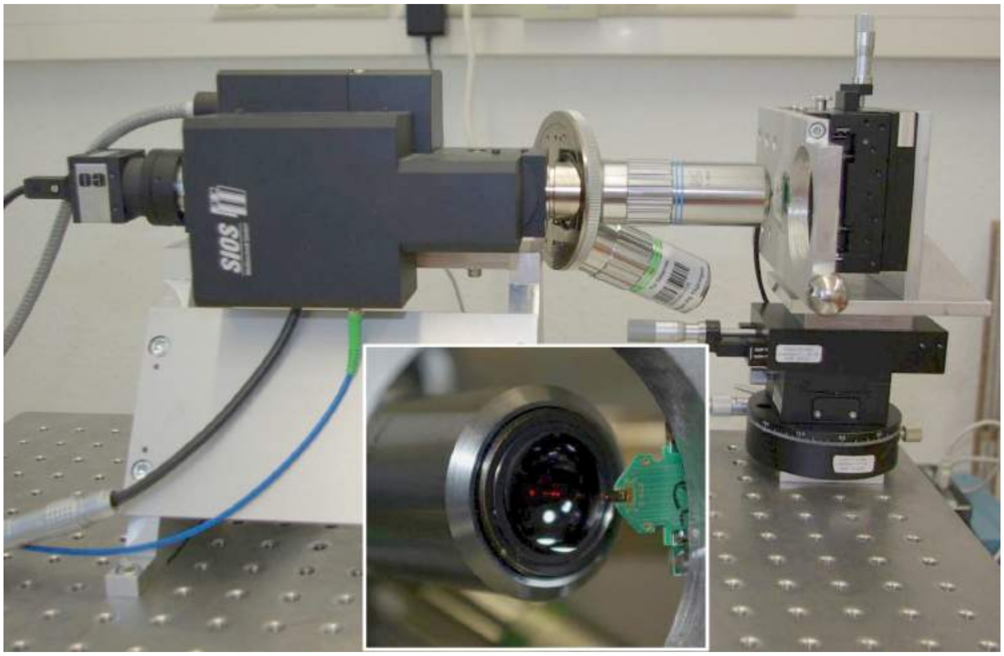

Figure 3.7: Interferometer setup on an anti-vibration table with a focused laser on a mounted cantilever (subfigure).

3.4 Focused Ion Beam

A FIB is utilized to structurally modify the active cantilevers. This is to achieve a desired dynamic behavior, as will be described in 9. Figure 3.8 is a photograph of the tool, which is a Helios NanoLab 600i. The dual beam FIB can generate both an electron and an ion beam. In contrast to single beam FIBs, the separate electron beam allows the non-invasive navigation and investigation of a sample without the need of the potentially damaging ion beam. Hence, the Helios can also be used as a regular SEM. A typical ion beam acceleration voltage and current is 30 kV and 2.3 nA, respectively, and typical electron beam settings are 5 kV and 86 pA. The gas pressure during operation is typically around 2×10^{-7} mbar.

Figure 3.8: FEI Helios 600i FIB tool for nano-manipulation of samples.

For milling, the ion species is Gallium (Ga^+) and the gases provided for deposition are carbon, platinum and Tetraethyl Orthosilicate (TEOS). With the help of the electron beam, a part of the TEOS is converted to SiO_2 that can be deposited as an insulator on the sample surface. The other part is gaseous and sucked out by the vacuum pumps. Iodine can be used as a precursor gas such that it combines with milled material and prevents it from a deposition back onto the sample.

3.5 FPGA Platforms

The discrete compensator developed in Chapter 5 and used in Chapters 6, 7 and 8 is implemented into FPGAs. Advantages over analog circuits are the fast prototyping as well as simple modifications of the design and controller/filter coefficients. After the AD conversion, no additional noise is introduced and the design is independent of device drift and uncertainties. Compared to an analog circuit with similar functionality, a major drawback can be the often lower bandwidth of a digital implementation.

Two different FPGA platforms with fast ADCs and DACs are used. The first platform is a National Instruments (NI) FlexRIO PXI-7954R board equipped with a Virtex 5 LX-110 FPGA, shown in Figure 3.9(a) and programmed in NI Laboratory Virtual Instrumentation Engineering Workbench (LabVIEW) FPGA. A Baseband Transceiver 5781 with 100 MHz ADCs and DACs is connected and the combination placed inside a PXI-1042 chassis. The chassis also hosts a real-time controller, which communicates with a Personal Computer (PC) running the LabVIEW programming environment. The second platform is a Trenz Electronic board with a Spartan 3A-DSP (Figure 3.9(b)), placed on a custom Hardware board equipped with 100 MHz converters. This setup is programmed in VHSIC (Very High Speed Integrated Circuit) Hardware Description Language (VHDL).

(a) NI FlexRIO PXI-7954R board equipped with a Virtex 5 LX-110 FPGA.

(b) Trenz Electronic board with a Spartan 3A-DSP FPGA.

Figure 3.9: The two different FPGA boards.

4 Initial Imaging and Characterization Experiments

In this chapter, some imaging and characterization tests are carried out with the active cantilevers. Here, all results are obtained in the frame of this work, confirming the concepts and theories introduced in Chapter 2. For a comparison, it includes imaging with modified parameters for the Lock-in amplifier, integrator of the z feedback loop, scan rate and set-point. In addition, resonance sweeps with different distances of the tip to the sample surface are obtained and indicate the introduced sample dependent damping. The amplitudes of an active cantilever at different input conditions are measured as well as the mode shapes up to the forth eigenmode. A self developed analog Q controller is used for initial imaging tests. It is also the first time that an analog Q controller is combined with an active cantilever.

4.1 Standard Imaging with Varied Imaging Settings

In this section, images are taken by a repeated line scan while certain parameters are changed and all others kept constant. It shows the influence of different settings on the tracking ability and image quality of the AFM during imaging.

4.1.1 Varied Lock-in Time Constant

The Lock-in amplifier in AM-AFM is used to demodulate the amplitude of the cantilever scanning the surface. Generally, a low pass filter is implemented after the demodulation to reject frequencies other the one of interest. The associated time constant determines the filter bandwidth and forms one of the bottlenecks in the closed loop feedback path. Figure 4.1 displays three images each taken with a different setpoint, as indicated. Beginning at the top of every image and for approximately 25 lines each, the Lock-in time constant is set to 0.2, 0.5, 1, 2, 5, 10, 20, 50, 100, 200 ms, respectively.

At different lower time constants, the tracking ability is not influenced and the bottleneck in the feedback path must be created by another component. Hence, the Lock-in amplifier is not limiting the imaging speed up to a time constant of around 1 ms. In contrast, higher time constants lead to significant delays and the Lock-in amplifier forms the dominant bottleneck. This is visible by the inability to track the sample surface in the lower half of every image in Figure 4.1. The oscillations arise due to the increased phase delay of the low pass filter, causing the phase and gain margin to drop significantly.

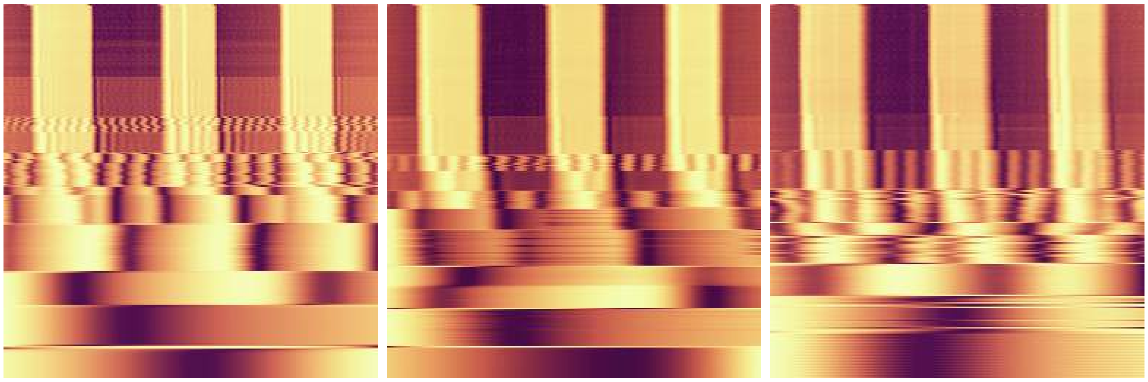

(a) Setpoint 30% (b) Setpoint 40% (c) Setpoint 50%

Figure 4.1: Lock-in time constants adjusted every 25 lines at the given setpoints.

4.1.2 Varied Integrator Feedback Gain and Setpoint

The integrator is part of the z feedback loop and its setting has influence on the tracking ability of the cantilever as well. High values result in oscillations and instabilities, whereas small ones decrease the tracking ability. An appropriate trade-off is necessary for every modified imaging condition, such as a changed imaging rate. Figure 4.2(a) shows an image, where the imaging is started at the top with a low integrator time constant. It is then gradually raised, changed around every 25 lines. Visible at the bottom, the integrator becomes too slow to track the surface properly. The z feedback setpoint in AM-AFM determines the amplitude to be kept constant during imaging. It is often indicated as a percentage value in respect to its amplitude in free air. Lower setpoints cause the amplitude to be damped more, as the cantilever is kept closer to the sample surface. In Figure 4.2(b), the setpoint is modified every 25 lines, starting from the the top and lowered towards the bottom. The setpoints are 65%, 60%, 55%, 50%, 45%, 40%, 35%, 30%, 25%, respectively. The improved tracking ability towards the bottom of Figure 4.2(b) is visible.

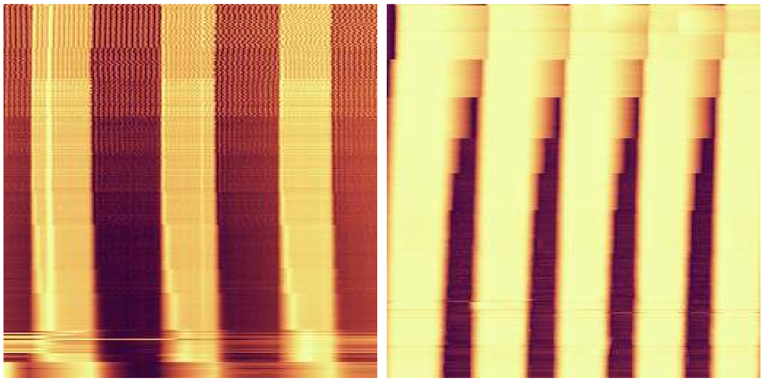

(a) Increased integrator time constant every 25 lines.

(b) Decreased setpoint every 25 lines.

Figure 4.2: Images with modified parameters for the integrator and set-point.

4.1.3 Varied Imaging Speed

The imaging speed also influences the tracking ability, as the frequency spectrum of surface features increases with an increasing imaging rate. In both images of Figure 4.3, the scan rate is modified from 1 to 2, 4, 8 and 16 lines/s every 50 lines. In Figure 4.3(a), the integrator gain is kept constant, whereas in Figure 4.3(b) it is adjusted manually with every scan rate modification.

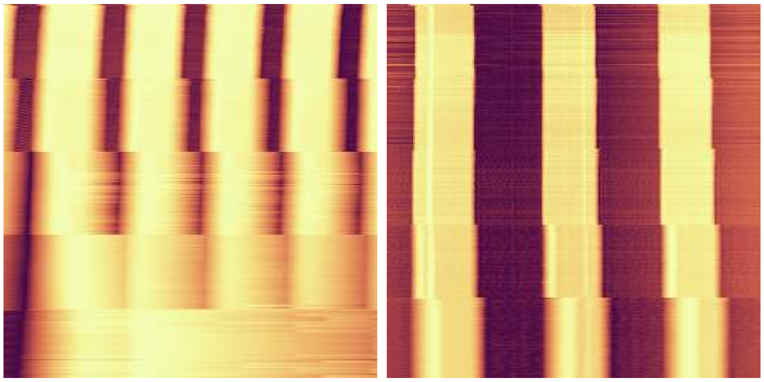

(a) Ki not adjusted.

(b) Ki adjusted.

Figure 4.3: Integrator time constant either adjusted or not while the imaging rate is modified.

4.2 Cantilever Resonances in the Vicinity of a Sample

The cantilever tip amplitude is reduced close to the sample as a function of the setpoint. Figure 4.4 shows the magnitude and phase of a cantilever with modified setpoints, starting at 100% (away from the sample) towards lower ones, as indicated. The amplitude in free air is 138 nm, and accordingly lowered based on the setpoint.

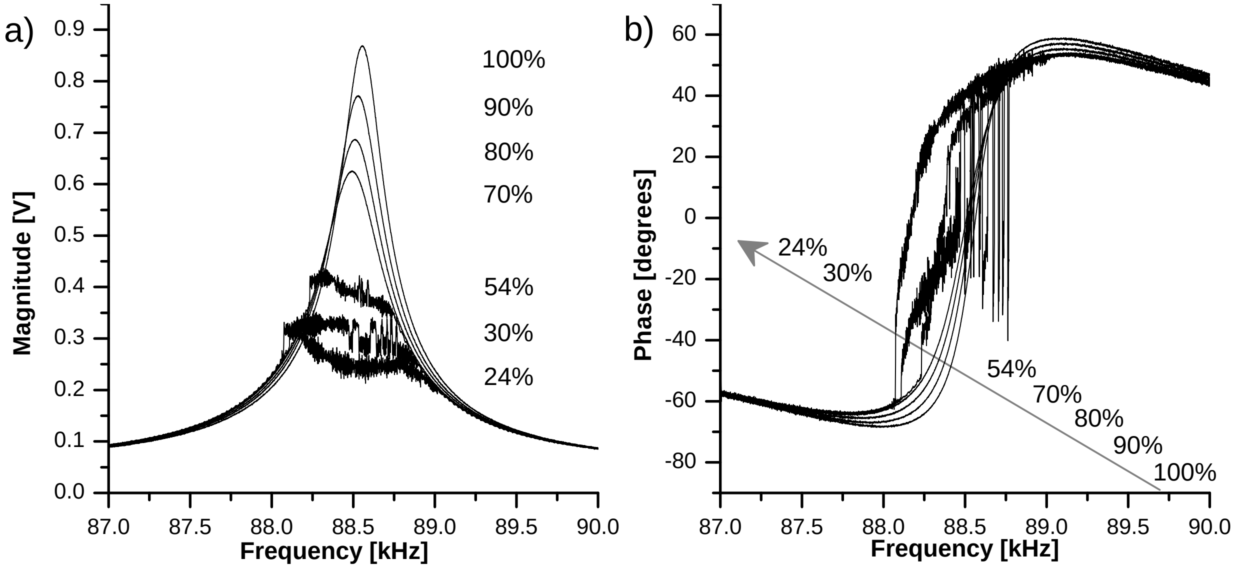

Figure 4.4: Magnitude and phase of an oscillating cantilever in contact with a sample surface at different set-points. The indicated set-points are in the corresponding order in respect to the frequency sweeps, from the top to the bottom for the magnitude and from the right to the left for the phase.

4.3 Cantilever Mode Shapes and Input Power Dependent Amplitudes

The mode shapes up to the forth transversal eigenmode as well as the amplitudes at the tip at different input voltages are determined. The mode shapes in Figure 4.5 are measured with the interferometer setup of Section 3.3. The cantilever is moved in discrete steps along its centerline from the tip to the base. The normalization is based on the peak amplitudes at the tip of 211 nm, 71 nm, 10.5 nm and 5 nm for the first, second, third and forth eigenmode, respectively. The resonance frequencies for the four eigenmodes were 35.825 kHz, 215.885 kHz, 580.379 kHz and 1.084 MHz, respectively. The experiments also agree well with simulations (not shown).

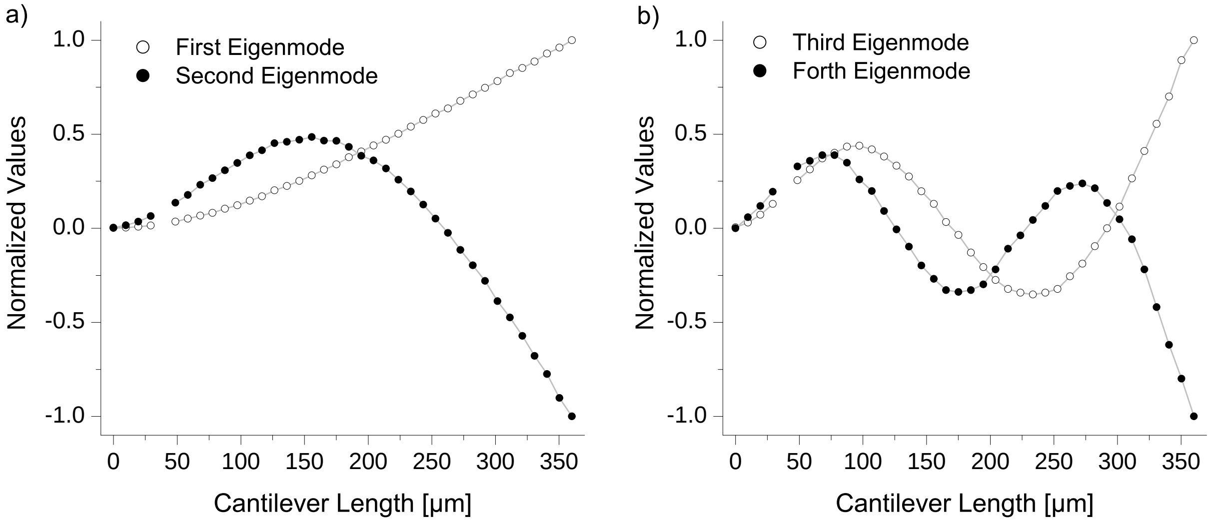

Figure 4.5: Measured mode shapes of an active microcantilever for the first four transversal eigenmodes. (a) displays the first and second and (b) the third and forth eigenmode.

Figure 4.6 shows various different animated displacement mode shapes obtained by simulations (COMSOL Multiphysics ©). In this case the Si_3N_4 passivation layer is objected. The animation can be viewed by opening the file in a supporting PDF reader, such as the *Adobe Acrobat Reader*. The color coding refers to the stress distribution upon bending. Red color means high and blue color low stress regions, respectively. It is clearly visible that with higher eigenmodes the area of maximum stress is pushed further towards the base of the cantilever. The influence of the stress concentration hole (Section 3.2) is also well visible.

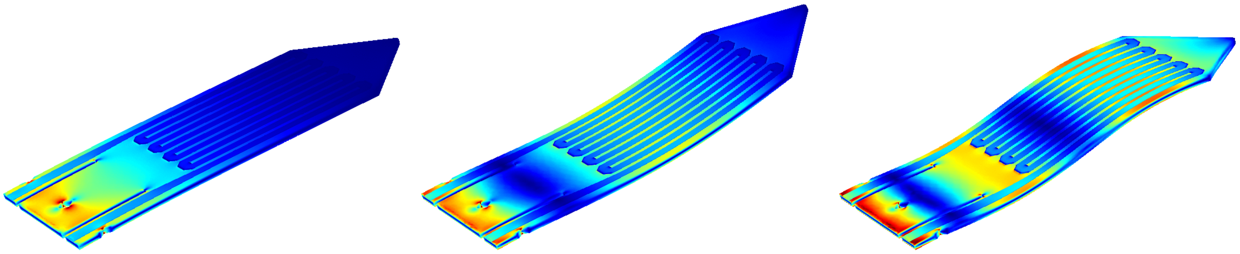

(a) 1. Transverse, 61.9kHz. (b) 2. Transverse, 395kHz. (c) 3. Transverse, 1.08MHz.

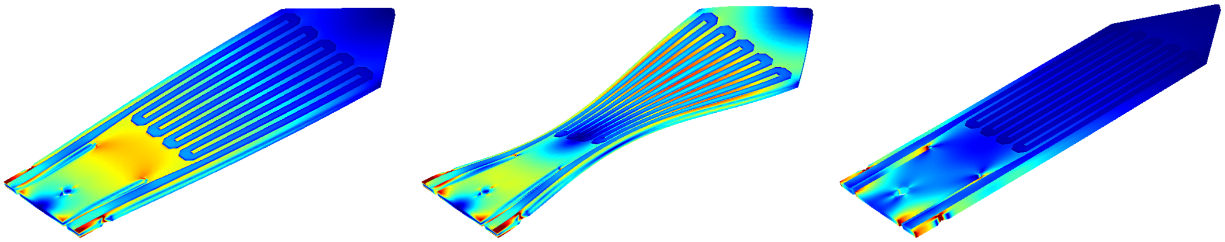

(d) 1. Shear, 334kHz. (e) 2. Shear, 1.11MHz. (f) 1. Transverse, 1.45MHz.

Figure 4.6: Various simulated and animated eigenmodes of active cantilevers as indicated, based on specific cantilever dimensions. (Animation works in *Adobe Acrobat Reader* or other compatible PDF reader.)

Figure 4.7 shows the first three transversal displacement mode shapes obtained from simulations in a different static perspective. In the top row, the highest stress occurs on the surface of the silicon substrate that is covered by the Si_3N_4 layer. The bottom row has the Si_3N_4 removed, as it is the case in Figure 4.6.

When actuated at its i^{th} resonance frequency, the cantilever's amplitude behaves linearly with the input dissipation power based on $P_i \propto 2V_{dc}V_{i,ac}sin(\omega t)$. V_{dc} and $V_{i,ac}$ are the applied DC and AC voltages, respectively. The voltages are applied to the heating meander with a known resistance R_{heater}, where the resulting power is dissipated. Due to the quadratic relationship of the power on the input voltages, the overall time varying dissipation of an actuation signal can be formed to $P_i = \frac{1}{R_{heater}}(V_{dc} + V_{i,ac}sin\omega t)^2 = \frac{1}{R_{heater}}(V_{dc}^2 + 2V_{dc}V_{i,ac}sin(\omega t) + V_{i,ac}^2 sin^2(\omega t))$. Hence, it causes additional components at DC and twice the AC frequency [11].

Figure 4.8 shows interferometric specified tip amplitudes of different applied input AC voltages. The DC power component $P_{dc} = V_{dc}^2/R_{heater} = (387\,\text{mV})^2/27.5\,\Omega = 5.4\,\text{mW}$ is constant throughout the measurements. The RMS AC power is variable and determined by $P_{i,ac,RMS} = \frac{V_{dc}\sqrt{2}V_{i,ac}}{R_{heater}}$. The voltages amplitudes of $V_{i,ac}$ are varied from $0\,\text{mV}$ to $102.5\,\text{mV}$.

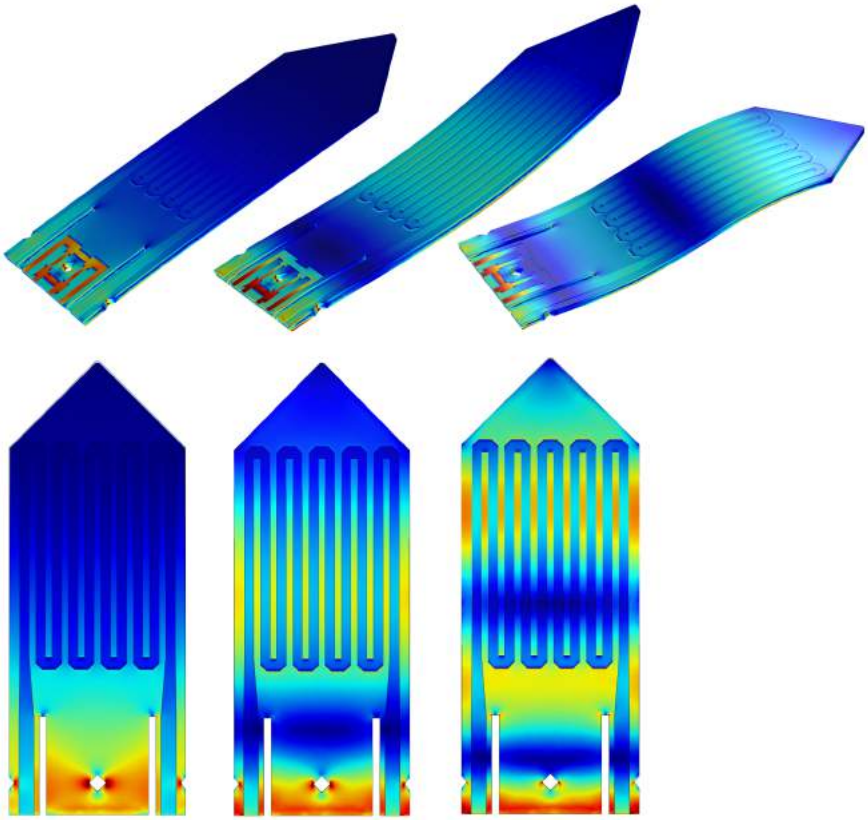

Figure 4.7: Top row: first three displacement mode shapes; bottom row: first three displacement mode shapes with Si_3N_4 removed for a better view. Red color means a high stress area and blue a low stress area.

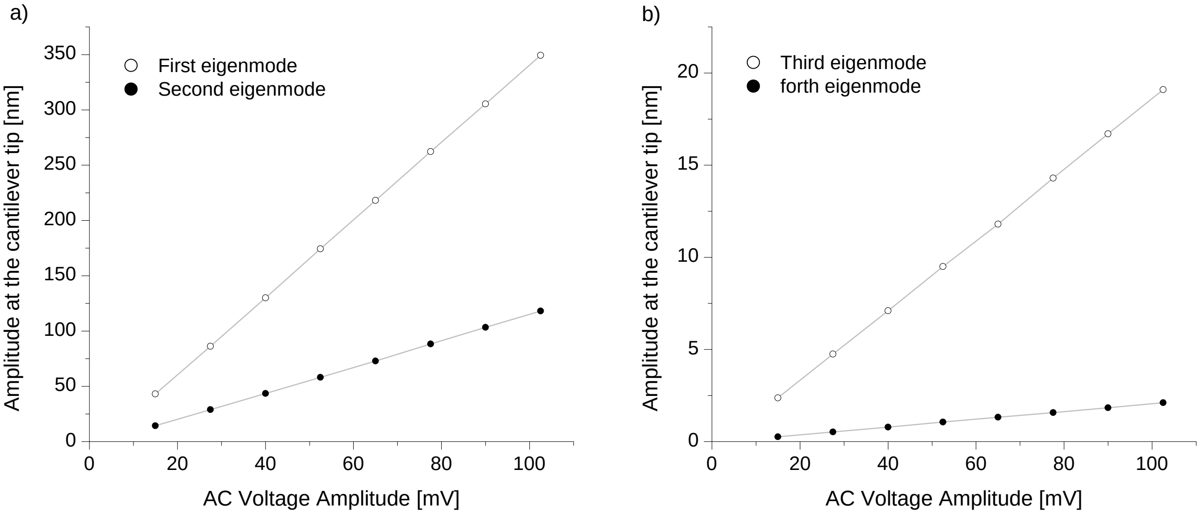

Figure 4.8: Amplitudes at the tip of the cantilever as a function of applied AC voltages corresponding to each eigenmode's resonance. (a) the first and second and (b) the third and forth eigenmode.

Table 4.1 shows a few combinations of applied DC and Peak-Peak AC voltages and that they are interchangeable to obtain a specific amplitude. It means that an RMS amplitude based on AC $= V_1$ and DC $= V_2$ can also be achieved by DC $= V_1$ and AC $= V_2$.

DC voltage	AC voltage Peak - Peak	AC RMS voltage	**Real Amplitude**
153 mV	148 mV	52.3 mV	42 nm
153 mV	215 mV	76.0 mV	63 nm
231 mV	148 mV	52.3 mV	67 nm
231 mV	215 mV	76.0 mV	92 nm
114 mV	288 mV	101.8 mV	70 nm
310 mV	118 mV	41.7 mV	63 nm

Table 4.1: Amplitude dependency on various different combinations of DC and AC voltages.

A frequency sweep including a total of 7 eigenmodes is shown in Figure 4.9.

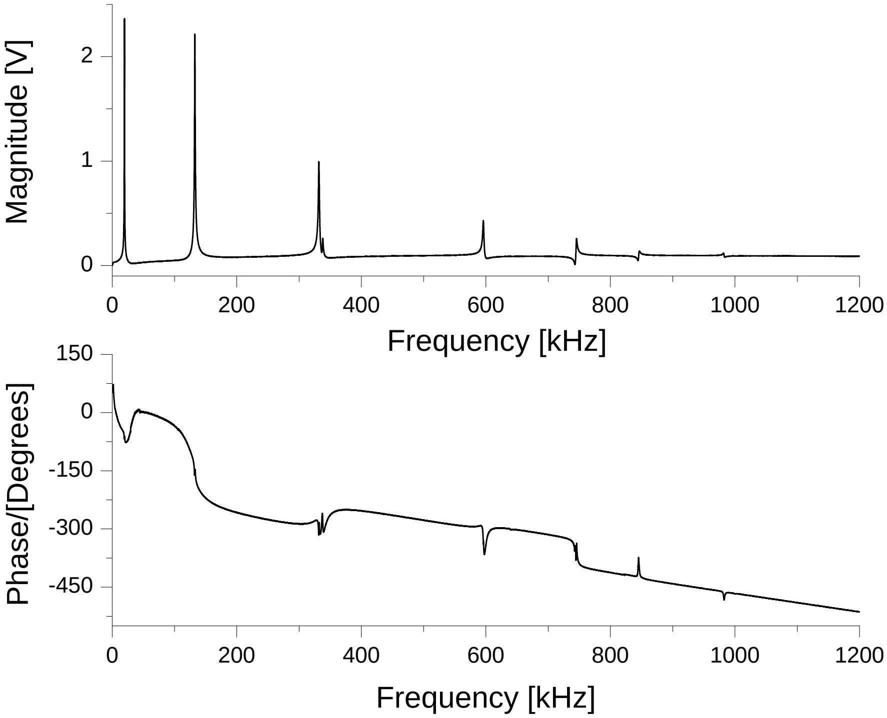

Figure 4.9: Example of a frequency sweep of an active cantilever showing a total of seven eigenmodes.

The Wheatstone bridge supply can either be positive or negative, since its output is based on the gradient between two potentials. Figure 4.10 indicates the effect of choosing positive and negative supply voltages for the piezo-resistive Wheatstone-bridge as introduced in Subsection 2.2.4. The resistors are created by ion implantation. Thus, depending on whether the supply voltage is positive or negative, the behavior is different. This is since the p-doped resistors are formed into the n-doped silicon wafer and form p-n junctions.

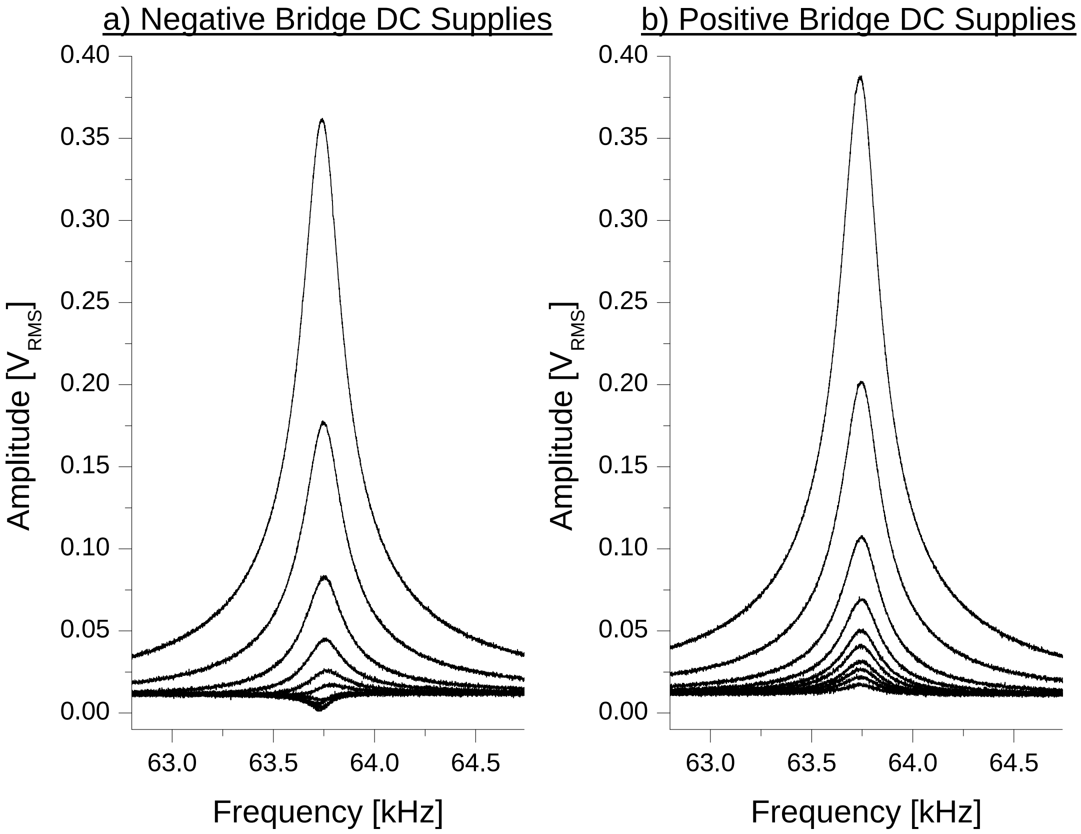

Figure 4.10: Effect of both a negative and positive Wheatstone bridge supply voltage.

4.4 Q-control of the First Eigenmode

The Q control theory requires a phase lead of -90 degrees achieved by the derivative of the sensor signal, as explained in 2.4. However, it can be difficult to implement, as e.g. the noise is amplified due to the differentiation. In the case of displacement proportional sensors, the literature often implements Q control as an added +90/+270 degrees phase lag. This is possible since $\frac{d}{dx}sin(x)+c = \iiint sin(x)dx^3$. For example, to achieve a phase shift of -90 degrees, one can apply a phase of +270 degrees. This in turn is similar to an inverted signal of +90 degrees phase shift. However, desired or undesired, the natural frequency is also influenced if the phase shift is not exactly the +90/+270 needed for pure Q-control.

An analog Q control circuit for active cantilevers has been developed as a first test. Figure 4.11 shows the function of the Q controller. The circuit is connected to the existing setup and uses high impedance inputs to not impose a load on the existing electronics' outputs. Figure 4.12 is the simulation schematic of the circuit that has been built. V4 simulates the actuation signal and V1 represents the cantilever sensor signal to be fed back. U4 and U5 realize the high impedance inputs based on voltage followers. U1 forms an all pass filter for the phase shift without modification of the amplitude. U2 is a simple inverter and U3 a summer for adding the actuation and sensor signal. Hence, the sensor signal is shifted with a proper phase and added to the actuation signal.

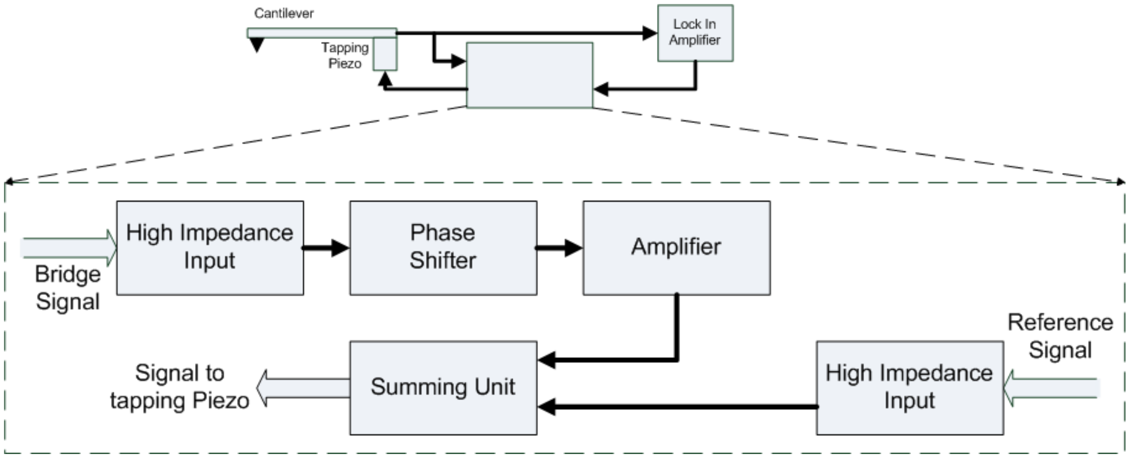

Figure 4.11: Function of the Q controller as it is connected to the existing setup.

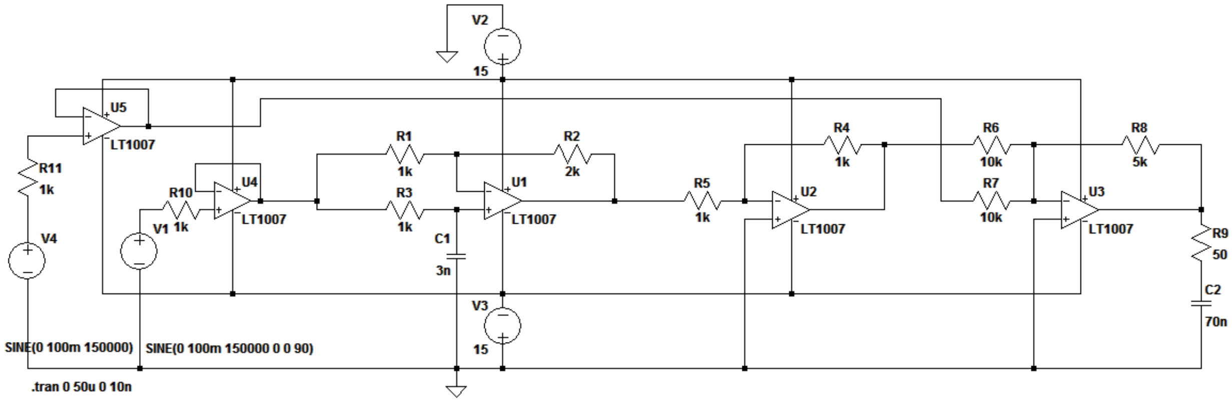

Figure 4.12: Schematic of the designed analog Q control circuit.

As an example, Figure 4.13(a) indicates the modification of the Q factor of a cantilever's resonance with the above analog controller. The natural Q factor of 230 can be changed almost arbitrarily anywhere from very low to high. In this case, it is modified to be 1050. The left image of Figure

4.13(b) is taken without Q control and the right Figure 4.13(b) with the substantially raised Q factor of 1050, both at a scan speed of 5 lines/s and a scan area of $(2.5\,\mu\text{m})^2$. The sample is a memory test-wafer from Samsung Electronics Inc.; the pronounced wave-like form of the lines are a manufacturing defect. Structures on the silicon wafer were clearly resolved in contrast to the left image in Figure 4.13(b). In this case, the cantilever is externally actuated by a piezo dither and the oscillation sensed by a piezo resistor integrated into the cantilever.

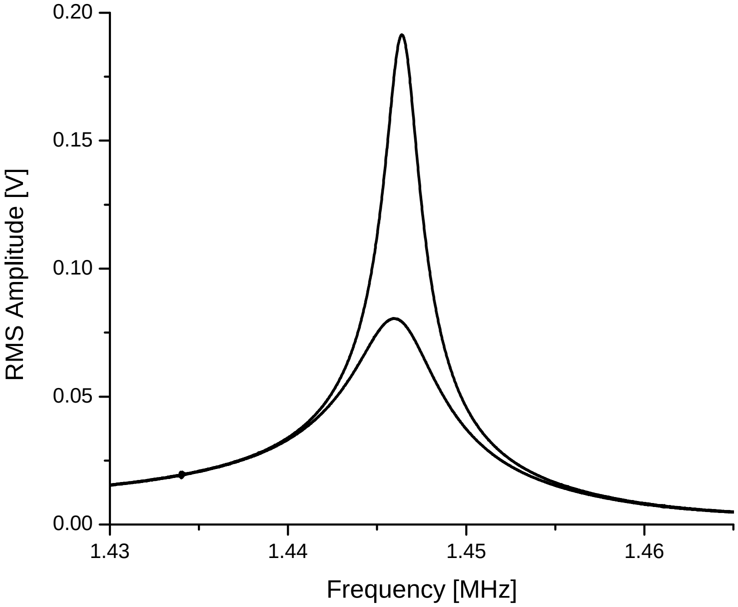

(a) Frequency sweep of the magnitude of the first resonance under analog Q control, with Q factors of 230 and 1050.

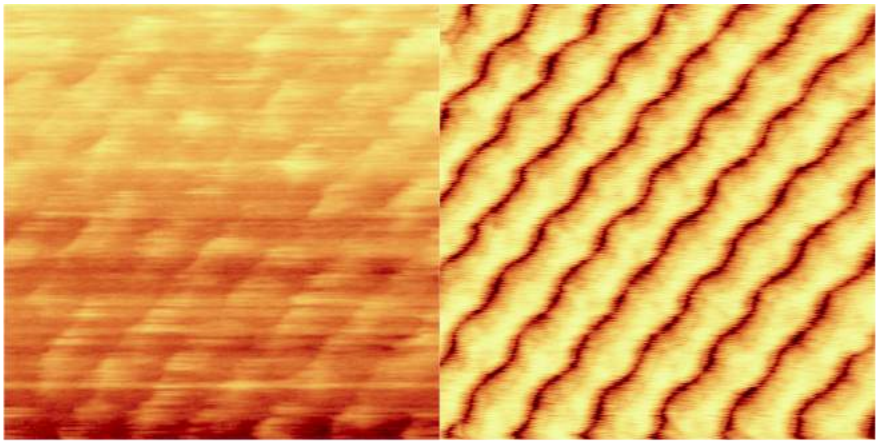

(b) Left is an image taken without Q control and right with a substantially raised Q factor of 1050, both at 5 lines/s.

Figure 4.13: Frequency sweep and images received under analog Q control.

Figure 4.14 is the domain signal of the cantilever under different Q factors. Here, the oscillating tip of the cantilever is brought into contact with the surface of an additional piezo actuator and a specific setpoint. The feedback loop of the cantilever's regular z actuator is then set to a very low bandwidth (slow controller). Rapidly retracting the additional piezo actuator causes the cantilever tip to be suddenly in free air. Meanwhile, the evolution of the amplitude is recorded. The different Q factors are indicated and the different time constants clearly visible.

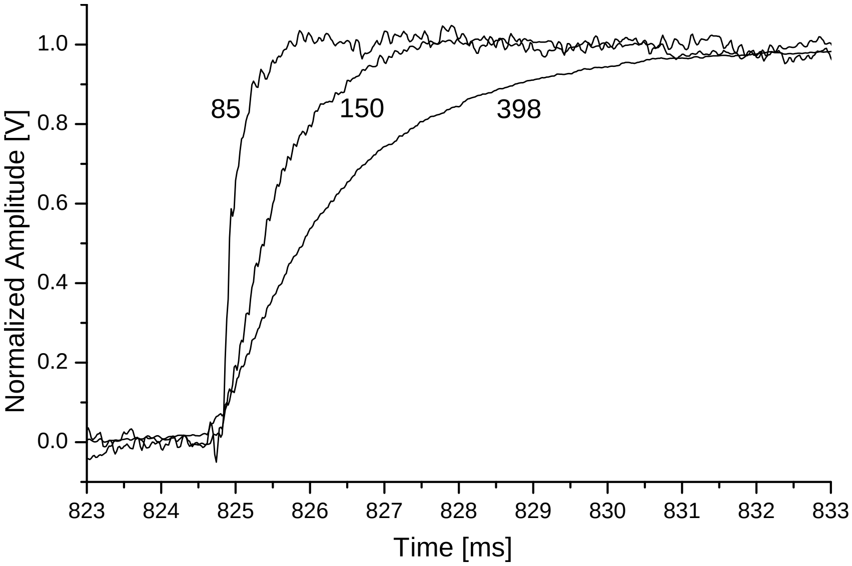

Figure 4.14: Time domain signal of the cantilever influenced by different Q factors. The data is collected by rapidly retracting a piezo actuator from the tip and causing the cantilever being free of any surface. The numbers next to the graphs indicate the corresponding Q factors.

4.5 Conclusion

In this chapter, several introductory experiments and initial control tests are performed. The influence of different parameters, such as Lock-in time constants, integrator constants, scan rates, setpoints and sensor bridge voltages are compared. In addition, resonance curves obtained in the vicinity of the sample surface indicate the effective Q factors. The mode-shapes and the dependency of actuation voltages on the tip deflection are obtained. At last, an analog Q controller is created to perform initial tests. All the experiments serve as a basis for the modeling, compensator design, imaging and characterization in Chapters 5 to 9

5 Derivation of Novel Multi-Eigenmode Compensator for Cantilevers

An estimator based multi-eigenmode compensator is derived in this chapter that is able to individually and simultaneously modify the dynamics of each of the modeled cantilever's resonances. First, a cantilever model is obtained by a system identification approach. Then, the compensator containing an estimator and controller is developed. The estimator is necessary to retrieve the cantilever's non-directly measured internal variables. A simulation of the compensator is performed to validate its function and the implementation into a digital FPGA system is outlined at last. The control of the Q factor and natural frequency is needed for the three consecutive Chapters 6, 7 and 8. There, improvements in imaging speed, material sensitivity and alternative demodulation are based on the compensator derived in this chapter. This and all following chapters are the core of this work and present novel concepts in the area of AFM.

5.1 Introduction

Mostly, AFM cantilevers only incorporate one kind of sensor that allows its vibrational sensing. For example, the acquired signals can be displacement or velocity proportional. In that case, gaining full control over the cantilever dynamics requires additional signals. This could be achieved by incorporating the appropriate sensors in the cantilever. However, this could be costly or even technologically impossible. In that case, an estimator can be used (Section 2.5), also called observer in a noise-free environment. It incorporates a cantilever model and estimates the missing information in parallel to the physical sensor. The estimator is used in the following Chapters 6, 7 and 8 for different objectives, such as improving the scan rate and material sensitivity.

In the following sections, the estimator based compensator is derived and connected as a feedback of the cantilever sensor to its actuation signal. A suitable multi-eigenmode model for the cantilever

	Ampl. Mode 1	Ampl. Mode 2	Ampl. Mode 3
Mode 1	244.8 nm	0 nm	0 nm
Mode 2	0 nm	84.5 nm	0 nm
Mode 3	0 nm	0 nm	13.5 nm
Mode 1+2	244.9 nm	84.8 nm	0 nm
Mode 1+3	244.8 nm	0 nm	13.9 nm
Mode 2+3	0 nm	84.5 nm	13.8 nm
Mode 1+2+3	244.8 nm	84.8 nm	13.9 nm

Table 5.1: Amplitudes in different cases, when one or more modes are excited simultaneously.

beam will be created as the basis for the compensator design, using one of the methods described in Section 2.3. A minimum order model is desirable to reduce computational effort and increase processing rates. However, the model still needs to sufficiently describe the behavior of the cantilever, most importantly at the frequencies of interest.

The resulting compensator is of general-order and can be applied with any cantilever model derived. It will be able to modify the Q factor, natural frequency or a combination of both for each modeled eigenmode independently and simultaneously. The implementation in a digital FPGA platform described in Section 3.5 needs to be order specific to maximize its performance. Despite its bandwidth limitation, the digital implementation proves to be flexible and convenient.

Small cantilever deflections of different eigenmodes are usually assumed to be linearly independent. Thus, in many theories the overall deflection is treated as a superposition of the individual ones, including the below linear compensator design. To justify the choice, an experiment is performed. In Table 5.1, the RMS amplitudes at the tip of an active cantilever are shown for the first three eigenmodes, measured by the interferometer introduced in Section 3.3. The cantilever is actuated at its first three transversal eigenmodes in different combinations by adding the respective actuation signals. When actuated, the DC component is constant at 387 mV and the AC actuation voltages are 150 mV peak-to-peak for every of the three eigenmodes. By taking the Fast Fourier Transforms (FFTs), the individual components remain nearly constant. A small effect can be seen on an eigenmode, when a lower one is actuated simultaneously.

The following chapter is organized as follows: The multi-eigenmode cantilever model is derived in Section 5.2. The compensator design, including both the estimator and controller, are developed in Section 5.3, which thereafter is validated in a simulation in Section 5.4. In Section 5.5, it is then implemented as a single- and multi-eigenmode compensator into both FPGA platforms introduced in Section 3.5. A conclusion is given in Section 5.6.

5.2 Cantilever Model

In this section, a proper model of the cantilever dynamics is derived from measurements that supports the compensator design. It is created according to one of the methods discussed in section 2.3. The cantilever beam can be described by either a distributed parameter system or an equivalent point mass model (Section 2.2). Although the distributed model offers a comprehensive description of the beam, a lumped point mass model is simpler to handle and often sufficient for control purposes. As a comparison, previous modeling in the state space has been performed by Stark *et al.* [181].

The process to be modeled can be in the form

$$\dot{\mathbf{q}}(\mathbf{t}) = \mathbf{A}\mathbf{q}(\mathbf{t}) + \mathbf{B}u(t) + w(t), \tag{5.1}$$

$$y(t) = \mathbf{C}\mathbf{q}(t) + v(t), \tag{5.2}$$

where $w(t)$ and $v(t)$ are additional terms incorporating the process and measurement noise, respectively. $\mathbf{A}$ is the state transition matrix, vector $\mathbf{B}$ the state input and vector $\mathbf{C}$ the state output, where all have constant parameters in the linear model. Here, Equation (5.1) describes the dynamic behavior of the cantilever while Equation (5.2) gives an expression for the measurements $y(t)$ in terms of the variables $\mathbf{q}(t)$ and measurement noise $v(t)$.

It is difficult to capture the overall system dynamics by a theoretical approach. Hence, the model of the cantilever including all the different parts of the closed feedback loop is obtained by a system identification in the frequency domain, specifically the Prediction Error Method (PEM). It is necessary to include the proper transfer function of the digital platform later used fo the compensator implementation. Hence, its containing FPGA is programmed to actuate the cantilever and capture its response for off-line processing. This procedure can be carried out automatically. Every time a new cantilever is mounted or the environment is changed, e.g. from air to liquid, the dynamic behavior is different and the model needs to be adjusted. If the experimental model derived is in the continuous time domain, it is then discretized by the First-Order-Hold method. Alternatively, by using the data in discrete time representation, the discrete model is obtained directly. The sampling time of the resulting model matches the compensator loop rate of the FPGA implementation in Section 5.5 [202].

The system matrices can be expressed as

$$\bar{\mathbf{A}} = \begin{bmatrix} \bar{\mathbf{A}}_\mathbf{1} & \mathbf{0} & \cdots \\ \mathbf{0} & \bar{\mathbf{A}}_\mathbf{2} & \\ \vdots & & \ddots \end{bmatrix}, \bar{\mathbf{B}} = \begin{bmatrix} \bar{\mathbf{B}}_\mathbf{1} \\ \bar{\mathbf{B}}_\mathbf{2} \\ \vdots \end{bmatrix}, \bar{\mathbf{C}} = \begin{bmatrix} \bar{\mathbf{C}}_\mathbf{1} & \bar{\mathbf{C}}_\mathbf{2} & \cdots \end{bmatrix}, \tag{5.3}$$

where $\bar{\mathbf{A}}$, $\bar{\mathbf{B}}$ and $\bar{\mathbf{C}}$ are the experimentally determined matrices/vectors of $\mathbf{A}$, $\mathbf{B}$ and $\mathbf{C}$, respectively. Each of them contains sub-matrices/vectors representing a modeled eigenmode, indicated by the indexes. Such block diagonal is suitable for the hardware implementation and will be discussed in detail in Section 5.5, as it requires a specific hardware component structure. Equation (5.2) does not include a direct feed-through term $Du(t)$. However, it could be added to separately model the cantilever's cross-talk of the actuation signal onto the piezo-resistive sensor bridge. This effect is solely dependent on the actuation without influence of the cantilever dynamics. Prior to the compensator design the system is reduced in its order to reduce computational effort. The Q_i factor and natural frequency $\omega_{n,i}$ of each eigenmode i can be found through the eigenvalues of the estimated model.

Figure 5.1(a) and 5.1(b) show the frequency domain magnitude and phase of a cantilever measured (black curve) and modeled (red, blue, green curves). The legend indicates the order of each model. Here, the input is the cantilever actuation signal and the output the displacement proportional signal of the piezo-resistive sensor bridge. The eighth order model correctly predicts the real system. The reduced forth order models indicate some error at off-resonance locations. However, the magnitude error is small considering the logarithmic vertical scale of the diagram. A zoom into both resonances of Figure 5.1(a) and 5.1(b) is shown in Figure 5.1(c), indicating the area of interest is modeled correctly even by a forth order model.

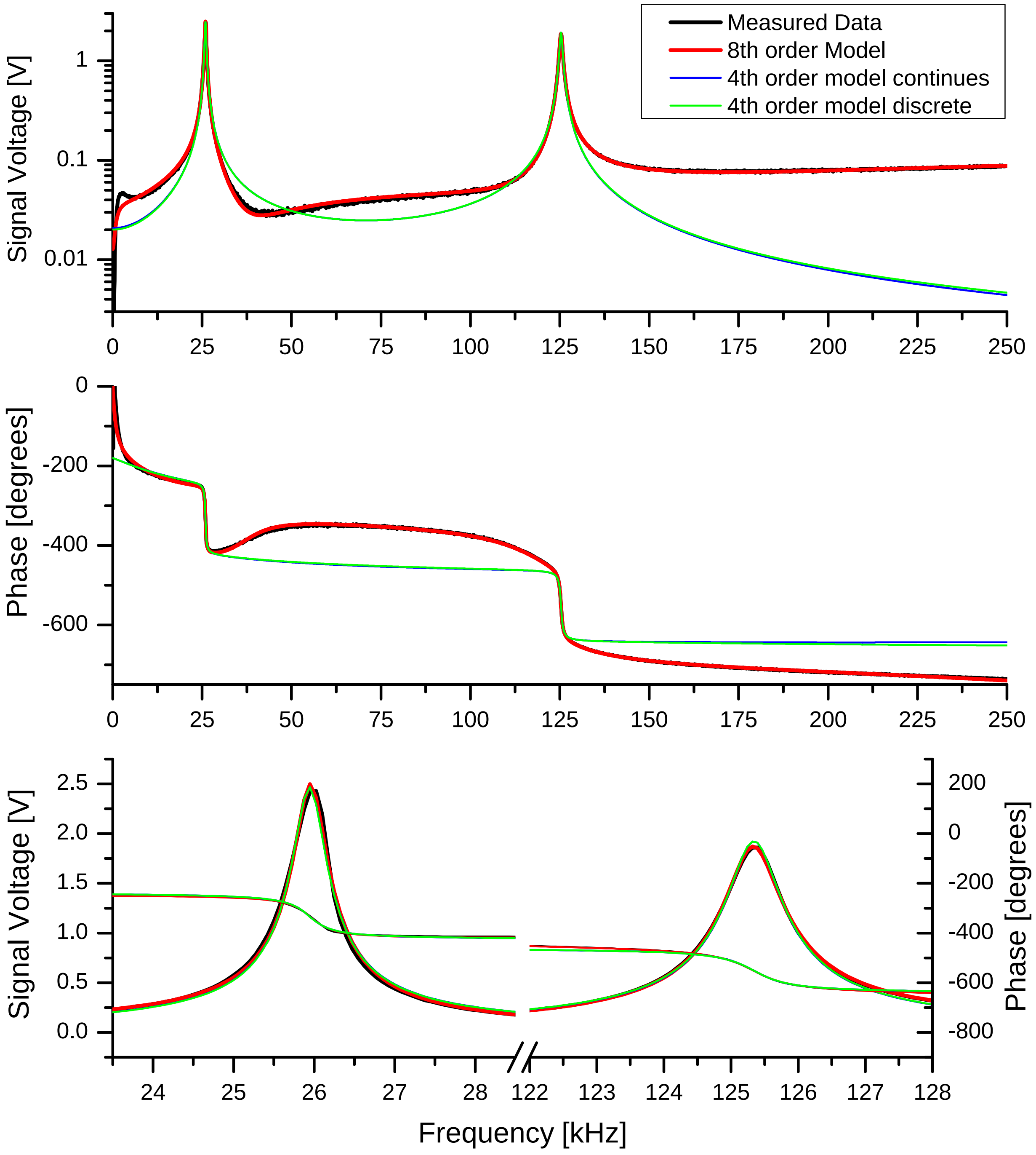

Figure 5.1: Comparison of the magnitude (a) and phase (b) of the cantilever and its various models. Diagram (c) is a zoom into both resonances for better visibility.

5.3 Control approach

In the following, the full state feedback control approach based on a prediction estimator is introduced. The estimator is derived first, giving access to the unmeasured states of the cantilever. This is necessary, as the cantilever sensor only supplies displacement proportional signals. The controller is designed thereafter, based on the cantilever's actual and desired dynamics. The combination of estimator and controller forms the compensator [202]. Note that the compensator incorporates a cantilever model describing its dynamics. Hence, it acts on the raw sensor signal prior any demodulation, such as by Lock-in amplifiers. The design is based on the separation principle and hence allows the separate design of controller and estimator and consecutive combination of both. Here, controllability and observability needs to be ensured for access to all states of the system.

5.3.1 Estimator Design

A full state estimator is chosen to estimate both the unmeasured velocity and measured displacement of the tip vibrations. Including the latter one improves noise in the system. The tip velocity is required as it directly affects the Q_i of the eigenmodes. Specifically, a steady state Kalman filter is used, which is an optimal filter in white noise. As the sampling rate is attempted to be maximized, the relationship of computation to sampling time is close to unity. Hence, the estimator is set up in the predictive form with its discrete time representation

$$\mathbf{\hat{q}_{k+1}} = \mathbf{\bar{A}}\mathbf{\hat{q}_k} + \mathbf{\bar{B}}u_k + \mathbf{L}(y_k - \hat{y}_k). \tag{5.4}$$

where the states $\mathbf{\hat{q}_k}$ are estimates of the states $\mathbf{q_k}$. $\hat{y}_k = \mathbf{\bar{C}}\mathbf{\hat{q}}_k$ and $y_k = \mathbf{C}\mathbf{q}_k + v_k$ are the estimated and measured cantilever displacement signal, respectively. y_k with its noise v_k forms one of the two inputs to the estimator and is multiplied by the estimator gain $\mathbf{L}$. Thus, higher gains result in faster poles that improve convergence, but also amplify the noise effects. As the estimator also acts as a filter the overall noise of the feedback signal, dependent on $\mathbf{L}$, is lower than with a regular phase-shift/gain Q controller. For clarification, the difference between current and prediction estimators are indicated in Subsection 2.5.2. Figure 5.2 is a block diagram of the estimator that is put in parallel to the cantilever.

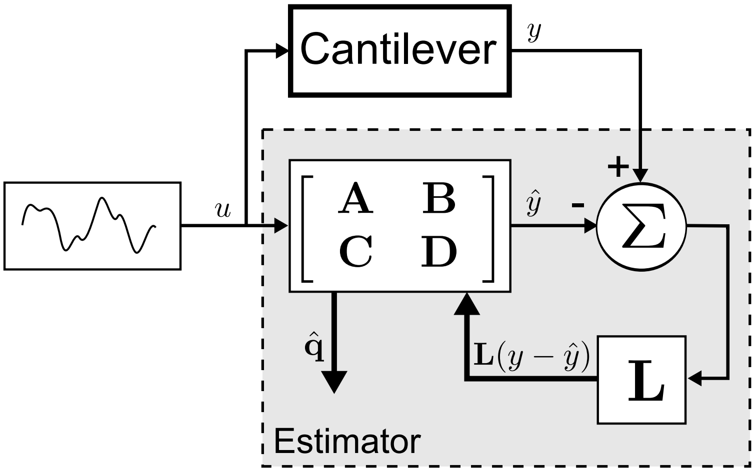

Figure 5.2: Estimator block diagram, estimating the cantilever states based on the input u and output y.

The Kalman filter is designed by providing the system model and the covariances for the model noise $w(t)$ and measurement noise $v(t)$. These can be true noise covariances or values treated as design parameters chosen by the user. Since only the relation between the values is important, one of the two can be a constant with the other being adjustable. The lower a covariance, the better the trust in the respective model or measurement. In addition, the estimator poles should be at least twice as fast as the modeled cantilever poles to minimize its influence on the cantilever dynamics.

5.3.2 Controller Design

The dynamics of each modeled eigenmode can be modified arbitrarily and independently, based on the model of Equation (5.3) and its independent complex conjugate pole pairs for each eigenmode. It offers the possibility to modify Q_i and/or the resonance frequency $\omega_{r,i}$ of the i^{th} eigenmode. However, a significant modification of the poles by the controller can require considerable control action. Based on the separation principle the availability of all cantilever states is assumed in this step.

The computation of the feedback coefficient vector (controller) **K** is based on the actual cantilever dynamics and desired pole locations. In combination with the reference signal r_k from the AFM controller a modified cantilever input signal u_k is formed as

$$u_k = -\mathbf{K}\mathbf{q_k} + Nr_k. \tag{5.5}$$

N can be used to eliminate the steady state error introduced by the state feedback.

In the following a strategy is outlined to determine the desired closed loop pole locations $p_{i1,2}$ based on a desired dynamic behavior of the cantilever. The dynamics of each eigenmode are modified either towards a desired Q factor $Q_{des,i}$, a desired resonance frequency $\omega_{r_{des},i}$ or a combination of both. The poles are defined in the continuous time (s-domain) that are converted into the discrete time domain (z-domain) afterwards.

A desired conjugate complex $p_{i1,2}$ pole pair for the control of each Q_i and $\omega_{r,i}$ can be found by the relationship

$$p_{i1,2} = \frac{\omega_{r,i}}{\sqrt{1 - 1/(2Q_{c,i}^2)}} \left(-\frac{1}{2Q_{des,i}} \pm \sqrt{\frac{1}{4Q_{des,i}^2} - 1} \right). \tag{5.6}$$

$Q_{c,i}$ is a design parameter and can be substituted by either Q_i or $Q_{des,i}$. The dynamics can be influenced in the following ways, where (A), (B) are for Q control, (C) for frequency control and (D) a combination of both:

(A) By substitution of $Q_{c,i} = Q_i$ and choosing $Q_{des,i}$, each eigenmode can be modified in its Q factor only. Here, $\omega_{r,i}$ naturally changes with varying closed loop $Q_{des,i}$ based on $\omega_{r,i} = \omega_{n,i}\sqrt{1 - 1/(2Q_{des,i}^2)}$. A variation of $Q_{des,i}$ in a sweep fashion causes the pole pairs to form a circular movement in the complex plane (Figure 5.3(a)). It starts close to the imaginary axis for high $Q_{des,i}$ and meets the negative real axis in the critically damped case of low $Q_{des,i}$. The increase of $Q_{des,i}$ moves the poles closer to the imaginary axis, potentially leading to instabilities,

(B) By substitution of $Q_{c,i} = Q_{des,i}$ and choosing $Q_{des,i}$, $\omega_{n,i}$ is modified such that $\omega_{r,i}$ is kept constant at $\omega_{n,i}\sqrt{1 - 1/(2Q_i^2)}$. Figure 5.3(b) indicates the formation of such poles in the complex plane with a sweep of $Q_{des,i}$. Note that in this case Q_i and $\omega_{n,i}$ are both modified,

(C) By substitution of $\omega_{r,i} = \omega_{r_{des},i}$ and $Q_{c,i} = Q_{des,i} = Q_i$ the resonance frequency is modified. This can be seen in Figure 5.3(c), indicating the formation of such poles in the complex plane with a sweep of $\omega_{r_{des},i}$. Q_i is kept constant in all cases, visible by the unmodified angle of the pole locations to the origin,

(D) By substitution of $\omega_{r,i} = \omega_{r_{des},i}$, $Q_{c,i} = Q_i$ and choosing $Q_{des,i}$ both resonance frequency and Q factor can be modified arbitrarily.

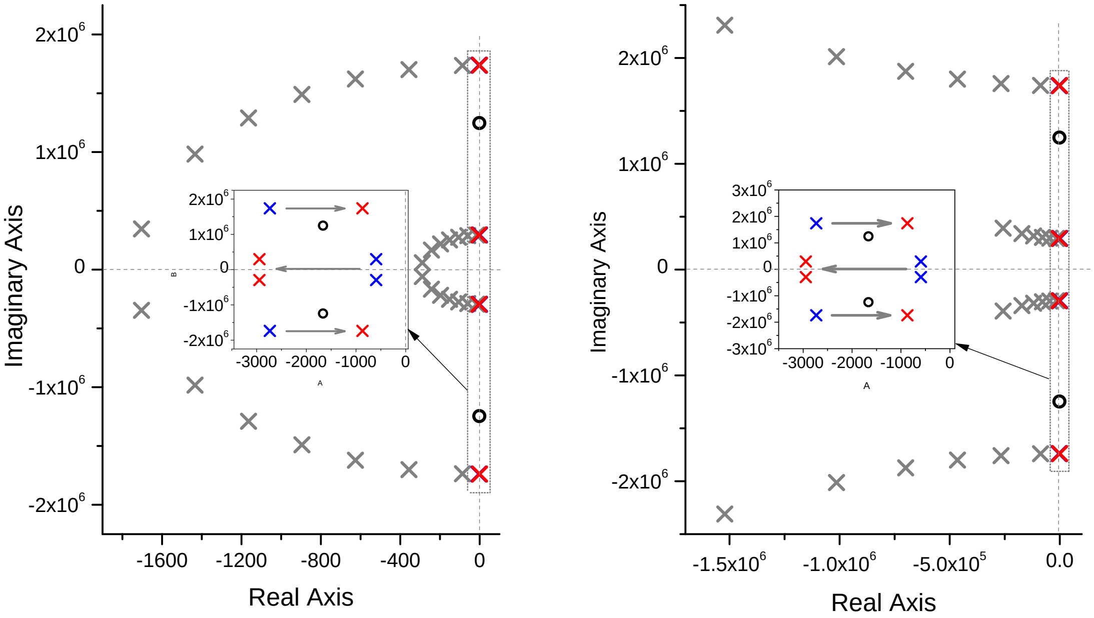

(a) Q Control pole formation keeping $\omega_{n,i}$ constant by substituting $Q_{c,i} = Q_i$.

(b) Q control pole formation keeping $\omega_{r,i}$ constant by substituting $Q_{c,i} = Q_{des,i}$

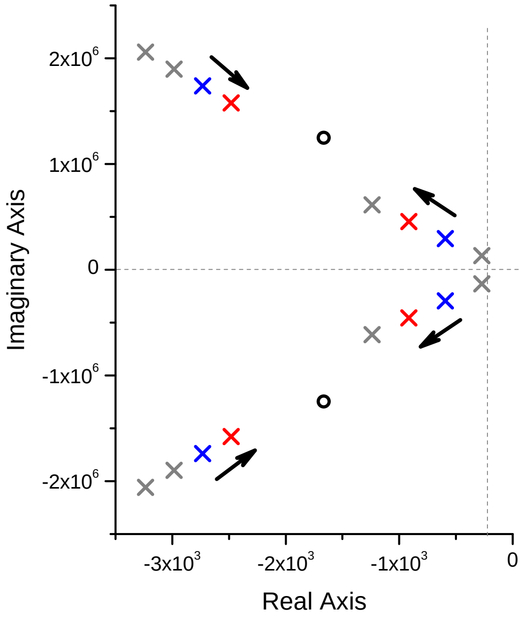

(c) F control pole formation modifying $\omega_{r,i}$ and keeping $Q_{c,i} = Q_i$ constant

Figure 5.3: In (a) and (b) either $\omega_{n,i}$ or $\omega_{r,i}$ are kept constant, resulting either in a naturally modified or a forced constant $\omega_{r,i}$ upon Q control. The inlets magnify a case, where, indicated by arrows, Q_1 is decreased and Q_2 increased. The zeros remain unaffected. In (c) $\omega_{r,i}$ of two eigenmodes are modified, where $Q_{c,i} = Q_i$ is kept constant.

Distinguishing between the two above cases (A) and (B) may result only in small differences in the resonances. This is in particular true for cantilevers in air and vacuum with relatively high Q_i and $Q_{des,i}$. In contrast, the cantilever's damping is much higher in water and the difference more pronounced, giving this strategy a potential application. On a side note, arbitrarily placed pole pairs are often not practicable. Increasing the Q factors towards very high values is prone to instabilities due to positive feedback of the compensator. In contrast, very low Q factors can be unfeasible as the resonance curves become flat. The maximum control action is mostly limited by the cantilever's actuator.

5.3.3 Combined System: Cantilever, Controller and Estimator

The controller of Section 5.3.2 is combined with the estimator of Section 5.3.1 and the resulting compensator connected to the cantilever. Hence, $\mathbf{q_k}$ of Equation (5.5) is replaced by the state estimates $\hat{\mathbf{q}}_\mathbf{k}$ of Equation (5.4):

$$u_k = -\mathbf{K}\hat{\mathbf{q}}_\mathbf{k} + N r_k. \tag{5.7}$$

Combination of controller and estimator results in

$$\hat{\mathbf{q}}_\mathbf{k+1} = (\bar{\mathbf{A}} - \bar{\mathbf{B}}\mathbf{K} - \mathbf{L}\bar{\mathbf{C}})\hat{\mathbf{q}}_\mathbf{k} + \mathbf{B}\mathbf{N}r_k + \mathbf{L}y_k, \tag{5.8}$$

which is combined with the cantilever's dynamics to form

$$\begin{bmatrix} \mathbf{q}_{k+1} \\ \hat{\mathbf{q}}_{k+1} \end{bmatrix} = \begin{bmatrix} \mathbf{A} & -\mathbf{B}\mathbf{K} \\ \mathbf{L}\mathbf{C} & \bar{\mathbf{A}} - \bar{\mathbf{B}}\mathbf{K} - \mathbf{L}\bar{\mathbf{C}} \end{bmatrix} \begin{bmatrix} \mathbf{q}_k \\ \hat{\mathbf{q}}_k \end{bmatrix} + \\ + \begin{bmatrix} \mathbf{B}N \\ \bar{\mathbf{B}}N \end{bmatrix} r_k + \begin{bmatrix} \mathbf{B} \\ 0 \end{bmatrix} w_k + \begin{bmatrix} 0 \\ \mathbf{L} \end{bmatrix} v_k, \tag{5.9}$$

$$\begin{bmatrix} y_k \\ \hat{y}_k \end{bmatrix} = \begin{bmatrix} \mathbf{C} & 0 \\ 0 & \bar{\mathbf{C}} \end{bmatrix} \begin{bmatrix} \mathbf{q}_k \\ \hat{\mathbf{q}}_k \end{bmatrix} + \begin{bmatrix} 1 \\ 0 \end{bmatrix} v_k. \tag{5.10}$$

The output equation $[y_k \; \hat{y}_k]'$ holds the cantilever sensor and estimated measurement, where the latter one is drastically reduced in noise. Figure 5.4 is a block diagram presenting the combined compensator and cantilever setup according to Equations (5.9) and (5.10).

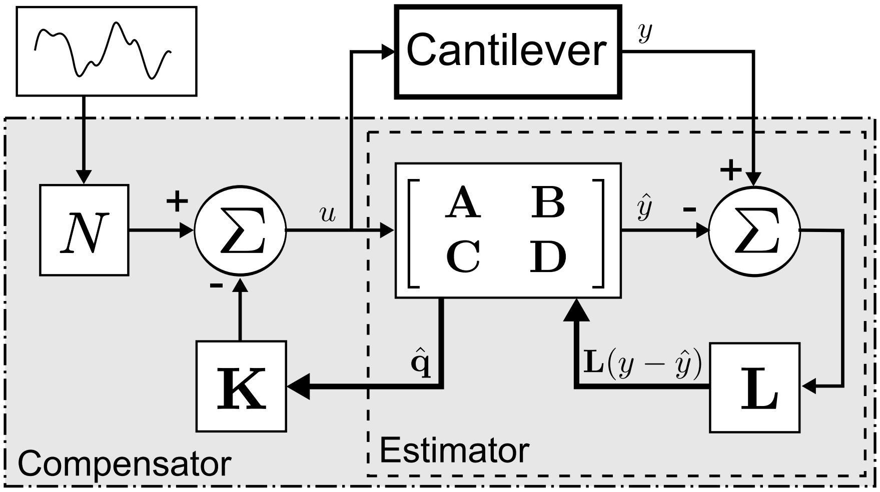

Figure 5.4: The compensator composed of controller and estimator, connected to the active cantilever and external actuation.

A common alternate representation includes the estimator error dynamics rather then the state dynamics. This is interchangeable by substituting $\hat{\mathbf{q}}_k = \mathbf{q}_k - \mathbf{e}_k$. The output equation holds the original cantilever sensor output as well as the estimated output, where the latter one is drastically reduced in noise. The estimated output can be used for a simplified amplitude demodulation scheme instead of using the cantilever output with consecutive Lock-in amplifier. An example and application will be given in Chapter 8.

The following section performs time and frequency domain simulation. The first one indicates the evolution of the estimator from its initial value towards the cantilever dynamics.

5.4 Simulation of a Combined Continuous/Discrete Time System

Combined continuous/discrete time simulation performed in the time and frequency domain are presented in the following to demonstrate the desired behavior of the estimator based approach. In this example and based on Figure 5.1, a compensator is designed with the reduced 4th order discrete time domain model. It is combined with and acting on the more accurate eighth order continuous time model to represent a realistic cantilever behavior. The Q factors Q_1 and Q_2 are modified to be reduced and increased in the first and second resonance, respectively. Figure 5.5 presents the simulation setup in Mathworks Simulink, where the inputs/outputs and vectors/matrices are connected to a script providing and receiving the data. The black colored blocks represent the cantilever with its components in the continuous time domain, whereas the compensator is formed by red blocks indicating a discrete time domain. Two noise sources are added for v and w and zero-order hold blocks form the interface between the two time domains.

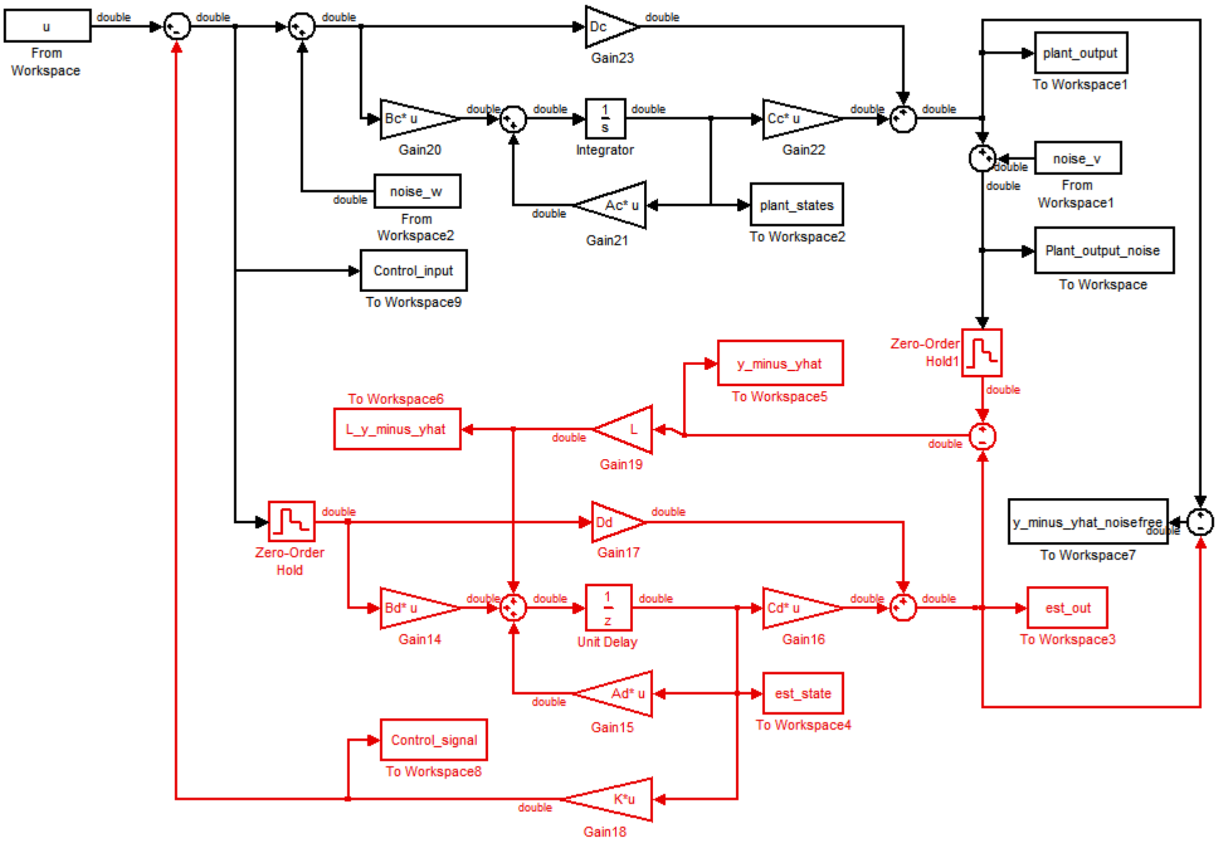

Figure 5.5: Simulink block diagram with continuous time (black) and discrete time domain (red) components.

The time domain simulation is performed on a cantilever actuated at its first two resonances. Figure 5.6(a) shows the actuation signal with two added frequencies as well as the outputs of the cantilever and estimator. The noise reduced estimator output with the two vibrational frequency components is clearly visible. Figure 5.6(b) and 5.6(c) plot the states q_1, q_2 and q_3, q_4 that belong to the first and second eigenmode of the cantilever, respectively. Similarly, the signals q_{1hat}, q_{2hat} and q_{3hat}, q_{4hat} are the estimated states that start at non-zero initial conditions and quickly converge to the real cantilever states.

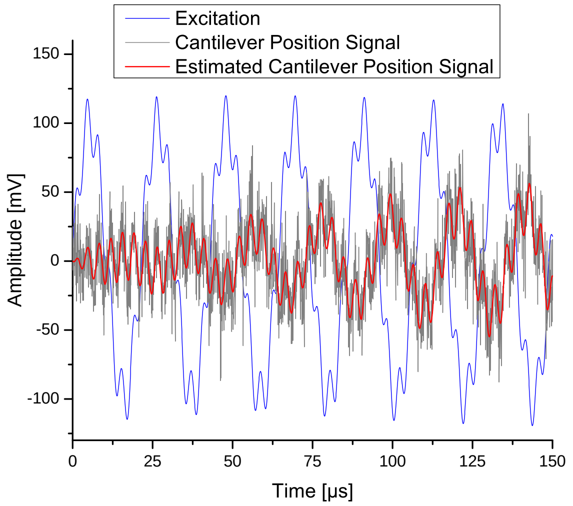

(a) Excitation (actuation) signal with two frequencies added, and the outputs of the cantilever and estimator.

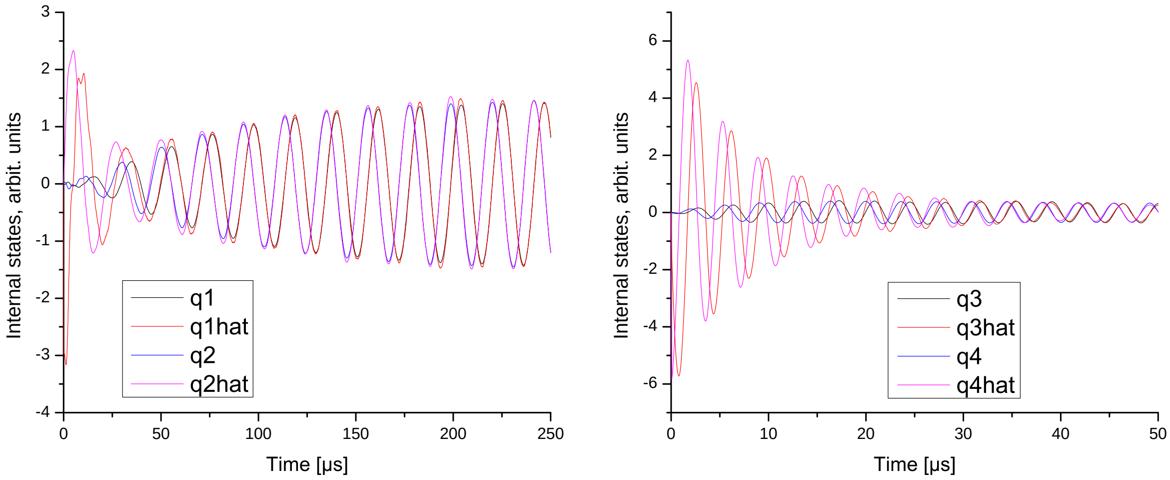

(b) Convergence of the estimator to the cantilever states q_1, q_2 of the first resonance.

(c) Convergence of the estimator to the cantilever states q_3, q_4 of the second resonance.

Figure 5.6: Time domain simulation with input, output and individual state signals plotted.

The simulation performed in the frequency domain is shown in Figure 5.7. Figure 5.7(c) is a zoom into both resonance of Figure 5.7(a) and 5.7(b). The black curve is the measured cantilever displacement signal and the red curve is a 8^{th} order model accurately following its magnitude and phase. The compensator is designed with the reduced 4^{th} order model that is indicated in green. The blue graph is the final actual displacement signal of the cantilever. The simultaneous modification of a designed reduced Q_1 and increased Q_2 is apparent. This example clearly shows that the lower order compensator is able to properly control the first and higher eigenmodes of the cantilever simultaneously.

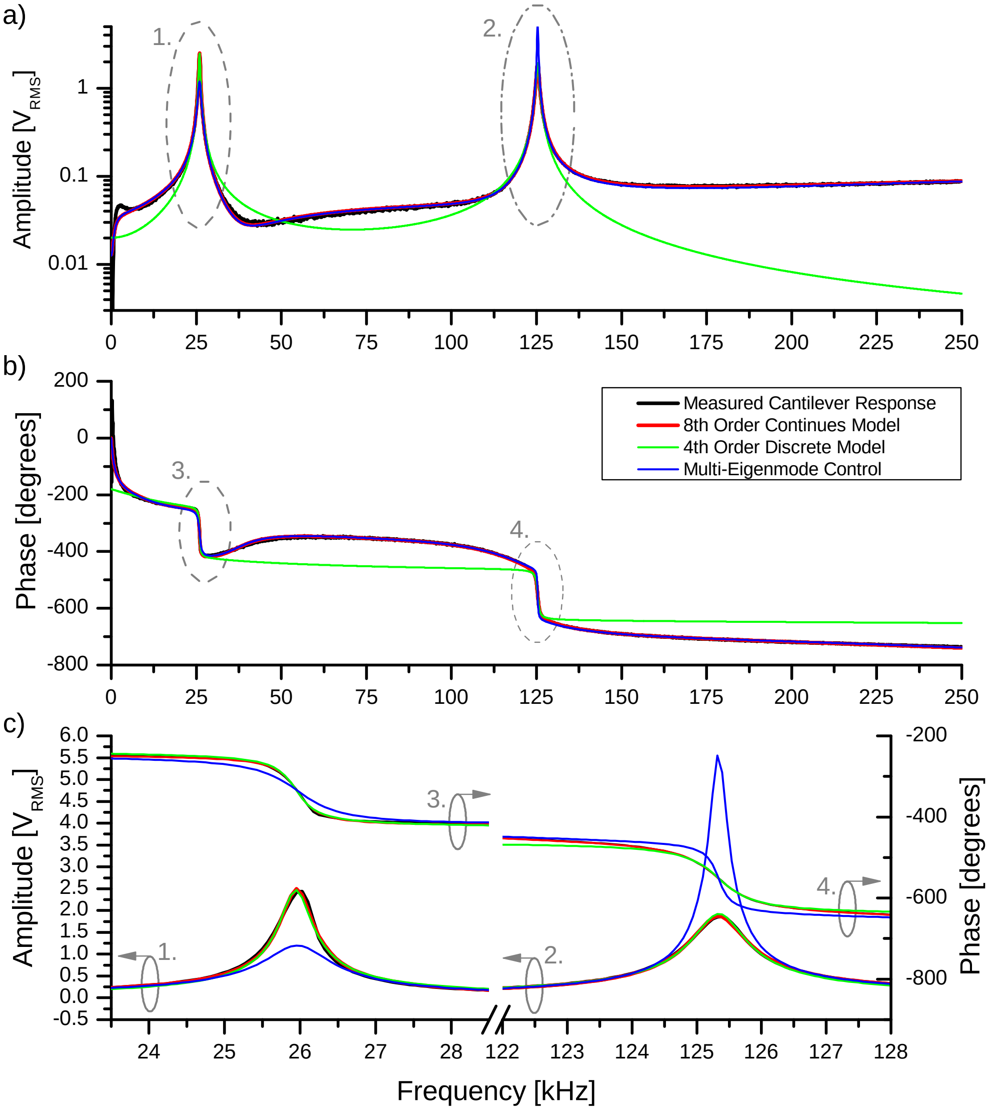

Figure 5.7: Comparison of magnitude (a) and phase (b) of the cantilever sensor signal (black curve) and its model estimates (red, green curves). A simulation decreasing Q_1 and increasing Q_2 is indicated by the blue curve. Diagram (c) is a zoom into both resonances for better visibility, whose locations are indicated by numbers and gray ellipses in (a) and (b).

5.5 Compensator Implementation in FPGAs

The compensator is implemented digitally into both FPGA systems (Virtex-5 and Spartan-3A DSP based) as outlined in Section 3.5, using a state-machine structure and floating point representation. However, the logic implementation is similar on both platforms.

Controlling higher cantilever resonances in digital circuits require fast components. The path with the highest delay in the design determines the maximum possible clock and hence compensator loop rate. It depends on factors such as the model order and implementation strategy. The compensator computation in the FPGA can be partly parallelized, mostly applying to matrix operations whose elements are independent of each other. Among digital systems, FPGAs are very suitable for this application, since they allow true parallelism in any desired degree with low latencies. This is in contrast to CPUs found in PCs and embedded systems.

The compensator feedback loop (Figure 5.8) determines the overall feedback bandwidth. It is executed and computed by different, faster loops that are capturing new samples, computing the consecutive control action and form the new actuation signal. It is apparent that even for cantilevers with low first resonances the computations for higher eigenmodes can be challenging. For example, a cantilever with a first transversal resonance frequency of 50 kHz has the second transversal resonance at around 314 kHz. Although the sampling theorem suggests using sampling rates of at least twice as high as the highest frequency appearing in the signal, it is generally advised to use at least a ratio of five to ten.

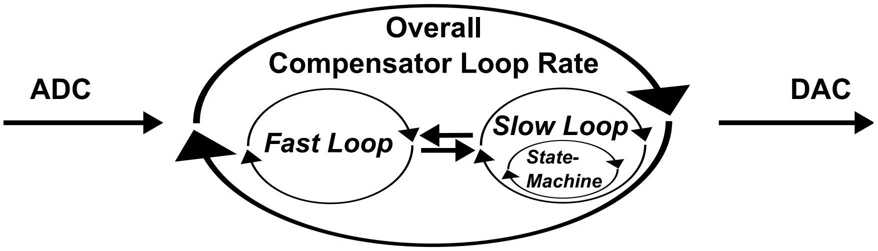

Figure 5.8: Brief overview of the implementation.

The implementation uses floating point arithmetic, which now can be easily realized in FPGAs and can greatly increase the dynamic range. In contrast, fixed point arithmetic needs proper optimization for a specific numeric range and can potentially lead to unmodeled non-linear saturations, resulting in instabilities of the compensator.

The state-space system can be put into different representations, such as the controller or observer canonical form. Although these forms are a direct representation of the transfer function, they might not be suitable for the implementation. Individual states can reach high numerical values that can be difficult to incorporate in any system. Hence, the state space system in this case is represented in modal form to obtain a better conditioning. In this case, the complex conjugate pole pairs of each eigenmode's second order transfer function occupy the four elements of each corresponding two-by-two sub-matrix, as shown earlier in Section 5.2.

XILINX Inc. offers the LogiCore IP library, which is a set of predefined, optimized functions. It is partly used in the following implementation to realize fundamental operations of the compensator computations. For example, it allows to define a particular usage of FPGA components: Look-Up Tables/Flip-Flops only or in combination with DSP48s. By using the DPS48 logic blocks, the design is likely to run at a faster clock rate. However, they are only available in a limited quantity throughout the FPGA. In addition, the degree of computational pipelining (affecting the latency) and internal hardware reuse (affecting the clock cycles needed per operation) can be set.

The compensator logic itself embedded in the overall design can be realized hardware independent. However, the implementation varies by compensator order. Subsection 5.5.1 outlines the design for a single-eigenmode (second order) and dual-eigenmode (forth order) compensator. Thereafter, the chosen compensator of Subsection 5.5.1 is implemented into the two different FPGA systems introduced in Section 3.5 and covered in Subsection 5.5.2. The platform specific implementation is explained for each FPGA system. As a result, the platform and compensator of a given order can be chosen separately. It can then be combined with the help of Subsections 5.5.1 and 5.5.2. Important to consider is the resulting overall achieved compensator feedback loop rate. It is also the frequency used for the model and compensator discretization in the mathematical design earlier in this chapter.

5.5.1 Platform Independent Implementation for Models of Different Orders

In the following, details on the implementation strategy for a high performance compensator are given. The compensator will then be placed inside the hardware platform dependent implementation of the following Subsection 5.5.2.

A state machine for the compensator computation is chosen for two reasons. First, hardware components can be reused and assigned with different tasks each state iteration. This saves potentially valuable space and components inside the FPGA, such as the XtremeDSP DSP48 Slices. Second, splitting the computation into many steps allows higher clock rates that otherwise introduces long signal paths. The author's experience has shown that the depth of pipelining and achieved clock rate do not form a linear relationship. An optimum trade-off exists, where the resulting compensator feedback loop rate is maximized.

In accordance with the predictive estimator in Equation (5.8), the state-machine is organized such that the updated actuation signal u can be computed as quickly as possible to reduce the compensator time delay. After new incoming samples it is the first computation performed in a time step k. All remaining compensator computations that are needed for time step $k+1$ are not dependent on consecutive incoming samples. Hence, all computations relevant for the time step $k+1$ can be prepared during the remaining time of time step k. Figure 5.9 is a graphical indication of the relationship of sampling time and computational time needed within a time frame, including the time step it belongs to. In contrast, a current estimator would require more computations before the actuation signal can be updated, introducing a higher delay.

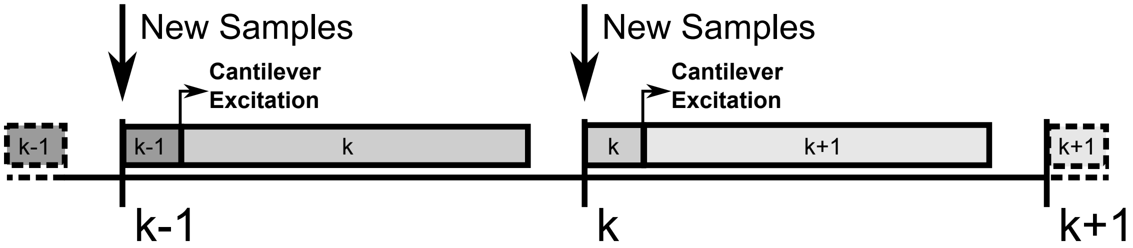

Figure 5.9: Compensator loop rate time interval between two incoming samples, where the gray bars represent the computational time needed to perform one compensator increment.

In the following, the implementation of a single-mode and dual-mode compensator is discussed as an example. The main difference between the two is the number of states and hardware components needed. However, the design can be modified to incorporate any model order. In general, the higher the order of the estimator, the lower the resulting feedback loop rate will be. Again, the compensator feedback loop rate determines the sampling time for the discretization of the model/compensator.

Implementation for Multi-Eigenmode Control

As an example, the implementation of a dual-eigenmode compensator (two eigenmodes, forth order model) is outlined, based on a nine states state-machine. The computations are performed by a total of four multipliers, four adders and one subtractor, all operating in single precision floating point.

The state machine in Figure 5.10 indicates the nine processing states and one default (waiting) state. The latter one is for the case of a new sample is not yet being available. For readability reasons, the bar on top of each letter, indicating the modeled coefficient, is objected in Figure 5.10. Otherwise, the matrices with their coefficient nomenclature are consistent with the derivation in Section 5.2:

$$\mathbf{A} = \begin{bmatrix} \mathbf{A_1} & \mathbf{0} \\ \mathbf{0} & \mathbf{A_2} \end{bmatrix}, \text{where } \mathbf{A_1} = \begin{bmatrix} a_{1,11} & a_{1,12} \\ a_{1,21} & a_{1,22} \end{bmatrix}, \mathbf{A_2} = \begin{bmatrix} a_{2,11} & a_{2,12} \\ a_{2,21} & a_{2,22} \end{bmatrix}, \tag{5.11}$$

$$\mathbf{B} = \begin{bmatrix} b_1 \\ b_2 \\ b_3 \\ b_4 \end{bmatrix}, \mathbf{C} = \begin{bmatrix} c_1 & c_2 & c_3 & c_4 \end{bmatrix}, \mathbf{K} = \begin{bmatrix} K_1 & K_2 & K_3 & K_4 \end{bmatrix}, \mathbf{L} = \begin{bmatrix} L_1 \\ L_2 \\ L_3 \\ L_4 \end{bmatrix}. \tag{5.12}$$

Upon start, the state machine enters at the *Default* state. If a new sample is available ($z = 1$), the state machine proceeds from the *Default* state to state 1, or directly from state 9 to state 1 after a computation is finished. Otherwise, it executes the *Default* state as often as it is awaiting a new sample. r_{ADC} and y_{ADC} are the actuation reference from the AFM controller and cantilever sensor signal, respectively. Certain new **case sensitive** variables are introduced to store intermediate values for consecutive states. This is since some calculations require more than one operation and hence clock cycle. Here, c_i, k_q, l_i, k_i and $a_{i,xx}$ are such variables. Bold variables indicate vectors or matrices. For example, the operation $\mathbf{b} = \mathbf{B} \cdot u$ are four multiplications carried out by the four multipliers in parallel and stored in four intermediate variables indicated as $\mathbf{b}$. The symbol $\circ$ indicates the Hadamard product, an element-wise operation that multiplies the corresponding elements according to $(A \circ B)_{ij} = A_{ij} \cdot B_{ij}$. This, again, is necessary because the desired operation, e.g. $\bar{\mathbf{C}}\hat{\mathbf{q}}$ cannot be numerically performed in a single step as it requires multiplication and consecutive addition. The proper application of the Hadamard product might need a previous transpose of a vector, as indicated by an apostrophe.

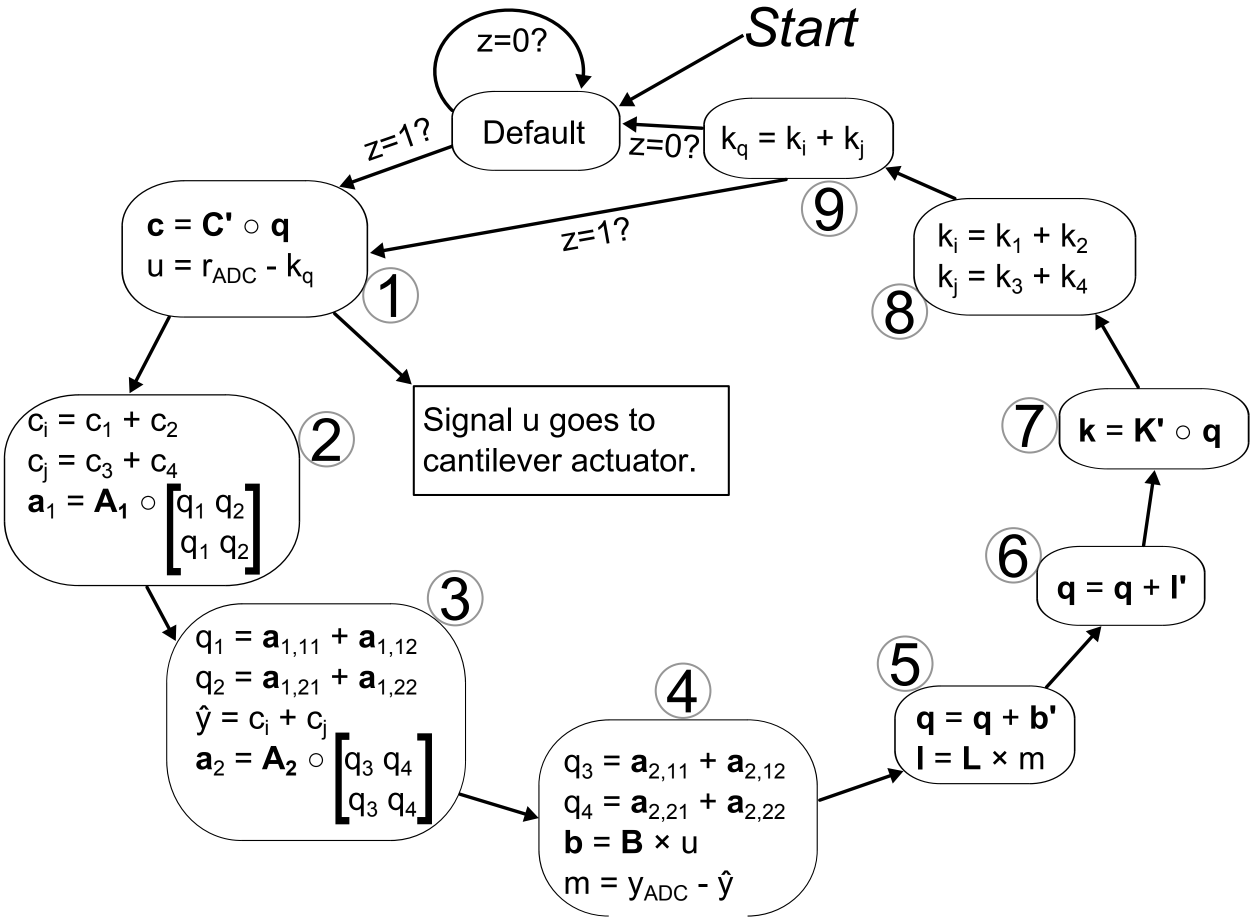

Figure 5.10: State-machine implementation of the multi-eigenmode compensator, here for a 4th order system.

Simplified Implementation for Single-Eigenmode Control

To control a single eigenmode, the compensator is reduced to a second order system based on a seven-states state machine, as presented in Figure 5.11. In addition, the hardware usage is reduced to two multipliers, two adders and one subtracter, which are all operating in single precision floating point:

$$\mathbf{A} = \begin{bmatrix} a_{11} & a_{12} \\ a_{21} & a_{22} \end{bmatrix}, \mathbf{B} = \begin{bmatrix} b_1 \\ b_2 \end{bmatrix}, \mathbf{C} = \begin{bmatrix} c_1 & c_2 \end{bmatrix}, \mathbf{K} = \begin{bmatrix} K_1 & K_2 \end{bmatrix}, \mathbf{L} = \begin{bmatrix} L_1 \\ L_2 \end{bmatrix}. \tag{5.13}$$

The nomenclature of the state-machine diagram is nearly identical to the one in the previous multi-eigenmode implementation and the reader is kindly referred to it if needed. A small change is made in the indices of the matrix **A** elements. The additional indication referring to the respective eigenmode is objected in this case.

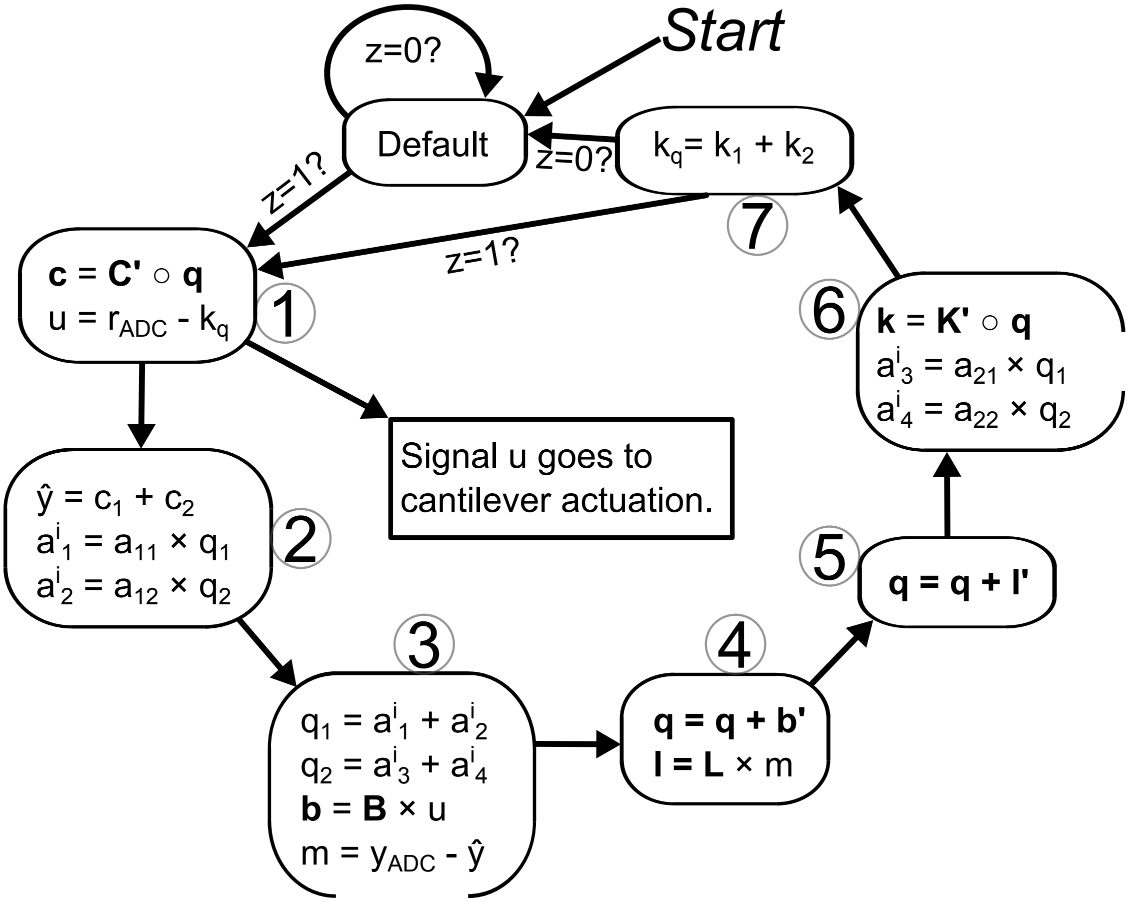

Figure 5.11: State-machine implementation of the single-eigenmode compensator modeled as a 2nd order system.

5.5.2 Implementation in Two Different FPGA Systems

In this section, the hardware independent compensator designed in Subsection 5.5.1 is implemented into the two different FPGA systems, as introduced in Section 3.5. The compensator clock rate is maximized in both FPGAs. As a result, the Virtex-5 rate is approximately twice as high as the one in the Spartan 3A-DSP. This is due to the improved and faster internal components of the Virtex-5, such as the DSP48s.

Virtex-5 LX110 Platform

Figure 5.12 shows an overview of the logical implementation in the Virtex-5. The design is divided into two different clock domains (see Figure 5.8). The *Fast Loop* captures the ADC values, performs a decimation, converts the 14-Bit fixed point into a single precision floating point number and puts it into a First In, First Out (FIFO), where it can be picked up by the *Slow Loop*. The *Slow Loop* performs the compensator calculation and puts the result back into a FIFO, where it can be picked up by the *Fast Loop* again. The consecutive components in the *Fast Loop* convert the floating point number back to fixed point, increase its sampling rate back to the original rate and outputs the value via the 16-Bit DACs. The magnification of the compensator in the same Figure shows its logic implementation, as it is covered in Subsection 5.5.1.

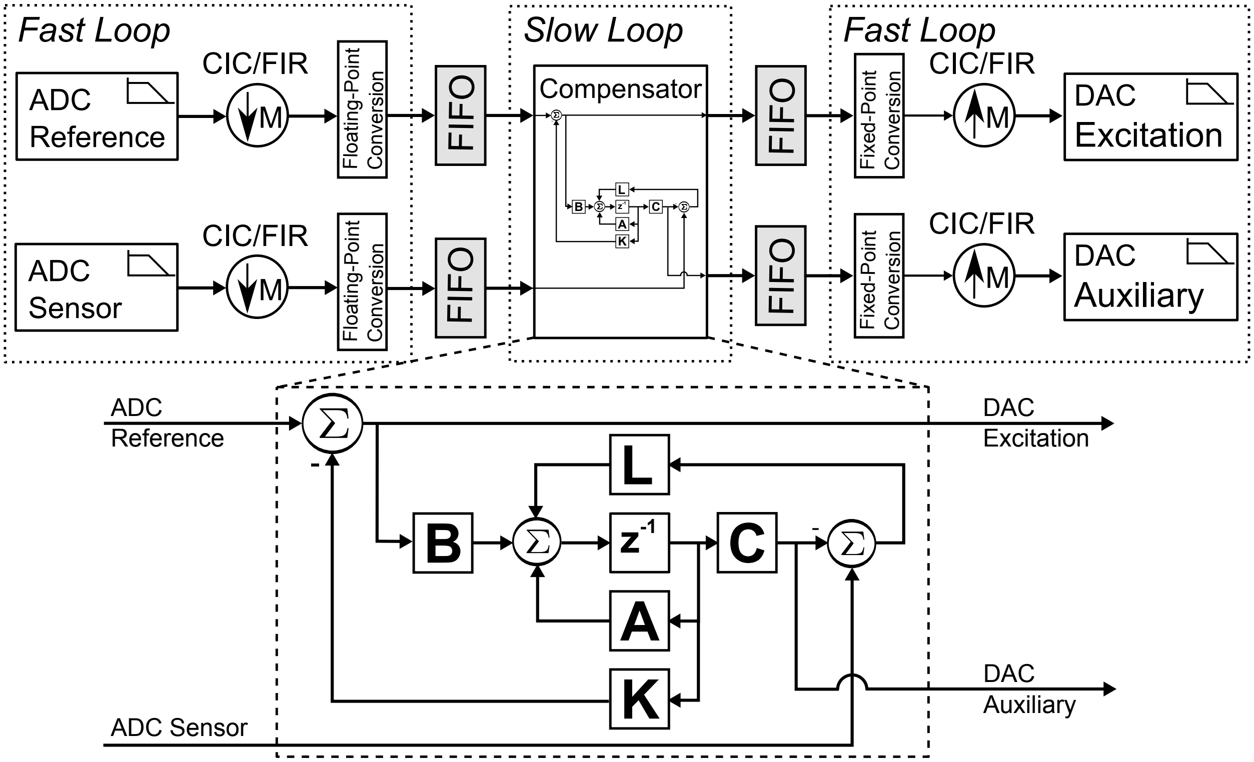

Figure 5.12: Overview of the full implementation in the Virtex-5 LX110 based system. The magnification of the compensator indicates a detailed view.

The *ADC Reference* and *ADC Sensor* are the actuation signal of the AFM controller and the cantilever's sensor signal, respectively. The *DAC Excitation* and *DAC Auxiliary* are the modified cantilever actuation and the estimated cantilever sensor signal $\hat{\mathbf{C}}\hat{\mathbf{q}}_k$, respectively. The latter one will be later used for an alternate amplitude demodulation approach in Chapter 8. It is significantly reduced in noise compared to the measured cantilever's sensor signal.

Here, the *Fast Loop* has a clock rate of 100 MHz sampling at 100 MSa/s. The *Slow Loop* has a rate of 52 MHz for the dual-eigenmode compensator of Subsection 5.5.1. The compensator loop rate is the *Slow Loop* rate divided by the number of compensator clock cycles needed to compute one iteration. Based on the 9 states state-machine, it results in a feedback loop rate of 5.56 MHz. The decimation factor is based on the ratio of the *Fast Loop* to the compensator feedback loop rate. Hence, it is 18, as it is rounded to the nearest higher integer to not feed the compensator faster than it can process. Also, the sampling rate of the discretized model needs to be adjusted accordingly. If the FIFO does not hold a value at a particular requested time, the compensator automatically goes into a waiting state.

Decimators/Interpolators are needed rather than simple Downsamplers/Upsamplers due to the 40 MHz bandwidth of the ADC's and DAC's analog anti-aliasing filters. This bandwidth would violate the Nyquist theorem in respect to the much slower compensator loop rate. It can potentially cause aliasing of unexpected frequencies above 2.9 MHz, based on the above example without appropriate filters before downsampling. As a note, the ADCs cannot be set to a lower sampling rate, as an appropriate analog anti-aliasing filter with a lower bandwidth is not available. The difference between the two types of sample rate change is outlined in Section 2.6.1.

The decimators/interpolators are formed with the help of FIR filters. An alternative is the usage of Cascaded Integrator-Comb (CIC) filters that are less complex in their implementation. However, the passband and stopband behavior are not optimal and might require a compensation filter for recovery. The two different types of decimation/interpolation filters can be easily designed, for example, using the filter design toolbox in Matrix Laboratory (MATLAB). Important is the order of the filter, with higher order improving the passband, transitional and stopband behavior, but increasing the phase delay. Here, the interpolation factor is equivalent to the decimation factor, because the samples are transferred back from the *Slow Loop* to the *Fast Loop*.

Spartan-3A DSP

The Spartan-3A DSP implementation is very similar to the one in the Virtex-5, as shown in Figure 5.13. The *Fast Loop* is clocked at 100 MHz sampling at 100 MSa/s and the *Slow Loop* is clocked at 25 MHz. After the AD conversion in the *Fast Loop*, the samples are converted into single precision floating point and put into single sample buffers. Here, new samples overwrite previous contained samples. The *Slow Loop* picks up the values at its compensator feedback loop rate. In case of the dual-eigenmode compensator, the loop rate is 2.78 MHz, resulting in a decimation factor of 36.

The single-eigenmode compensator is computed at a rate of 3.57 MHz, which is faster than the dual-eigenmode case due to the lower model complexity. Here, the decimation factor is 29. As an example, the VHDL code of the *Slow Loop* (Compensator Core) is attached on page 171.

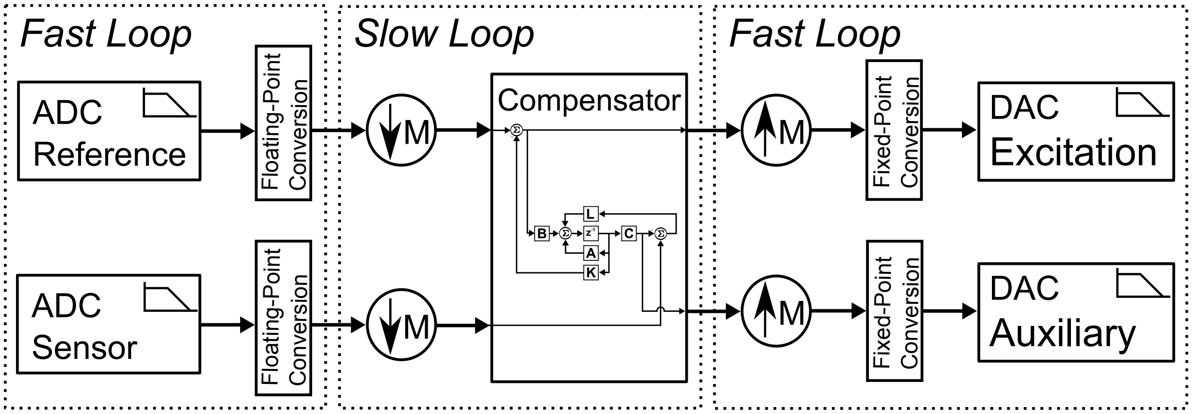

Figure 5.13: Overview of the full implementation in the Spartan-3A DSP based system. The compensator implementation is identical to the one in Figure 5.12, which shows the magnification for a better view.

The ADC's analog anti-aliasing filters have a bandwidth of approximately 1 MHz. Based on the above example, a typical compensator loop rate is about 2.5 MHz to 4 MHz. Hence, the containing frequencies in the signal are typically below the Nyquist frequency of the compensator feedback loop rate. Simple downsampling and upsampling is then sufficient without the need of additional digital filters.

After each compensator calculation cycle, the results are put back into single sample buffers inside the *Fast Loop*. This results in the upsampling, causing samples to be read repetitively until the buffer is updated by the *Slow Loop*.

5.6 Conclusion

In this chapter, the compensator including the estimator and controller has been derived, discretized and simulated in an hybrid analog/digital Simulink based simulation. The design has then been implemented into two different FPGA based systems in two different model orders. However, any cantilever model order can be used and implemented with the method presented here. The maximum achievable compensator feedback loop rate depends on the compensator order. The following three chapters 6, 7 and 8 use the design method of this chapter to utilize the compensator during different imaging approaches.

6 Control of First and Higher Cantilever Eigenmodes

High speed imaging in AFM tapping mode depends on the cantilever's effective resonance frequency and Q factor. Imaging in higher cantilever eigenmodes implies increased acquisition bandwidths based on the frequency. However, in combination with the corresponding Q factor it leads to a specific time constant of each eigenmode. The detection and control of the higher eigenmodes has become easily available with the development of powerful data acquisition and processing hardware. To achieve a greater flexibility the estimator based compensator of Chapter 5 is utilized in a single-eigenmode control setup (Section 5.5). It results in the modification of both Q factors and resonance frequencies. Using higher eigenmodes in combination with lowered Q factors considerably enhances the image acquisition rate. A 20 times increase in imaging bandwidth is achieved by using the presented methodology. On the other side, the resolution can be enhanced by using increased Q factors. The modification of the resonance frequency (F control) allows imaging at resonances that are not natural to the cantilever. This can be useful to match excited higher eigenmodes with nearby harmonics to increase the contrast in material property imaging, whose benefit is discussed later in Chapter 9. The single-eigenmode compensator is applied as a simple modification to an AFM characterization and imaging environment. The performance is evaluated on different samples in tapping mode in air.

6.1 Motivation

A convenient method to achieve faster cantilever dynamics is active feedback control [53,73,166]. It can be easily incorporated into existing AFMs, either through an externally connected or internally implemented circuit, both either analog or digital. Further, most AFMs utilize reconfigurable digital platforms, where the control algorithm can be incorporated as a simple configuration update.

In the past, cantilever feedback control has been applied in various applications to mostly modify the Q factor. It has been usually used with the first eigenmode, mainly for an increased imaging sensitivity [166]. Previous approaches have also introduced state-space control methods for the first resonance only [53, 169]. Imaging in higher eigenmodes has been attempted without dynamic control [57] [58] [89] or controlled second eigenmode [203]. Kokavecz *et al.* have performed a comprehensive study evaluating the imaging bandwidth based on Q factor, set-point, adhesion, etc. involving the first resonance of a cantilever in the tapping mode [204]. An actuation frequency lower than the first eigenmode's resonance has been used by Balantekin *et al.* The first eigenmode then coincides with one of the excited harmonics. This scheme is used for enhanced material property mapping [205]. A more thorough introduction into the speed limitation, in particular in cantilevers, is given in Section 2.1.3.

In this chapter, the single-eigenmode compensator of Section 5.5 is used to modify the Q factor and natural frequency of the cantilever. It enables the modification of Q_i, the resonance frequency $\omega_{r,i}$ or a combination of both. Q control of the first three transverse eigenmodes is performed and used for scanning the topography of a sample surface. This scheme gives a great flexibility to tune the imaging bandwidth. The differences in the images are noticeable, both in tracking speed and image quality. Also, frequency control (F control) is applied to the first eigenmode to modify its resonance frequency.

Section 6.2 introduces the modified AFM setup. In Section 6.3, Q control on the first three transversal resonances is used while scanning the topography of a sample surface. Results are evaluated towards its imaging and time domain performance. F control is applied to the first eigenmode to modify its resonance frequency in Section 6.4, with images obtained thereafter. This is particularly interesting for tuning the ratio of eigenmodes towards each other, as will be discussed in Chapter 9. This chapter closes with a conclusion in Section 6.5.

6.2 Modified AFM Setup and Resonances

The setup in Figure 6.1 is a modification of the AFM I setup of Section 3.1 in combination with the active cantilevers of Section 3.2. The new parts and signals are represented by dashed lines and boxes. The active cantilever is modeled according to Chapter 5 and specifically implemented with the single-eigenmode compensator, as outlined in Subsections 5.5.1 and 5.5.2. Hence, each eigenmode is represented by a second order system in the modal state space form.

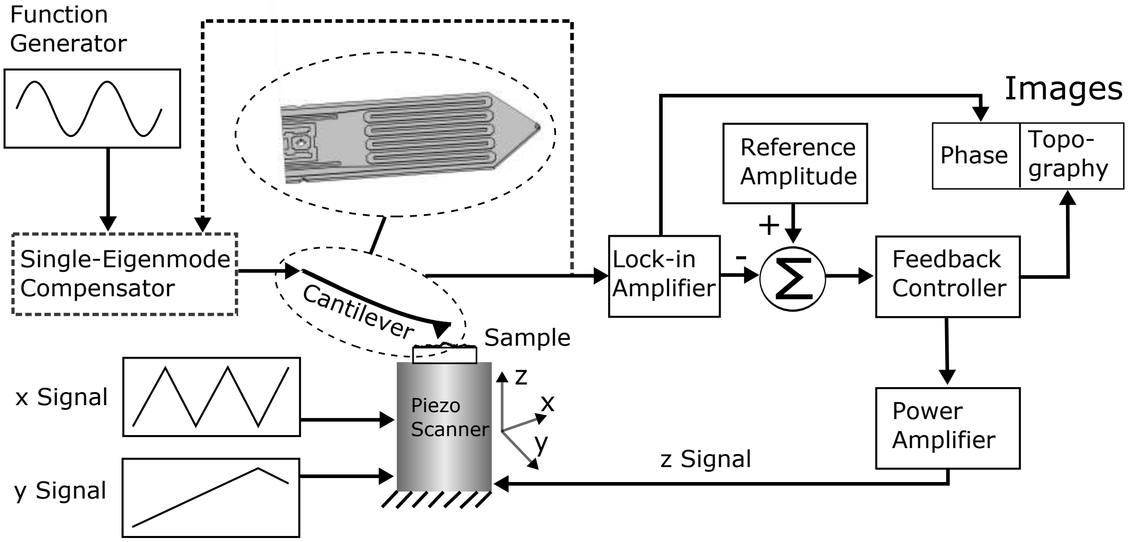

Figure 6.1: Modified AFM I setup for the single eigenmode approach. Dashed lines and boxes indicate the modification of the standard setup in Figure 3.1.

Figure 6.2(a)-(c) indicate the first three transverse eigenmodes of an active cantilever under Q control. This is achieved by the implemented compensator with desired pole locations based on Equation 5.6 in Section 5.3 (Page 70). Each resonance is modified towards both an increased and decreased Q_i, as listed by the table in Figure 6.2. Also, the phase is indicative of the different Q factors. Figure 6.3 indicates the first eigenmode under F control, based on the pole selection case (D) of Equation (5.6). The Q factor appears to be altered in the different cases of Figure 6.3. The shape of the resonance broadens the larger the modification of $\omega_{n,i}$. After all, the off-resonance is a forced response without a coinciding natural frequency and requires considerable actuation power.

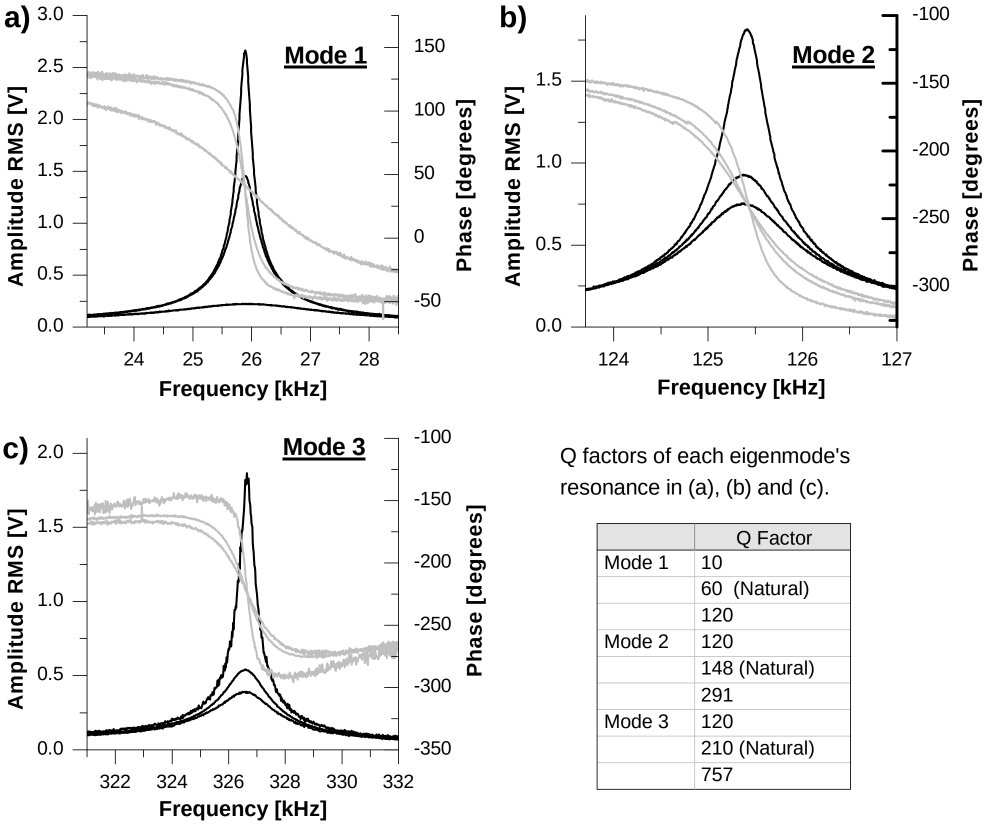

Q factors of each eigenmode's resonance in (a), (b) and (c).

	Q Factor
Mode 1	10
	60 (Natural)
	120
Mode 2	120
	148 (Natural)
	291
Mode 3	120
	210 (Natural)
	757

Figure 6.2: Frequency sweep of each eigenmode's resonance with modified Q-factors. The table lists natural/modified Q factors.

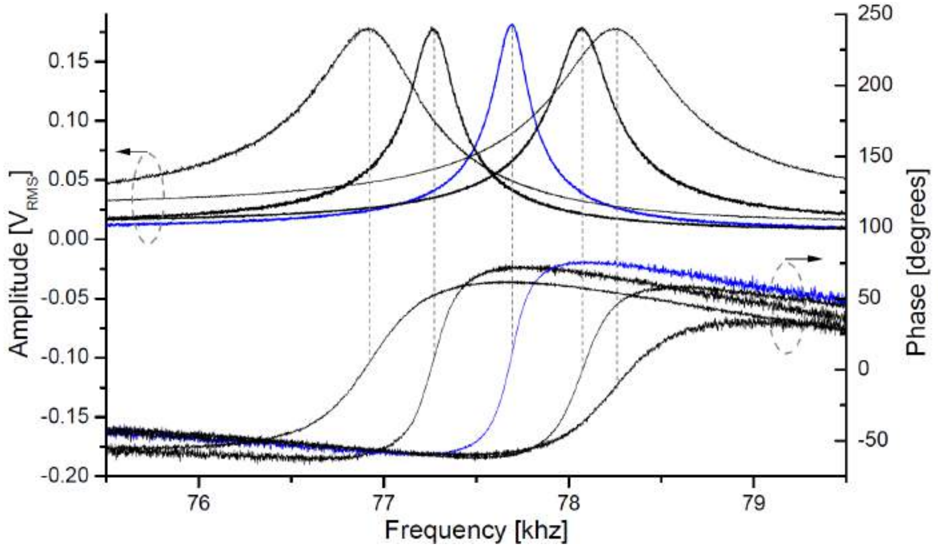

Figure 6.3: Different modified resonances according to Equation (5.6). The blue curve represents the resonance with an unmodified $\omega_{r,1}$.

6.3 Imaging and Time Domain Results under Q control

In this section, the implemented compensator is used to perform imaging and time domain measurements. The Anfatec UMG03/PtSi sample offers two different patterns that are used for imaging. One pattern, hereby named (i), has 2 μm wide and 58 nm high parallel SiO_2 lines on a silicon substrate with a pitch of 4 μm. The other pattern, in the following named (ii), is a 58 nm high SiO_2 chess pattern, formed on the silicon substrate with a pitch of 1 μm by 1 μm. In all images the fast scan direction is horizontal, from the right side towards the left side. The slow scan direction is vertical, from the top to the bottom of the image.

The actuation voltage of each unmodified and modified eigenmode is adjusted to achieve matching amplitudes at the cantilever's tip. Note that this is in contrast to Figure 6.2 where the actuation signal is constant. This effort attempts to create comparable imaging conditions. Hence, the free air amplitudes A_i are always $A_1 = 325\,\text{nm}$, $A_2 = 118\,\text{nm}$ and $A_3 = 69\,\text{nm}$. Note that a different cantilever is used for the time domain measurements throughout the Subsections.

6.3.1 Q control on the First Eigenmode

The first eigenmode of the active cantilever is combined with different Q_1 factors. Figure 6.4 are measured time domain responses of the cantilever upon a step in the actuation amplitude. Figure 6.4(a) and (b) are the responses with $\tau_1 = 4.5\,\text{ms}$ ($Q_1 = 500$) and $\tau_1 = 450\,\mu\text{s}$ ($Q_1 = 50$), respectively. Here, $\omega_{n,1}$ is 221.8 kHz. The different noticeable time constants and amplitudes are consistent with the Q factor ratio of 10:1. The amplitudes are directly influenced by the Q factor via $G(j\omega)|_{max} \propto Q_i$ as an amplification at resonance.

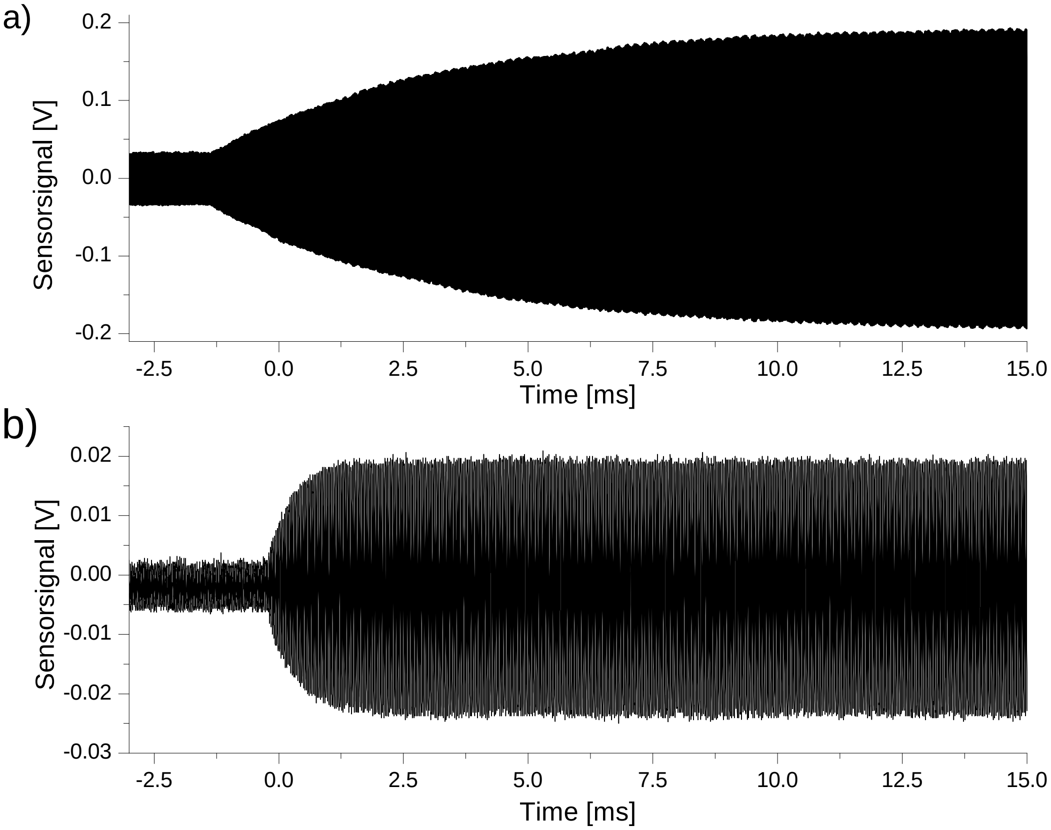

Figure 6.4: Measured time domain signals of a cantilever's first resonance with (a) $\tau_1 = 4.5\,\mathrm{ms}$ ($Q_1 = 500$) and (b) $\tau_1 = 450\,\mu\mathrm{s}$ ($Q_1 = 50$). The step actuation amplitudes are similar in both cases.

Based on the time constant, the different Q_1 factors influence the topographical tracking ability of the cantilever. It can be seen in the images of the sample structure (i) by comparing the different scan conditions in Figure 6.5. The scale (in nm) of Figure 6.5(c) applies to all images in the same Figure. At a low scan rate of 2 lines/s (Figure 6.5(a)-(c)) the cantilever is able to properly track the sample topography with any of its Q_1. However, the images obtained with the medium and high Q_1 appear clearer. This is due to the lower forces exerted on the sample surface. In Figure 6.5(d)-(f) the scan rate is increased to 15 lines/s. Figure 6.5(f), obtained with a high $Q_1 = 120$, cannot follow the sample properly due to the higher τ_1. A similar behavior would be observable with the low and medium Q_1 factors, when the imaging rate is further increased. In Figure 6.5(g)-(i) the setpoint is increased with an imaging rate of 15 lines/s. This lowers the influence of the sample on the cantilever and results in $Q_{eff,1}$ to increase. Hence, τ_1 increases as it is visible on the slow tracking in Figure 6.5(h). In Figure 6.5(i) (bottom right image) tracking is lost altogether.

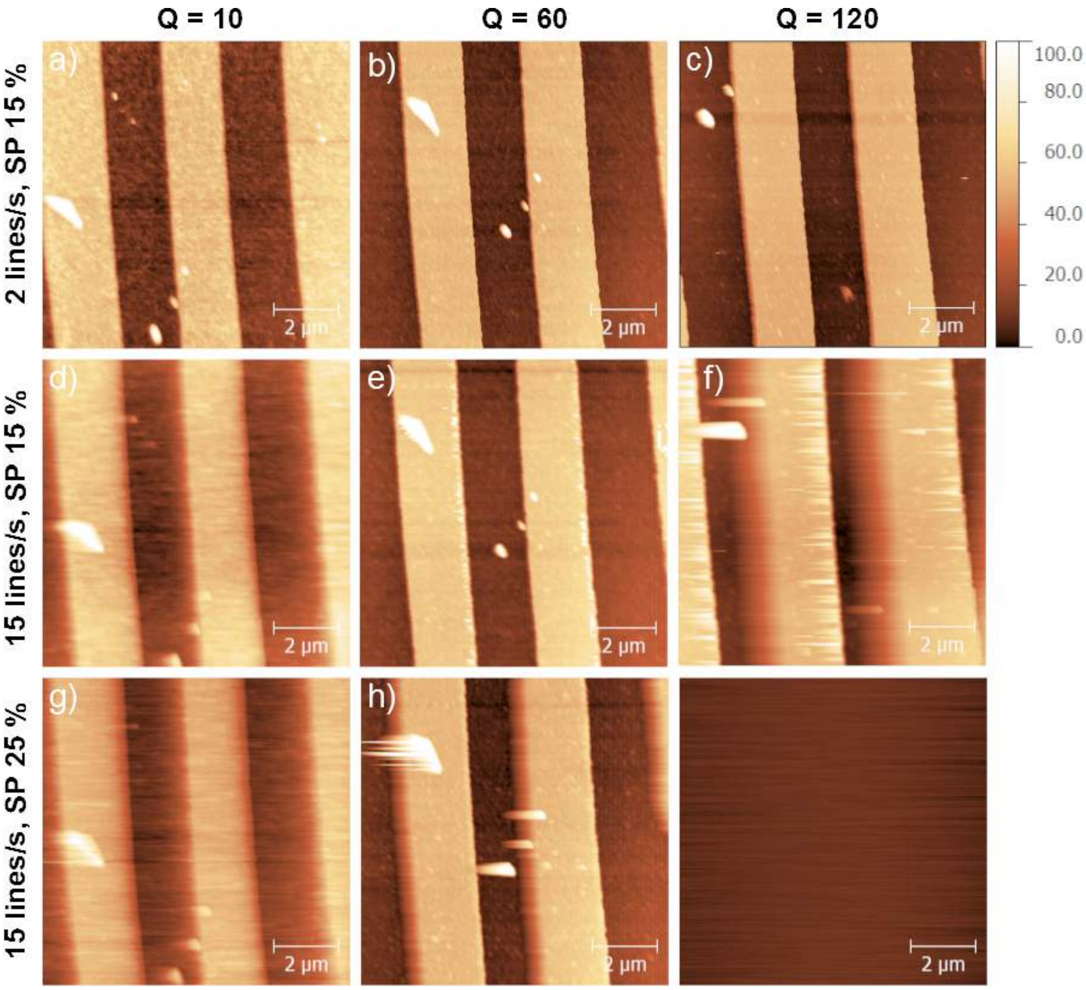

Figure 6.5: Images obtained with the first eigenmode and modified Q_1 factors as indicated. In addition, the scan rates and setpoints are modified. The square scan areas are $(9\,\mu\mathrm{m})^2$ obtained with the cantilever of Figure 6.2. (Scale of (c) in nm.)

6.3.2 Q Control on Higher Eigenmodes

The active cantilever with modified Q_i factors is actuated at one of its first three transverse eigenmodes and used for imaging of the test sample structure (i). Different scenarios with varying imaging speeds are demonstrated. It includes conditions where all three eigenmodes result in either a matched τ_i or Q_i. In addition, the influence of the modified Q factor on the set-point is indicated.

First, the non-compensated cantilever with its natural Q_i factors is used to image the sample at different scanning rates. Figure 6.6 shows the set of images. As indicated, each column presents images obtained with a different eigenmode, whereas rows represent modified scanning speeds.

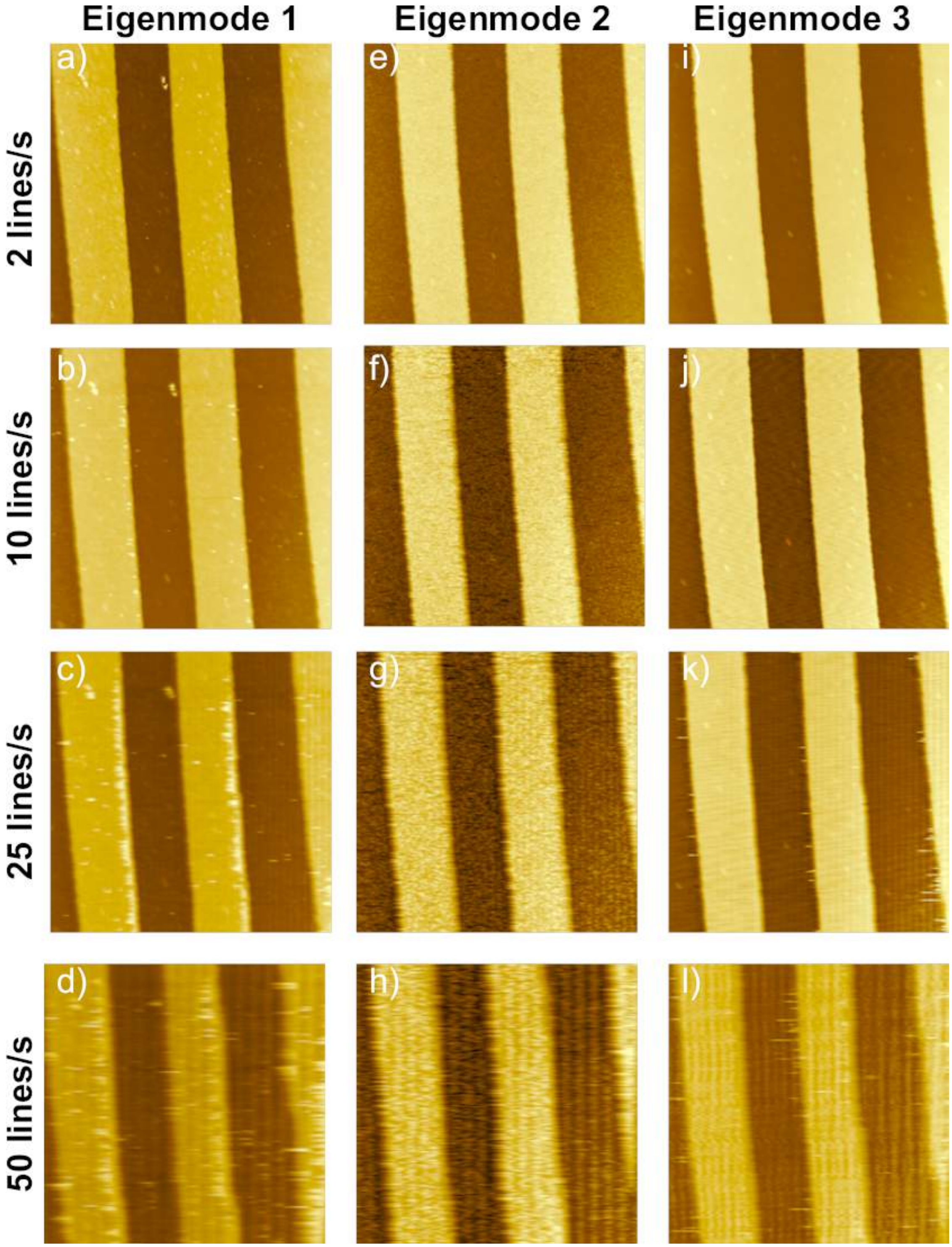

Figure 6.6: Images obtained with the first three eigenmodes and natural Q_i factors. The square scan area is $(9\,\mu\mathrm{m})^2$.

The square scan area is $(9\,\mu\text{m})^2$ and the natural Q factors are $Q_1 = 60$, $Q_2 = 148$ and $Q_3 = 210$. In particular the images at higher scan rates show ringing perpendicular to the (horizontal) fast scan direction. This is due to an adjustment of the z feedback parameters to improve the tracking ability at higher scan rates. However, the increased bandwidth of the z feedback causes the phase/gain margin to drop and resonances appear.

Next, the performance of the non-compensated cantilever eigenmodes is compared to Q_i controlled eigenmodes. Figure 6.7(a)-(c) shows the set of images, obtained at 2 lines/s and a square scan area of $(9\,\mu\text{m})^2$ (Similar to Figure 6.6). The scale (nm) of 6.7(c) applies to all images in the same Figure.

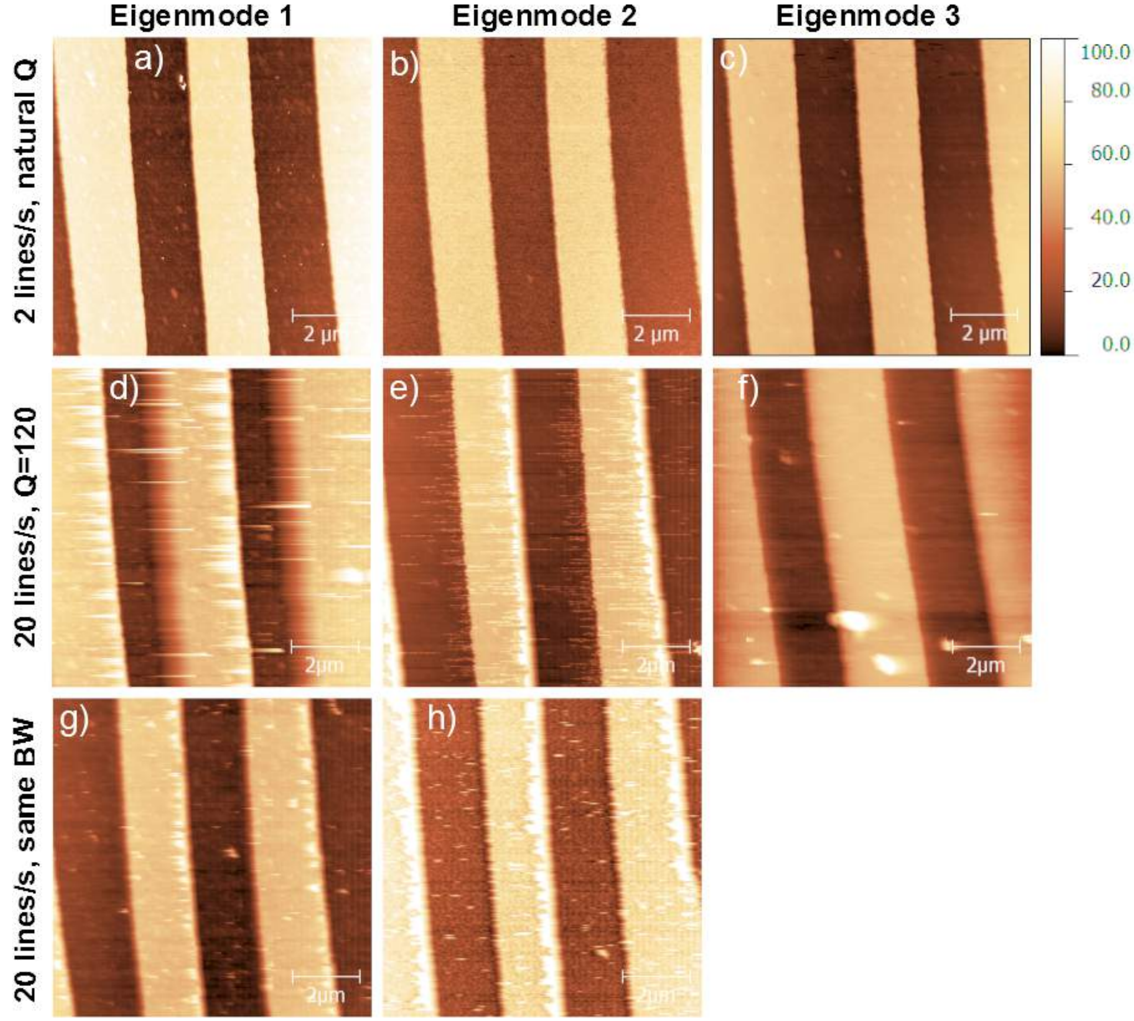

Figure 6.7: Images obtained with the first three transverse eigenmodes and natural Q_i factors in (a)-(c). In (d)-(f) all Q_i factors are matched to be 120. (g) and (h) use $Q_1 = 60$ and $Q_2 = 291$, respectively, resulting in $\tau_1 = \tau_2$. The scan area is $(9\,\mu\text{m})^2$ scanned with the cantilever of Figure 6.2. (Vertical scale of (c) in nm and applies to all images.)

The images in Figure 6.7(d)-(f) are obtained with $Q_{1,2,3} = 120$ in each eigenmode. At a scan rate of 20 lines/s the higher eigenmodes are able to properly follow the sample pattern. A time domain signal is presented in Figure 6.8, where the Q_i's of the three eigenmodes are equally set to 100. Here, the applied step in the actuation amplitude reveals different time constants of $\tau_1 = 900\,\mu$s, $\tau_2 = 146\,\mu$s and $\tau_3 = 54\,\mu$s. $\omega_{n,1-3}$ are 221.8 kHz, 1.370 MHz and 3.671 MHz, respectively. The inlet in the sub-figure of the third eigenmode is a magnification of the transitional part. The low time constant τ_3 increases the potential imaging rate by 20 times or more. This is compared to the unmodified first eigenmode that often has time constants in the millisecond range with Q factors above 200.

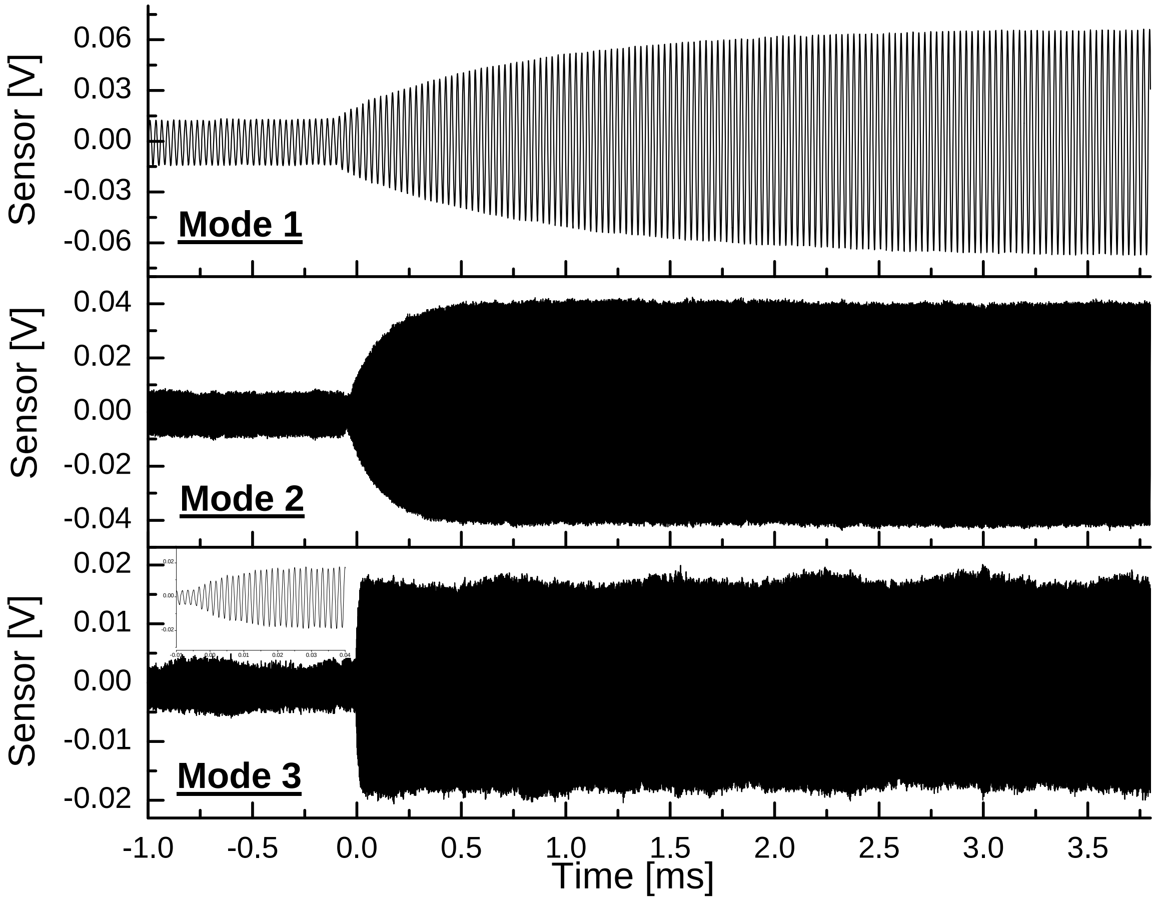

Figure 6.8: Measured time domain signals of the first three transverse eigenmodes of a cantilever, all set to a $Q_{1,2,3} = 100$. The different τ_i are noticeable by the slope of the envelope signal.

In Figure 6.7(g) and (h) the time constants are set to equal values of $\tau_{1,2} = 738\,\mu$s ($Q_1 = 60$ and $Q_2 = 291$). Hence, both images indicate similar tracking abilities. An image representing the third eigenmode's Q_3 of 757 is missing, as the feedback loop is unstable due to the high Q factor. Figure 6.9 shows the time domain step response. Here, $Q_1 = 50$, $Q_2 = 335$ and $Q_3 = 942$, where the time constants are about $\tau_{1,2,3} = 450\,\mu$s.

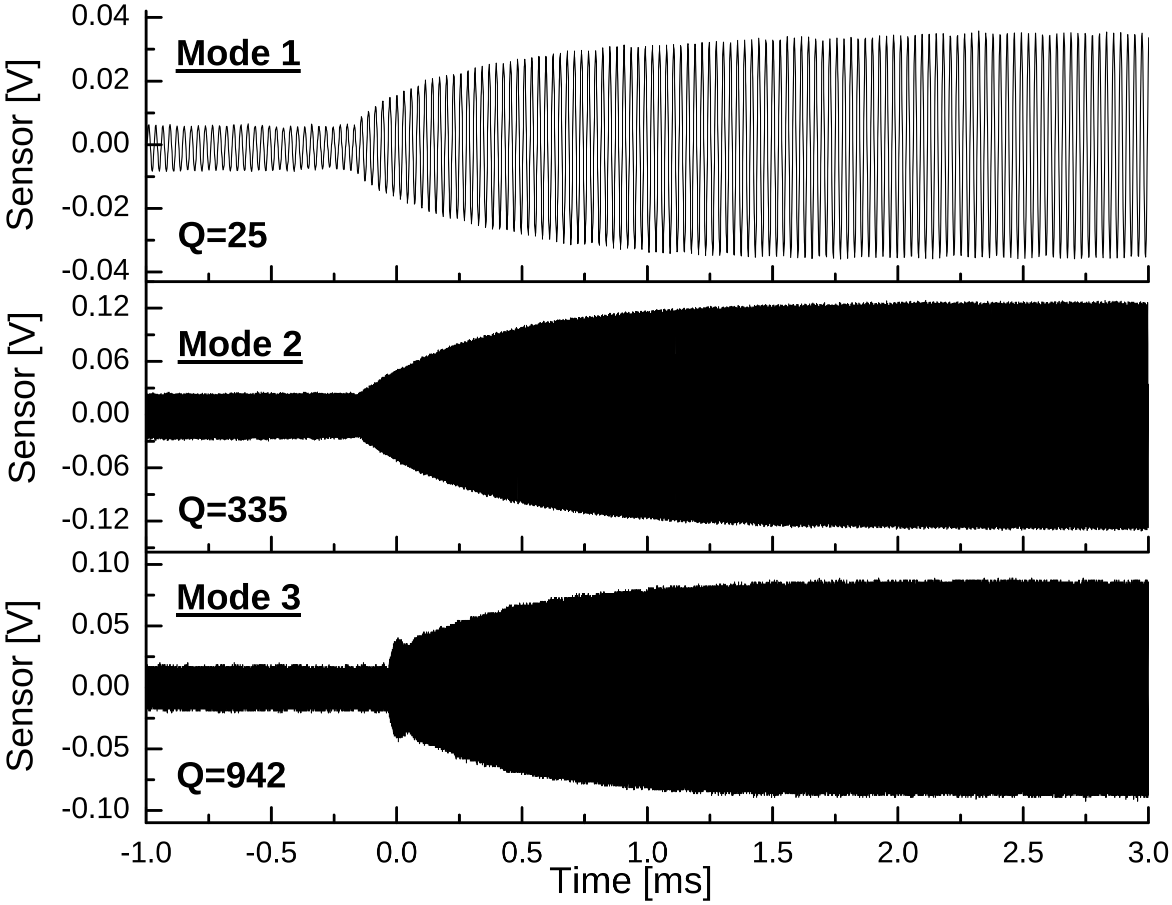

Figure 6.9: Measured time domain signals of the first three transverse eigenmodes of a cantilever, set to $Q_1 = 50$, $Q_2 = 335$ and $Q_3 = 942$ ($\tau_{1,2,3} = 450\,\mu$s).

6.4 F Control on the First Eigenmode

The cantilever's first eigenmode $\omega_{r,1}$ is modified and the different resonances used for imaging, as indicated in Section 6.2. The scanned images of the sample structure (ii) (chess pattern) are shown in Figure 6.10, where each image indicates the corresponding used resonance frequency. A deterioration of the image quality is visible the more the modified resonance differs from the original resonance.

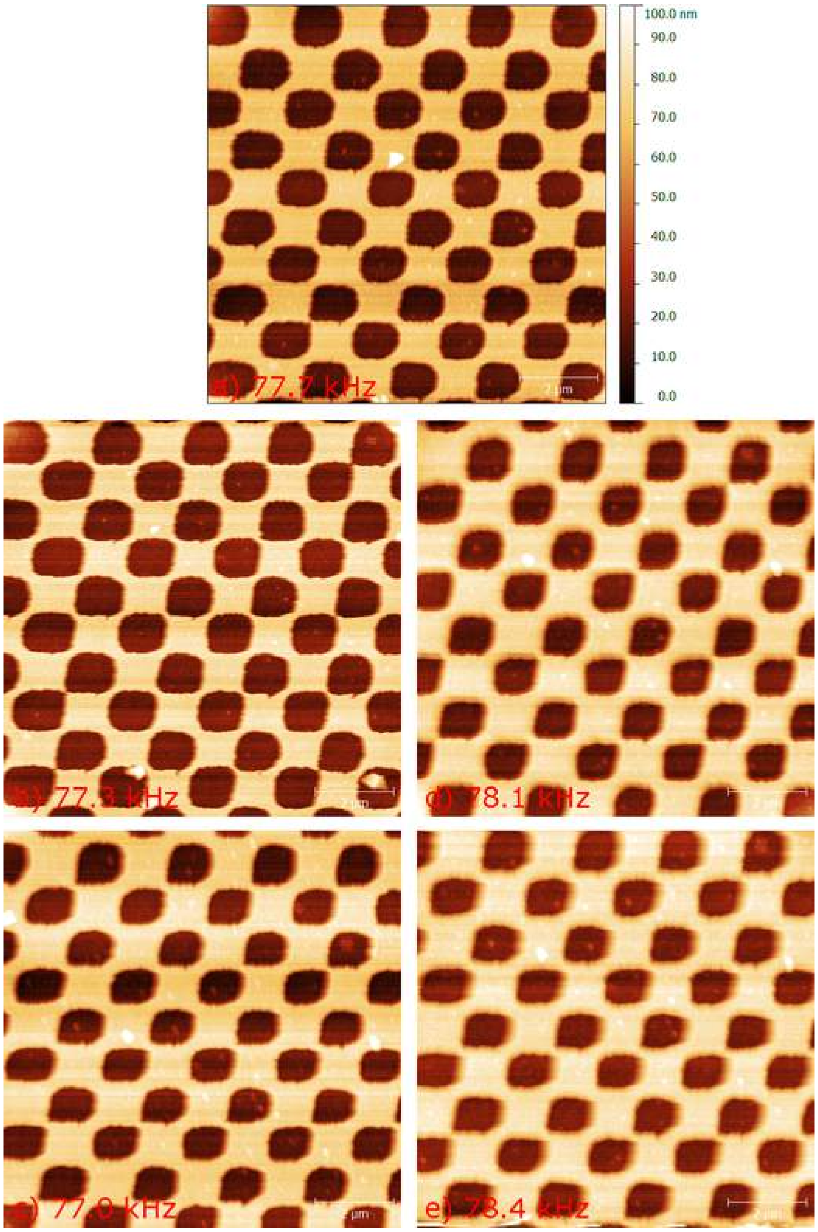

Figure 6.10: Images taken at the resonance frequencies as indicated. The sweeps are presented in Figure 6.3. The scale of (a) applies to all Subfigures (a)-(e).

A potential application of this approach is the investigation of nanomechanical sample properties. This has been conceptually introduced in Section 2.7 and will be further covered in Chapter 9. Here, the AFM is used to scan the sample with the first resonance. The appearing harmonics form integer multiples of the first resonance, where their magnitudes are material dependent. The harmonics are amplified in the vicinities of the higher eigenmodes [59]. The presented F control methodology can be used to modify the first resonance to match the higher resonances in integer multiples. Then, certain higher harmonics coincide with higher eigenmodes and the SNR is maximized, similar to the idea presented in [205].

6.5 Conclusion

The cantilever is one of the bottlenecks in the AFM, often preventing high speed imaging in tapping mode. Its first and higher transverse eigenmodes in combination with modified Q factors can considerably enhance the image acquisition rate. The presented control methodology is applied to the first and higher eigenmodes of the cantilever. This combination offers high flexibility for setting desired imaging conditions, even in real-time during scanning. Hence, this approach helps to overcome the relatively low acquisition rates of an otherwise powerful instrument. This is particularly important in vacuum applications where the absence of external damping results in high Q factors. The unmodified first eigenmode of a typical cantilever with Q_1 around 200 results in $\tau_1 = 1$ to $2\,\mathrm{ms}$. Combined with Q control, the free air τ_3 of one of the presented cantilevers is $54\,\mu\mathrm{s}$. Hence, the imaging rate capability of the cantilever can be increased by 20 times or more in our case. Also, the resonance of the first eigenmode is modified and used for imaging. Such F control can be useful for enhanced SNR of higher harmonics during nanoscale mechanical property mapping. This can be instead or in combination with the harmonic cantilevers described in Chapter 9. The presented control methodology can be easily extended to any cantilever sensor/actuator configuration, such as optical readout and piezo actuation. In the following Chapter 7 a higher order version of the compensator is used in a multi-eigenmode control fashion.

7 Multi-Eigenmode Control of Cantilevers in a Multifrequency Approach

High speed imaging and mapping of nanomechanical properties in AFM allows the observation and characterization of dynamic sample processes. Recent developments involve several cantilever frequencies in a multifrequency approach, as introduced in Section 2.7. One method actuates the first eigenmode for topography imaging and records the excited higher harmonics to map nanomechanical properties of the sample (Subsection 2.7.1). To enhance the higher frequencies' response two or more eigenmodes are actuated simultaneously, where the higher eigenmode(s) are used to quantify the nanomechanics (Subsection 2.7.2). In this chapter, each imaging scheme is combined with the estimator based multi-eigenmode compensator of Chapter 5 that modifies the Q factor of each resonance independently to enhance the force sensitivity and imaging bandwidth. It allows to satisfy the different requirements for the first and higher eigenmode. The presented methodology is compatible with existing AFMs and can be simply attached with minimal modifications. Different samples are used to demonstrate the improvement in nanomechanical contrast mapping and imaging speed of tapping mode AFM in air. The experiments indicate most enhanced nanomechanical contrast with low Q factors of the first and high Q factors of the higher eigenmode. In this scenario, the cantilever topography imaging rate can also be easily improved by a factor of 10. This chapter is also published in references [73], ©2015 IOP Publishing, and [74], ©2015 IEEE.

7.1 Motivation

In this chapter, the novel combination of both the multifrequency and higher harmonic methodologies introduced in Section 2.7 with the active multi-eigenmode compensator of Chapter 5 is demonstrated. The cantilever's different eigenmodes of vibration can be controlled simultaneously and independently, as outlined in Chapter 5, and used for imaging. It opens up the possibility to set optimal imaging conditions for topography and material contrast mapping, such as measuring sample stiffness. The multi-eigenmode compensator is implemented in a modified AFM setup with an additional Lock-in amplifier to capture the higher frequencies. It also utilizes active cantilevers with integrated bimorph actuation and piezo-resistive sensors introduced in Section 3.2. The approach is experimentally evaluated. Best results are achieved with low and high Q factors in the first and second eigenmode, respectively.

Very few attempts have been previously reported to incorporate such a control scheme. However, these have not addressed the multifrequency imaging aspects, in particular towards material contrasts. Such work includes topography imaging with the Q controlled first eigenmode and the suppression of undesired excitations of the second eigenmode. This is done by using a demodulating/modulating based compensator [206] and has led to sharper edges on sample features while scanning with the first resonance. Ruppert *et al.* have introduced an H_∞ approach to suppress undesired excitations of the first eigenmode while performing topography imaging with the second eigenmode [203]. In other areas, multimode control has been applied as vibration control of plates involving distributed actuators/sensors and active damping in buildings [207–213].

This chapter is organized as follows. In Section 7.2 the modified AFM setup is introduced and the multi-eigenmode compensator experimentally validated in the frequency domain without contact to a sample. Section 7.3 presents frequency domain measurement results in combination with a two component polymer sample. Performance of the compensator towards increased acquisition rates and material contrast during imaging in both introduced multifrequency methods is shown in Section 7.4. A conclusion is given in Section 7.5.

7.2 Modified AFM Setup and Resonances

In this section, the modified setup is described in more detail including the added components and resulting frequency sweeps under multi-eigenmode control. The active cantilever is modeled in a multi-eigenmode fashion according to Chapter 5. The compensator is implemented into both the Spartan-3A DSP and Virtex-5 LX-110 (Section 3.5). The implementation is outlined in Subsections 5.5.1 and 5.5.2. Hence, each eigenmode is represented by a second order system in the modal state space form.

The modification of the used AFM II setup of section 3.1 is shown in Figure 7.1, extended by the multi-eigenmode compensator and a second Lock-in amplifier. The new parts and signals are represented by dashed lines and boxes. The demodulated signals of the added Lock-in amplifier are sampled by the AFM controller and plotted alongside with the topography and phase that correspond to the first resonance. The compensator acts on the raw sensor signal to modify the cantilever's dynamics. In contrast, the Lock-in amplifiers are only used to demodulate the signals for data presentation and control of the z-piezo.

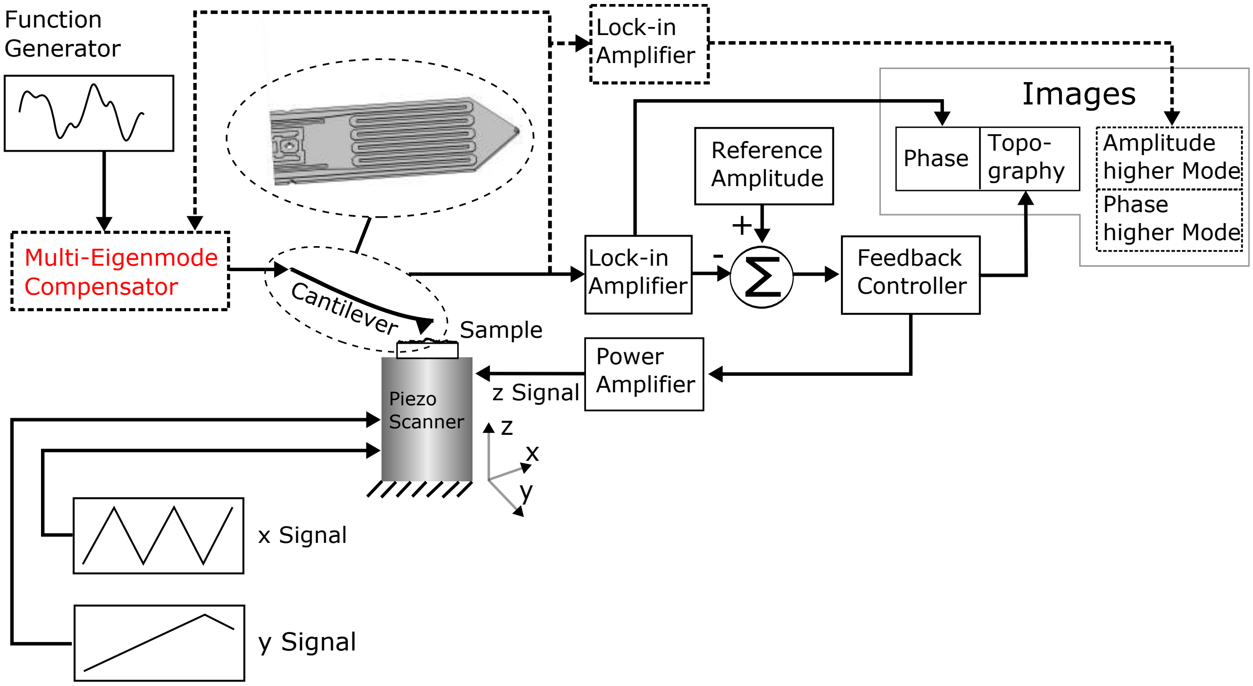

Figure 7.1: Modified AFM II setup for the multi-eigenmode approach. Dashed lines and boxes indicate the modification of the standard setup.

Figure 7.2 indicates the bimodal actuation of the active cantilever in its first two resonances simultaneously in the setup of Figure 7.1. The filtered/amplified response also carries both components. The gray signal is the raw sensor signal, whereas the red one is the compensator estimated and hence filtered sensor signal (with an additional gain).

Figure 7.3 shows various experimental frequency sweeps of the first two transverse eigenmodes with the modified Q_i's as indicated. Each combination of Q_1 and Q_2 is a single sweep including both eigenmodes. Hence, the curves with similar Q_i's in either eigenmode are on top of each other, drawn with varying line thicknesses. This is to indicate the independent tuning capabilities of the two eigenmodes by the compensator. The actuation voltage results in different vibration amplitudes in each eigenmode. The interferometric determined values are indicated by gray ordinates, with arrows pointing towards the respective eigenmode.

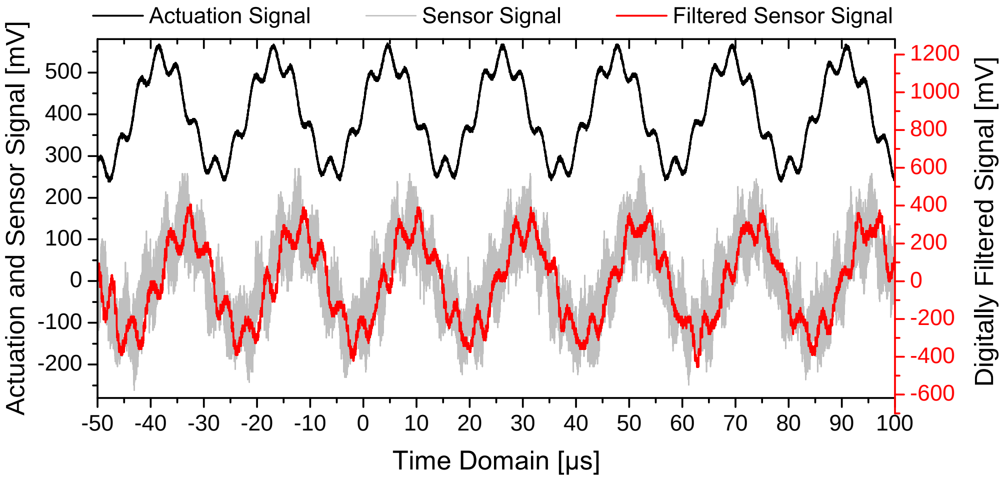

Figure 7.2: Time domain signals of the cantilever actuator and sensor upon a bimodal actuation (black signal) of the first two resonances. The gray signal is the raw sensor signal, whereas the red one is the compensator estimated and hence filtered sensor signal.

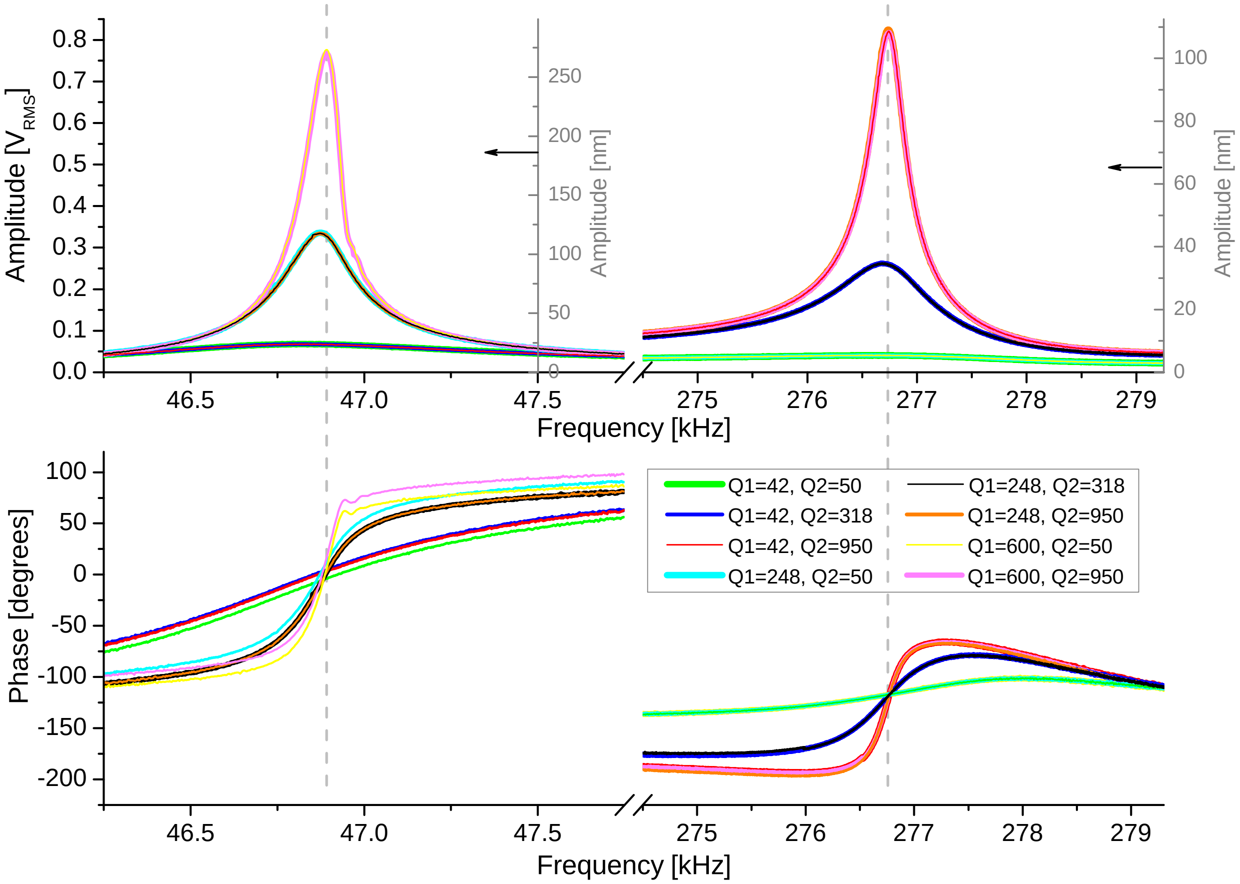

Figure 7.3: Frequency sweeps of the first two transverse eigenmodes with applied multi-eigenmode Q control. Every curve is colored based on an individual combination of Q_1 and Q_2. The vibrational amplitude of each eigenmode is indicated by the gray ordinates.

The sample used is a Bruker PS-LDPE-12M, a two component polymer with different elastic moduli spun on a silicon substrate. The Polystyrene (PS) appears as a film on the surface, whereas the Polyolefin Elastomer (LDPE) forms (half-) spheres. The PS and LDPE regions have Young's moduli of around 2 GPa and 0.1 GPa, respectively.

7.3 Frequency Domain Measurement Results

The modification of Q_1 and Q_2 considerably enhances the response of nearby harmonics. This can be seen in Figure 7.4. A topographic image of the polymer sample allows to locate the different materials. One at a time, the tip of the cantilever is brought into an intermittent contact with each polymer. Here, the AFM controls the average distance of the tip to the sample without scanning the surface. Figure 7.4(a) shows a cantilever's Discrete Fourier Transform (DFT) spectrum. Visible are the first resonance at 47 kHz (1^{st} harmonic) and its excited higher harmonics (Subsection 2.7.1). The 6^{th} harmonic is pronounced due to the vicinity of the second eigenmode. Figure 7.4(b) and (c) are zooms into the 6^{th} harmonics on both hard PS and soft LDPE regions, respectively. Concurrently, Q_1 and Q_2 are modified in different combinations, as indicated by the legend of Figure 7.4(c). The combination of low Q_1 and high Q_2 results in the largest SNR on both polymers.

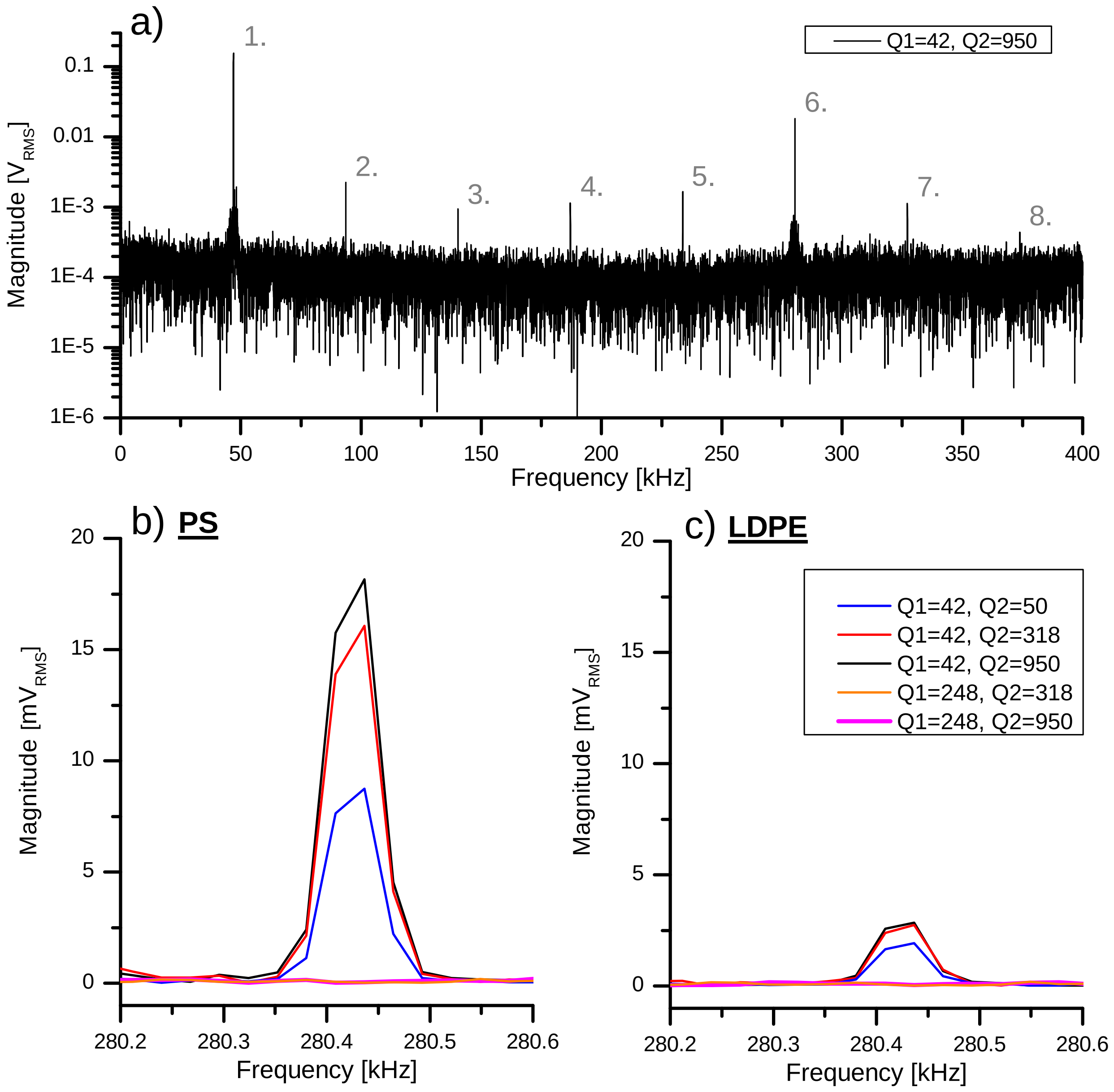

Figure 7.4: a) A selected DFT to indicate the first resonance at 47 kHz and its excited harmonics. The n^{th} harmonics are indicated by numbers, (b) and (c) are the responses of 6^{th} harmonics while the cantilever intermittently contacts the different polymers. Concurrently, Q_1 and Q_2 are modified. (Legend in (c) applies to both subfigures (b) and (c).)

In bimodal actuation (Subsection 2.7.2), Figure 7.5 presents two frequency sweeps obtained of the second resonance with $Q_1 = 42$ and $Q_2 = 950$ (first resonance not shown). The black curve is a sweep of the cantilever in free air. The cantilever is then brought into intermittent contact with a set-point of 45 % in the first resonance. The gray curve indicates the influence of the sample surface on the higher cantilever eigenmode's dynamics.

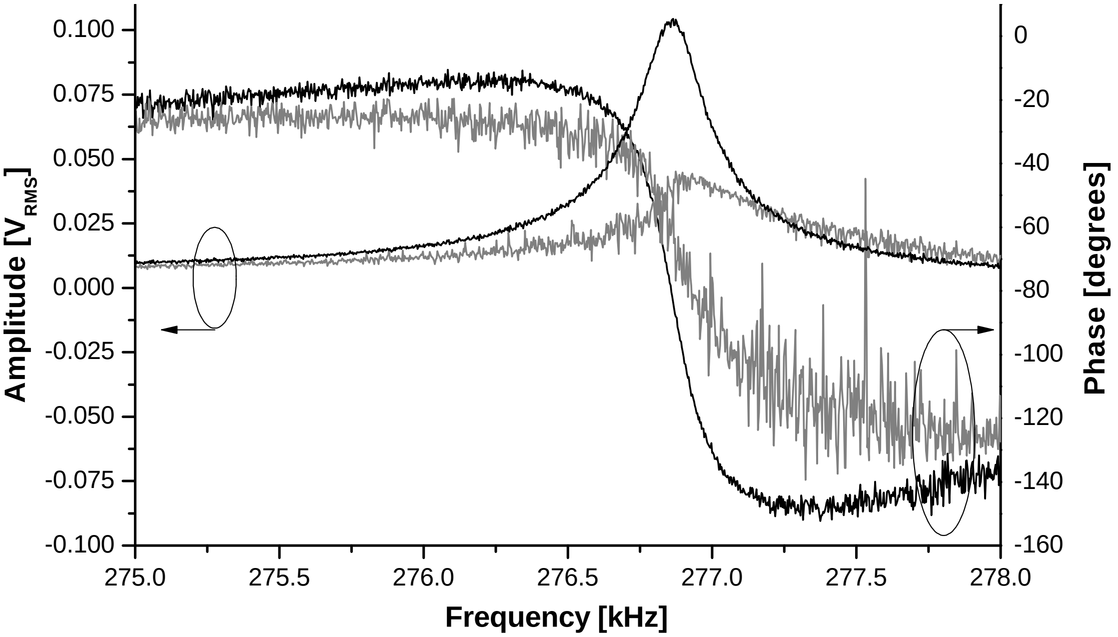

Figure 7.5: Two frequency sweeps of the cantilever's second resonance; black when the cantilever is in free air and gray when the first resonance's amplitude is used to regulate a specific distance to the sample surface.

7.4 Imaging Results

The imaging performance of the two discussed multifrequency methods with different combinations of Q_1 and Q_2 is investigated. Figure 7.6 and Figure 7.7 contain images obtained concurrently with the first and second eigenmode/6th harmonic, respectively. All images are within the same scan area of the polymer sample. The different combinations of modified Q factors are indicated as well as the type of response captured. The qualitative comparison indicates enhanced stiffness contrasts such that more details on the sample surface become visible. As stated earlier, the material stiffnesses are known to be 2 GPa and 0.1 GPa. A sample with unknown materials can then be measured quantitatively by a preceding calibration with a sample of known characteristics.

Figure 7.6(a) and (b) are the topography and phase (ϕ_1) obtained with the first eigenmode and the natural $Q_1 = 248$ at an actuation frequency of 46.848 kHz. As presented later, in particular a lowered Q_1 factor enables pronounced responses and contrast in the higher eigenmode and harmonic. Hence, Figure 7.6(c) and (d) are the topography and ϕ_1 obtained with the first eigenmode and a modified $Q_1 = 42$. This also causes a slightly different resonance and hence actuation frequency of 46.699 kHz, based on the influence of Q_1 on $\omega_{r,1}$. As expected with lower Q factors, the topography in Figure 7.6(c) has a lower resolution, as compared to Figure 7.6(a). The features appear to be squeezed due to the higher forces exerted on the sample. In both cases of Figure 7.6, the free air amplitude at the tip of the cantilever is about 117 nm. This is set by an appropriate actuation signal. The cantilever amplitude set-points are 50 %. The scan areas are $(10\,\mu\text{m})^2$ at a scan rate of 2 lines/s.

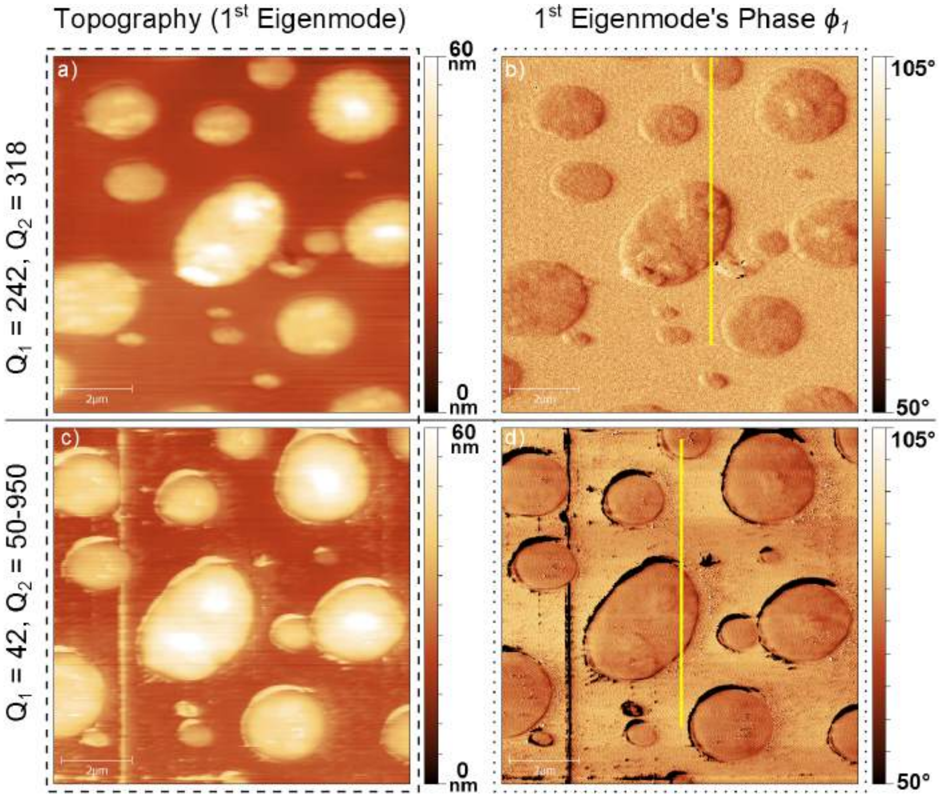

Figure 7.6: All images are obtained with the first eigenmode. (a) and (b) are the topography and ϕ_1 by using the natural Q factors, (c) and (d) are the topography and ϕ_1 obtained with modified cantilever Q factors, as indicated.

A set of images with captured responses of the second eigenmode/6th harmonic with different Q_2 factors is presented in Figure 7.7. The images are simultaneously obtained with the images of Figure 7.6. The column and row labels indicate the type of response measured and used Q factors, respectively. The yellow straight lines are the locations of cross sections presented below in Figure 7.8. In bimodal AFM, the actuation frequencies are between 277.100 kHz and 277.300 kHz for the second eigenmode. The variation of actuation frequencies is due to the modified Q_2 and its resulting altered $\omega_{r,2}$. The column presenting the 6th harmonic is without actuation of the second eigenmode. In this case, the external Lock-in amplifier is set to demodulate the response at 6 times the first eigenmode's actuation frequency. This, e.g., results in 280.194 kHz at a $Q_1 = 42$.

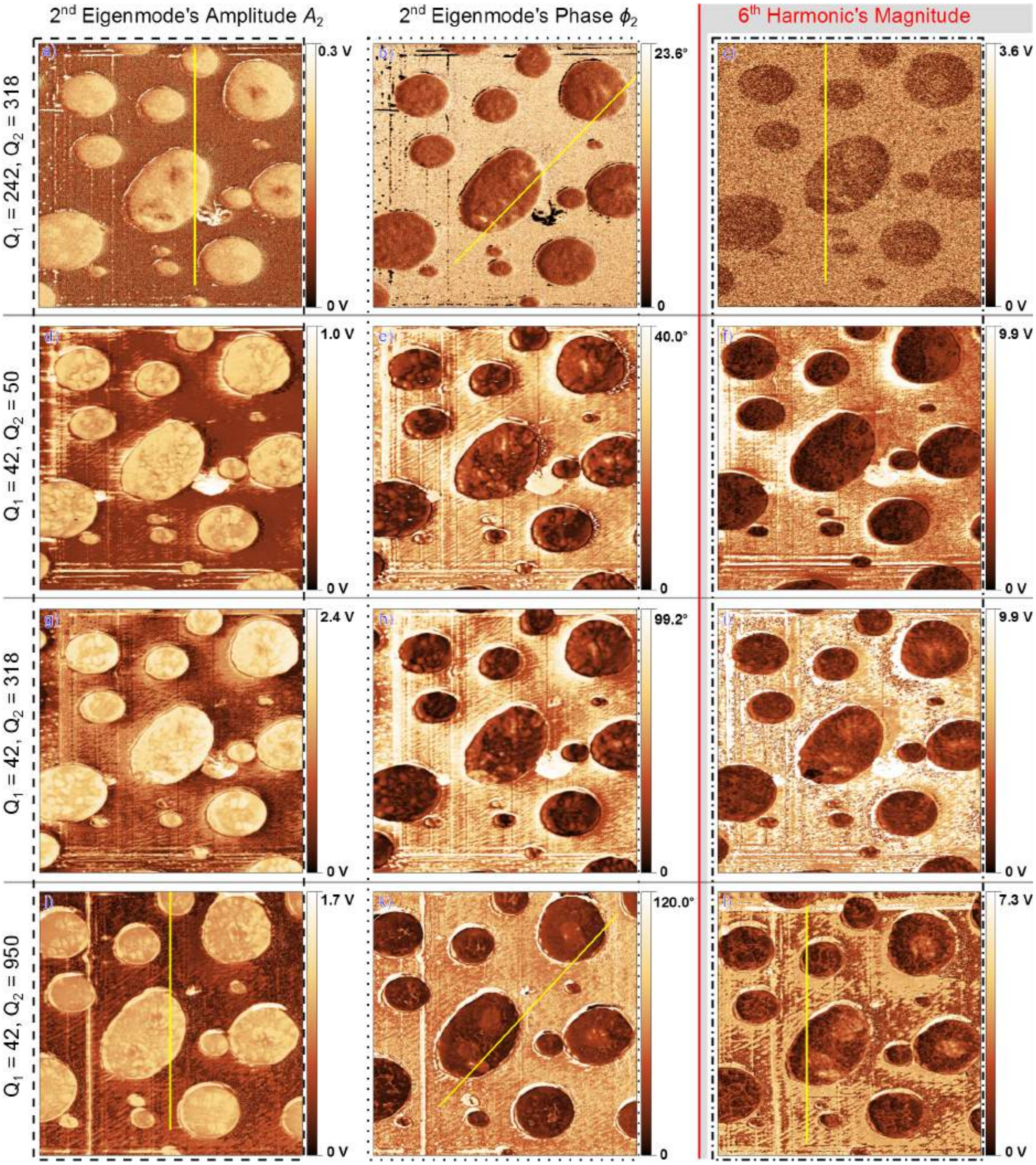

Figure 7.7: Images presenting A_2 (dashed frame) and ϕ_2 (in degrees, dotted frame) of the second actuated eigenmode as well as the 6th harmonic's signal (dash-dotted frame). Combinations of Q_1 and Q_2 are indicated for each row of the images.

The first row of Figure 7.7 is obtained with the natural $Q_1 = 248$ and $Q_2 = 318$, whereas all others are with a $Q_1 = 42$ and different Q_2's. As indicated earlier, the effect of the lower Q_1 is apparent by comparing images obtained with $Q_1 = 248$ and $Q_1 = 42$, but with a $Q_2 = 318$ in both cases (Figure 7.7(a), (b), (c) and (g), (h), (i), respectively). At similar set-points, the increased tip-sample forces of the first eigenmode tapping the surface result in amplified second eigenmode/6$^{\text{th}}$ harmonic signals. Then, the modified Q_2's and constant $Q_1 = 42$ result in differently pronounced features captured from the sample surface. This example shows that the presented compensator enhances the contrast in both imaging methods. Hence, the user would be able to adapt it to the one he might be already using.

In bimodal actuation, in particular ϕ_2 has pronounced sub-features on the soft LDPE half-spheres. These are less pronounced in the A_2 images of the same Figure, and not visible in the topography and ϕ_1 images of the first eigenmode (Figure 7.6). This strong effect onA_2 and ϕ_2 can be attributed to the increased second eigenmode's sensitivity to dissipative forces of the sample's materials. Hence, the images form a dissipation map of the different polymers.

The response of the 6$^{\text{th}}$ harmonic also captures an increased level of details (Figure 7.7). Dark areas indicate an increased contact time (lower stiffness) resulting in lower harmonic amplitudes, as it is the case for the softer LDPE. Lower Q factors in the higher eigenmodes lead to increased harmonic excitations that damp out more quickly [60, 133]. Hence, various details are visible at different Q_2's. These are not visible in the images of the topography and ϕ_1 of the first eigenmode (Figure 7.6). In particular the 6$^{\text{th}}$ harmonic's image obtained with $Q_1 = 42$ and $Q_2 = 950$ (Figure 7.7(l)) has very pronounced contrasts, compared to the images obtained using lower Q_2 factors.

The cross sections highlighted in yellow in Figures 7.6 and 7.7 are compared in Figure 7.8, with two cross sections per signal type. The ordinate's label and legend of each sub-diagram refers to the response captured at specific Q factors. The phase of the first resonance, ϕ_1, does not indicate any difference by decreasing the first eigenmode's Q factor Q_1. In contrast, all signals of the higher eigenmode/harmonic show up to five times higher steps at the material interfaces with overall improved SNRs. The presented methodology is able to detect the different materials both without and with attached compensator. This is due to the large difference in polymer stiffnesses of the used sample. As a conclusion, the compensator's improved contrast allows for the measurement of much smaller material differences that would otherwise be indistinguishable from noise.

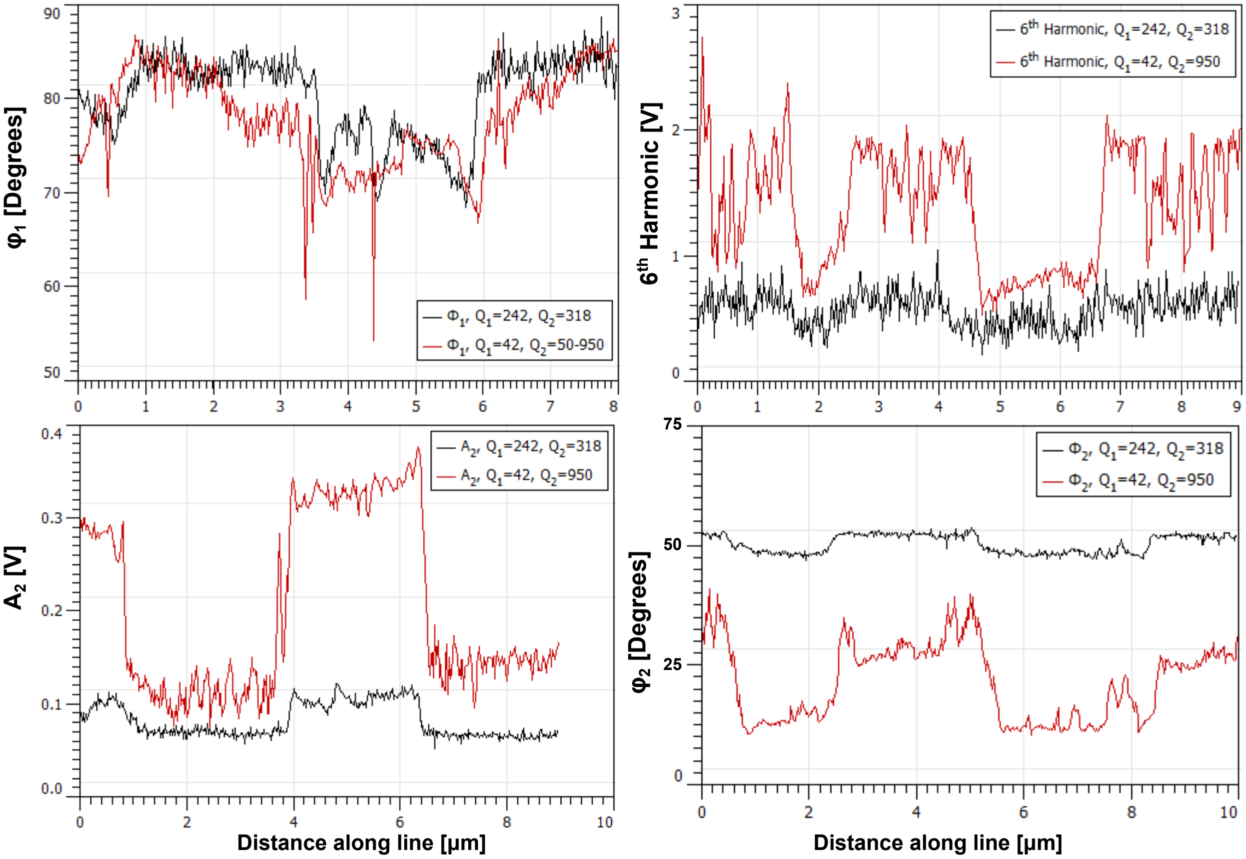

Figure 7.8: Cross sections comparing various images of Figure 7.6 and Figure 7.7 at locations indicated by yellow lines. The ordinate's label and legend of each sub-diagram's label refers to the respective response captured.

Figure 7.9 is an image that consists of various harmonics captured at different demodulation frequencies with $Q_1 = 42$ and $Q_2 = 950$. Scan speed, size and set-point are similar to those in Figure 7.6/7.7. As indicated, and for approximately 50 lines each, the 512 lines image presents the 2nd to the 11th harmonic responses. As expected, the 6th one is most pronounced.

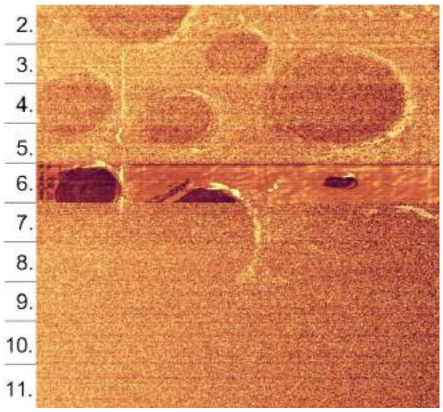

Figure 7.9: Capture of the different harmonics in a sweep fashion created with $Q_1 = 42$ and $Q_2 = 950$. For 50 lines each, the image of a total of 512 lines presents the harmonics starting at the 2nd one to the 11th one.

Beside the enhanced material contrast, the combination of a low Q_1 and high Q_2 has an additional advantage. The following is discussed in more detail in Chapter 6, but briefly described here in the frame of multifrequency AFM. As the first eigenmode is used for the topography feedback mapping, a low Q_1 has an increased imaging bandwidth. This results in faster tracking speed and thus image acquisition. However, one needs to be cautious as the increased tip-sample forces resulting from a low Q_1 can potentially damage the tip and sample. Hence, a trade-off between gentle and fast imaging is required. Figure 7.10 is a scan of a calibration sample (Anfatec UMG03/PtS) that has 2 μm wide and 58 nm nm high parallel SiO_2 lines on a silicon substrate with a pitch of 4 μm. The scan rate is 15 line/s and the different Q_1's are indicated. The tracking issues at the higher $Q_1 = 120$ are visible and the lower Q_1's are clearly superior in following the steps. At $Q_1 = 10$ the increased tip-sample force results in a reduced step resolution.

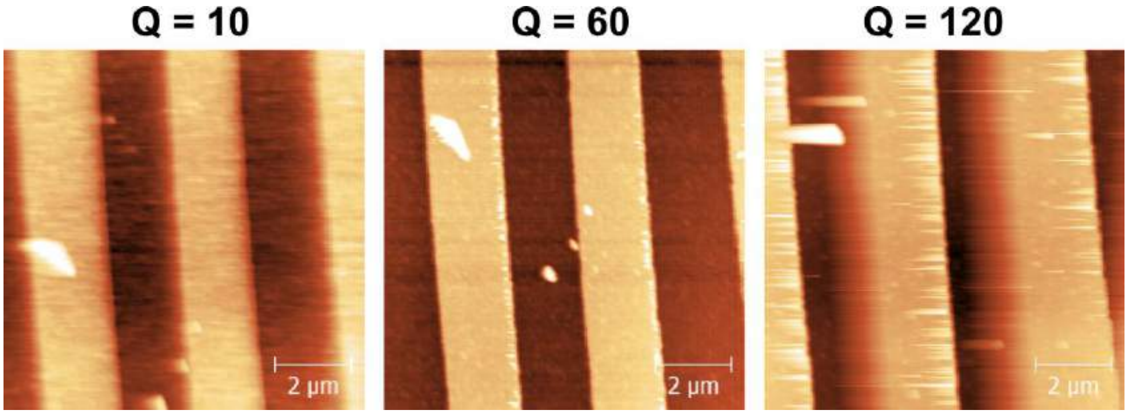

Figure 7.10: Calibration sample imaged at a scan rate of 15 lines/s and Q_1's as indicated.

Further, Figure 7.11 compares two combinations of Q factors and their ability to track the polymer sample at 4 lines/s including higher eigenmodes. Figures 7.11(a) and 7.11(b) are the topography and ϕ_2 with $Q_1 = 242$ and $Q_2 = 318$ during bimodal imaging. The images start to smear in both eigenmodes, indicating a feature tracking limit and partially loosing contact to the surface. Figures 7.11(c) and 7.11(d) are the topography and ϕ_2 obtained with $Q_1 = 42$ and$Q_2 = 950$, both showing an improved tracking ability and enhanced material contrast.

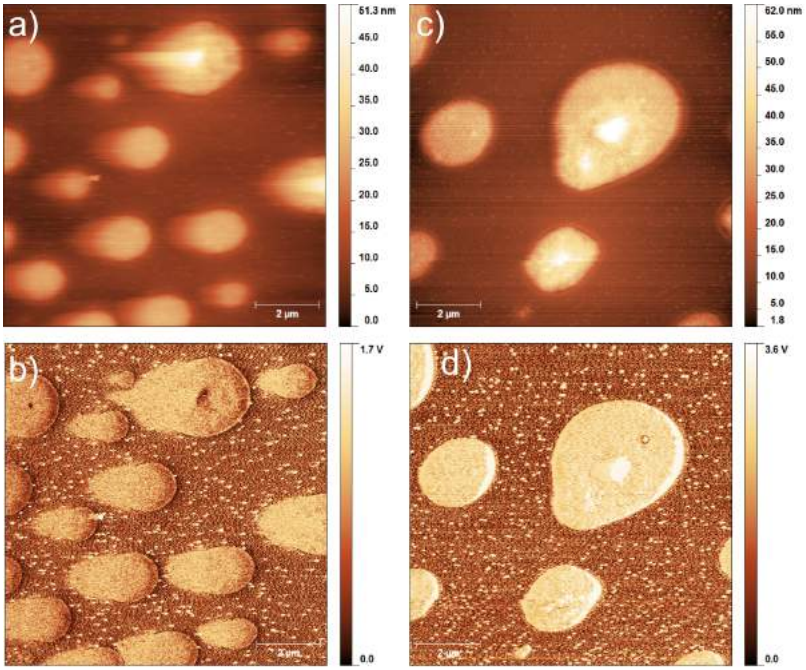

Figure 7.11: Two combinations of Q factors and their ability to track the sample features. (a) and (b) are the topography and ϕ_2, respectively, with $Q_1 = 242$ and$Q_2 = 318$. (c) and (d) are the topography and ϕ_2, respectively, obtained with $Q_1 = 42$ and $Q_2 = 950$.

7.5 Conclusion

In this chapter, enhanced material contrast and increased imaging rates accomplished by small modifications of a conventional AFM setup have been demonstrated. The improvements are achieved by a digital multi-eigenmode compensator that is attached to the AFM. Demonstrated for the first time, the compensator individually modifies each cantilever eigenmode's dynamics and provides imaging capabilities in a multifrequency approach. The proposed methodology allows a flexible way to satisfy the different requirements of the involved eigenmodes, such as fast topography imaging in the first eigenmode and sensitive nanomechanical property mapping in the higher frequencies.

Towards material contrast mapping, the best result is achieved with a low Q factor $Q_1 = 42$ for the first and a high Q factor $Q_2 = 950$ for the second eigenmode. With the help of the compensator sample features become visible that are not detected without the modification of the cantilever's dynamics. Further, the compensator can help to distinguish sample stiffnesses that could be indistinguishable from noise otherwise. The low Q_1 also offers the potential for high speed imaging, as discussed in more detail in Chapter 6. For example, the cantilever with a $Q_1 = 60$ is able follow a sample structure more accurate at $30\,\mu$m/s tip velocity than with a $Q_1 = 120$. This is in particular beneficial in vacuum environments, where high Q factors prohibit fast scanning.

In cantilevers, the ratios of the higher eigenmodes to the first one usually do not follow integer multiples. However, improved contrast can be achieved by matching those ratios in combination with the higher harmonic imaging technique. As a future step, it is anticipated to include the modification of the first resonance's natural frequency used for topography imaging. In combination with the multi-eigenmode Q control, this could further amplify the harmonic response. An alternative would be using harmonic cantilevers that are structurally modified to satisfy the ratio requirement, as will be covered in Chapter 9. Also, the estimated cantilever output is considerably reduced in noise that offers the possibility for a simplified demodulation scheme in a multi-eigenmode approach. For example, it can be based on the detection of maximum and minimum of the estimated signal instead of a Lock-in amplifier applied on the measured sensor signal. This will be introduced in the following Chapter 8. Future extensions of this work could also, for example, use the multi-eigenmode compensator to influence the transition between stable oscillation states [214] by using different Q factors.

8 Compensator based Amplitude Demodulation

The amplitude demodulation in tapping mode atomic force microscopy is one of the key elements in the z axis feedback loop. In combination with a controller it is used to keep an average distance of the cantilever to the sample and to form different signals for surface mapping. The demodulator's time constant and noise rejection is crucial for both image quality and imaging rate. Commonly, Lock-in amplifiers are used for this task with their inherent bandwidth limitations. Alternative techniques proved to be faster but some with decreased robustness. Such methods include a demodulation based on the detection of each cycle's minimum and maximum. In this chapter, an alternative demodulation technique is presented. It is based on the combination of the minimum-maximum approach with the compensator's estimated cantilever sensor output $\bar{\mathbf{C}}\hat{\mathbf{q}}_k$ *(Section 5.3.1). The estimator provides a noise reduced and decoupled sensor signal for each modeled eigenmode. Excited unmodeled eigenmodes and harmonics are filtered out that otherwise can distort a regular minimum-maximum method. As a result, dynamic modification and demodulation can be achieved simultaneously. In combination with the compensator the demodulation is a simple extension to the existing implementation of Section 5.5 with little added complexity, compared to a compensator/Lock-in based setup. The demodulation methodology is validated by time domain signals and imaging of a calibration sample in the intermittent mode in air.*

8.1 Motivation

Most AFMs use a Lock-in amplifier for the demodulation of the amplitude, frequency and/or phase, as introduced in Subsection 2.1.2. Its filter time constant plays a crucial role in the feedback bandwidth and rejection of sensor noise. High feedback bandwidths require low filter time constants, whereas a good noise rejection requires higher constants. Usually, a trade-off between the two is to be found.

To increase the imaging bandwidth, Ando *et al.* have introduced an alternative approach based on peak holding [26]. The minimum and maximum peaks of each cycle of the cantilever's vibration signal are determined by an analog circuit. The resulting amplitude is then used instead of a Lock-in amplifier. A different detector is introduced by Blais and Rioux [215] and works with an FIR filter in discrete time. Fourier based methods have been developed by Kokavecz *et al.* that calculate the Fourier coefficients [216]. An improved method also conform with multifrequency AFM techniques is introduced by Karvinen and Moheimani [217], based on phase cancellation. Their publication also delivers an excellent overview of other existing methods.

One of the potential problems of a simple minimum-maximum demodulator is noise and signals of different frequencies superimposed on the sensor signal. This also prevents the operation in multifrequency AFM methods [59]. For example, excited higher harmonics appear in the cantilever during imaging in the intermittent mode. Such detected signal is indicated in Figure 8.1. The gray and black curves are the raw sensor signal and its noise filtered counterpart, respectively. Without proper precaution, such as bandpass filtering, these superimposed signals have an impact on the reliability of the detected amplitude.

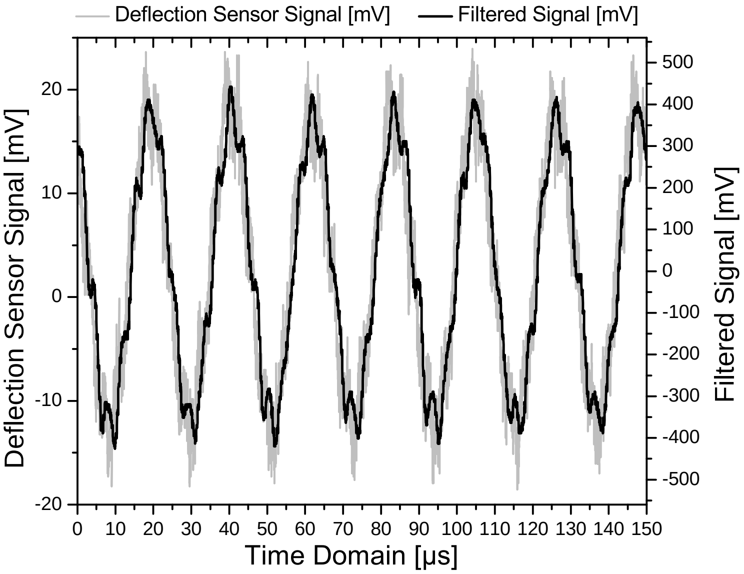

Figure 8.1: Higher harmonics excited while scanning a sample in the tapping mode. The pronounced higher frequency is the 6th harmonic superimposed on the first resonance.

In this chapter, the estimated cantilever sensor signal $\bar{\mathbf{C}}\hat{\mathbf{q}}_{\mathbf{k}}$ of the compensator output (Section 5.3.1) is used to demodulate the amplitude in the time domain. The estimated compensator output represents a filtered copy of the cantilever sensor deflection signal. The numerical difference of the two signals is used to correct the model uncertainties. In the following, the estimated sensor signal is used to connect the amplitude demodulators, one for each modeled eigenmode. The approach is also conform with multifrequency AFM techniques, such as bimodal AFM [67,71]. The methodology is based on finding the minimum and maximum of the estimated sensor deflection signal. It can simply be operated in addition to the control functionality of the compensator. The demodulator can be used by switching the AFM controller into contact mode and connecting the demodulated signals. In combination with the compensator the demodulator extension is of less complexity than adding a regular Lock-in amplifier to the compensator extended AFM setup. Also, the estimator incorporates similar dynamics as the cantilever. Following, the time constant of the demodulators are always matched with the time constants of the cantilever eigenmodes. The utilized cantilevers are the active probes introduced in Chapter 3.

In the following, Section 8.2 introduces the extension to the previously developed compensator. The modification to the standard AFM setup is presented in Section 8.3. The validation is presented in the time domain in Section 8.4 and by scanning a sample in tapping mode in air in Section 8.5, both with the modified AFM setup. A conclusion is given in Section 8.6.

8.2 Amplitude Demodulator Design

The amplitude demodulator is formed as an extension to the existing compensator (Figure 8.2). With its model, the estimator simulates the cantilever dynamics and is corrected via a feedback of gain $\mathbf{L}$. The estimated deflection output $\hat{y}$ ideally matches the sensed cantilever deflection signal y. Depending on $\mathbf{L}$, $\hat{y}$ is much reduced in noise. As a result, the decoupled $\hat{y}_i$ of the modeled eigenmodes i are used for the amplitude demodulation instead of y, each with its own demodulator D_i.

In case of a single eigenmode compensator, the estimated output signal $\bar{\mathbf{C}}\hat{\mathbf{q}} = \hat{y}$ is used as the input to the amplitude demodulator. In contrast, in the case of a multi-eigenmode compensator acting on two or more resonances, the output vector $\hat{y}_k$ needs to be slightly reorganized. The estimated output of each eigenmode needs to be fed to an individual demodulator, before they are added together to form $\bar{\mathbf{C}}\hat{\mathbf{q}}$.

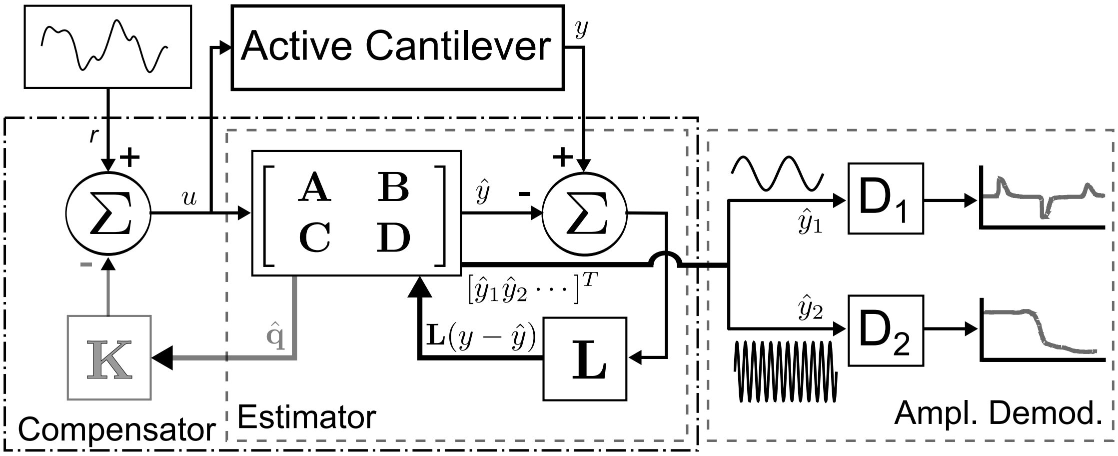

Figure 8.2: The overall amplitude demodulator attached to the compensator. Each $\hat{y}_i$ is fed to its own demodulator D_i.

The vector $\hat{y}_k$ is separated into each eigenmode's $\hat{y}_{k,i}$, which is simple in the model's modal form. $\hat{y}_k$ is then formed by summing all $\hat{y}_{k,i}$:

$$\begin{bmatrix} \hat{y}_{k,1} \\ \hat{y}_{k,2} \\ \vdots \end{bmatrix} = \begin{bmatrix} \bar{\mathbf{C}}_\mathbf{1} & 0 & \cdots \\ 0 & \bar{\mathbf{C}}_\mathbf{2} & \\ \vdots & & \ddots \end{bmatrix} \begin{bmatrix} \hat{\mathbf{q}}_{\mathbf{k},\mathbf{1}} \\ \hat{\mathbf{q}}_{\mathbf{k},\mathbf{2}} \\ \vdots \end{bmatrix} \Rightarrow \hat{y}_k = \hat{y}_{k,1} + \hat{y}_{k,2} + \cdots \tag{8.1}$$

Each $\hat{y}_{k,i}$ is connected to its own demodulator D_i, as indicated in Figure 8.2. This approach does not add any computational effort to the compensator itself, since computing $\hat{y}_{k,i}$ are intermediate steps towards the overall $\hat{y}_k$. As each $\hat{y}_{k,i}$ only represents the signal at a particular frequency, other eigenmodes and excited harmonics are filtered and not present. This strongly enhances the reliability of the attached demodulators.

As indicated earlier, the D_i's are based on the minimum-maximum methodology. The working principle of each D_i is schematically introduced in Figure 8.3. The red dash-dotted curve is the estimated $\hat{y}_{k,i}$. Two levels *H-T* and *L-T* are set, giving a High and Low Threshold, respectively. It prevents the undesired activation of a new cycle near the '0' line due to noise. Hence, $\hat{y}_{k,i}$ needs to pass through both '0' and *H-T*/*L-T* before the consecutive cycle is activated. This is analog to the principle of a Schmitt trigger with its hysteresis. This behavior is also indicated by the gray dashed arrows in Figure 8.3. Then, the respective positive *Temp-Max* or negative *Temp-Min* detectors are activated, starting at value '0'. In each cycle, it stores the current sample if it is larger (positive part) or smaller (negative part) than its predecessor. After the following cycle is started (*L-T* or *H-T*) the respective previous value in *Temp-Max* or *Temp-Min* is stored as a new

Max or *Min* value. Subtraction of *Min* from *Max* gives the demodulated peak-to-peak amplitude, which is updated every half-period of the vibration signal. It results in intermediate steps in the demodulated amplitude and an update time of twice the corresponding frequency. Following, a change in the amplitude requires up to a full signal period to be correctly detected.

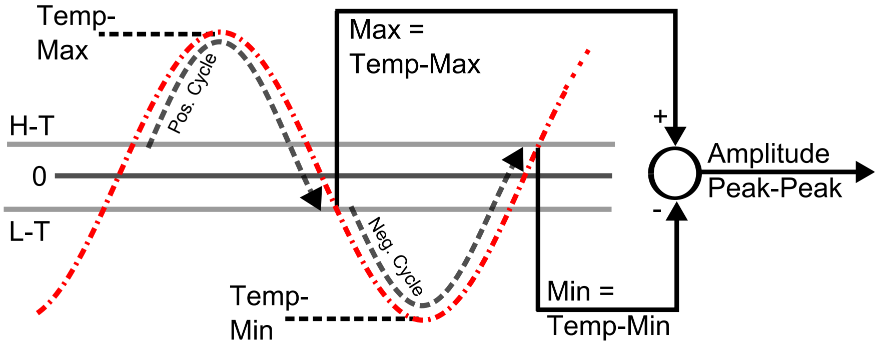

Figure 8.3: Functionality of the amplitude demodulator on a sinusoid $\hat{y}_{k,i}$ cantilever signal.

In this work, only the amplitude demodulation has been realized. However, the phase information can be easily added in a similar fashion. This is achieved by first obtaining a time stamp at a particular point in time of both the actuation and sensor signal. For example, when the signals are either crossing *H-T* or *L-T*. The time difference of both time stamps in respect to a full period of the vibration frequency gives a phase between 0 and close to 1. The resolution is based on the demodulators internal clock frequency f_d. Hence, the maximum numerical phase would be $1-1/f_d$. A phase of 1 represents a full period and is equal to a phase of 0. Proper scaling can be used to adapt the phase to familiar values of 0 to 360.

8.3 Modified AFM Setup

The experiments are carried out on a modified AFM II setup of Section 3.1, combined with the active cantilevers of Section 3.2. Figure 8.4 shows the setup with the compensator extended by the demodulator. The Lock-in amplifier usually used is removed from the feedback loop. The AFM controller is switched to contact mode the new parts and signals are represented by dashed lines and boxes. In this case, the amplitude demodulation of only one resonance is implemented. The potential implementation of its phase and the amplitude/phase of additional resonances is indicated by the gray dashed signal paths. However, the realization of those additional demodulators is straight forward and explained in the following sections.

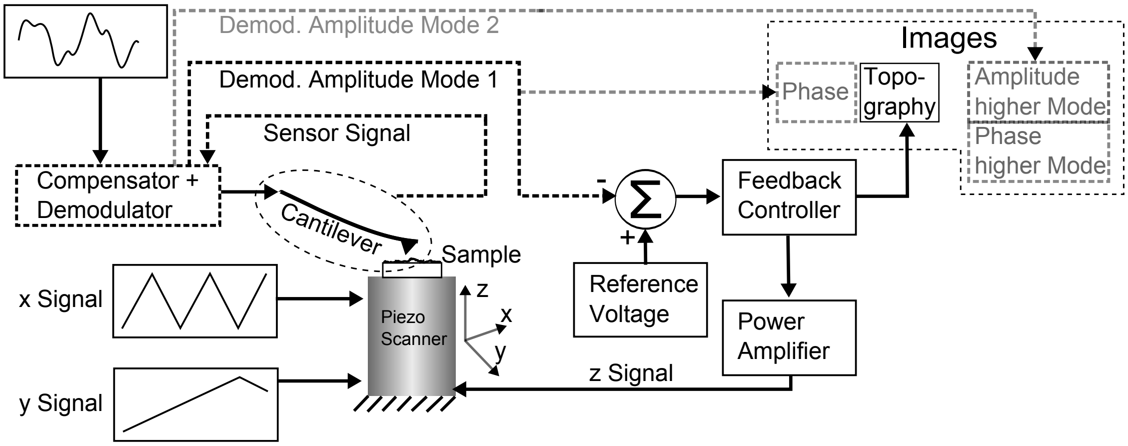

Figure 8.4: Specific setup of the estimator based demodulator, shown for a potential application involving 2 eigenmodes. The new parts and signals are represented by dashed lines and boxes. The gray paths and boxes are not yet realized in this implementation.

8.4 Time Domain Results

The amplitude detector evaluated in the time domain is presented in Figure 8.5. The bottom graph in Figure 8.5(a) is an amplitude modulated test signal with a modulation depth of about 15 %. It forms the input to a standalone demodulator. The top curve in Figure 8.5(a) is the demodulated signal, representing the envelope of the bottom input signal. The clearly resolved amplitude shows intermediate steps upon a change in amplitude. As explained in Section 8.2, its nature lies in the evaluation of the amplitude every half period of a cantilever vibration cycle. The resulting demodulated signal is amplified and hence does not exactly match the numerical difference of the two input amplitudes.

Figure 8.5(b) is the demodulation on a real active cantilever sensor signal. The noisy gray curve at the bottom of the diagram is the vibrating cantilever's deflection signal y_k in the transition to a new amplitude. The black curve is the estimated $\hat{y}_{k,1}$. The top signal of Figure 8.5(b) is the demodulated amplitude as obtained by the implementation of Figure 8.2. The noise originally present in y_k is reduced in its estimation $\hat{y}_{k,1}$. Hence, the demodulated amplitude is clearly resolved and usable for consecutive processing within the feedback loop.

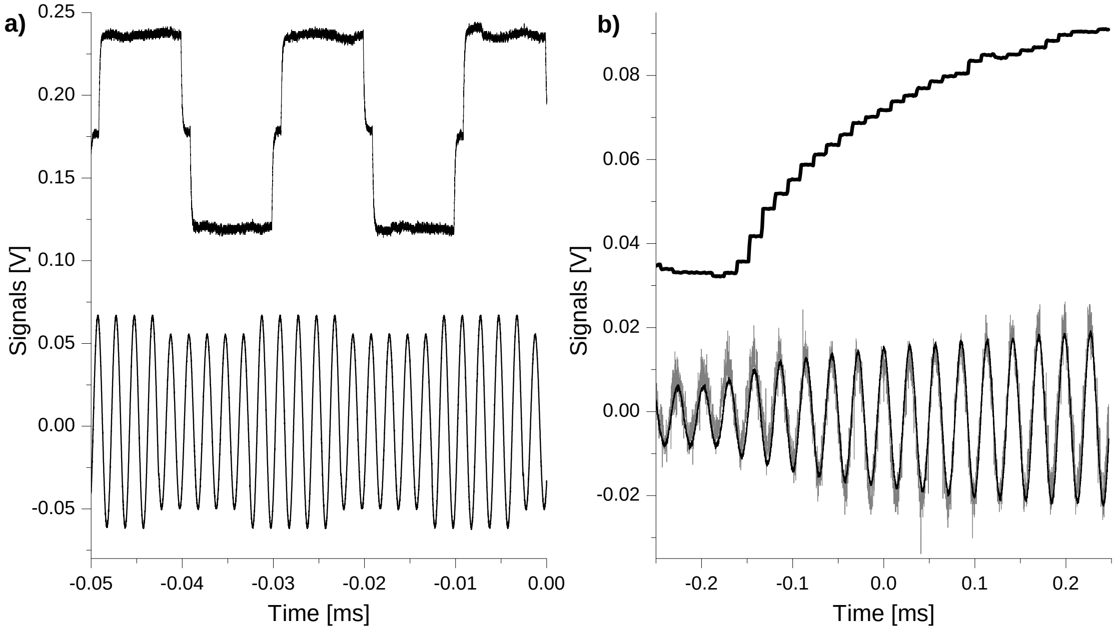

Figure 8.5: The bottom curves in both sub-figures show input data to the compensator/demodulator. The top curves indicate the demodulated amplitudes. (a) is performed on a test signal using the demodulator only, (b) is performed on a real active cantilever's deflection signal y_k processed by the compensator and demodulator.

8.5 Imaging Results

The amplitude demodulation methodology presented is validated by imaging a calibration sample. Figure 8.6 is the image of a Nanodevices Inc. calibration grid with 200 nm deep line trenches and a 2 μm pitch. The set-point is 40 %, set as a corresponding static deflection in the contact mode AFM software. The imaging area is $(9\,\mu\text{m})^2$ at a rate of 2 lines/s. Additionally, the Q factor of the first resonance (76.249 kHz) is set to 100.

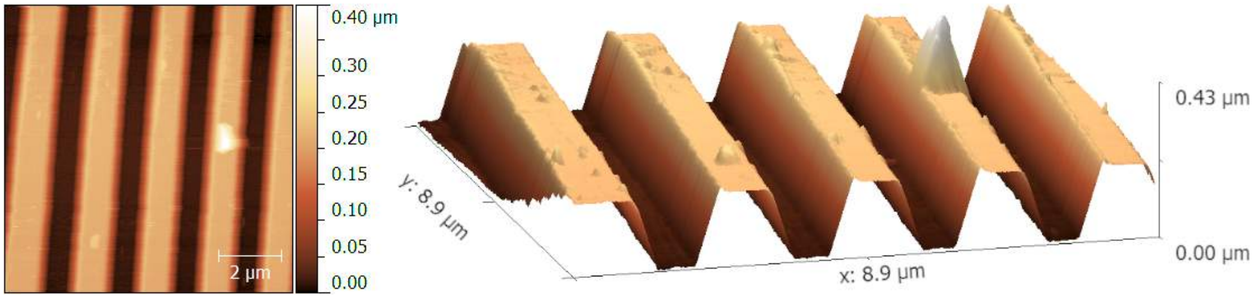

Figure 8.6: 2D and 3D view of an image of a calibration sample using the compensator based demodulator in the z feedback loop. The utilized cantilever resonance is the first transverse eigenmode with a modified Q factor of 100.

The time constant of the demodulation technique depends on the cantilever's time constant τ_1. In this case, the Q factor of 100 results in $\tau_1 = 417\,\mu s$ in free air. During imaging, the effective Q factor is considerably lowered at the set-point of 40 %, resulting in a smaller τ_1. Following, the presented demodulation technique has its greatest benefits at low Q factors, such as during imaging in water. In that environment the presented technique can be helpful to increase the overall speed of the microscope.

The two demodulation techniques, Lock-in amplifier and compensator/estimator based demodulator, can also be compared directly during imaging. Figure 8.7 shows the performance side-by-side in different perspectives. The left and right images are obtained by using the estimator based demodulator and standard Lock-in amplifier in the z feedback loop, respectively. The controller is switched to contact mode for obtaining the images by the estimator based approach in Figure 8.7(a), since the amplitude is already demodulated. In contrast, the Lock-in time constant is set to 0.2 ms for Figure 8.7(b). All other imaging parameters are set as in Figure 8.6.

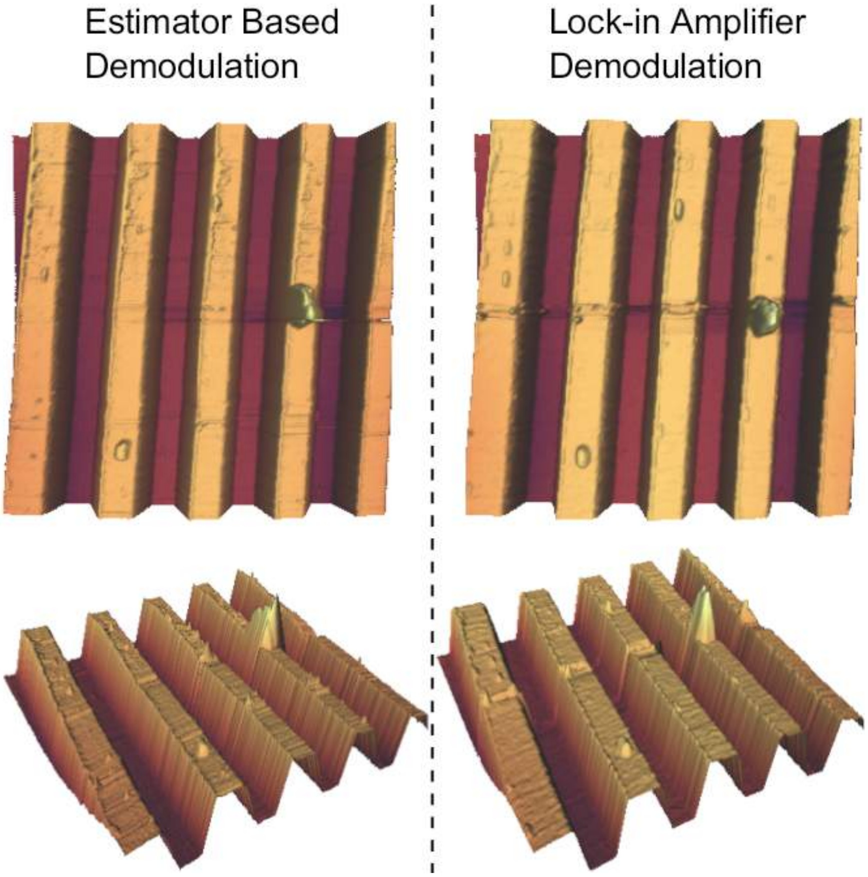

Figure 8.7: (a) and (b) are obtained by using the estimator based demodulator and standard Lock-in amplifier in the z feedback loop, respectively.

Here, the resulting time constant is larger than the lock-in amplifier's time constant of 0.2 ms. Hence, the overall bandwidth is limited by the cantilever rather than the Lock-in amplifier. To uncover a difference in the two images, if no other part in the feedback loop is at fault, the time constant of the cantilever has to be lower than the Lock-in's. Hence, it would need effective Q factors of 5 or lower. Although this is usually not feasible in air, imaging in liquid works with such low factors as indicated earlier.

8.6 Conclusion

Atomic force microscopy is a powerful but still relatively slow and complex instrument. The cantilever and demodulation techniques are two bottlenecks in the z feedback loop. Increasing the bandwidth of both components can potentially increase the imaging rates. The previously developed compensator offers the potential to adjust the cantilever's Q factor and perform an amplitude demodulation simultaneously. The compensator delivers a filtered and decoupled cantilever deflection signal. The decoupling suppresses frequencies other than the frequencies of modeled eigenmodes, such as excited higher harmonics and noise. The amplitude demodulator is a simple extension to the compensator. It leads to a distortion free estimated amplitude that can be used in the z feedback loop. Given the estimator, the presented compensator/demodulation methodology is of lower overall complexity than attaching a compensator/Lock-in combination to the AFM. Decreased cantilever time constants, based on lower Q factors or higher resonance frequencies, can increase the demodulation speed and imaging bandwidth. The estimator based demodulator can be easily used for high speed imaging in higher eigenmodes. It can also be extended to work in a multi-eigenmode control approach for multifrequency AFM.

9 Harmonic Active Cantilevers for High Material Contrast

Atomic Force Microscope probes are mechanical beams that can be used to simultaneously map topography and material properties. Upon contact of the tip with the sample surface at each cycle in the intermittent mode, higher harmonics are excited. The harmonics in the vicinity of higher eigenmodes are enhanced and present an amplified response, ultimately carrying information about the material properties. In this work, active cantilevers with integrated actuation and sensing are used as a basis to create harmonic cantilevers for the Signal-to-Noise Ratio improved measurement of time varying-forces. Focused Ion Beam milling is used to remove mass from specific areas in the cantilever such that the first and higher eigenmodes are tuned towards each other. Two methods are tested, where the shape and location of mass removal is determined, first, by simulation and, second, through an in-situ approach. Higher harmonics of the harmonic cantilevers with piezo-resistive deflection sensors indicate a significant response of up to 10 % in respect to the first harmonic. The improved material contrast mapping abilities of the modified cantilevers are validated by characterization and AFM images. The modification presented here can be used instead or in combination with the compensator in Chapter 5 and imaging techniques in Chapters 6 and 7. This chapter is also published in reference [75], ©2015 IEEE.

9.1 Motivation

Recent methods involve the first and excited higher harmonics to simultaneously map topography and material properties [61–64]. As described in Section 2.7.1, the periodic impact of the tip onto the sample results in a non-linear tip-sample force interaction in the intermittent mode. The contact time of tip and sample hereby depends on the Young's modulus E [182,188]. Such contact time determines the magnitudes of the excited higher harmonics. The first harmonic represents the average tapping force and depends on the cantilever and its actuation/set-point. Hence, it has a constant magnitude across different materials [65].

Higher cantilever eigenmodes directly influence the harmonic excitation process [66, 133, 189, 190]. The frequencies of the higher transverse eigenmodes follow specific ratios in respect to the first eigenmode. According to the Euler-Bernoulli beam theory, the ratios of homogeneous rectangular cantilevers are 6.28:1 and 17.86:1 of the second and third in respect to the first eigenmode, respectively. As a result, the magnitudes of the nearby excited 6^{th} and 18^{th} harmonics are amplified. Enhancement of harmonic responses and improvement of SNRs during imaging can thus be achieved by matching higher eigenmodes with integer multiples of the imaging resonance.

Specifically matched harmonic cantilevers have been partially explored in the past. Sahin *et al.* have demonstrated matching the third eigenmode by creating holes in the cantilever during its fabrication. The matched higher harmonic is amplified, as tested on optically sensed cantilevers [218, 219]. AFM images indicate surface properties that are invisible otherwise. However, this fabrication method is plagued by a low reproducibility and yield, based on uncertainties in the fabrication process itself. A different approach by Sahin *et al.* is the fabrication of torsional harmonic cantilevers [220]. Excited torsional harmonics during imaging indicate higher SNRs as compared to transverse harmonics. Rinaldi *et al.* have included holes of different sizes and shapes for a general purpose demonstration of its capabilities, for example to minimize the squeeze film effect [221, 222]. The holes are calculated by the Rayleigh-Ritz energy method. Cantilevers used are piezo-electric actuated and optically sensed. In contrast, Li *et al.* have attached a concentrated mass at specific locations on the cantilever's surface [223]. The modification results in a match of the second and third transverse eigenmodes with the 5^{th} and 15^{th} harmonic of the first resonance, respectively. A proposed approach by Balantekin *et al.* uses an imaging frequency that is the first transverse eigenmode divided by an integer value. The first eigenmode is then used to capture and amplify the harmonic response [205]. Sadewasser *et al.* have fabricated cantilevers with a wider anchored part and a narrower free end, moving the higher resonances as close as possible to the first resonance [224]. As such, the higher resonances are better accessible for the bandwidth limited vibration sensing. The unnecessity of harmonic cantilevers for high sensitive imaging of soft materials in liquid has been reported by Xu *et al.* [60].

In this work, both second and third eigenmodes are simultaneously matched with nearby harmonics by an enhanced approach. The modifications are carried out in a FIB as a post cantilever fabrication step. Two different methods are employed. The first one is based on the cantilever's known characteristics to obtain proper sizes and locations of holes beforehand through FEM simulations. This method leads to a higher reproducibility, ultimately to a success with every processed cantilever. The second method is based on an in-situ modification, where the cantilever is actuated and sensed inside the FIB chamber. The milling process is carried out for short periods of time with consequent frequency sweeps, until the eigenmodes match desired frequencies. With both methods the hole locations are decided beforehand. Holes can either be placed in the vibrational mass or stiffness domain of the cantilever effecting each eigenmode's local kinetic or potential energy, respectively. This either increases or decreases each eigenmode's frequency, as further investigated in [190, 222]. The numerical FEM is chosen based on the utilized cantilevers' non-homogeneity in both material and shape.

An alternative approach would be adding mass in specific shapes and locations along the beam. This introduces a frequency shift of the individual eigenmodes due to increased stiffness or mass, as thoroughly discussed in the area of cantilever based mass detection [24, 225]. However, this approach is not feasible since a considerable amount of deposited material would be necessary for a meaningful impact. This leads to long FIB processing times with large amounts of expensive source materials. Such depositions also incorporate other undesired materials present in the vacuum chamber. The resulting amorphous structure is of low and unpredictable stiffness.

In the following, Section 9.2 describes the modified standard AFM setup used in this work. Section 9.3 outlines the cantilever FEM modeling process including the simulation of topological modifications. The consecutive FIB based fabrication including both digital mask and in-situ methods is described in Section 9.4. In Section 9.5 the harmonic cantilevers are evaluated towards their performance and imaging results are presented in Section 9.6 Conclusions are given in Section 9.7.

9.2 Modified AFM Setup

For this work, the AFM II setup of Section 3.1 is combined with the active cantilevers of Section 3.2. An additional external Lock-in amplifier, a 210 MSample/s a Zürich Instruments HF2LI, is connected to demodulate the higher harmonics. The resulting signals and topography are simultaneously plotted within the AFM software to keep the dependencies on the lateral scan directions. Figure 9.1 shows the modified setup with its components used for imaging and characterization of the cantilevers. The new parts and signals are represented by dashed lines and boxes.

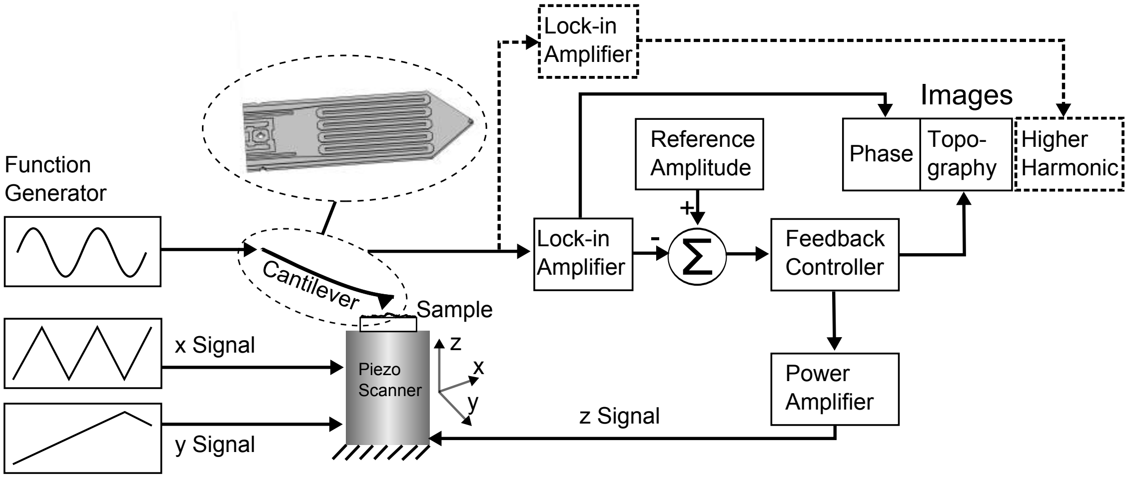

Figure 9.1: Customized AFM setup including self-fabricated components. Dashed gray paths and boxes indicate the extension of the standard setup.

Figure 9.2(a) indicates the excited harmonics of an active cantilever in the tapping mode close to a sample surface and maintaining a specific set-point. Note that the ordinate has a break as the first resonance's magnitude is larger than the introduced harmonics. However, the piezo-resistive sensor efficiently detects the harmonics with magnitudes of up to 10% of the first resonance. The enhanced harmonics close to cantilever eigenmodes are clearly visible. The fabricated active cantilevers may not follow the theoretical ratios of analytical models (Enhanced 15th instead of 18th harmonic in Figure 9.2(a)). Figure 9.2(b) presents raw and digitally filtered piezo-resistive sensor signals in time domain after its pre-amplification. The filtered signal is additionally amplified in respect to the raw signal to fit the analog-digital converters' ranges for an optimal resolution. In both cases, the excitation of the superimposed 6th harmonic is highly pronounced. The high Q factors of each eigenmode cause low damping of the higher harmonics' periodic excitation, as indicated in [133, 189, 190]. Figure 9.2(c) is an image of various different harmonics. The sample is a Bruker PS-LDPE-12M, a two component polymer blend with different elastic moduli. It is used to indicate the harmonics' dependency on the sample stiffness. The PS appears as a film on the surface, whereas the LDPE forms half-spheres. The PS and LDPE regions have Young's moduli of around 2 GPa and 0.1 GPa, respectively. For approx. 40 lines each, the 512 lines of the image represent the harmonics starting at the 2nd to the 13th one. As expected, the 6th harmonic is best pronounced.

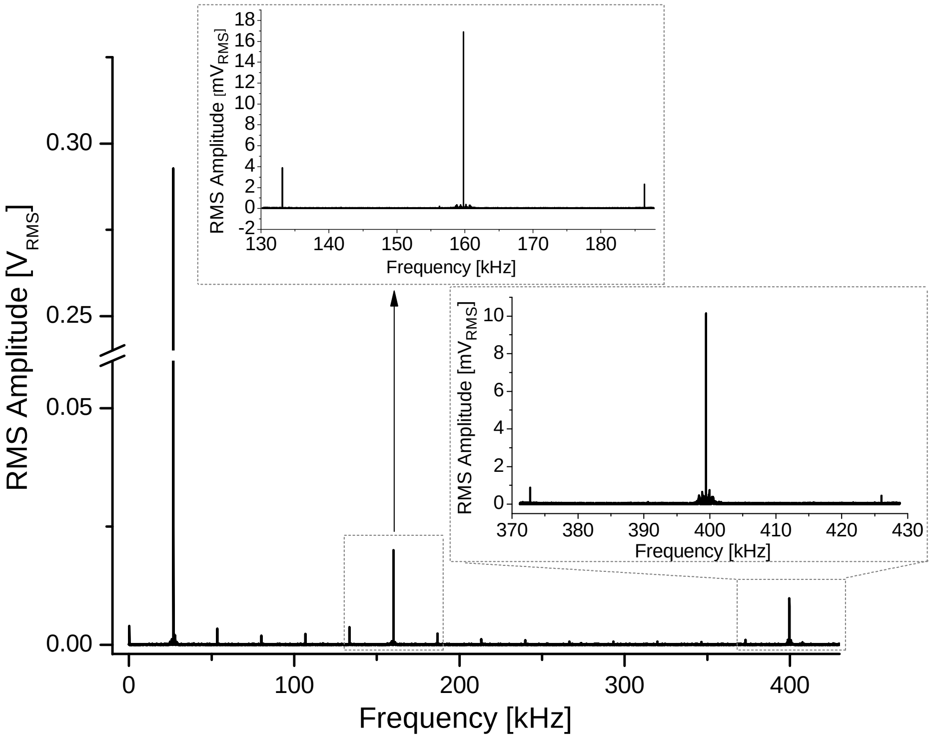

(a) FFT of the sensor signal indicating harmonics created in a cantilever in the tapping mode and in the vicinity of a sample surface.

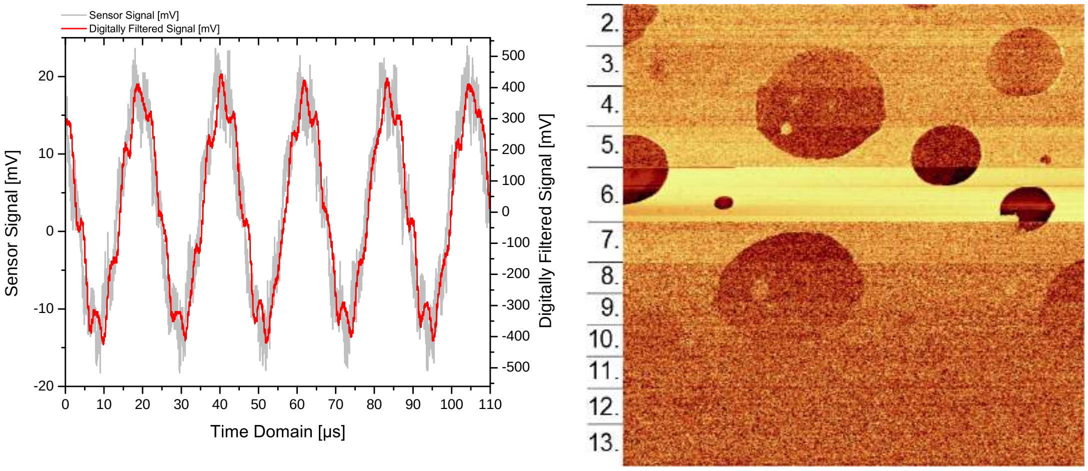

(b) Both raw and filtered cantilever time domain sensor signals show the first resonance and 6th harmonic superposed.

(c) Harmonic sweep of different frequencies created with approx. 40 lines each. The sections of the corresponding harmonics are indicated to the left of the image.

Figure 9.2: Different images show FFTs of harmonics, corresponding time domain signals and a harmonic sweep.

9.3 Cantilever FEM Simulation for Harmonic Optimization

In this section, a three-dimensional model of the active cantilever is created and an eigenmode analysis performed by FEM simulations. The topological modifications are included in the simulation in a parameterized fashion. The prospective hole dimensions are swept according to a predefined range and step size. A milling structure is then chosen to introduce the proper modal shifts.

Figure 9.3 indicates the parametrized simulation cycle. In a first step, a model of the described cantilever is created in the CAD software Autodesk Inventor Professional. The 200 nm Si_3N_4 passivation layer is omitted as the dynamic behavior is dominated by the other layers. According to the simulation, the frequency ratios of the unmodified beam are 6.39:1 for the second to the first and 17.46:1 for the third to the first transverse eigenmode. The rectangular holes are then placed into the model with one or two sides variable during the simulation. A potential location is near the free end of the cantilever, where the nodes and thus stiffness domains of both second and third eigenmode are close to each other. The heating meander restricts the surface for mass removal to about 50 % of the total width. In addition, the area between the cantilever edge and outer wires is not included to be less prone to twisting. Although the active cantilevers impose some constraints regarding the shapes of holes, the overall milling effect is equivalent to using regular cantilevers without this restriction.

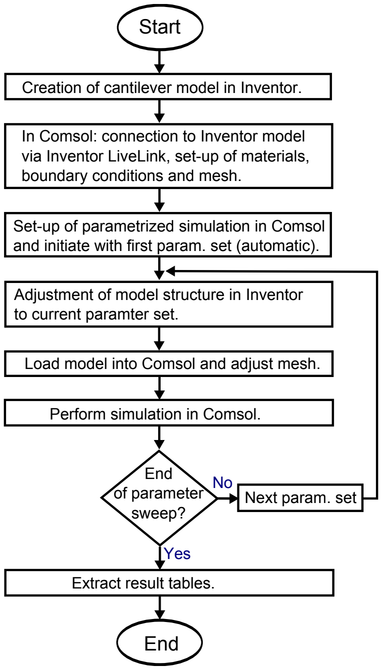

Figure 9.3: Parameterized simulation cycle.

In a second step, the model is connected to the FEM simulation software Comsol Multiphysics via the LiveLink interface. A following parameterized simulation solves for the cantilever's eigenfrequencies and corresponding mode shapes based on variable hole sizes.

First, Comsol takes the model with initialized hole dimensions from the concurrent Inventor session. The model is then assigned with material properties, boundary conditions and a mesh, followed by the first simulation. Figure 9.4 shows the full model with the mesh and holes visible. Afterwards, Comsol assigns new parameters based on a given range and step size. These are communicated to Inventor, which in turn modifies the model. The modified model is sent back to Comsol and the mesh is automatically fitted to the new structure. This is followed by the next simulation. A completed parametrized simulation cycle consists of a set of different hole dimensions with corresponding eigenfrequency information. The count of individual simulations increases exponentially by using two or more variable parameters. Hence, the simulation complexity imposes a time constraint. Typically, our cantilever mesh consists of approximately 500.000 elements. This results in about 3-5 minutes per simulation on a Xeon 12-core Workstation.

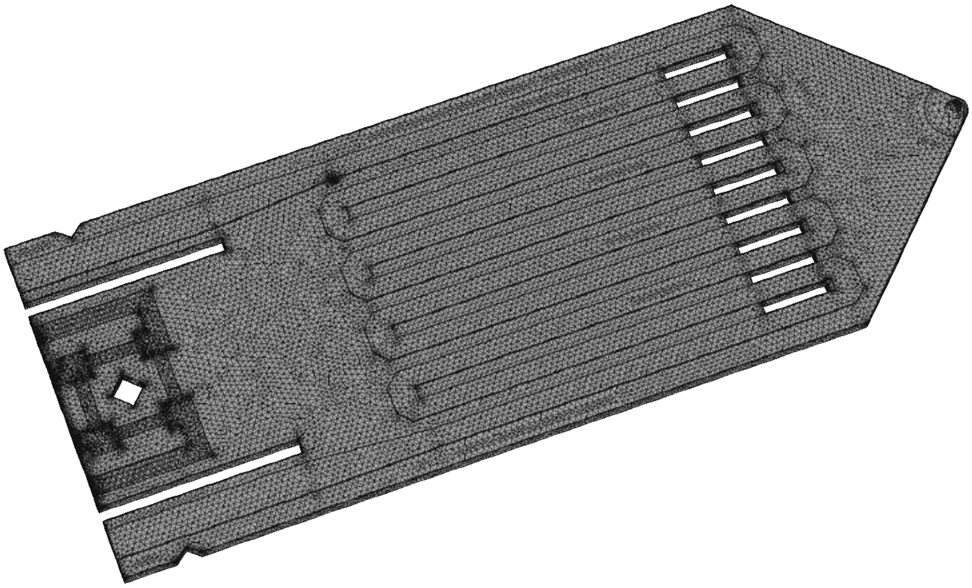

Figure 9.4: Full model that is created in Autodesk Inventor and simulated in a parametrized fashion in Comsol Multiphysics. Here, it is shown after the meshing step.

In this work, simulations with various hole configurations have been performed. The different configurations modify the ratios with dissimilar slopes when compared to each other. A specific configuration is then chosen based on a target cantilever such that the desired ratios are achieved at similar hole sizes. This approach is necessary as the fabricated cantilevers often do not follow the theoretical frequency ratios. The true ratio of the second to the first eigenmode is mostly observed between 6.1:1 and 6.4:1. Similarly, the true ratio of the third to the first eigenmode is often between 16.5:1 and 17.2:1. Hence, the ratio of third to second eigenmode also depends on the cantilever.

The black curves in Figure 9.5 are an example indicating the modified frequency ratios obtained by the parameterized simulation. The length of the specific hole shapes is swept simultaneously and the width kept constant. The ratios of second and third eigenmodes to the first eigenmode change linearly for a wide range of hole dimensions (black curves in Figure 9.5(a) and 9.5(b)). Note that in this case the required hole lengths are different in order to achieve the ratios of 6:1 and 16:1. However, as the truly required ratio shifts differ from the simulation this can be a potential fit with a real cantilever. A result is chosen that only removes as much material as needed to introduce the required ratio shifts in the real cantilever. Herby most cantilevers and their targeted modifications fall within the linear range.

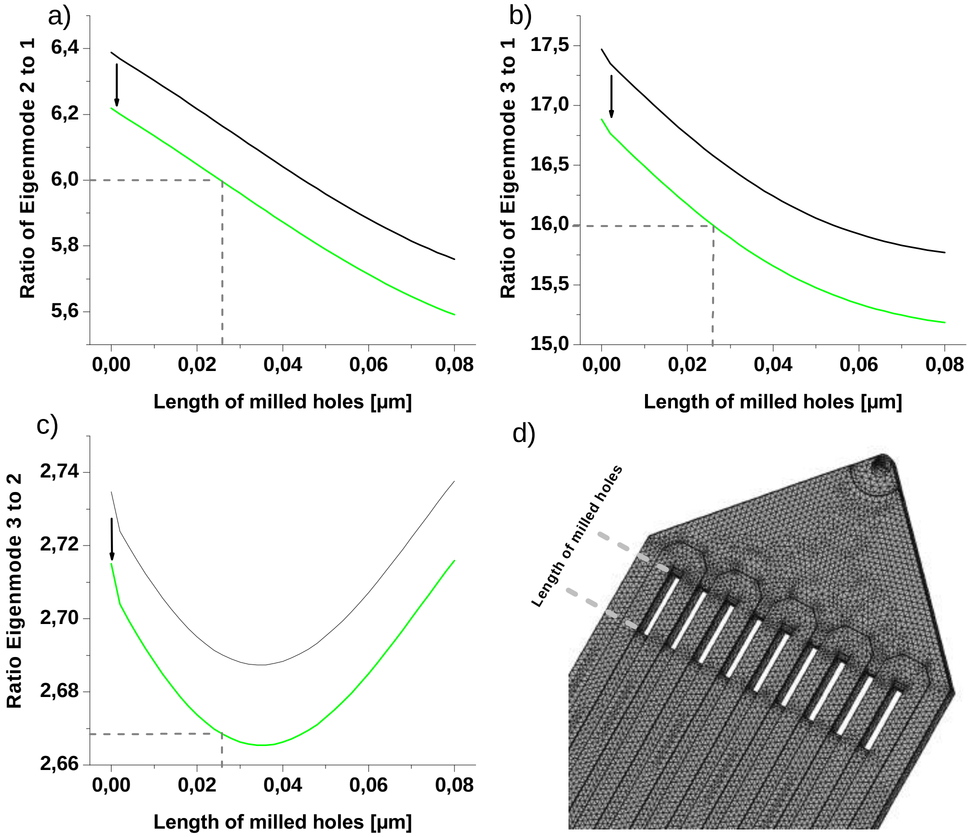

Figure 9.5: Simulated ratios of the indicated transverse eigenmodes. The model in (d) shows the hole configuration of the parameterized simulation to create (a)-(c). The black curve is the simulated frequency shift and the green curve its correction towards a specific real cantilever.

The cantilever in Figure 9.6(a) has true ratios of 6.219:1 and 16.885:1. The simulated hole configuration of Figure 9.5 with a specific size is chosen to modify the ratios by 0.219 and 0.885 to receive ratios of 6:1 and 16:1, respectively. The green curves in Figure 9.5 are the adjusted frequency ratio shifts based on the true initial ratios of the real cantilever. Both desired frequency modifications are achieved by a hole length of 26 μm (indicated by dashed lines). Hereby, the model's ratios are only lowered to 6.171 and 16.575, which is well within the linear domain of both ratios. The thereafter generated digital mask is shown in Figure 9.6(b). It is used in the following Section 9.4 to modify the cantilever of Figure 9.6(a). The mask has a monochrome color coding, where black blocks and white requests a set FIB ion beam current.

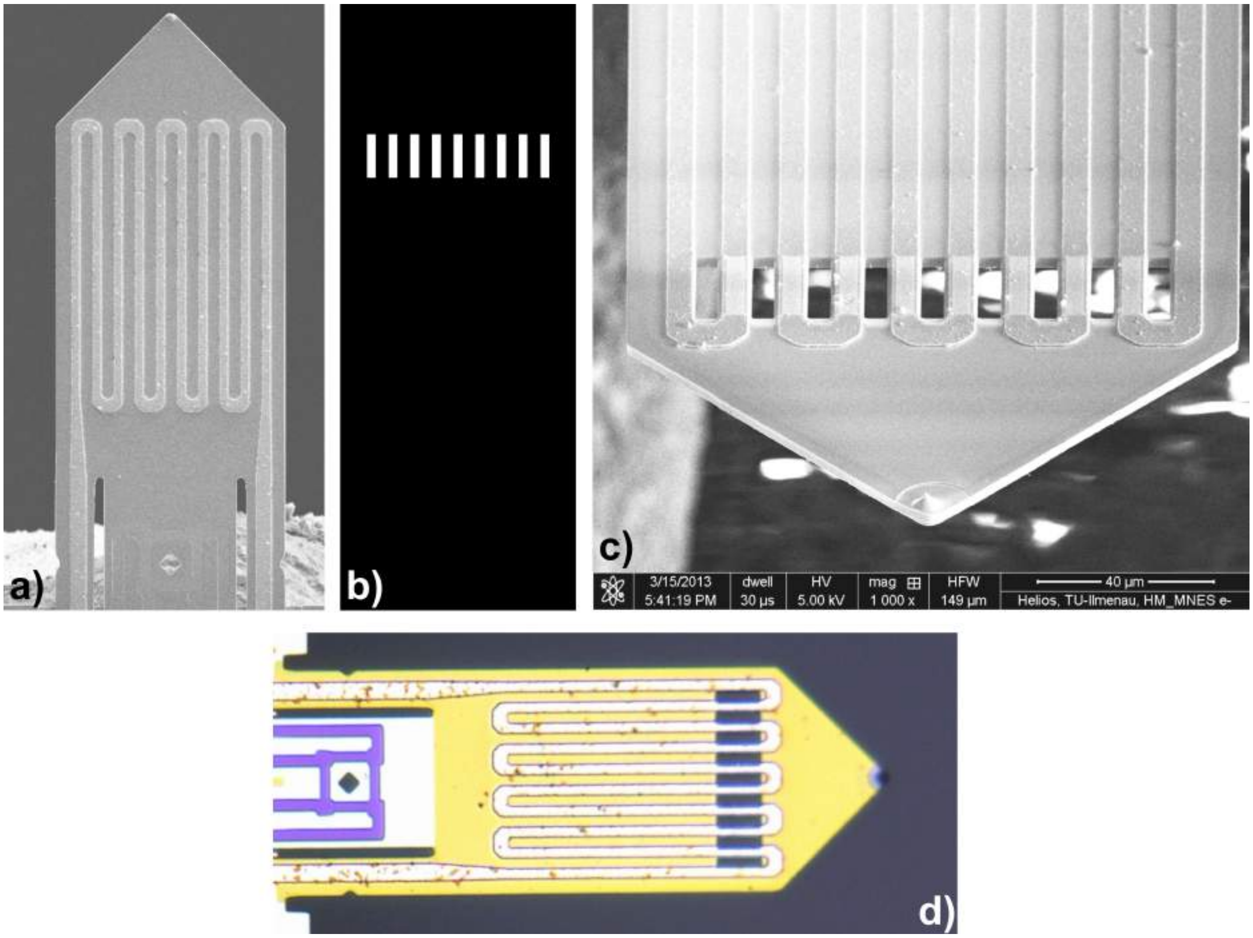

Figure 9.6: (a) SEM image of the cantilever before processing; (b) Digital mask; (c) SEM image of fabricated harmonic cantilever using cantilever of (a) and mask of (b); (d) Cantilever of (c) observed in an optical microscope.

9.4 Fabrication of Harmonic Cantilevers

In the following, the two different fabrication strategies of modifying the cantilever dynamics are presented. In Method I (Subsection 9.4.1) the generated digital mask (bitmap) of Section 9.3 is used. Method II (Subsection 9.4.2) is carried out in-situ by performing repeated frequency sweeps and hereof based hole depth and area. In both cases, the Helios FEI 600i Dual Beam FIB introduced in Section 3.4 is used. Alignment of its Ga^+ ion beam to the electron beam allows alternating ion milling and non-invasive navigation/mask alignment.

Advantages of Method I are good repeatability and exactness of achieved ratios for every processed cantilever. Both factors depend on carefully measured cantilever characteristics and proper hole configurations. In contrast, Method II has a much lower repeatability and exactness. As the removal of mass influences each eigenmode differently it renders the result hard to predict on-the-go. A carefully chosen initial hole configuration and location is helpful. In addition, the frequency shifts are observed in vacuum with slightly different resonances than in air. Method I has a net process time of 1 - 5 min., whereas the manual procedure of Method II can take 30 minutes or more per cantilever. Method I requires preparation time for cantilever characterization and simulation. Although no such preparation needed with Method II it requires a suitable setup within the vacuum chamber. It includes electrical connections and a vacuum capable pre-amplifier.

9.4.1 Method I: Automatic Approach with Digital Mask

The bitmap file is loaded into the FIB software and used as a milling mask by placing it on top of the cantilever. The milling time is a function of beam current (typically 10 nA), acceleration voltage (typically 10 kV), milling area and depth. Figure 9.6(c) shows the harmonic cantilever in the FIB chamber. Figure 9.6(d) is an optical image of the cantilever of Figure 9.6(c). Due to the cantilever fabrication process they can slightly vary in length, width and/or thickness. However, this can be corrected by properly aligning (stretching or quenching) the mask onto the cantilever, which adjusts for the shifted nodes.

Three additional milled cantilevers are shown in Figure 9.7(a)-(c). Figure 9.7(d) is a photo from inside the chamber with a mounted cantilever ready to be processed. In Figure 9.7(c), the milled holes are too wide, causing the undesired removal of the heating meander. The milling process works well without using precursor gases. Those are often used to bind the sputtered material and avoid its deposition back to the sample. The SEM images of processed cantilevers indicate a contrast of the heating meander between milled holes. It is due to charges created and trapped inside the top passivation layer. As will be confirmed in Section 9.5 this does not influence the resistance of the heating meander. This effect has been observed before as well as with a regular SEM. The FIB milling procedure is used as a parallel process, such that the heating meander is crossed over continuously. Setting the milling to a serial process might be able to prevent this effect.

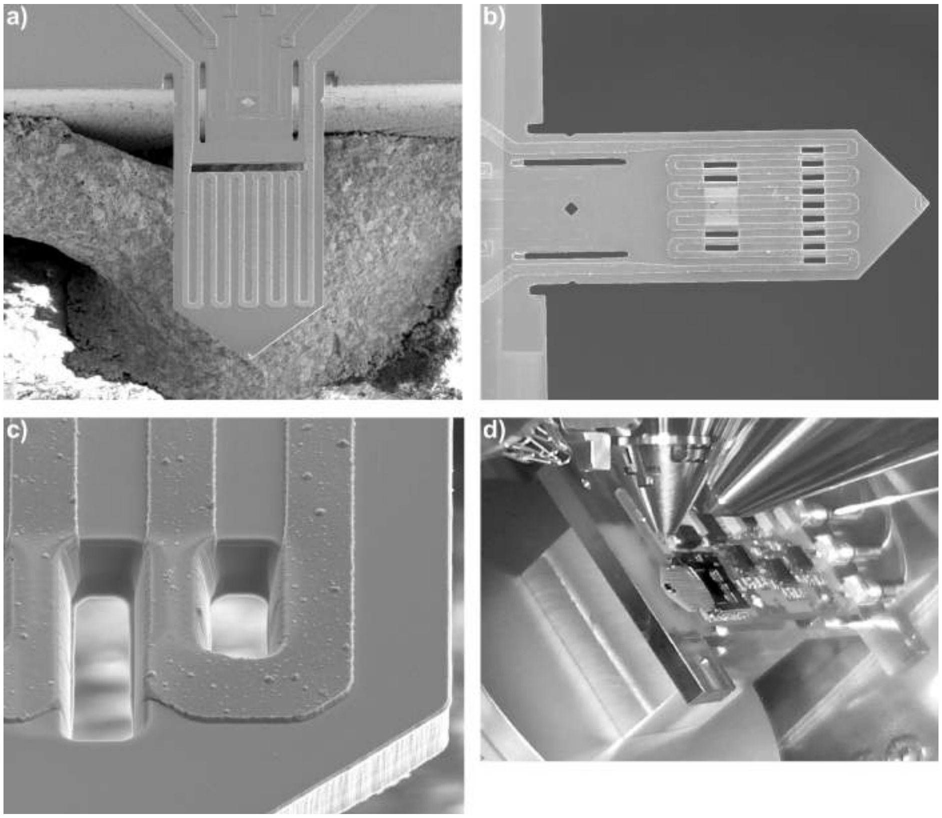

Figure 9.7: (a)-(c) Three additional milled cantilevers, (d) photo from inside the chamber with a mounted cantilever. In (c) the milling process caused the undesired removal of some of the aluminum meander layer.

9.4.2 Method II: In-Situ Approach by Resonance Observation

The cantilever can be modified by observing its frequency shifts in-situ. Here, the cantilever is mounted on a vacuum capable PCB containing a pre-amplifier for the piezo-resistive sensor signal, as seen in Figure 9.7(d). All connections are routed to the ZI HF2LI outside the chamber that is used to obtain the frequency sweeps. Repeated sweeps are carried out to observe the shifts, while the ion beam is turned on for short times. Figure 9.8 shows frequency shifts at different milling stages for the first three resonances. In all subfigures, the first and second modification refers to the milled material between the heating meander and the large area towards the free end of the cantilever, respectively. Figure 9.8(c) shows cantilever images for corresponding frequency sweeps during milling near the free end (read from bottom to top). The difference between the first and second sweep is before and after milling between the meander.

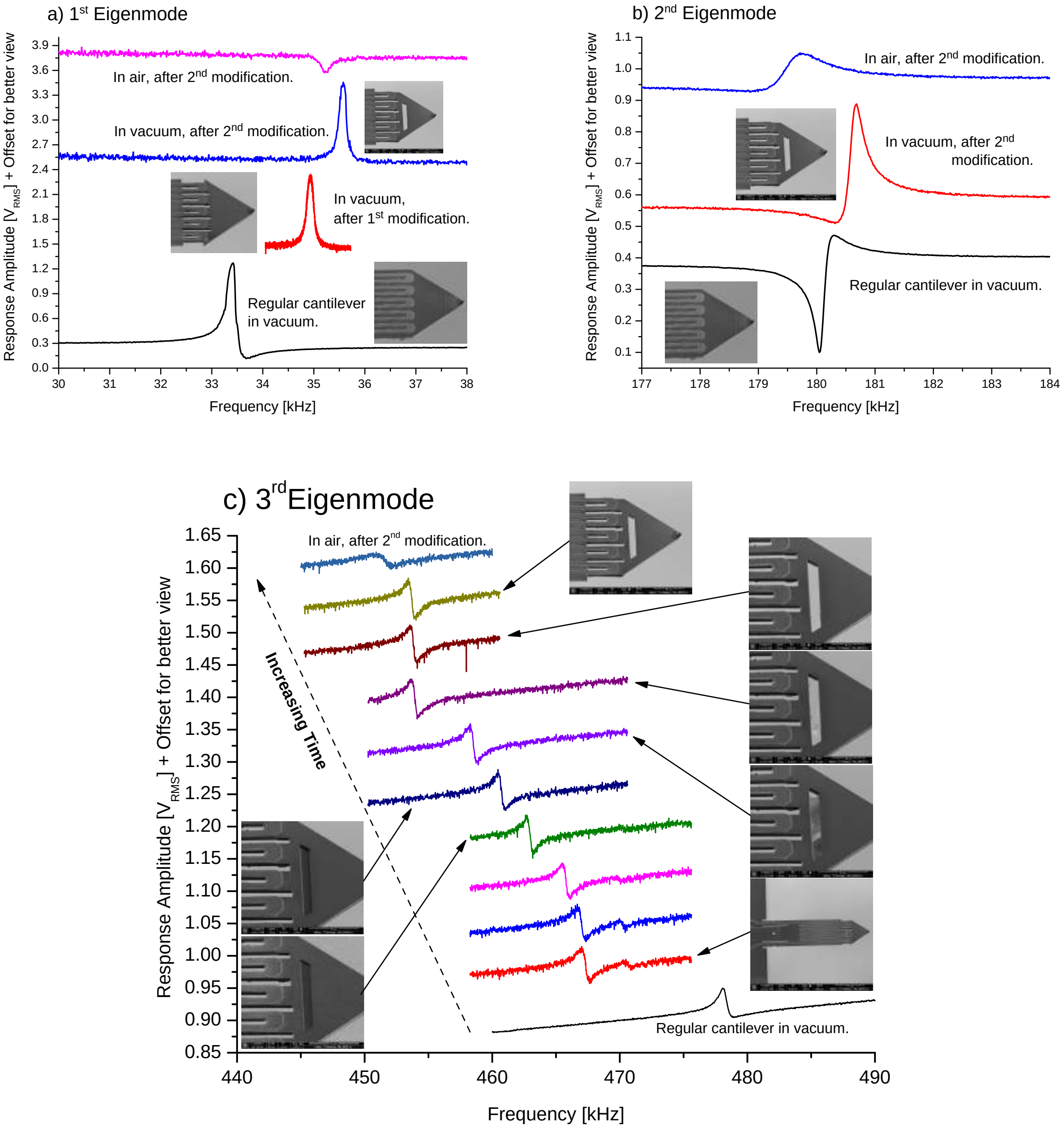

Figure 9.8: Frequency shifts of the first three resonances during the modification in the FIB. All diagrams need to be read from the bottom to the top.

Artifacts are caused by the configuration of piezo-sensor and vacuum pre-amplifier. The design of the pre-amplifier utilizes only one of the four resistors of the sensor bridge. This causes distortion of the shape of some resonances (for example top resonance in Figure 9.8(a)). It also causes the shape of some frequency sweeps to appear as dynamic zeros near the resonances (Figure 9.8). The artifacts disappear by using a pre-amplifier utilizing the full Wheatstone sensor bridge.

9.5 Cantilever Performance Evaluation (Before and After)

In this section, the resistances of the heating meander, frequency sweeps in air, mode shapes of the cantilever's transverse resonances, enhancements in harmonic responses and imaging performances before and after the milling process are compared. The data presented in subsections 9.5.1 and 9.5.2 is created with the same cantilever before and after the FIB process. In contrast, the data in subsections 9.5.3 and 9.5.4 is obtained with the cantilever shown in Figure 9.6(c)/(d) and compared to an almost identical and unmodified cantilever. Initially, both of them were fabricated as direct neighbors on the wafer and are therefore very similar in their characteristics.

9.5.1 Electrical Resistance of the Cantilever Actuator

It can be confirmed that resistances of the heating meander are not influenced by the milling process. The cantilever in Figure 9.6(c) indicates an altered contrast of the aluminum between the holes. Table 9.1 lists the resistances measured before and after the FIB modifications, referring to respective cantilevers shown in different figures. The values are matching, considering the measurement uncertainties, error of the measurement device, and slightly different contact resistances at the contact pads of each measurement.

Cantilever in	**Resistor value before milling**	**Resistor value after milling**
Figure 9.6	25.8 Ω	25.8 Ω
Figure 9.7(a)	21.9 Ω	22.1 Ω
Figure 9.7(b)	25.9 Ω	26.2 Ω
Figure 9.8	25.8 Ω	25.8 Ω

Table 9.1: Heating meander resistor values before and after the FIB milling.

9.5.2 Cantilever Resonances

Frequency sweeps in air before and after the milling of the cantilever in Figure 9.6 are compared in Figure 9.9. The resonances before the modification are 48.004, 298.532 and 810.439 kHz. As discussed in Section 9.3 the original ratios are 6.219 and 16.883. After milling, the resonances have changed to 49.442, 296.781 and 791.488 kHz. The new ratios of the second and third transverse eigenmode to the first eigenmode are 6.003 and 16.009 in air, respectively. Using similar actuation and sensing settings in the AFM, it can also be noted that the amplitude of the first resonance is slightly decreased after the FIB modification, as seen in Figure 9.9. Also, the two peak amplitudes of the higher resonances are slightly increased. A similar behavior has been observed on different FIB milled cantilevers.

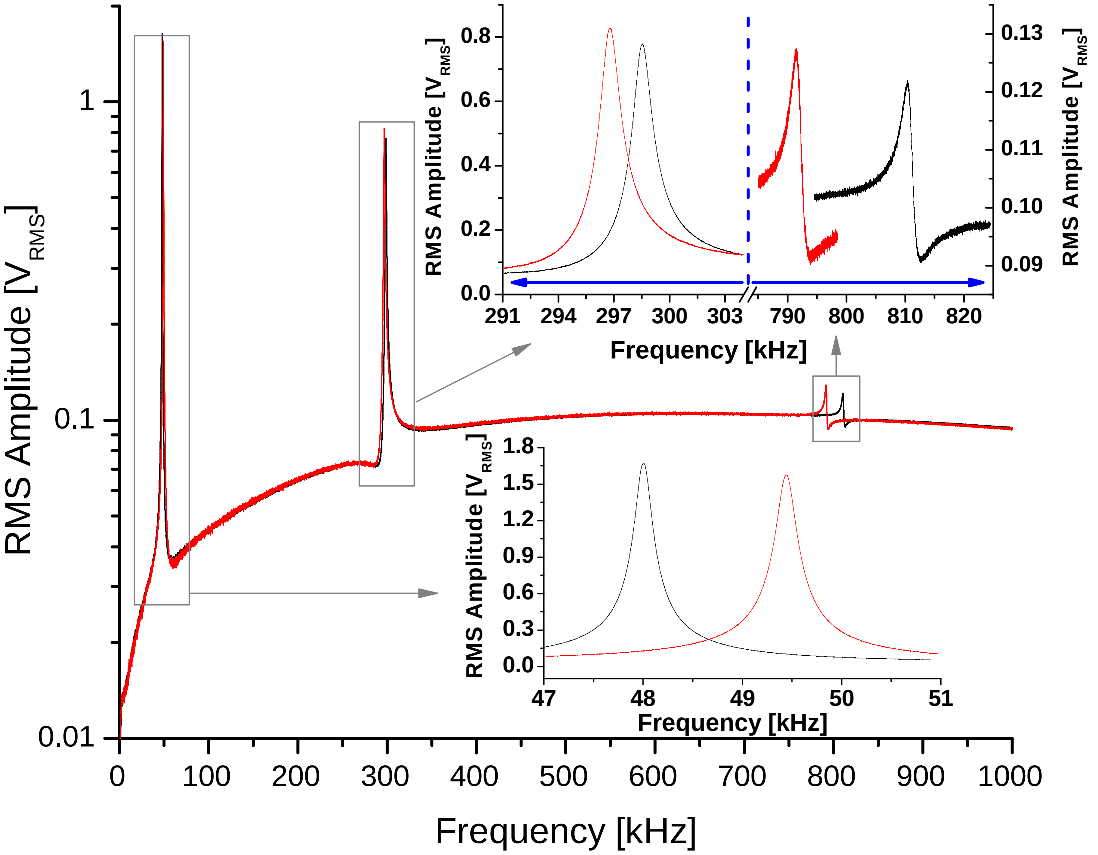

Figure 9.9: Frequency sweeps of the active cantilever (Figure 9.6) before (black curve) and after (red curve) FIB milling. The inlets provide magnifications for a better view.

The plot in Figure 9.9 indicates an amplitude roll-off towards lower frequencies. This is particularly pronounced in the presented logarithmic scale. It is caused by a High-Pass filter at the input of the AFM controller. This is to filter static cantilever sensor signals in dynamic AFM modes.

In the following, the frequency shifts of the cantilevers in Figure 9.7(a) and 9.7(b) are briefly indicated. All resonances of the cantilever in Figure 9.7(a) have decreased. Equivalently, the first, second and third resonance of the cantilever in Figure 9.7(b) are increased, decreased and decreased, respectively. Upon milling, one of the two eigenmode ratios changes more rapidly in respect to the other, as compared to the discussed cantilever of Figures 9.5 and 9.6. Such hole configurations can be necessary for different cantilevers depending on the initial ratios.

In ambient pressure the influence of the holes on the Q factors is evaluated. It is based on the shape of the resonance curves of a different cantilever. The center frequency of the resonance is divided by its bandwidth, evaluated at its half-power points (70.7% of peak amplitude) on both sides of the curve. The measurements are based on the same cantilever, obtained before and after the modification with the FIB. The Q factors for the first, second and third transverse resonances are reduced from 134 to 109, from 253 to 223 and from 286 to 278, respectively. As a comparison, the authors in [226] place holes in regular cantilevers to minimize the squeeze-film damping effect on the Q factor while being close to a sample surface.

9.5.3 Modeshapes of the Cantilever Vibrations

The shapes of the first three transverse cantilever eigenmodes without and with the modifications are compared with each other (Figure 9.10). The utilized harmonic cantilever is the one discussed in Section 9.3 and presented in Figure 9.6. In this case, the modification of the stiffness domain is dominant. It shifts the nodes of vibration and thus changes the mode shapes. This is most pronounced in the third eigenmode, where the nodes are considerably shifted towards the free end of the cantilever.

The curves are not always smooth as they carry uncertainties based on the measurement technique. A SIOS GmbH, Germany, interferometer (Nano Vibration Analyzer) with <0.1 nm resolution is mounted on an anti-vibration table. The laser is focused onto the cantilever, which in turn is mounted on a stage adjustable by three micrometer screws. During the experiment the cantilever is adjusted in steps of 10 μm along its length. This results in 36 to 38 measurements depending on the actual length of the cantilever. The major uncertainties in the measurement arise from the

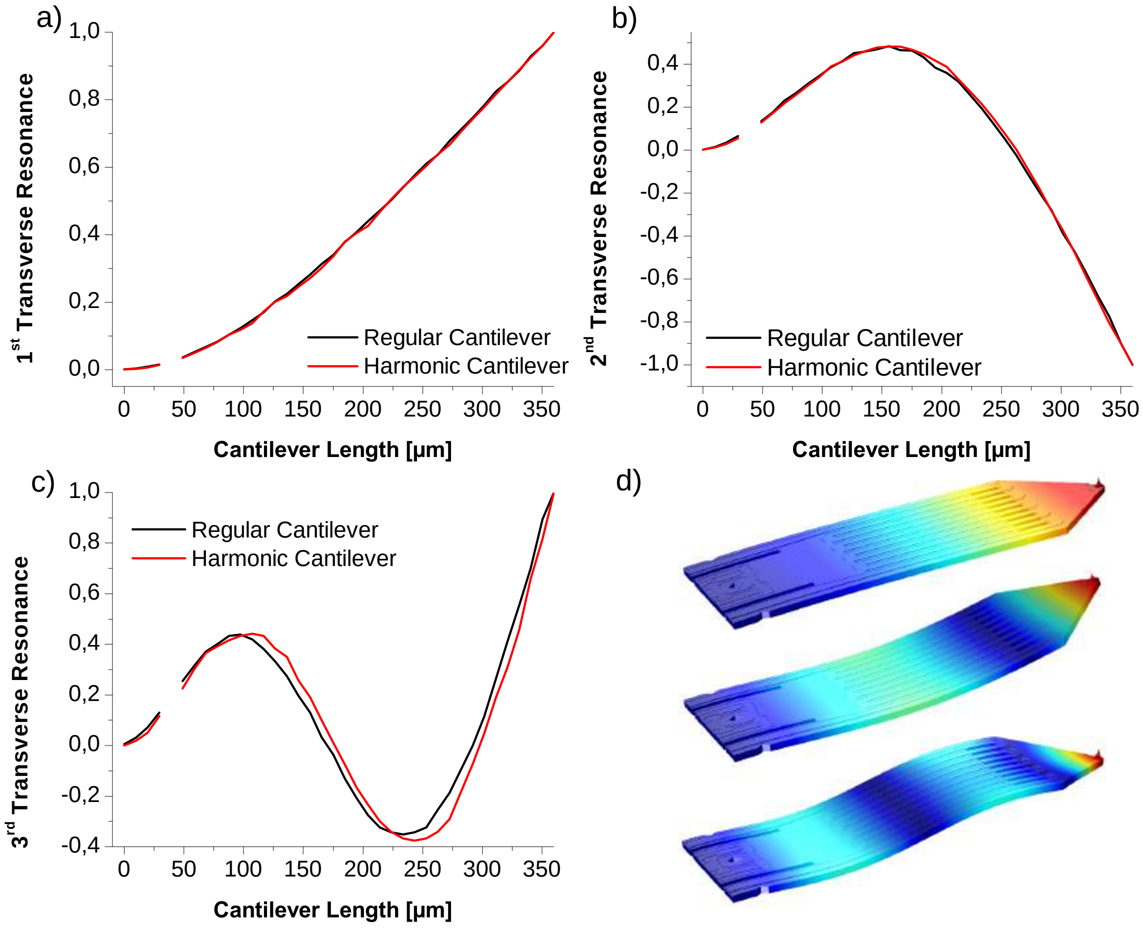

Figure 9.10: Measured mode shapes of the first three transverse eigenmodes: (a) First, (b) second and (c) third mode shape, respectively. 3-dimensional mode shape simulations of the harmonic cantilever are shown in (d).

use of the micrometer screw, with a placement error estimated to be around ±1 μm each interval. In addition, the start point at the free end of the cantilever can vary by a few micrometers. All diagrams in Figure 9.10 show an interruption with missing values close to the fixed end of the cantilever. It occurs when the interferometer laser hits the small stress concentration hole while it is moved along the centerline of the cantilever. For example, the hole can be seen in Figure 9.6(a). Figure 9.10(d) shows the 3-dimensional simulated transverse mode shapes of the active cantilever. They correspond to the measurements in Figure 9.10(a)-(c). Table 9.2 indicates the amplitude at the tip of each cantilever and transverse eigenmode that is used to normalize the mode shape. Hence, the values correspond to the value ’1’ in the curves of Figure 9.10. The remaining amplitudes along the cantilever are hence proportionally scaled.

Regular cantilever	**Amplitude**
Mode 1	211.3 nm
Mode 2	71.1 nm
Mode 3	10.5 nm
Harmonic cantilever	
Mode 1	195.6 nm
Mode 2	58.0 nm
Mode 3	12.1 nm

Table 9.2: Peak amplitudes at the cantilever tips used for mode shape measurements and normalizations.

9.5.4 Amplification of Harmonics

The amplification of the harmonics is demonstrated in the following. Each cantilever is actuated at its first resonance frequency. Here, the amplitudes in free air are 149 nm and 139 nm for the regular and harmonic cantilever, respectively. Both are then put into an intermittent contact with a sample surface. The distance is specified by a set-point of 35%. The sample is the Bruker PS-LDPE-12M as described in Section 9.2. A topographic image of the sample is taken to locate the different polymers. One at a time, the tip of each cantilever is placed on each polymer type. Here, the AFM is only used to control the distance of the tip to the sample without scanning the surface. The ZI HF2LI computes the 32768 points FFTs of each cantilever's sensor signals tapping the two different polymers. Note that the signals are measured right after their pre-amplification. Hence, the AFM controller's High-Pass filter with its roll-off present in Figure 9.9 does not influence the measurements.

Figure 9.11 shows the different FFTs. Figure 9.11(a) and 9.11(c) are obtained with the harmonic cantilever and Figure 9.11(b) and 9.11(d) with the regular cantilever. The sub-figures indicate the polymers measured with each FFT. In addition, the noise appears to be different for both cantilevers, visible due to the logarithmic scale. The regular cantilever's FFTs are obtained without averaging, whereas the harmonic cantilever's FFTs have an RMS averaging setting of 10 cycles. However, the FFTs are obtained after a steady state is reached during acquisition. The peaks around 50 kHz correspond to the first resonances and are constant in all cases, as it is used for distance feedback control.

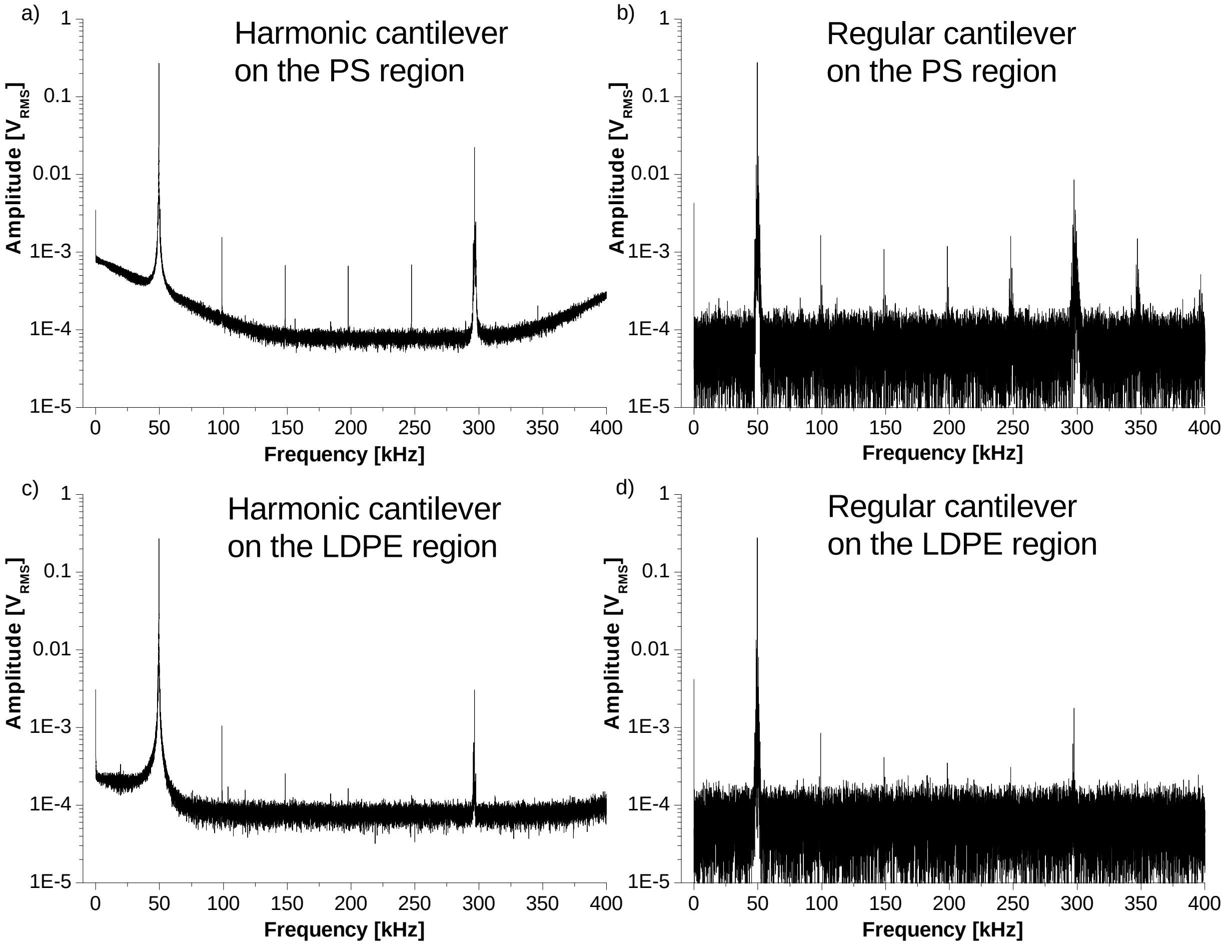

Figure 9.11: Harmonic response of the harmonic and regular cantilevers tapping on the PS-LDPE-polymer sample at different locations that are indicated in the sub-diagrams.

For comparison, Figure 9.12 presents a typical FFT of the vibrating cantilevers in free air with the absence of excited harmonics.

Figure 9.13 is a subset of Figure 9.11, where the 6^{th} harmonics are shown on a linear scale for better comparison. Figure 9.13(a) and 9.13(b) compare the two cantilevers positioned on the PS and LDPE regions, respectively. On the PS region, the response of the harmonic cantilever has increased by 2.70 times compared to the regular cantilever; the response on the LDPE has increased by 1.99 times. As a note, the 6^{th} harmonic of the harmonic cantilever reaches almost 10% of the first resonance's signal.

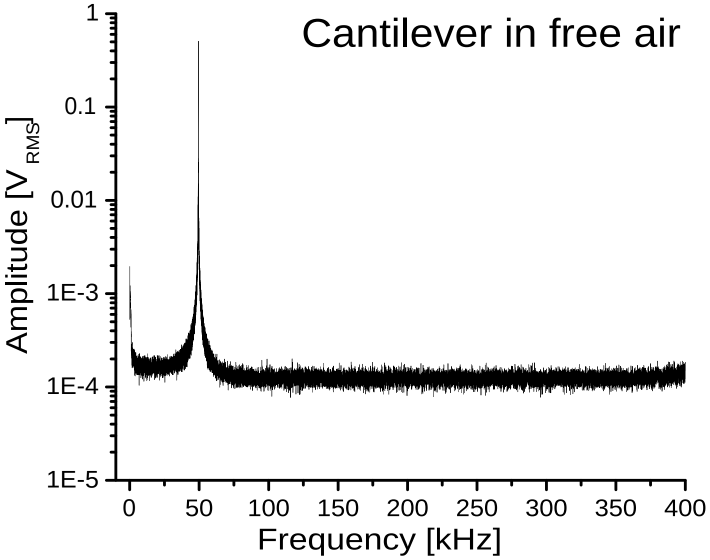

Figure 9.12: FFT of the cantilever signals in free air.

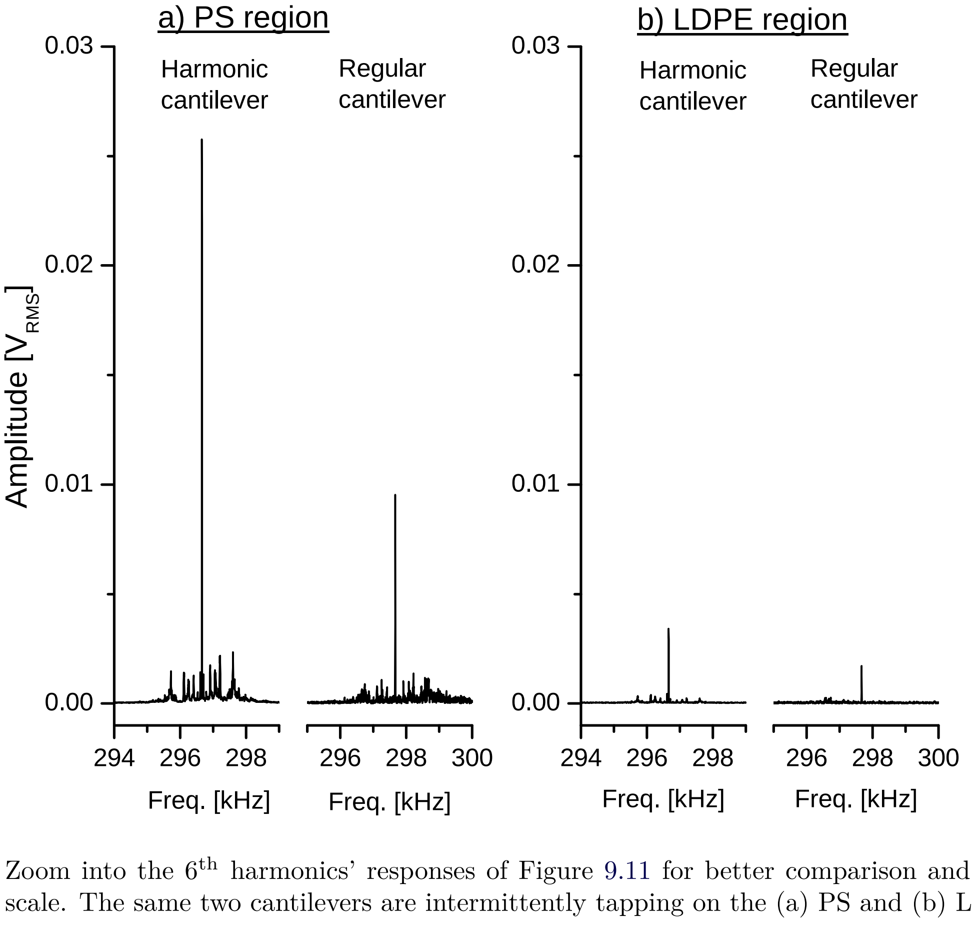

Figure 9.13: Zoom into the 6th harmonics' responses of Figure 9.11 for better comparison and in a linear scale. The same two cantilevers are intermittently tapping on the (a) PS and (b) LDPE.

9.6 Imaging Results

The improvements in material contrast are shown in scanned AFM images. The sample under investigation consists of a silicon substrate with gold particles spun onto the surface. The cantilevers compared are the harmonic cantilever of Figure 9.6(c) and a regular cantilever similar in its characteristics, as discussed earlier in Section 9.5.

Two sets of images are taken with the setup of Figure 9.1, one with each cantilever. Each image set contains the topography and phase obtained with the first resonance as well as an image by monitoring the 6th harmonic (Figure 9.14). The latter is demodulated by the external ZI HF2LI Lock-in amplifier. It is locked onto the frequency that is 6 times higher than the first resonance frequency used for scanning. The magnitude of the 6th harmonic is plotted simultaneously with the other two images to keep the lateral dependencies.

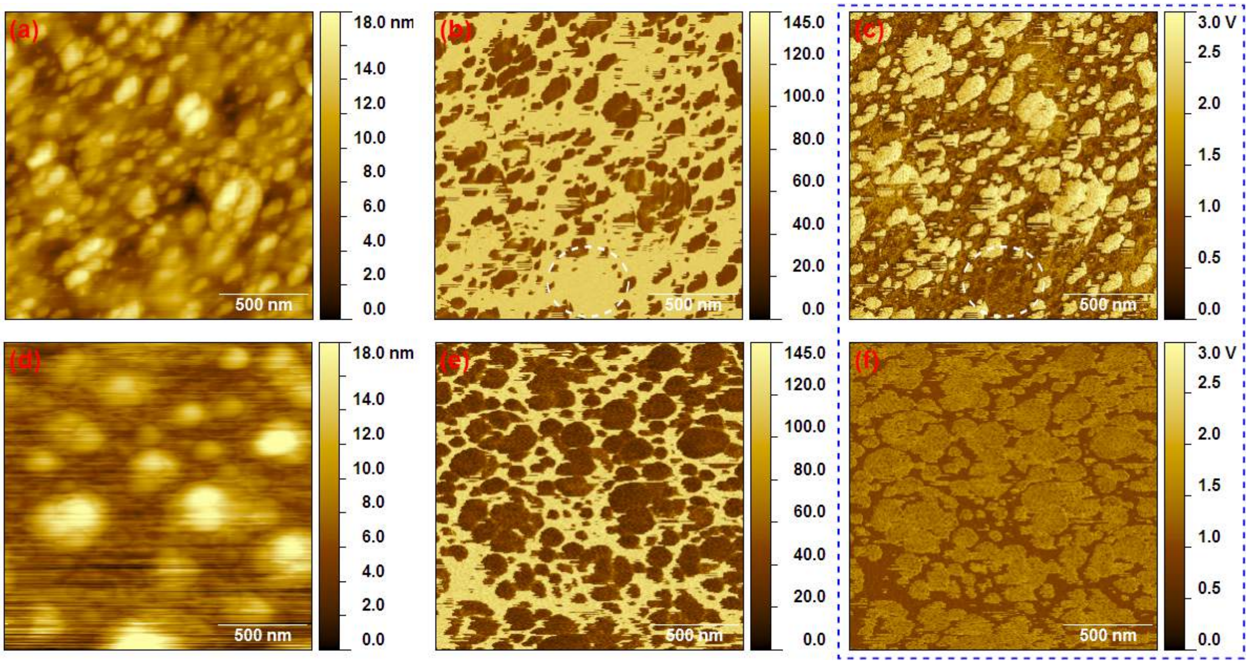

Figure 9.14: (a) to (c) (top row) are obtained with the harmonic cantilever, whereas (d) to (f) (bottom row) are acquired with the regular cantilever. (a), (b), (c) and (d), (e), (f) present the images of the topography obtained with the first resonances, their phases and the responses of the 6th harmonics, respectively.

In all cases the scan ranges are $(1.7\,\mu\mathrm{m})^2$ at a rate of 1 line/s and set-point of 35%. The free amplitudes of the first resonances are 88 nm and 95 nm for the harmonic and regular cantilever, respectively. The 6th harmonic of the regular cantilever (Figure 9.14(f)) does not indicate an increase in information compared to the topography or phase of the first eigenmode (Figure 9.14(d) and (e)). In contrast, the 6th harmonic of the harmonic cantilever (Figure 9.14(c)) shows various features between the gold particles that cannot be seen in the topography or phase images (Figure 9.14(a) and (b)). An example area for comparison is indicated by dashed white circles. That contrast is assumed to originate from residuals of the fluid that contains and is used to spin the gold particles onto the silicon substrate. The harmonic cantilever is hence able to pick up these residues, whereas the regular cantilever is not.

On a last note, a small part of the contrast improvement achieved by extracting the higher harmonics can be attributed to other FIB modified cantilever parameters. As indicated in Section 9.5.2 the Q factors of all eigenmodes are lowered by 18% or less. This suggests increased tip-sample forces of the first transverse resonance tapping the surface and results in amplified higher harmonic signals. The lower Q factors in the higher eigenmodes lead to slightly increased harmonic excitations that damp out more quickly [60, 133]. Another factor is the modified dynamic stiffness of each eigenmode. However, in the first eigenmode the mass domain is mostly affected by the FIB modification.

9.7 Conclusion

In this chapter, harmonic active cantilevers are created to enhance the material contrast of AFMs. It is based on the sample's excitation of higher harmonics dependent on the local material properties. Here, the SNR is improved by matching the cantilever's higher transverse eigenmodes with nearby harmonics. A FIB is used as a rapid prototyping tool to shift the eigenfrequencies of the cantilever. This is achieved by removing mass at locations specified by FEM simulations beforehand or in-situ during milling. The resulting cantilevers' harmonic responses are amplified and result in material contrast improvements during imaging. In addition, the higher harmonics of the piezo-resistive sensor based cantilevers show a significant response of up to 10 % of the first harmonic. This makes these cantilevers extremely suitable for the described method, as the response is much higher than of regular cantilevers reported in the literature. The compact and fully integrated cantilevers can also be easily combined with fluid and vacuum environments. For example, this allows the observation of the dynamics of biological samples and their mechanical properties in fluid. As another example, the cross-linking effect of a microelectronic polymer resist upon lithography can be investigated in its locally modified stiffnesses.

A few future improvements of the presented work can be formulated. The parameterized simulation method utilized results in several simulation runs. This is required to obtain a set of masks to account for various different cantilevers. As a future step, we anticipate to introduce an automatic topology optimization. In that case, an objective function is minimized according to given criteria such that the targeted dynamic behavior and milling mask is found automatically for a given cantilever. In addition, the repetition of the frequency sweeps in Figure 9.8 can be replaced by a PLL based approach to track the resonance shifts in real-time. The harmonic cantilever could also be combined with the compensator of Chapter 5 to further increase the response of the higher harmonics, for example, by modifying the Q factor of the higher eigenmodes.

10 Summary and Outlook

For the first time, independent and concurrent modified cantilever eigenmodes are used for multi-frequency imaging. The material contrast and tracking speed is considerably improved, enabling the measurement of small material differences. This can be useful in the field of material and life sciences, etc. In a second approach, cantilever topology optimization leads to similar benefits for material mapping. The fast amplitude detector can potentially increase the AFM imaging speed, for example enabling the observation of quick biological processes. The described work is not limited to the used type of cantilevers. Upon proper modeling and simulations, cantilevers with any kind of actuation and sensing can be use. To be more specific:

First, an estimator based compensator approach was introduced, which was able to modify the cantilever dynamics in each eigenmode individually. By using the first and higher eigenmodes one at a time, the imaging rate or sensitivity was considerably enhanced in combination with a modified Q factor. As the developed estimator based compensator was able to arbitrarily move the poles of the cantilever in the complex plane, the natural frequency of the cantilever was be modified and used for imaging. Such F control can be useful for material dependent imaging to match excited higher eigenmodes with appearing harmonics.

Second, the compensator order was increased to incorporate two or more eigenmodes simultaneously. Two imaging techniques, bimodal and higher harmonics, were used to demonstrate the effectiveness of the digital compensator towards enhanced material contrast. Resulting time domain measurements and images clearly showed the improved response of the higher eigenmode: features became visible that were not detected without the compensator. The most pronounced increase in details was achieved with a low Q factor in the first and a high Q factor in the higher eigenmode. Overall, the compensator offers a high flexibility for setting desired imaging conditions.

Third, the compensator was extended by a high speed amplitude demodulator that could potentially replace a Lock-in amplifier. The demodulator was tested in a single eigenmode approach. Time domain signals and images showed the effectiveness of the extension. Demodulation of the amplitude and phase of additional eigenmodes can be added as outlined. In the presence of the compensator, the complexity of the demodulator is less than a Lock-in amplifier in the loop. In addition, the compensator based demodulation can easily be extended for the multi-eigenmode approach. Here, proper state space representation delivers the signals of each eigenmode seperatley.

Forth, A FIB was used as a rapid prototyping tool to shift the eigenfrequencies of the cantilever by removing mass from specific locations. These were specified by FEM simulations beforehand or in-situ during milling. The resulting cantilevers showed amplification at higher harmonics that resulted in material contrast improvements during imaging. In addition, the higher harmonics of the piezo-resistive sensor based cantilevers showed a significant response of up to 10 % compared to the first resonance. This makes the cantilevers very suitable for higher harmonic imaging. Further, this technique can also be used to lower the frequencies of higher eigenmodes to make them accessible for bandwidth limited control electronics that would be unaccessible otherwise. This opens further applications, such as regular imaging in higher eigenmodes or bimodal/trimodal imaging.

In the following, a few suggestions are made to further improve this work.

10.1 Suggestion: Analog State-Space Multi-Eigenmode Compensator

Although FPGAs are continuously improved and increased in potential clock rates, it might be necessary to consider an analog implementation. In case of a similar function, analog circuit are likely to be faster du to their potentially higher bandwidth. This can even outweigh its drawbacks such as component drift, uncertainties and additional noise.

Figure 10.1 shows a second order analog state space circuit that could be used as a compensator. Since each eigenmode of the cantilever is modeled as a second order system, this circuit can control one resonance. The poles and zeros are set by the circuit's components. However, as the total cantilever response is treated as a superposition of the individual eigenmodes, this circuit can be simply extended. Then, each modeled eigenmode requires its own second order state space circuit, whose responses are added by an additional summing amplifier before U2.

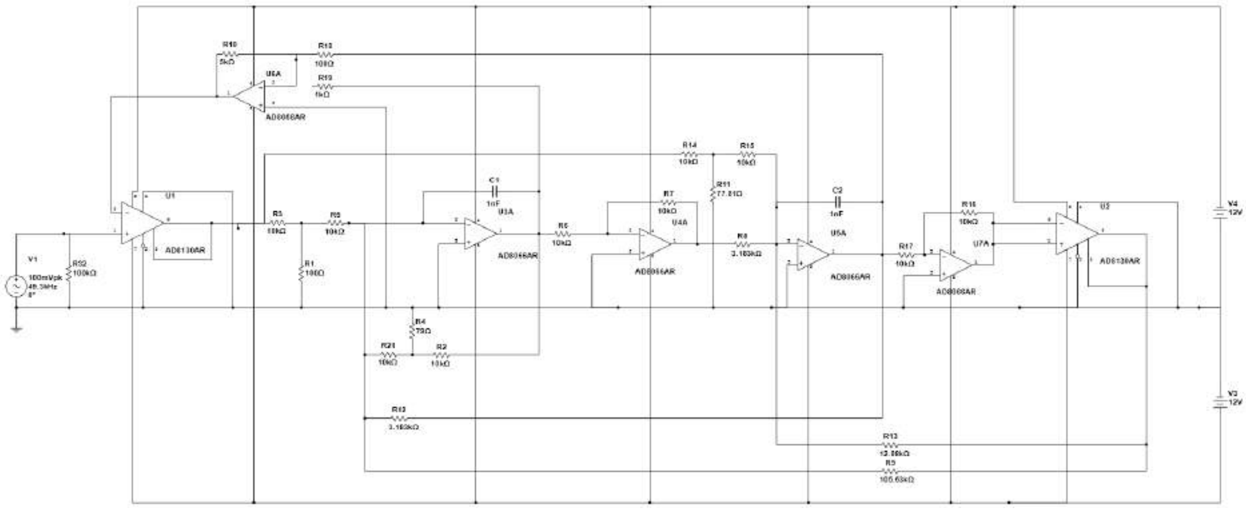

Figure 10.1: Suggested analog full state feedback compensator (See electronic version for better details).

In contrast to a biquad filter, this particular design allows the independent modification of Q factor and natural frequency. In particular, the design allows very high Q factors, which is important to incorporate the cantilever model. The estimator gains are added and the controller gain is fed back to form the overall compensator. For simulation purposes, $\mathbf{Cq}$ and $\bar{\mathbf{C}}\hat{\mathbf{q}}$ are both taken from the same circuit in Figure 10.1. This implies that the model is a perfect match of the cantilever's behavior. To connect the real cantilever, the output of U1 is the actuation signal and the positive input of U2 is connected to the cantilever sensor circuit.

Each component value needs to be chosen specifically to match the characteristics of the cantilever dynamics and to achieve a proper estimator and controller feedback. It is based on a mathematical continues time model, whose coefficients are matched with the underlying dynamic system, such as the simple version:

$$\ddot{x}(t) = -\frac{1}{R_1C}\dot{x}(t) - \frac{1}{R_2C}x(t) - \frac{1}{R_3C}u(t). \tag{10.1}$$

By choosing a specific value for the capacitor C, the resistor values are calculated by $1/(R_iC) = a_i => R = 1/(a_iC)$, where a_i is the corresponding continues time coefficient of the mathematical model. The T circuit included in the diagram of Figure 10.1 is equivalent to

$$R_T = R_1(1 + \frac{R_2}{R_3}). \tag{10.2}$$

Resistors create different noise profiles depending on their values, such that high values create higher noise. In contrast, low values create lower noise, but the higher current forms an increased load on the circuit.

Here, the model can also be implemented in the modal form, so that internal signals do not cause a saturation of the circuit. A simulation of the circuit is shown in Figure 10.2. Initially, the circuit has a high Q factor that is substantially lowered upon feedback.

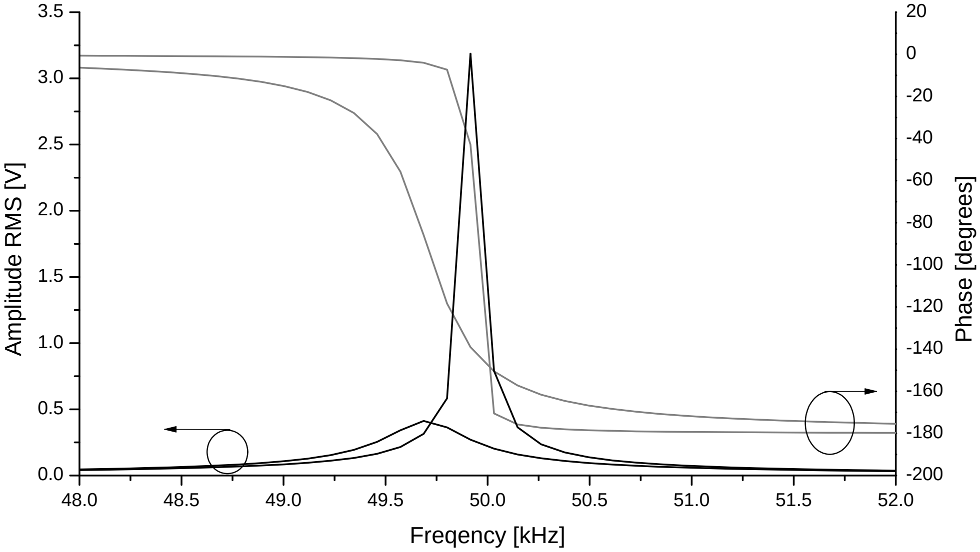

Figure 10.2: Simulation of the circuit that initially has a high Q factor and is substantially lowered upon feedback.

10.2 Other Suggestions

Reduced Order Compensator

A reduced order estimator only retrieves the states that are not measured by a sensor. In the case of the piezo-resistive and most other cantilevers, this would be the velocity proportional signal. This results in a lower order of the estimator that in turn leads to a lower implementation complexity. This again results in lower computational effort. This can be useful or even necessary for implementing compensators controlling three or more eigenmodes simultaneously, as the feedback loop rate in the FPGA can be likely increased. A different justification can be the need of a less powerful digital platform e.g. based on power consumption restrictions. However, the full state estimation offers a noise reduction of the measured sensor signal. The noise of the senor could be too high to allow a reduced order system.

Use of the Compensator to Match Higher Harmonics of Regular Cantilevers

Control over the natural frequency could be used to e.g. change the resonance frequency of the first eigenmode that is used for the topography imaging. The new resonance frequency is chosen to match one of the desired higher eigenmodes by an integer multiple. Hence, the excitement of higher harmonics coinciding with the higher eigenmodes are maximized. This scheme mimics the usage of a harmonic cantilever. Scanning the topography of a sample with a modified resonance frequency is shown in Section 6.4. The benefit of matching higher eigenmodes with integer multiple of the first resonance used for imaging is covered in Chapter 9. In addition, the Q factor of the first resonance could be modified to gain an improvement. Hence, experiments could be conducted to show an improvement in material sensitivity by using control means instead of structurally modified cantilevers.

Further, by using the Multi-Eigenmode compensator, the higher eigenmode could be modified as well. Chapter 7 has improved the harmonic response of higher eigenmodes due to higher eigenmode Q control. This can then be combined with the resonance adjustment of the previous paragraph.

Combined Compensator and Harmonic Cantilever

Either a Single or Multi-Eigenmode compensator could be combined with the harmonic cantilever to further improve its response by modifying the Q factor. This would be similar to the previous suggestion, but with the addition of an harmonic cantilever. Further, the harmonic cantilever might not have a perfect matching after its modification. A change of the first resonance frequency could be utilized to match the harmonics.

Unknown Input Observer

The estimator could be extended by one or more states to estimate the force acting on the tip. The so called unknown input observer can be modeled as, e.g., a single state estimating an input as a constant. That way, the dynamics and force acting on the tip are separated and can in particular give improved information about the sample surface forces. Further, the separated dynamics of tip-sample forces could allow for an improved alternative amplitude demodulator. While scanning, the additional states incorporate the change of the amplitude, whereas the cantilever dynamic states are decoupled.

Automatic Optimization of Harmonic Cantilevers

In the described work regarding the harmonic cantilevers in Chapter 9 a set of simulations was performed and the best solution selected manually. Structural topology optimization could be used to optimize the modification needed to create harmonic cantilevers, which would results in a single solution. An objective cost function could be set up to minimize the derivation from the harmonic match based on the amount and location of the mass removal of the cantilever. The modification of the cantilever is constrained by geometrical means, such as the heating meander that is not allowed to be removed. This needs to be included as design constraints into the optimization problem setup.

The resulting solution could be different from the presented one in Chapter 9 and might show a better dynamic behavior. For example, a solution could exist, where the first resonance keeps constant and only the higher eigenmodes are influenced. This might be possible by incorporating holes at various different location anywhere on the cantilever. The influence of every point along the cantilever is different on the kinetic and potential energy of each eigenmode.

Bibliography

[1] G. Binnig, C. F. Quate, and C. Gerber. Atomic force microscope. *Physical Review Letters*, 56(9):930–933, 1986. `doi:10.1103/PhysRevLett.56.930`.

[2] Y. Martin, C. C. Williams, and H. K. Wickramasinghe. Atomic force microscope–force mapping and profiling on a sub 100-å scale. *Journal of Applied Physics*, 61(10):4723, 1987. `doi:10.1063/1.338807`.

[3] Q. Zhong, D. Inniss, K. Kjoller, and V. B. Elings. Fractured polymer/silica fiber surface studied by tapping mode atomic force microscopy. *Surface Science*, 290(1-2):L688–L692, 1993. `doi:10.1016/0039-6028(93)90582-5`.

[4] O. M. El Rifai and K. Youcef-Toumi. Trade-offs and performance limitations in mechatronic systems: a case study. *Annual Reviews in Control*, 28(2):181–192, 2004. `doi:10.1016/j.arcontrol.2004.02.001`.

[5] G. E. Fantner, P. Hegarty, J. H. Kindt, G. Schitter, G. A. G. Cidade, and P. K. Hansma. Data acquisition system for high speed atomic force microscopy. *The Review of scientific instruments*, 76(2):026118, 2005. `doi:10.1063/1.1850651`.

[6] G. E. Fantner, G. Schitter, J. H. Kindt, T. Ivanov, K. Ivanova, R. Patel, N. Holten-Andersen, J. Adams, P. J. Thurner, I. W. Rangelow, and P. K. Hansma. Components for high speed atomic force microscopy. *Ultramicroscopy*, 106(8-9):881–7, 2006. `doi:10.1016/j.ultramic.2006.01.015`.

[7] T. Ando, T. Uchihashi, N. Kodera, D. Yamamoto, A. Miyagi, M. Taniguchi, and H. Yamashita. High-speed afm and nano-visualization of biomolecular processes. *Pflugers Archiv European Journal of Physiology*, 456(1):211–225, 2008. `doi:10.1007/s00424-007-0406-0`.

[8] A. J. Fleming, B. J. Kenton, and K. K. Leang. Bridging the gap between conventional and video-speed scanning probe microscopes. *Ultramicroscopy*, 110(9):1205–1214, 2010. `doi:10.1016/j.ultramic.2010.04.016`.

[9] M. J. Rost, L. Crama, P. Schakel, E. van Tol, G. B. E. M. van Velzen-Williams, C. F. Overgauw, H. ter Horst, H. Dekker, B. Okhuijsen, M. Seynen, a. Vijftigschild, P. Han, a. J. Katan, K. Schoots, R. Schumm, W. van Loo, T. H. Oosterkamp, and J. W. M. Frenken. Scanning probe microscopes go video rate and beyond. *Review of Scientific Instruments*, 76(5):053710, 2005. `doi:10.1063/1.1915288`.

[10] G. Schitter, G. Fantner, J. Kindt, P. Thurner, and P. Hansma. On recent developments for high-speed atomic force microscopy. *Proceedings, 2005 IEEE/ASME International Conference on Advanced Intelligent Mechatronics*, pages 261–264, 2005. doi:10.1109/AIM.2005.1501000.

[11] R. Pedrak, T. Ivanov, K. Ivanova, T. Gotszalk, N. Abedinov, I. W. Rangelow, K. Edinger, E. Tomerov, T. Schenkel, and P. Hudek. Micromachined atomic force microscopy sensor with integrated piezoresistive sensor and thermal bimorph actuator for high-speed tapping-mode atomic force microscopy phase-imaging in higher eigenmodes. *Journal of Vacuum Science & Technology B: Microelectronics and Nanometer Structures*, 21(6):3102, 2003. doi:10.1116/1.1614252.

[12] T. Gotszalk, P. Grabiec, and I. W. Rangelow. Piezoresistive sensors for scanning probe microscopy. *Ultramicroscopy*, 82(1-4):39–48, 2000. doi:10.1016/S0304-3991(99)00171-0.

[13] M. Woszczyna, P. Zawierucha, P. Pałetko, M. Zielony, T. Gotszalk, Y. Sarov, T. Ivanov, A. Frank, J.-P. Zöllner, and I. W. Rangelow. Micromachined scanning proximal probes with integrated piezoresistive readout and bimetal actuator for high eigenmode operation. *Journal of Vacuum Science & Technology B: Microelectronics and Nanometer Structures*, 28(6):C6N12, 2010. doi:10.1116/1.3518465.

[14] I. W. Rangelow. Scanning proximity probes for nanoscience and nanofabrication. *Microelectronic Engineering*, 83(4-9):1449–1455, 2006. doi:10.1016/j.mee.2006.01.199.

[15] T. Michels, E. Guliyev, M. Klukowski, and I. W. Rangelow. Micromachined self-actuated piezoresistive cantilever for high speed spm. *Microelectronic Engineering*, 97:265–268, 2012. doi:10.1016/j.mee.2012.03.029.

[16] P. P. Lehenkari, G. T. Charras, A. Nykänen, and M. A. Horton. Adapting atomic force microscopy for cell biology. *Ultramicroscopy*, 82(1-4):289–95, 2000. doi:10.1016/S0304-3991(99)00138-2.

[17] R. Lal and S. A. John. Biological applications of atomic force microscopy. *The American journal of physiology*, 266(C1), 1994.

[18] H. Lin, D. O. Clegg, and R. Lal. Imaging real-time proteolysis of single collagen i molecules with an atomic force microscope. *Biochemistry*, 38(31):9956–63, 1999. doi:10.1021/bi990800q.

[19] M. A. Poggi, L. A. Bottomley, and P. T. Lillehei. Scanning probe microscopy. *Analytical chemistry*, 74(12):2851–62, 2002. doi:10.1021/ac025695w.

[20] D. J. Burns. *On Single-Molecule DNA Sequencing with Atomic Force Microscopy using Functionalized Carbon Nanotube Probes*. PhD thesis, Massachusetts Institute of Technology, 2004.

[21] C. C. W. A. L. C. Hafner J.H. Structural and functional imaging with carbon nanotube afm probes. *Progress in Biophysics and Molecular Biology*, 77(1):73–110, 2001. doi:10.1016/S0079-6107(01)00011-6.

[22] A. Noy, D. V. Vezenov, and C. M. Lieber. Chemical force microscopy. *Annual Review of Materials Science*, 27(1):381–421, 1997. `doi:10.1146/annurev.matsci.27.1.381`.

[23] M. Ru, Y. Li, C. Hagleitner, and A. Hierlemann. Magnetically actuated complementary metal oxide semiconductor resonant cantilever gas sensor systems. *Analytical chemistry*, 77(9):2690–2699, 2005. `doi:10.1021/ac048378t`.

[24] J. D. Parkin and G. Hähner. Mass determination and sensitivity based on resonance frequency changes of the higher flexural modes of cantilever sensors. *Review of Scientific Instruments*, 82(035108), 2011. `doi:10.1063/1.3563724`.

[25] M. Viani, L. Pietrasanta, J. Thompson, A. Chand, I. Gebeshuber, J. Kindt, M. Richter, H. Hansma, and P. Hansma. Probing protein–protein interactions in real time. *Nature Structural & Molecular Biology*, 7(8):644–647, 2000. `doi:10.1038/77936`.

[26] T. Ando, N. Kodera, E. Takai, D. Maruyama, K. Saito, and A. Toda. A high-speed atomic force microscope for studying biological macromolecules. *Proceedings of the National Academy of Sciences of the United States of America*, 98(22):12468–72, 2001. `doi:10.1073/pnas.211400898`.

[27] A. Quist, I. Doudevski, H. Lin, R. Azimova, D. Ng, B. Frangione, B. Kagan, J. Ghiso, and R. Lal. Amyloid ion channels: a common structural link for protein-misfolding disease. *Proceedings of the National Academy of Sciences of the United States of America*, 102(30):10427–32, 2005. `doi:10.1073/pnas.0502066102`.

[28] G. E. Fantner, R. J. Barbero, D. S. Gray, and A. M. Belcher. Kinetics of antimicrobial peptide activity measured on individual bacterial cells using high-speed atomic force microscopy. *Nature nanotechnology*, 5(4):280–5, 2010. `doi:10.1038/nnano.2010.29`.

[29] S. Kasas, N. Thomson, B. Smith, H. Hansma, X. Zhu, M. Guthold, C. Bustamante, E. Kool, M. Kashlev, and P. Hansma. Escherichia coli rna polymerase activity observed using atomic force microscopy†. *Biochemistry*, 36(3):461–468, 1997.

[30] G. Schitter, K. J. Åström, B. DeMartini, G. E. Fantner, K. Turner, P. J. Thurner, and P. K. Hansma. Design and modeling of a high-speed afm-scanner. *IEEE Transactions on Control Systems Technology*, 15(5):906–915, 2007. `doi:10.1109/TCST.2007.902953`.

[31] E. Guliyev, B. E. Volland, Y. Sarov, T. Ivanov, M. Klukowski, E. Manske, and I. W. Rangelow. Quasi-monolithic integration of silicon-mems with piezoelectric actuators for high-speed non-contact atomic force microscopy. *Measurement Science and Technology*, 23(7):074012, 2012. `doi:10.1088/0957-0233/23/7/074012`.

[32] D. J. Burns, K. Youcef-Toumi, and G. E. Fantner. Indirect identification and compensation of lateral scanner resonances in atomic force microscopes. *Nanotechnology*, 22(31):315701, 2011. `doi:10.1088/0957-4484/22/31/315701`.

[33] T. Ando. Control techniques in high-speed atomic force microscopy. In *2008 American Control Conference (ACC)*, pages 3194–3200. IEEE. `doi:10.1109/ACC.2008.4586984`.

[34] S. Salapaka, A. Sebastian, J. P. Cleveland, and M. V. Salapaka. High bandwidth nanopositioner: A robust control approach. *Review of Scientific Instruments*, 73(9):3232, 2002. `doi:10.1063/1.1499533`.

[35] G. Schitter and A. Stemmer. Model-based signal conditioning for high-speed atomic force and friction force microscopy. *Microelectronic Engineering*, 67-68:938–944, 2003. `doi:10.1016/S0167-9317(03)00157-6`.

[36] J. K. Hobbs, C. Vasilev, and Humphris, Andrew D. L. Videoafm—a new tool for high speed surface analysis. *The Analyst*, 131(2):251, 2006. `doi:10.1039/b511330j`.

[37] J. P. Howard-Knight and J. K. Hobbs. Video rate atomic force microscopy using low stiffness, low resonant frequency cantilevers. *Applied Physics Letters*, 93:104101, 2008. `doi:10.1063/1.2979698`.

[38] K. El Rifai, O. El Rifai, and K. Youcef-Toumi. On dual actuation in atomic force microscopes. In *2004 American Control Conference (ACC)*, volume 4, pages 3128 – 3133. IEEE.

[39] G. E. Fantner, D. J. Burns, A. M. Belcher, I. W. Rangelow, and K. Youcef-toumi. Dmcmn: In depth characterization and control of afm cantilevers with integrated sensing and actuation. *Journal of Dynamic Systems, Measurement, and Control*, 131(6):061104, 2009. `doi:10.1115/1.4000378`.

[40] G. Schitter, W. Rijkee, and N. Phan. Dual actuation for high-bandwidth nanopositioning. In *47th IEEE Conference on Decision and Control, 2008.* IEEE, 2008. `doi:10.1109/CDC.2008.4738876`.

[41] J. H. Kindt, G. E. Fantner, J. a. Cutroni, and P. K. Hansma. Rigid design of fast scanning probe microscopes using finite element analysis. *Ultramicroscopy*, 100(3-4):259–65, 2004. `doi:10.1016/j.ultramic.2003.11.009`.

[42] A. Sebastian and S. M. Salapaka. Design methodologies for robust nano-positioning. *IEEE Transactions on Control Systems Technology*, 13(6):868–876, 2005. `doi:10.1109/TCST.2005.854336`.

[43] N. Kodera, H. Yamashita, and T. Ando. Active damping of the scanner for high-speed atomic force microscopy. *Review of Scientific Instruments*, 76(5):053708, 2005. `doi:10.1063/1.1903123`.

[44] I. S. Bozchalooi, K. Youcef-Toumi, D. J. Burns, and G. E. Fantner. Compensator design for improved counterbalancing in high speed atomic force microscopy. *Review of Scientific Instruments*, 82(11):113712, 2011. `doi:10.1063/1.3663070`.

[45] G. Schitter, F. Allgöwer, and A. Stemmer. A new control strategy for high-speed atomic force microscopy. *Nanotechnology*, 15(1):108–114, 2004. `doi:10.1088/0957-4484/15/1/021`.

[46] I. Gunev, A. Varol, S. Karaman, and C. Basdogan. Adaptive q control for tapping-mode nanoscanning using a piezoactuated bimorph probe. *Review of Scientific Instruments*, 78:043707, 2007. `doi:10.1063/1.2722381`.

[47] N. Kodera, M. Sakashita, and T. Ando. Dynamic proportional-integral-differential controller for high-speed atomic force microscopy. *Review of Scientific Instruments*, 77(8):083704, 2006. `doi:10.1063/1.2336113`.

[48] T. Sulchek, R. Hsieh, J. D. Adams, G. G. Yaralioglu, S. C. Minne, C. F. Quate, J. P. Cleveland, A. Atalar, and D. M. Adderton. High-speed tapping mode imaging with active q control for atomic force microscopy. *Applied Physics Letters*, 76(11):1473, 2000. `doi:10.1063/1.126071`.

[49] A. Varol, I. Gunev, B. Orun, and C. Basdogan. Numerical simulation of nano scanning in intermittent-contact mode afm under q control. *Nanotechnology*, 19(7):075503, 2008. `doi:10.1088/0957-4484/19/7/075503`.

[50] T. R. Rodriguez and R. Garcia. Theory of q control in atomic force microscopy. *Applied Physics Letters*, 82(26):4821, 2003. `doi:10.1063/1.1584790`.

[51] M. B. Viani, T. E. Schaeffer, A. Chand, M. Rief, H. E. Gaub, and P. K. Hansma. Small cantilevers for force spectroscopy of single molecules. *Journal of Applied Physics*, 86(4):2258, 1999. `doi:10.1063/1.371039`.

[52] D. Ebeling, H. Hölscher, H. Fuchs, B. Anczykowski, and U. D. Schwarz. Imaging of biomaterials in liquids: a comparison between conventional and q-controlled amplitude modulation ('tapping mode') atomic force microscopy. *Nanotechnology*, 17(7):S221–6, 2006. `doi:10.1088/0957-4484/17/7/S20`.

[53] B. Orun, S. Necipoglu, C. Basdogan, and L. Guvenc. State feedback control for adjusting the dynamic behavior of a piezoactuated bimorph atomic force microscopy probe. *Review of Scientific Instruments*, 80:063701, 2009. `doi:10.1063/1.3142484`.

[54] J. P. Cleveland, B. Anczykowski, a. E. Schmid, and V. B. Elings. Energy dissipation in tapping-mode atomic force microscopy. *Applied Physics Letters*, 72(20):2613, 1998. `doi:10.1063/1.121434`.

[55] R. Garcia, C. Gomez, N. Martinez, S. Patil, C. Dietz, and R. Magerle. Identification of nanoscale dissipation processes by dynamic atomic force microscopy. *Physical Review Letters*, 97(1):1–4, 2006. `doi:10.1103/PhysRevLett.97.016103`.

[56] J. Melcher, C. Carrasco, X. Xu, J. L. Carrascosa, J. Gómez-Herrero, de Pablo, P. J., and A. Raman. Origins of phase contrast in the atomic force microscope in liquids. *Proceedings of the National Academy of Sciences of the United States of America*, 106(33):13655–13660, 2009. `doi:10.1073/pnas.0902240106`.

[57] R. W. Stark, T. Drobek, and W. M. Heckl. Tapping-mode atomic force microscopy and phase-imaging in higher eigenmodes. *Applied Physics Letters*, 74(22):3296, 1999. `doi:10.1063/1.123323`.

[58] A. Ulcinas and V. Snitka. Intermittent contact afm using the higher modes of weak cantilever. *Ultramicroscopy*, 86(1-2):217–22, 2001. `doi:10.1016/S0304-3991(00)00084-X`.

[59] R. Garcia and E. T. Herruzo. The emergence of multifrequency force microscopy. *Nature Nanotechnology*, 7(4):217–226, 2012. doi:10.1038/nnano.2012.38.

[60] X. Xu, J. Melcher, S. Basak, R. Reifenberger, and A. Raman. Compositional contrast of biological materials in liquids using the momentary excitation of higher eigenmodes in dynamic atomic force microscopy. *Physical Review Letters*, 102(6), 2009. doi:10.1103/PhysRevLett.102.060801.

[61] A. Raman, S. Trigueros, A. Cartagena, A. Stevenson, M. Susilo, E. Nauman, and S. A. Contera. Mapping nanomechanical properties of live cells using multi-harmonic atomic force microscopy. *Nature Nanotechnology*, 6(12):809–814, 2011. doi:10.1038/nnano.2011.186.

[62] M. Stark, R. W. Stark, W. M. Heckl, and R. Guckenberger. Inverting dynamic force microscopy: From signals to time-resolved interaction forces. *Proceedings of the National Academy of Sciences of the United States of America*, 99(13):8473, 2002. doi:10.1073/pnas.122040599.

[63] J. A. Turner and J. S. Wiehn. Sensitivity of flexural and torsional vibration modes of atomic force microscope cantilevers to surface stiffness variations. *Nanotechnology*, 12:322, 2001. doi:10.1088/0957-4484/12/3/321.

[64] M. Stark, R. W. Stark, W. M. Heckl, and R. Guckenberger. Spectroscopy of the anharmonic cantilever oscillations in tapping-mode atomic-force microscopy. *Applied Physics Letters*, 77(20):3293–3295, 2000. doi:10.1063/1.1325404.

[65] O. Sahin, C. F. Quate, O. Solgaard, and F. J. Giessibl. Higher harmonics and time-varying forces in dynamic force microscopy. In B. Bhushan, editor, *Springer Handbook of Nanotechnology*, pages 711–729. Springer Berlin Heidelberg, 2010. doi:10.1007/978-3-642-02525-9_25.

[66] R. W. Stark. Spectroscopy of higher harmonics in dynamic atomic force microscopy. *Nanotechnology*, 15(3):347–351, 2004. doi:10.1088/0957-4484/15/3/020.

[67] N. F. Martinez, J. R. Lozano, E. T. Herruzo, F. Garcia, C. Richter, T. Sulzbach, and R. Garcia. Bimodal atomic force microscopy imaging of isolated antibodies in air and liquids. *Nanotechnology*, 19(38):384011, 2008. doi:10.1088/0957-4484/19/38/384011.

[68] S. D. Solares and G. Chawla. Frequency response of higher cantilever eigenmodes in bimodal and trimodal tapping mode atomic force microscopy. *Measurement Science and Technology*, 21(12):125502, 2010. doi:10.1088/0957-0233/21/12/125502.

[69] D. Ebeling and S. D. Solares. Amplitude modulation dynamic force microscopy imaging in liquids with atomic resolution: comparison of phase contrasts in single and dual mode operation. *Nanotechnology*, 24(13):135702, 2013. doi:10.1088/0957-4484/24/13/135702.

[70] G. Chawla and S. D. Solares. Single-cantilever dual-frequency-modulation atomic force microscopy. *Measurement Science and Technology*, 20(1):015501, 2009. doi:10.1088/0957-0233/20/1/015501.

[71] R. Proksch. Multifrequency, repulsive-mode amplitude-modulated atomic force microscopy. *Applied Physics Letters*, 89(11):113121, 2006. `doi:10.1063/1.2345593`.

[72] N. F. Martinez, S. Patil, J. R. Lozano, and R. Garcia. Enhanced compositional sensitivity in atomic force microscopy by the excitation of the first two flexural modes. *Applied Physics Letters*, 89(15):153115, 2006. `doi:10.1063/1.2360894`.

[73] A. Schuh, I. S. Bozchalooi, I. W. Rangelow, and K. Youcef-toumi. Multi-eigenmode control for high material contrast in bimodal and higher harmonic atomic force microscopy. *Nanotechnology*, 26(23):235706, 2015. ©2015 IOP Publishing, Reprinted with permission. `doi:10.1088/0957-4484/26/23/235706`.

[74] A. Schuh, I. S. Bozchalooi, I. W. Rangelow, and K. Youcef-toumi. Estimator based multi-eigenmode control of cantilevers in multifrequency atomic force microscopy. In *2015 American Control Conference (ACC)*, pages 1905–1910. ©2015 IEEE, Reprinted with permission. `doi:10.1109/ACC.2015.7171011`.

[75] A. Schuh, M. Hofer, T. Ivanov, and I. W. Rangelow. Active microcantilevers for high material contrast in harmonic atomic force microscopy. *Journal of Microelectromechanical Systems*, 24(5):1622–1631, 2015. ©2015 IEEE, Reprinted with permission. `doi:10.1109/JMEMS.2015.2428677`.

[76] J. E. Sader and L. White. Theoretical analysis of the static deflection of plates for atomic force microscope applications. *Journal of Applied Physics*, 74(1), 1993. `doi:10.1063/1.354137`.

[77] H. Butt, B. Cappella, and M. Kappl. Force measurements with the atomic force microscope: Technique, interpretation and applications. *Surface Science Reports*, 59(1-6):1–152, 2005. `doi:10.1016/j.surfrep.2005.08.003`.

[78] F. J. Giessibl. Advances in atomic force microscopy. *Reviews of Modern Physics*, 75(3):949–983, 2003. `doi:http://dx.doi.org/10.1103/RevModPhys.75.949`.

[79] Anthony C. Fischer-Cripps. *Nanoindentation*. Springer Science+Business Media, LLC, Springer New York Dordrecht Heidelberg London, 2011. `doi:10.1007/978-1-4419-9872-9`.

[80] A. Kuehle, A. H. Sorensen, and J. Bohr. Role of attractive forces in tapping tip force microscopy. *Journal of Applied Physics*, 81(10):6562, 1997. `doi:10.1063/1.365194`.

[81] A. Checco, Y. Cai, O. Gang, and B. M. Ocko. High resolution non-contact afm imaging of liquids condensed onto chemically nanopatterned surfaces. *Ultramicroscopy*, 106(8-9):703–8, 2005. `doi:10.1016/j.ultramic.2005.11.009`.

[82] G. Couturier, R. Boisgard, L. Nony, and J. P. Aime. Noncontact atomic force microscopy: Stability criterion and dynamical responses of the shift of frequency and damping signal. *The Review of scientific instruments*, 74(5):2726, 2003. `doi:10.1063/1.1564274`.

[83] G. Couturier, R. Boisgard, D. Dietzel, and J. P. Aime. Damping and instability in non-contact atomic force microscopy: the contribution of the instrument. *Nanotechnology*, 16(8):1346–1353, 2005. `doi:10.1088/0957-4484/16/8/061`.

[84] F. Giessibl, Y. Sugawara, S. Morita, H. Hosoi, K. Sueoka, K. Mukasa, A. Sasahara, and H. Onishi. Noncontact atomic force microscopy and related topics. In B. Bhushan, editor, *Springer Handbook of Nanotechnology*, pages 651–678. Springer Berlin Heidelberg, Berlin and Heidelberg, 2007. `doi:10.1007/978-3-540-29857-1\_24`.

[85] P. K. Hansma, J. P. Cleveland, M. Radmacher, D. A. Walters, P. E. Hillner, M. Bezanilla, M. Fritz, D. Vie, H. G. Hansma, C. B. Prater, J. Massie, L. Fukunaga, J. Gurley, and V. Elings. Tapping mode atomic force microscopy in liquids. *Applied Physics Letters*, 64(13):1738–1740, 1994. `doi:10.1063/1.111795`.

[86] S. Santos, V. Barcons, J. Font, and N. H. Thomson. Cantilever dynamics in amplitude modulation afm: continuous and discontinuous transitions. *Journal of Physics D: Applied Physics*, 43(27):275401, 2010. `doi:10.1088/0022-3727/43/27/275401`.

[87] Prof. Dr. Ricardo García. *Amplitude Modulation Atomic Force Microscopy*. WILEY-VCH Verlag & Co. KGaA, Boschstr. 12, 69469 Weinheim, Germany, 1. edition, 2010.

[88] A. GarcSan Paulo. Dynamics of a vibrating tip near or in intermittent contact with a surface. *Physical Review B*, 61(20):R13381–R13384, 2000. `doi:10.1103/PhysRevB.61.R13381`.

[89] M. Hoummady and E. Farnault. Enhanced sensitivity to force gradients by using higher flexural modes of the atomic force microscope cantilever. *Applied Physics A: Materials Science & Processing*, 66(7):S361–S364, 1998. `doi:10.1007/s003390051164`.

[90] S. H. Crandall. The role of damping in vibration theory. *Journal of Sound and Vibration*, 11(1):3–18, 1970. `doi:10.1016/S0022-460X(70)80105-5`.

[91] A. Tofighi. The intrinsic damping of the fractional oscillator. *Physica A: Statistical Mechanics and its Applications*, 329(1-2):29–34, 2003. `doi:10.1016/S0378-4371(03)00598-3`.

[92] M. L. Meade. Advances in lock-in amplifiers. *Journal of Physics E: Scientific Instruments*, 15(4):395–403, 1982. `doi:10.1088/0022-3735/15/4/001`.

[93] O. El Rifai and K. Youcef-Toumi. Design and control of atomic force microscopes. *Proceedings of the 2003 American Control Conference, 2003*, pages 3714–3719, 2003. `doi:10.1109/ACC.2003.1240412`.

[94] T. Ando, N. Kodera, Y. Naito, T. Kinoshita, K. Furuta, and Y. Y. Toyoshima. A high-speed atomic force microscope for studying biological macromolecules in action. *Chemphyschem : a European journal of chemical physics and physical chemistry*, 4(11):1196–202, 2003. `doi:10.1002/cphc.200300795`.

[95] Y. K. Yong, Moheimani, S. O. R., B. J. Kenton, and K. K. Leang. Invited review article: High-speed flexure-guided nanopositioning: Mechanical design and control issues. *Review of Scientific Instruments*, 83(12):121101, 2012. `doi:10.1063/1.4765048`.

[96] G. M. Clayton, S. Tien, K. K. Leang, Q. Zou, and S. Devasia. A review of feedforward control approaches in nanopositioning for high-speed spm. *Journal of Dynamic Systems, Measurement, and Control*, 131(6):061101, 2009. `doi:10.1115/1.4000158`.

[97] T. Ando, T. Uchihashi, N. Kodera, D. Yamamoto, M. Taniguchi, A. Miyagi, and H. Yamashita. High-speed atomic force microscopy for observing dynamic biomolecular processes. *Journal of Molecular Recognition*, 20(6):448–458, 2007. `doi:10.1002/jmr`.

[98] A. Ahmad, A. Schuh, and I. W. Rangelow. Adaptive afm scan speed control for high aspect ratio fast structure tracking. *Review of Scientific Instruments*, 85:103706, 2014. `doi:10.1063/1.4897141`.

[99] T. De, P. Agarwal, D. Sahoo, and M. Salapaka. Real-time detection of probe loss in atomic force microscopy. *Applied Physics Letters*, 89(13):133119, 2009. `doi:10.1063/1.2357876`.

[100] T. Kowalewski and J. Legleiter. Imaging stability and average tip-sample force in tapping mode atomic force microscopy. *Journal of Applied Physics*, 99:064903, 2006. `doi:10.1063/1.2175473`.

[101] P. D. Ashby. Gentle imaging of soft materials in solution with amplitude modulation atomic force microscopy: Q control and thermal noise. *Applied Physics Letters*, 91(25):254102, 2007. `doi:10.1063/1.2824576`.

[102] Y. Jeong, G. R. Jayanth, S. Jhiang, and C. Menq. Direct tip-sample interaction force control for the dynamic mode atomic force microscopy. *Applied Physics Letters*, 88:204102, 2006. `doi:10.1063/1.2203958`.

[103] W. E. Baker, W. E. Woolam, and D. Young. Air and internal damping of thin cantilever beams. *International Journal of Mechanical Sciences*, 9(11):743–766, 1967. `doi:10.1016/0020-7403(67)90032-X`.

[104] F. Zypman. Internal damping for noncontact atomic force microscopy cantilevers. *Journal of Vacuum Science & Technology B: Microelectronics and Nanometer Structures*, 28(March):C4E24, 2010. `doi:10.1116/1.3374736`.

[105] J. Dorignac, A. Kalinowski, S. Erramilli, and P. Mohanty. Dynamical response of nanomechanical oscillators in immiscible viscous fluid for in vitro biomolecular recognition. *Physical Review Letters*, 96(18):1–4, 2006. `doi:10.1103/PhysRevLett.96.186105`.

[106] H. Hosaka and K. Itao. Theoretical and experimental study on airflow damping of vibrating microcantilevers. *Journal of Vibration and Acoustics*, 121(1):64–69, 1999. `doi:10.1115/1.2893949`.

[107] A. T. Jones. Vibration of beams immersed in a liquid. *Experimental Mechanics*, 10(2):84–88, 1970. `doi:10.1007/BF02320137`.

[108] D. Niu, Y. Chen, and W. Huang. Dynamics of an atomic force microscope probe in liquid investigated via three-dimensional mode. *Measurement Science and Technology*, 21(10):105503, 2010. `doi:10.1088/0957-0233/21/10/105503`.

[109] J. Sader. Frequency response of cantilever beams immersed in viscous fluids with applications to the atomic force microscope. *Journal of Applied Physics*, 84(64), 1998. `doi:10.1063/1.368002`.

[110] M. Martin, B. Houston, J. Baldwin, and M. Zalalutdinov. Damping models for microcantilevers, bridges, and torsional resonators in the free-molecular-flow regime. *Journal of Microelectromechanical Systems*, 17(2):503–511, 2008. `doi:10.1109/JMEMS.2008.916321`.

[111] C. Bergaud, L. Nicu, and A. Martinez. Multi-mode air damping analysis of composite cantilever beams. *Jpn. J. Appl. Phys., Part 1*, 38(11):6521–6525, 1999.

[112] D. Kiracofe and A. Raman. On eigenmodes, stiffness, and sensitivity of atomic force microscope cantilevers in air versus liquids. *Journal of Applied Physics*, 107(3):033506, 2010. `doi:10.1063/1.3284206`.

[113] S. M. Han, H. Benaroya, and T. Wei. Dynamics of transversely vibrating beams using four engineering theories. *Journal of Sound and Vibration*, 225(5):935–988, 1999. `doi:10.1006/jsvi.1999.2257`.

[114] O. J. Aldraihem, R. C. Wetherhold, and T. Singh. Intelligent beam structures: Timoshenko theory vs. euler-bernoulli theory. In *Proceedings of the 1996 IEEE International Conference on Control Applications*, pages 976–981. IEEE. `doi:10.1109/CCA.1996.559047`.

[115] J. Claeyssen. The timoshenko beam model in vibrating afm cantilevers. In *DINCON'10 Proceedings of the 9th Brazilian Conference on Dynamics Control and their Applications*, pages 60–70, 2010.

[116] J. M. Dietl, A. M. Wickenheiser, and E. Garcia. A timoshenko beam model for cantilevered piezoelectric energy harvesters. *Smart Materials and Structures*, 19(5):055018, 2010. `doi:10.1088/0964-1726/19/5/055018`.

[117] N. Ganesan and R. C. Engels. Timoshenko beam finite elements using the assumed modes method. *Journal of Sound and Vibration*, 156(1):109–123, 1992. `doi:10.1016/0022-460X(92)90815-F`.

[118] T. Kaneko. On timoshenko‘s correction for shear in vibrating beams. *Journal of Physics D: Applied Physics*, 8(16):1927, 1975. `doi:10.1088/0022-3727/8/16/003`.

[119] P. RUGE and C. BIRK. A comparison of infinite timoshenko and euler–bernoulli beam models on winkler foundation in the frequency- and time-domain. *Journal of Sound and Vibration*, 304(3-5):932–947, 2007. `doi:10.1016/j.jsv.2007.04.001`.

[120] L. Zietsman. A timoshenko beam with tip body and boundary damping. *Wave Motion*, 39(3):199–211, 2004. `doi:10.1016/j.wavemoti.2003.08.003`.

[121] J.-C. Hsu, H.-L. Lee, and W.-J. Chang. Flexural vibration frequency of atomic force microscope cantilevers using the timoshenko beam model. *Nanotechnology*, 18(28):285503, 2007. `doi:10.1088/0957-4484/18/28/285503`.

[122] R. W. Traill-Nash and a. R. Collar. the effects of shear flexibility and rotatory inertia on the bending vibrations of beams. *The Quarterly Journal of Mechanics and Applied Mathematics*, 6(2):186–222, 1953. `doi:10.1093/qjmam/6.2.186`.

[123] T. Kaneko. An experimental study of the timoshenko's shear coefficient for flexurally vibrating beams. *Journal of Physics D: Applied Physics*, 11(14):1979–1988, 1978. `doi:10.1088/0022-3727/11/14/010`.

[124] U. Rabe, K. Janser, and W. Arnold. Vibrations of free and surface-coupled atomic force microscope cantilevers: Theory and experiment. *Review of Scientific Instruments*, 67(9):3281, 1996. `doi:10.1063/1.1147409`.

[125] Y. Zhang and Y.-p. Zhao. An effective method of determining the residual stress gradients in a micro-cantilever. *Microsystem Technologies*, 12(4):357–364, 2005. `doi:10.1007/s00542-005-0065-z`.

[126] Y. Zhang, Q. Ren, and Y.-p. Zhao. Modelling analysis of surface stress on a rectangular cantilever beam. *Journal of Physics D: Applied Physics*, 37(15):2140–2145, 2004. `doi:10.1088/0022-3727/37/15/014`.

[127] G. Y. Chen, T. Thundat, E. A. Wachter, and R. J. Warmack. Adsorption-induced surface stress and its effects on resonance frequency of microcantilevers. *Journal of Applied Physics*, 77(8):3618, 1995. `doi:10.1063/1.359562`.

[128] Q. Ren and Y.-P. Zhao. Influence of surface stress on frequency of microcantilever-based biosensors. *Microsystem Technologies*, 10(4):307–314, 2004. `doi:10.1007/s00542-003-0329-4`.

[129] J. E. Sader. Surface stress induced deflections of cantilever plates with applications to the atomic force microscope: Rectangular plates. *Journal of Applied Physics*, 89(5):2911, 2001. `doi:10.1063/1.1342018`.

[130] C. L. Dym and I. H. Shames. *Solid Mechanics: A Variational Approach, Augmented Edition*. Springer, April 5, 2013 (2013 edition).

[131] P. Laura and P. Deirassar. Vibrations of a beam fixed at one end and carrying a guided mass at the other. *Applied Acoustics*, 14(2):93–99, 1981. `doi:10.1016/0003-682X(81)90011-6`.

[132] D. K. Miu. Physical interpretation of transfer function zeros for simple control systems with mechanical flexibilities. *Journal of Dynamic Systems, Measurement, and Control*, 113(3):419, 1991. `doi:10.1115/1.2896426`.

[133] T. Rodriguez and R. Garcia. Tip motion in amplitude modulation (tapping-mode) atomic-force microscopy: Comparison between continuous and point-mass models. *Applied Physics Letters*, 80(9):1646, 2002. `doi:10.1063/1.1456543`.

[134] A. Raman, J. Melcher, and R. Tung. Cantilever dynamics in atomic force microscopy. *nanotoday*, 3(1):20–27, 2008. `doi:10.1016/S1748-0132(08)70012-4`.

[135] S.-H. Tsai and H.-C. Kan. Mathematical analysis on a model for the rectangular cantilever beam. *Journal of Physics D: Applied Physics*, 40(19):6129–6137, 2007. `doi:10.1088/0022-3727/40/19/055`.

[136] J. E. Sader. Parallel beam approximation for v-shaped atomic force microscope cantilevers. *Review of Scientific Instruments*, 66(9):4583, 1995. `doi:10.1063/1.1145292`.

[137] F. J. Rubio-Sierra, R. Vazquez, and R. W. Stark. Transfer function analysis of the micro cantilever used in atomic force microscopy. *IEEE Transactions On Nanotechnology*, 5(6):692–700, 2006. `doi:10.1109/TNANO.2006.883479`.

[138] T. Lam and R. Darling. Physical modeling of mems cantilever beams and the measurement of stiction force. *Journal of Modeling and Simulation of Microsystems*, 4:418–421, 2001.

[139] S. O. Abetkovskaya and S. a. Chizhik. Model of motion of the probe of an atomic-force microscope in the semicontact regime. *Journal of Engineering Physics and Thermophysics*, 80(2):395–402, 2007. `doi:10.1007/s10891-007-0052-6`.

[140] R. Curtain and K. Morris. Transfer functions of distributed parameter systems: A tutorial. *Automatica*, 45(5):1101–1116, 2009. `doi:10.1016/j.automatica.2009.01.008`.

[141] H. Dankowicz. Nonlinear dynamics as an essential tool for non-destructive characterization of soft nanostructures using tapping-mode atomic force microscopy. *Philosophical transactions. Series A, Mathematical, physical, and engineering sciences*, 364(1849):3505–20, 2006. `doi:10.1098/rsta.2006.1907`.

[142] M. Gauthier, R. Pérez, T. Arai, M. Tomitori, and M. Tsukada. Interplay between nonlinearity, scan speed, damping, and electronics in frequency modulation atomic-force microscopy. *Physical Review Letters*, 89(14):1–4, 2002. `doi:10.1103/PhysRevLett.89.146104`.

[143] M. Tortonese, R. C. Barrett, and C. F. Quate. Atomic resolution with an atomic force microscope using piezoresistive detection. *Applied Physics Letters*, 62(8):834, 1993. `doi:10.1063/1.108593`.

[144] T. Ivanov. *Piezoresistive cantilever with an integrated bimorph actuator*. PhD thesis, University of Kassel, Kassel, 2004.

[145] T. E. Schäffer. Calculation of thermal noise in an atomic force microscope with a finite optical spot size. *Nanotechnology*, 16(6):664–670, 2005. `doi:10.1088/0957-4484/16/6/007`.

[146] M. V. Salapaka, H. S. Bergh, J. Lai, A. Majumdar, and E. McFarland. Multi-mode noise analysis of cantilevers for scanning probe microscopy. *Journal of Applied Physics*, 81(6):2480, 1997. `doi:10.1063/1.363955`.

[147] R. E. Kalman. A new approach to linear filtering and prediction problems. *Journal of Basic Engineering*, 82(1):35–45, 1960. `doi:doi:10.1115/1.3662552`.

[148] M. Stark, R. Guckenberger, A. Stemmer, and R. Stark. Estimating the transfer function of the cantilever in atomic force microscopy: A system identification approach. *Journal of Applied Physics*, 98:114904, 2005. `doi:10.1063/1.2137887`.

[149] P. Agarwal and M. V. Salapaka. Real time estimation of equivalent cantilever parameters in tapping mode atomic force microscopy. *Applied Physics Letters*, 95(8):083113, 2009. `doi:10.1063/1.3206740`.

[150] L. Ljung. Perspectives on system identification. *Annual Reviews in Control*, 34(1):1–12, 2010. `doi:10.1016/j.arcontrol.2009.12.001`.

[151] L. Lennart. *System Identification: Theory for the User*. Prentice Hall, 2nd edition, 1999.

[152] N. a. Burnham. Comparison of calibration methods for atomic-force microscopy cantilevers. *Nanotechnology*, 3009(1):53–6, 2002. `doi:10.1088/0957-4484/14/1/301`.

[153] J. P. Cleveland, S. Manne, D. Bocek, and P. K. Hansma. A nondestructive method for determining the spring constant of cantilevers for scanning force microscopy. *The Review of Scientific Instruments*, 64(2):403–405, 1993. `doi:10.1063/1.1144209`.

[154] C. Clifford and M. Seah. Improved methods and uncertainty analysis in the calibration of the spring constant of an atomic force microscope cantilever using static experimental methods. *Measurement Science and Technology*, 20:125501, 2009. `doi:10.1088/0957-0233/20/12/125501`.

[155] G. V. Lubarsky and G. Hähner. Calibration of the normal spring constant of microcantilevers in a parallel fluid flow. *The Review of scientific instruments*, 78(9):095102, 2007. `doi:10.1063/1.2782792`.

[156] G. V. Lubarsky and G. Hähner. Hydrodynamic methods for calibrating the normal spring constant of microcantilevers. *Nanotechnology*, 19(32):325707, 2008. `doi:10.1088/0957-4484/19/32/325707`.

[157] M. Poggi, A. McFarland, J. Colton, and L. Bottomley. A method for calculating the spring constant of atomic force microscopy cantilevers with a nonrectangular cross section. *Analytical Chemistry*, 77(4):1192–1195, 2005. `doi:10.1021/ac048828h`.

[158] J. Sader, J. Chon, and P. Mulvaney. Calibration of rectangular atomic force microscope cantilevers. *Review of Scientific Instruments*, 70(10):3967–3969, 1999. `doi:10.1063/1.1150021`.

[159] Z. C. Ying, M. G. Reitsma, and R. S. Gates. Direct measurement of cantilever spring constants and correction for cantilever irregularities using an instrumented indenter. *The Review of scientific instruments*, 78(6):063708, 2007. `doi:10.1063/1.2747095`.

[160] J. Melcher, S. Hu, and A. Raman. Equivalent point-mass models of continuous atomic force microscope probes. *Applied Physics Letters*, 91(5):053101, 2007. `doi:10.1063/1.2767173`.

[161] G. Hähner. Normal spring constants of cantilever plates for different load distributions and static deflection with applications to atomic force microscopy. *Journal of Applied Physics*, 104(8):084902, 2008. `doi:10.1063/1.3000055`.

[162] G. Hähner. Dynamic spring constants for higher flexural modes of cantilever plates with applications to atomic force microscopy. *Ultramicroscopy*, 110(7):801–6, 2010. `doi:10.1016/j.ultramic.2010.02.008`.

[163] Y. M. Tseytlin. Atomic force microscope cantilever spring constant evaluation for higher mode oscillations: a kinetostatic method. *Review of Scientific Instruments*, 79(2):025102, 2008. `doi:10.1063/1.2839019`.

[164] G. F. Franklin, J. D. Powell, and A. Emami-Naeini. *Feedback control of dynamic systems*. Pearson, 6th edition, 2010.

[165] D. Ebeling and H. Hölscher. Analysis of the constant-excitation mode in frequency-modulation atomic force microscopy with active q-control applied in ambient conditions and liquids. *Journal of Applied Physics*, 102(11):114310, 2007. `doi:10.1063/1.2817952`.

[166] H. Hölscher, D. Ebeling, and U. D. Schwarz. Theory of q-controlled dynamic force microscopy in air. *Journal of Applied Physics*, 99:084311, 2006. `doi:10.1063/1.2190070`.

[167] N. Kobayashi, Y. J. Li, Y. Naitoh, M. Kageshima, and Y. Sugawara. Theoretical investigation on force sensitivity in q-controlled phase-modulation atomic force microscopy in constant-amplitude mode. *Journal of Applied Physics*, 103(5):054305, 2008. `doi:10.1063/1.2890380`.

[168] J. Kokavecz, Z. L. Horvath, and A. Mechler. Dynamical properties of the q-controlled atomic force microscope. *Applied Physics Letters*, 85(15):3232, 2004. `doi:10.1063/1.1785863`.

[169] D. R. Sahoo, T. d. Murti, and V. Salapaka. Observer based imaging methods for atomic force microscopy. In *44th IEEE Conference on Decision and Control*, pages 1185–1190, 12-15 Dec. 2005. `doi:10.1109/CDC.2005.1582319`.

[170] B. Friedland. *Control system design: An introduction to state-space methods*. Dover Publications, 1st edition, March 24, 2005.

[171] R. E. Kalman and R. S. Bucy. New results in linear filtering and prediction theory. *Journal of Basic Engineering*, 83(1):95, 1961. `doi:10.1115/1.3658902`.

[172] K. Cho, N. Hori, and J. Angeles. On the controllability and observability of flexible beams under rigid-body motion. *Proceedings IECON '91: 1991 International Conference on Industrial Electronics, Control and Instrumentation*, pages 455–460, 1991. `doi:10.1109/IECON.1991.239342`.

[173] J. Respondek. In *Observability of 4th order dynamical systems*. 8th WSEAS International Conference on Simulation, Modelling and Optimization (SMO '08), 2008.

[174] A. V. Oppenheim, R. W. Schafer, and J. R. Buck. *Discrete-time signal processing*. Prentice-Hall Signal Processing Series. Prentice Hall, 2nd edition, 1999.

[175] T. Ould Bachir and J.-P. David. Fpga-based real-time simulation of state-space models using floating-point cores. In *14th International Power Electronics*, volume 2010, pages S2–26–S2–31. `doi:10.1109/EPEPEMC.2010.5606584`.

[176] S. Basak and A. Raman. Dynamics of tapping mode atomic force microscopy in liquids: Theory and experiments. *Applied Physics Letters*, 91(6):064107, 2007. `doi:10.1063/1.2760175`.

[177] P. J. James, M. Antognozzi, J. Tamayo, T. J. McMaster, J. M. Newton, and M. J. Miles. Interpretation of contrast in tapping mode afm and shear force microscopy. a study of nafion. *Langmuir*, 17(2):349–360, 2001. `doi:10.1021/la000332h`.

[178] S. N. Magonov, V. Elings, and M.-H. Whangbo. Phase imaging and stiffness in tapping-mode atomic force microscopy. *Surface Science*, 375(2-3):L385–L391, 1997. `doi:10.1016/S0039-6028(96)01591-9`.

[179] N. F. Martinez and R. Garcia. Measuring phase shifts and energy dissipation with amplitude modulation atomic force microscopy. *Nanotechnology*, 17(7):S167–S172, 2006. `doi:10.1088/0957-4484/17/7/S11`.

[180] S. Crittenden, A. Raman, and R. Reifenberger. Probing attractive forces at the nanoscale using higher-harmonic dynamic force microscopy. *Physical Review B*, 72(23):1–13, 2005. `doi:10.1103/PhysRevB.72.235422`.

[181] R. W. Stark, G. Schitter, M. Stark, R. Guckenberger, and A. Stemmer. State-space model of freely vibrating and surface-coupled cantilever dynamics in atomic force microscopy. *Physical Review B*, 69(8):85412, 2004. `doi:10.1103/PhysRevB.69.085412`.

[182] L. Yuan, Q. Jian-Qiang, and L. Ying-Zi. Theory of higher harmonics imaging in tapping-mode atomic force microscopy. *Chinese Physics B*, 19(5):050701, 2010. `doi:10.1088/1674-1056/19/5/050701`.

[183] T. R. Rodriguez and R. Garcia. Compositional mapping of surfaces in atomic force microscopy by excitation of the second normal mode of the microcantilever. *Applied Physics Letters*, 84(3):449, 2004. `doi:10.1063/1.1642273`.

[184] S. D. Solares and G. Chawla. Triple-frequency intermittent contact atomic force microscopy characterization: Simultaneous topographical, phase, and frequency shift contrast in ambient air. *Journal of Applied Physics*, 108(5):054901, 2010. `doi:10.1063/1.3475644`.

[185] Y. Sugimoto, S. Innami, M. Abe, Ó. Custance, and S. Morita. Dynamic force spectroscopy using cantilever higher flexural modes. *Applied Physics Letters*, 91:093120, 2007. `doi:10.1063/1.2775806`.

[186] D. Platz, E. a. Tholen, D. Pesen, and D. B. Haviland. Intermodulation atomic force microscopy. *Applied Physics Letters*, 92(15):153106, 2008. `doi:10.1063/1.2909569`.

[187] B. J. Rodriguez, C. Callahan, S. V. Kalinin, and R. Proksch. Dual-frequency resonance-tracking atomic force microscopy. *Nanotechnology*, 18(47):475504, 2007. `doi:10.1088/0957-4484/18/47/475504`.

[188] R. W. Stark and W. M. Heckl. Higher harmonics imaging in tapping-mode atomic-force microscopy. *Review of Scientific Instruments*, 74(12):5111, 2003. `doi:10.1063/1.1626008`.

[189] R. Hillenbrand, M. Stark, and R. Guckenberger. Higher-harmonics generation in tapping-mode atomic-force microscopy: Insights into the tip–sample interaction. *Applied Physics Letters*, 76(23):3478, 2000. `doi:10.1063/1.126683`.

[190] R. W. Stark and W. M. Heckl. Fourier transformed atomic force microscopy: tapping mode atomic force microscopy beyond the hookian approximation. *Surface Science*, 457(1-2):219–228, 2000. `doi:10.1016/S0039-6028(00)00378-2`.

[191] M. Stark, R. W. Stark, W. M. Heckl, and R. Guckenberger. Spectroscopy of the anharmonic cantilever oscillations in tapping-mode atomic-force microscopy. *Applied Physics Letters*, 77(20):3, 2000. doi:10.1063/1.1325404.

[192] J. Preiner, J. Tang, V. Pastushenko, and P. Hinterdorfer. Higher harmonic atomic force microscopy: Imaging of biological membranes in liquid. *Physical Review Letters*, 99(4), 2007. doi:10.1103/PhysRevLett.99.046102.

[193] M. Kaestner, T. Ivanov, A. Schuh, A. Ahmad, T. Angelov, Y. Krivoshapkina, M. Budden, M. Hofer, S. Lenk, J.-P. Zoellner, I. W. Rangelow, A. Reum, E. Guliyev, M. Holz, and N. Nikolov. Scanning probes in nanostructure fabrication. *Journal of Vacuum Science & Technology B, Nanotechnology and Microelectronics: Materials, Processing, Measurement, and Phenomena*, 32(6):06F101, 2014. doi:10.1116/1.4897500.

[194] G. E. Fantner, W. Schumann, R. J. Barbero, A. Deutschinger, V. Todorov, D. S. Gray, A. M. Belcher, I. W. Rangelow, and K. Youcef-Toumi. Use of self-actuating and self-sensing cantilevers for imaging biological samples in fluid. *Nanotechnology*, 20(43):434003, 2009. doi:10.1088/0957-4484/20/43/434003.

[195] I. W. Rangelow, S. Skocki, and P. Dumania. Plasma etching for micromechanical sensor applications. *Microelectronic Engineering*, 23(1-4):365–368, 1994. doi:10.1016/0167-9317(94)90174-0.

[196] Y. Kanda. A graphical representation of the piezoresistance coefficients in silicon. *IEEE Transactions on Electron Devices*, 29(1):64–70, 1982. doi:10.1109/T-ED.1982.20659.

[197] A. A. Barlian, W.-T. Park, J. R. Mallon, A. J. Rastegar, and B. L. Pruitt. Review: Semiconductor piezoresistance for microsystems. *Proceedings of the IEEE. Institute of Electrical and Electronics Engineers*, 97(3):513–552, 2009. doi:10.1109/JPROC.2009.2013612.

[198] G. Jozwiak, D. Kopiec, J. Radojewski, W. Majstrzyk, P. Slupski, P. Zawierucha, T. Gotszalk, Y. Sarov, T. Ivanov, and I. W. Rangelow. Comprehensive measurement system for calibration and investigation of cantilever mems devices with integrated actuator and deflection sensor. *Submitted*, 2014.

[199] T. Ivanov, T. Gotszalk, T. Sulzbach, and I. W. Rangelow. Quantum size aspects of the piezoresistive effect in ultra thin piezoresistors. *Ultramicroscopy*, 97(1-4):377–384, 2003. doi:10.1016/S0304-3991(03)00064-0.

[200] I. W. Rangelow. Critical tasks in high aspect ratio silicon dry etching for microelectromechanical systems. *Journal of Vacuum Science & Technology A: Vacuum, Surfaces, and Films*, 21(4):1550, 2003. doi:10.1116/1.1580488.

[201] G. Jóźwiak, D. Kopiec, P. Zawierucha, T. Gotszalk, P. Janus, P. Grabiec, and I. W. Rangelow. The spring constant calibration of the piezoresistive cantilever based biosensor. *Sensors and Actuators B: Chemical*, 170:201–206, 2012. doi:10.1016/j.snb.2012.02.007.

[202] G. F. Franklin, J. D. Powell, and M. L. Workman. *Digital control of dynamic systems*. Addison-Wesley, Menlo Park, California, 3rd edition, December 29, 1997.

[203] M. G. Ruppert, M. W. Fairbairn, and Moheimani, S. O. R. Multi-mode resonant control of a microcantilever for atomic force microscopy. In *2013 IEEE/ASME International Conference on Advanced Intelligent Mechatronics (AIM)*, pages 77–82. `doi:10.1109/AIM.2013.6584071`.

[204] J. Kokavecz, O. Marti, P. Heszler, and A. Mechler. Imaging bandwidth of the tapping mode atomic force microscope probe. *Physical Review B*, 73(15):155403, 2006. `doi:10.1103/PhysRevB.73.155403`.

[205] M. Balantekin and A. Atalar. Enhancing higher harmonics of a tapping cantilever by excitation at a submultiple of its resonance frequency. *Physical Review B*, 71(12), 2005. `doi:10.1103/PhysRevB.71.125416`.

[206] K. S. Karvinen and Moheimani, S. O. R. Control of the higher eigenmodes of a microcantilever: applications in atomic force microscopy. *Ultramicroscopy*, 137:66–71, 2014. `doi:10.1016/j.ultramic.2013.11.011`.

[207] S. Li, J. Li, Y. Mo, and R. Zhao. Composite multi-modal vibration control for a stiffened plate using non-collocated acceleration sensor and piezoelectric actuator. *Smart Materials and Structures*, 23(1):015006, 2014. `doi:10.1088/0964-1726/23/1/015006`.

[208] V. Sethi and Gangbing Song. Multimodal vibration control of a flexible structure using piezoceramic sensor and actuator. *Journal of Intelligent Material Systems and Structures*, 19(5):573–582, 2007. `doi:10.1177/1045389X07077853`.

[209] V. Sethi. Optimal vibration control of a model frame structure using piezoceramic sensors and actuators. *Journal of Vibration and Control*, 11(5):671–684, 2005. `doi:10.1177/1077546305053396`.

[210] K. O. Prakah-Asante and K. C. Craig. The application of multi-channel design methods for vibration control of an active structure. *Smart Materials and Structures*, 3(3):329–343, 1994. `doi:10.1088/0964-1726/3/3/009`.

[211] W. S. Lee, H. J. Lee, J. H. Hwang, N. K. Lee, G. A. Lee, S. M. Bae, and D. M. Kim. An experimental study on multi-mode control methods of flexible structure using pzt actuator and modified imsc algorithm. *Intelligent Control and Automation, Volume 344 of the series Lecture Notes in Control and Information Sciences*, pages 486–493, 2006.

[212] C.-K. Lee and F. C. Moon. Modal sensors/actuators. *Journal of Applied Mechanics*, 57(2):434, 1990. `doi:10.1115/1.2892008`.

[213] C.-Q. Chen and Y.-P. Shen. Optimal control of active structures with piezoelectric modal sensors and actuators. *Smart Materials and Structures*, 6(4):403–409, 1997. `doi:10.1088/0964-1726/6/4/003`.

[214] D. Kiracofe, A. Raman, and D. Yablon. Multiple regimes of operation in bimodal afm: understanding the energy of cantilever eigenmodes. *Beilstein journal of nanotechnology*, 4:385–393, 2013. `doi:10.3762/bjnano.4.45`.

[215] F. Blais and M. Rioux. Real-time numerical peak detector. *Signal Processing*, 11(2):145–155, 1986. `doi:10.1016/0165-1684(86)90033-2`.

[216] J. Kokavecz, Z. Tóth, Z. L. Horváth, P. Heszler, and A. Mechler. Novel amplitude and frequency demodulation algorithm for a virtual dynamic atomic force microscope. *Nanotechnology*, 17(7):S173–7, 2006. `doi:10.1088/0957-4484/17/7/S12`.

[217] K. S. Karvinen and Moheimani, S O R. A high-bandwidth amplitude estimation technique for dynamic mode atomic force microscopy. *The Review of scientific instruments*, 85(2):023707, 2014. `doi:10.1063/1.4865841`.

[218] O. Sahin, G. Yaralioglu, R. Grow, S. F. Zappe, A. Atalar, C. Quate, and O. Solgaard. High-resolution imaging of elastic properties using harmonic cantilevers. *Sensors and Actuators A: Physical*, 114(2-3):183–190, 2004. `doi:10.1016/j.sna.2003.11.031`.

[219] O. Sahin, C. Quate, O. Solgaard, and A. Atalar. Resonant harmonic response in tapping-mode atomic force microscopy. *Physical Review B*, 69(16), 2004. `doi:10.1103/PhysRevB.69.165416`.

[220] O. Sahin, S. Magonov, C. Su, C. F. Quate, and O. Solgaard. An atomic force microscope tip designed to measure time-varying nanomechanical forces. *Nature nanotechnology*, 2(8):507–514, 2007. `doi:10.1038/nnano.2007.226`.

[221] G. Rinaldi, M. Packirisamy, and I. Stiharu. Frequency tuning afm optical levers using a slot. *Microsystem Technologies*, 14(3):361–369, 2008. `doi:10.1007/s00542-007-0456-4`.

[222] Gino Rinaldi, Muthukumaran Packirisamy, Ion Stiharu. Tuning the dynamic behaviour of cantilever mems based sensors and actuators. *Sensor Review*, 27(2):9, 2007. `doi:10.1108/02602280710731704`.

[223] H. Li, Y. Chen, and L. Dai. Concentrated-mass cantilever enhances multiple harmonics in tapping-mode atomic force microscopy. *Applied Physics Letters*, 92(15):151903, 2008. `doi:10.1063/1.2909535`.

[224] S. Sadewasser, G. Villanueva, and J. A. Plaza. Special cantilever geometry for the access of higher oscillation modes in atomic force microscopy. *Applied Physics Letters*, 89(3):033106, 2006. `doi:10.1063/1.2226993`.

[225] S. Dohn, R. Sandberg, W. Svendsen, and A. Boisen. Enhanced functionality of cantilever based mass sensors using higher modes. *Applied Physics Letters*, 86(23):233501, 2005. `doi:10.1063/1.1948521`.

[226] A. Perez-Cruz, A. Dominguez-Gonzalez, I. Stiharu, and R. A. Osornio-Rios. Optimization of q-factor of afm cantilevers using genetic algorithms. *Ultramicroscopy*, 115:61–67, 2012. `doi:10.1016/j.ultramic.2012.01.014`.

VHDL Code of Compensator FPGA Core

In this attachment the VHDL code of the compensator core functionality with its state machine is presented as an example, according to the *Slow Loop* in Figure 5.13 on page 85 of Chapter 5.

```
---------------------------------------------------------
-- Company: MIT/TUI
-- Engineer: Andreas Schuh
--
-- Create Date:    20:14:04 02/07/2013
-- Design Name:    Multi-eigenmode Compensator -
     Statemachine
-- Module Name:    Statemachine - Behavioral
-- Project Name:   Multi-eigenmode Compensator
-- Target Devices: Spartan 3A DSP
-- Tool versions:  XILINX ISE 14
-- Description:    Core for computing compensator
     iterations
-- Revision: 1
-- Additional Comments:
--------------------------------------------------------
library IEEE;
use IEEE.STD_LOGIC_1164.ALL;

--ENTITY
entity SystemID is
Port(
        ADC1in : in  STD_LOGIC_VECTOR (31 downto 0);
        ADC2in : in  STD_LOGIC_VECTOR (31 downto 0);
        DAC1out : out  STD_LOGIC_VECTOR (31 downto 0);
        DAC2out : out  STD_LOGIC_VECTOR (31 downto 0);
        clock : in  STD_LOGIC );
end SystemID;

-- ARCHITECTURE
architecture Behavioral of SystemID is

------------------------------------
-- DECLARE COMPENSATOR COEFFICIENTS
------------------------------------
constant a11 : std_logic_vector :=
     "00111111011111101000001010110010";
constant a12 : std_logic_vector :=
     "00111101110110001001011101011111";
constant a21 : std_logic_vector :=
     "10111101110110001001011101011111";
constant a22 : std_logic_vector :=
     "00111111011111101000001010110010";
constant a33 : std_logic_vector :=
     "00111111010011110100100101011111";
constant a34 : std_logic_vector :=
     "00111111000101011100110100100011";
constant a43 : std_logic_vector :=
     "10111111000101011100110100100011";
constant a44 : std_logic_vector :=
     "00111111010011110100100101011111";
constant b1 : std_logic_vector :=
     "10111011100101011111001010000110";
constant b2 : std_logic_vector :=
     "00111100010101100110011000100000";
constant b3 : std_logic_vector :=
     "10111011011001000111010100110001";
constant b4 : std_logic_vector :=
     "10111100110010111000011111101011";
constant c1 : std_logic_vector :=
     "00111100010101100010100101100000";
constant c2 : std_logic_vector :=
     "10111011100101010110010010000101";
constant c3 : std_logic_vector :=
     "10111100110010110101101110110001";
constant c4 : std_logic_vector :=
     "10111011011001111000101100010100";
constant k1 : std_logic_vector :=
     "10111101010100011110001110111000";
constant k2 : std_logic_vector :=
     "00111101111000111001100001101000";
constant k3 : std_logic_vector :=
     "00111101101000010100111110001011";
constant k4 : std_logic_vector :=
     "10111111000011011010110001111001 1";
constant l1 : std_logic_vector :=
     "00111111101000100100001001100101";
constant l2 : std_logic_vector :=
     "10111110100100111111011000000000";
constant l3 : std_logic_vector :=
     "11000000000100100001111011010000";
constant l4 : std_logic_vector :=
     "10111110111111101110100111111000";

------------------------------------
-- DECLARE COMPONENTS
------------------------------------
COMPONENT AddFloat
PORT (
        a : IN STD_LOGIC_VECTOR(31 DOWNTO 0);
        b : IN STD_LOGIC_VECTOR(31 DOWNTO 0);
        operation_nd : IN STD_LOGIC;
        operation_rfd : OUT STD_LOGIC;
        result : OUT STD_LOGIC_VECTOR(31 DOWNTO 0);
        underflow : OUT STD_LOGIC;
        overflow : OUT STD_LOGIC;
        invalid_op : OUT STD_LOGIC;
        rdy : OUT STD_LOGIC );
END COMPONENT;

COMPONENT MultFloat
        PORT (
        a : IN STD_LOGIC_VECTOR(31 DOWNTO 0);
        b : IN STD_LOGIC_VECTOR(31 DOWNTO 0);
        operation_nd : IN STD_LOGIC;
        operation_rfd : OUT STD_LOGIC;
        result : OUT STD_LOGIC_VECTOR(31 DOWNTO 0);
        underflow : OUT STD_LOGIC;
        overflow : OUT STD_LOGIC;
        invalid_op : OUT STD_LOGIC;
        rdy : OUT STD_LOGIC );
END COMPONENT;

COMPONENT SubFloat
        PORT (
        a : IN STD_LOGIC_VECTOR(31 DOWNTO 0);
```

```
        b : IN STD_LOGIC_VECTOR(31 DOWNTO 0);
        operation_nd : IN STD_LOGIC;
        operation_rfd : OUT STD_LOGIC;
        result : OUT STD_LOGIC_VECTOR(31 DOWNTO 0);
        underflow : OUT STD_LOGIC;
        overflow : OUT STD_LOGIC;
        invalid_op : OUT STD_LOGIC;
        rdy : OUT STD_LOGIC );
END COMPONENT;

------------------------------------
-- FOR NON Trimming OF SIGNALS
------------------------------------
attribute KEEP : string;
attribute S    : string;

------------------------------------
-- DECLARE SIGNALS
------------------------------------
signal mult1a : STD_LOGIC_VECTOR(31 DOWNTO 0);
signal mult1b : STD_LOGIC_VECTOR(31 DOWNTO 0);
signal result_mult1 : STD_LOGIC_VECTOR(31 DOWNTO 0);

signal mult2a : STD_LOGIC_VECTOR(31 DOWNTO 0);
signal mult2b : STD_LOGIC_VECTOR(31 DOWNTO 0);
signal result_mult2 : STD_LOGIC_VECTOR(31 DOWNTO 0);

signal mult3a : STD_LOGIC_VECTOR(31 DOWNTO 0);
signal mult3b : STD_LOGIC_VECTOR(31 DOWNTO 0);
signal result_mult3 : STD_LOGIC_VECTOR(31 DOWNTO 0);

signal mult4a : STD_LOGIC_VECTOR(31 DOWNTO 0);
signal mult4b : STD_LOGIC_VECTOR(31 DOWNTO 0);
signal result_mult4 : STD_LOGIC_VECTOR(31 DOWNTO 0);

signal add1a : STD_LOGIC_VECTOR(31 DOWNTO 0);
signal add1b : STD_LOGIC_VECTOR(31 DOWNTO 0);
signal result_add1 : STD_LOGIC_VECTOR(31 DOWNTO 0);

signal add2a : STD_LOGIC_VECTOR(31 DOWNTO 0);
signal add2b : STD_LOGIC_VECTOR(31 DOWNTO 0);
signal result_add2 : STD_LOGIC_VECTOR(31 DOWNTO 0);

signal add3a : STD_LOGIC_VECTOR(31 DOWNTO 0);
signal add3b : STD_LOGIC_VECTOR(31 DOWNTO 0);
signal result_add3 : STD_LOGIC_VECTOR(31 DOWNTO 0);

signal add4a : STD_LOGIC_VECTOR(31 DOWNTO 0);
signal add4b : STD_LOGIC_VECTOR(31 DOWNTO 0);
signal result_add4 : STD_LOGIC_VECTOR(31 DOWNTO 0);

signal sub1a : STD_LOGIC_VECTOR(31 DOWNTO 0);
signal sub1b : STD_LOGIC_VECTOR(31 DOWNTO 0);
signal result_sub1 : STD_LOGIC_VECTOR(31 DOWNTO 0);

signal vresult: std_logic_vector(31 downto 0);
signal vX1 : STD_LOGIC_VECTOR(31 DOWNTO 0)
                     := (others => ’0’);
signal vX2 : STD_LOGIC_VECTOR(31 DOWNTO 0)
                     := (others => ’0’);
signal vX3 : STD_LOGIC_VECTOR(31 DOWNTO 0)
                     := (others => ’0’);
signal vX4 : STD_LOGIC_VECTOR(31 DOWNTO 0)
                     := (others => ’0’);
signal vKX : STD_LOGIC_VECTOR(31 DOWNTO 0)
                     := (others => ’0’);
signal vCX : STD_LOGIC_VECTOR(31 DOWNTO 0)
                     := (others => ’0’);
signal vRminusKX : STD_LOGIC_VECTOR(31 DOWNTO 0)
             := (others => ’0’);
signal vSensorMinusCX : STD_LOGIC_VECTOR(31 DOWNTO 0)   :=
      (others => ’0’);
signal vInter_add1 : STD_LOGIC_VECTOR(31 DOWNTO 0)
             := (others => ’0’);
signal vInter_add2 : STD_LOGIC_VECTOR(31 DOWNTO 0)
             := (others => ’0’);
signal vInter_add3 : STD_LOGIC_VECTOR(31 DOWNTO 0)
             := (others => ’0’);
signal vInter_add4 : STD_LOGIC_VECTOR(31 DOWNTO 0)
             := (others => ’0’);
signal vInter_misc1 : STD_LOGIC_VECTOR(31 DOWNTO 0)
             := (others => ’0’);
signal vInter_misc2 : STD_LOGIC_VECTOR(31 DOWNTO 0)
             := (others => ’0’);

signal operation_nd1 : STD_LOGIC;
signal operation_nd2 : STD_LOGIC;
signal operation_nd3 : STD_LOGIC;
signal operation_nd4 : STD_LOGIC;
signal operation_nd5 : STD_LOGIC;
signal operation_nd6 : STD_LOGIC;
signal operation_nd7 : STD_LOGIC;
signal operation_nd8 : STD_LOGIC;
signal operation_nd9 : STD_LOGIC;
signal ADCbuff : STD_LOGIC_VECTOR(31 DOWNTO 0);

------------------------------------
-- STATE DEFINITIONS
------------------------------------
type state_type is (Zero,One,Two,Three,Four,Five,Six,Seven
     ,Eight,Nine);
signal state : state_type;

------------------------------------
-- BEGIN
------------------------------------
begin

------------------------------------
-- INSTANTIATION OF COMPONENTS
------------------------------------
AddFloat1 : AddFloat
PORT MAP (
        a => add1a,
        b => add1b,
        operation_nd => operation_nd1,
        operation_rfd => open,
        result => result_add1,
        underflow => open,
        overflow => open,
        invalid_op => open,
        rdy => open );

AddFloat2 : AddFloat
PORT MAP (
        a => add2a,
        b => add2b,
        operation_nd => operation_nd2,
        operation_rfd => open,
        result => result_add2,
        underflow => open,
        overflow => open,
        invalid_op => open,
        rdy => open );

AddFloat3 : AddFloat
PORT MAP (
        a => add3a,
        b => add3b,
        operation_nd => operation_nd3,
        operation_rfd => open,
        result => result_add3,
        underflow => open,
        overflow => open,
        invalid_op => open,
        rdy => open );

AddFloat4 : AddFloat
PORT MAP (
        a => add4a,
        b => add4b,
        operation_nd => operation_nd4,
        operation_rfd => open,
        result => result_add4,
        underflow => open,
        overflow => open,
```

```
        invalid_op => open,
        rdy => open );

MultFloat1 : MultFloat
PORT MAP (
        a => mult1a,
        b => mult1b,
        operation_nd => operation_nd5,
        operation_rfd => open,
        result => result_mult1,
        underflow => open,
        overflow => open,
        invalid_op => open,
        rdy => open );

MultFloat2 : MultFloat
PORT MAP (
        a => mult2a,
        b => mult2b,
        operation_nd => operation_nd6,
        operation_rfd => open,
        result => result_mult2,
        underflow => open,
        overflow => open,
        invalid_op => open,
        rdy => open );

MultFloat3 : MultFloat
PORT MAP (
        a => mult3a,
        b => mult3b,
        operation_nd => operation_nd7,
        operation_rfd => open,
        result => result_mult3,
        underflow => open,
        overflow => open,
        invalid_op => open,
        rdy => open );

MultFloat4 : MultFloat
PORT MAP (
        a => mult4a,
        b => mult4b,
        operation_nd => operation_nd8,
        operation_rfd => open,
        result => result_mult4,
        underflow => open,
        overflow => open,
        invalid_op => open,
        rdy =>open );

SubFloat1: SubFloat
PORT MAP (
        a => sub1a,
        b => sub1b,
        operation_nd => operation_nd9,
        operation_rfd => open,
        result => result_sub1,
        underflow => open,
        overflow => open,
        invalid_op => open,
        rdy => open );

------------------------------------
-- SERIAL, SYNCHRONOUS PROCESS
-- All of the state machine is synchronous, no asyn. (
     combinatorial) code
------------------------------------
process (clock)

begin
if(clock’event and clock=’1’) then
-- Default values for signal, to enforce full assigment.
mult1a  <=      (others => ’0’); --mult1a;
mult1b  <=      (others => ’0’); --mult1b;
mult2a  <=      (others => ’0’); --mult2a;
mult2b  <=      (others => ’0’); --mult2b;
mult3a  <=      (others => ’0’); --mult3a;
mult3b  <=      (others => ’0’); --mult3b;
mult4a  <=      (others => ’0’); --mult4a;
mult4b  <=      (others => ’0’); --mult4b ;
add1a   <=      (others => ’0’); --add1a;
add1b   <=      (others => ’0’); --add1b;
add2a   <=      (others => ’0’); --add2a;
add2b   <=      (others => ’0’); --add2b;
add3a   <=      (others => ’0’); --add3a;
add3b   <=      (others => ’0’); --add3b;
add4a   <=      (others => ’0’); --add4a;
add4b   <=      (others => ’0’); --add4b;
sub1a   <=      (others => ’0’); --sub1a;
sub1b   <=      (others => ’0’); --sub1b;

vresult <=      vresult;
vX1     <=      vX1;
vX2     <=      vX2;
vX3     <=      vX3;
vX4     <=      vX4;
vKX     <=      vKX;
vCX     <=      vCX;
vRminusKX       <=      vRminusKX;
vSensorMinusCX  <=      vSensorMinusCX;
vInter_add1     <=      vInter_add1;
vInter_add2     <=      vInter_add2;
vInter_add3     <=      vInter_add3;
vInter_add4     <=      vInter_add4;
vInter_misc1    <=      vInter_misc1;
vInter_misc2    <=      vInter_misc2;

operation_nd1   <=      ’0’;
operation_nd2   <=      ’0’;
operation_nd3   <=      ’0’;
operation_nd4   <=      ’0’;
operation_nd5   <=      ’0’;
operation_nd6   <=      ’0’;
operation_nd7   <=      ’0’;
operation_nd8   <=      ’0’;
operation_nd9   <=      ’0’;

DAC1out <=      vRminusKX;
DAC2out <=      vCX;

state <= state;

------------------------------------
-- START STATE MACHINE
------------------------------------
case state is

when Zero =>

        mult1a  <=      (others => ’0’);
        mult1b  <=      (others => ’0’);
        mult2a  <=      (others => ’0’);
        mult2b  <=      (others => ’0’);
        mult3a  <=      (others => ’0’);
        mult3b  <=      (others => ’0’);
        mult4a  <=      (others => ’0’);
        mult4b  <=      (others => ’0’);
        add1a   <=      (others => ’0’);
        add1b   <=      (others => ’0’);
        add2a   <=      (others => ’0’);
        add2b   <=      (others => ’0’);
        add3a   <=      (others => ’0’);
        add3b   <=      (others => ’0’);
        add4a   <=      (others => ’0’);
        add4b   <=      (others => ’0’);
        sub1a   <=      (others => ’0’);
        sub1b   <=      (others => ’0’);

        vresult <=      (others => ’0’);
        vX1     <=      (others => ’0’);
        vX2     <=      (others => ’0’);
        vX3     <=      (others => ’0’);
        vX4     <=      (others => ’0’);
        vKX     <=      (others => ’0’);
        vCX     <=      (others => ’0’);
```

```
        vRminusKX       <=      (others => ’0’);
        vSensorMinusCX  <=      (others => ’0’);
        vInter_add1     <=      (others => ’0’);
        vInter_add2     <=      (others => ’0’);
        vInter_add3     <=      (others => ’0’);
        vInter_add4     <=      (others => ’0’);
        vInter_misc1    <=      (others => ’0’);
        vInter_misc2    <=      (others => ’0’);
        DAC1out <=      (others => ’0’);
        DAC2out <=      (others => ’0’);

        operation_nd1   <=      ’0’;
        operation_nd2   <=      ’0’;
        operation_nd3   <=      ’0’;
        operation_nd4   <=      ’0’;
        operation_nd5   <=      ’0’;
        operation_nd6   <=      ’0’;
        operation_nd7   <=      ’0’;
        operation_nd8   <=      ’0’;
        operation_nd9   <=      ’0’;

        state <= One;

when One =>

        add1a <= (others=>’0’);
        add1b <= (others=>’0’);
        operation_nd1 <= ’0’;

        add2a <= (others=>’0’);
        add2b <= (others=>’0’);
        operation_nd2 <= ’0’;

        add3a <= (others=>’0’);
        add3b <= (others=>’0’);
        operation_nd3 <= ’0’;

        add4a <= (others=>’0’);
        add4b <= (others=>’0’);
        operation_nd4 <= ’0’;

        mult1a <= vX1;
        mult1b <= c1;
        operation_nd5 <= ’1’;

        mult2a <= vX2;
        mult2b <= c2;
        operation_nd6 <= ’1’;

        mult3a <= vX3;
        mult3b <= c3;
        operation_nd7 <= ’1’;

        mult4a <= vX4;
        mult4b <= c4;
        operation_nd8 <= ’1’;

        sub1a <= ADC1in;
        sub1b <= result_add1;
        vKX <= result_add1;
        operation_nd9 <= ’1’;

        state <= Two;


when Two =>

        add1a <= result_mult1;
        add1b <= result_mult2;
        operation_nd1 <= ’1’;

        add2a <= result_mult3;
        add2b <= result_mult4;
        operation_nd2 <= ’1’;

        add3a <= (others=>’0’);
        add3b <= (others=>’0’);
        operation_nd3 <= ’0’;

        add4a <= (others=>’0’);
        add4b <= (others=>’0’);
        operation_nd4 <= ’0’;

        mult1a <= vX1;
        mult1b <= a11;
        operation_nd5 <= ’1’;

        mult2a <= vX2;
        mult2b <= a12;
        operation_nd6 <= ’1’;

        mult3a <= vX1;
        mult3b <= a21;
        operation_nd7 <= ’1’;

        mult4a <= vX2;
        mult4b <= a22;
        operation_nd8 <= ’1’;

        vRminusKX <= result_sub1;

        sub1a <= (others => ’0’);
        sub1b <= (others => ’0’);
        operation_nd9 <= ’0’;

        state <= Three;

when Three =>

        add1a <= result_mult1;
        add1b <= result_mult2;
        operation_nd1 <= ’1’;

        add2a <= result_mult3;
        add2b <= result_mult4;
        operation_nd2 <= ’1’;

        add3a <= result_add1;
        add3b <= result_add2;
        operation_nd3 <= ’1’;

        add4a <= (others=>’0’);
        add4b <= (others=>’0’);
        operation_nd4 <= ’0’;

        mult1a <= vX3;
        mult1b <= a33;
        operation_nd5 <= ’1’;

        mult2a <= vX4;
        mult2b <= a34;
        operation_nd6 <= ’1’;

        mult3a <= vX3;
        mult3b <= a43;
        operation_nd7 <= ’1’;

        mult4a <= vX4;
        mult4b <= a44;
        operation_nd8 <= ’1’;

        sub1a <= (others => ’0’);
        sub1b <= (others => ’0’);
        operation_nd9 <= ’0’;

        state <= Four;


when Four =>

        add1a <= result_mult1;
        add1b <= result_mult2;
        operation_nd1 <= ’1’;
        vX1 <= result_add1;

        add2a <= result_mult3;
```

```
        add2b <= result_mult4;
        operation_nd2 <= ’1’;
        vX2 <= result_add2;

        add3a <= (others=>’0’);
        add3b <= (others=>’0’);
        operation_nd3 <= ’0’;

        add4a <= (others=>’0’);
        add4b <= (others=>’0’);
        operation_nd4 <= ’0’;

        mult1a <= vRminusKX;
        mult1b <= b1;
        operation_nd5 <= ’1’;

        mult2a <= vRminusKX;
        mult2b <= b2;
        operation_nd6 <= ’1’;

        mult3a <= vRminusKX;
        mult3b <= b3;
        operation_nd7 <= ’1’;

        mult4a <= vRminusKX;
        mult4b <= b4;
        operation_nd8 <= ’1’;

        sub1a <= ADC2in;
        sub1b <= result_add3;
        operation_nd9 <= ’1’;
        vCX   <= result_add3;

        state <= Five;

when Five =>

        add1a <= vX1;
        add1b <= result_mult1;
        operation_nd1 <= ’1’;

        add2a <= vX2;
        add2b <= result_mult2;
        operation_nd2 <= ’1’;

        add3a <= result_add1;
        add3b <= result_mult3;
        vX3 <= result_add1;
        operation_nd3 <= ’1’;

        add4a <= result_add2;
        add4b <= result_mult4;
        vX4 <= result_add2;
        operation_nd4 <= ’1’;

        vSensorMinusCX <= result_sub1;
        mult1a <= result_sub1;
        mult1b <= l1;
        operation_nd5 <= ’1’;

        mult2a <= result_sub1;
        mult2b <= l2;
        operation_nd6 <= ’1’;

        mult3a <= result_sub1;
        mult3b <= l3;
        operation_nd7 <= ’1’;

        mult4a <= result_sub1;
        mult4b <= l4;
        operation_nd8 <= ’1’;

        sub1a <= (others => ’0’);
        sub1b <= (others => ’0’);
        operation_nd9 <= ’0’;

        state <= Six;


when Six =>

        add1a <= result_add1;
        add1b <= result_mult1;
        operation_nd1 <= ’1’;
        vX1 <= result_add1;

        add2a <= result_add2;
        add2b <= result_mult2;
        operation_nd2 <= ’1’;
        vX2 <= result_add2;

        add3a <= result_add3;
        add3b <= result_mult3;
        operation_nd3 <= ’1’;
        vX3 <= result_add3;

        add4a <= result_add4;
        add4b <= result_mult4;
        operation_nd4 <= ’1’;
        vX4 <= result_add4;

        mult1a <= (others => ’0’);
        mult1b <= (others => ’0’);
        operation_nd5 <= ’0’;

        mult2a <= (others => ’0’);
        mult2b <= (others => ’0’);
        operation_nd6 <= ’0’;

        mult3a <= (others => ’0’);
        mult3b <= (others => ’0’);
        operation_nd7 <= ’0’;

        mult4a <= (others => ’0’);
        mult4b <= (others => ’0’);
        operation_nd8 <= ’0’;

        sub1a <= (others => ’0’);
        sub1b <= (others => ’0’);
        operation_nd9 <= ’0’;

        state <= Seven;


when Seven =>

        vX1 <= result_add1;
        vX2 <= result_add2;
        vX3 <= result_add3;
        vX4 <= result_add4;

        add1a <= (others=>’0’);
        add1b <= (others=>’0’);
        operation_nd1 <= ’0’;

        add2a <= (others=>’0’);
        add2b <= (others=>’0’);
        operation_nd2 <= ’0’;

        add3a <= (others=>’0’);
        add3b <= (others=>’0’);
        operation_nd3 <= ’0’;

        add4a <= (others=>’0’);
        add4b <= (others=>’0’);
        operation_nd4 <= ’0’;

        mult1a <= result_add1;
        mult1b <= k1;
        operation_nd5 <= ’1’;

        mult2a <= result_add2;
        mult2b <= k2;
        operation_nd6 <= ’1’;

        mult3a <= result_add3;
```

```
        mult3b <= k3;
        operation_nd7 <= ’1’;

        mult4a <= result_add4;
        mult4b <= k4;
        operation_nd8 <= ’1’;

        sub1a <= (others => ’0’);
        sub1b <= (others => ’0’);
        operation_nd9 <= ’0’;

        state <= Eight;


when Eight =>

        add1a <= result_mult1;
        add1b <= result_mult2;
        operation_nd1 <= ’1’;

        add2a <= result_mult3;
        add2b <= result_mult4;
        operation_nd2 <= ’1’;

        add3a <= (others=>’0’);
        add3b <= (others=>’0’);
        operation_nd3 <= ’0’;

        add4a <= (others=>’0’);
        add4b <= (others=>’0’);
        operation_nd4 <= ’0’;

        mult1a <= (others => ’0’);
        mult1b <= (others => ’0’);
        operation_nd5 <= ’0’;

        mult2a <= (others => ’0’);
        mult2b <= (others => ’0’);
        operation_nd6 <= ’0’;

        mult3a <= (others => ’0’);
        mult3b <= (others => ’0’);
        operation_nd7 <= ’0’;

        mult4a <= (others => ’0’);
        mult4b <= (others => ’0’);
        operation_nd8 <= ’0’;

        sub1a <= (others => ’0’);
        sub1b <= (others => ’0’);
        operation_nd9 <= ’0’;

        state <= Nine;


when Nine =>

        add1a <= result_add1;
        add1b <= result_add2;
        operation_nd1 <= ’1’;

        add2a <= (others=>’0’);
        add2b <= (others=>’0’);
        operation_nd2 <= ’0’;

        add3a <= (others=>’0’);
        add3b <= (others=>’0’);
        operation_nd3 <= ’0’;

        add4a <= (others=>’0’);
        add4b <= (others=>’0’);
        operation_nd4 <= ’0’;

        mult1a <= (others => ’0’);
        mult1b <= (others => ’0’);
        operation_nd5 <= ’0’;

        mult2a <= (others => ’0’);
        mult2b <= (others => ’0’);
        operation_nd6 <= ’0’;

        mult3a <= (others => ’0’);
        mult3b <= (others => ’0’);
        operation_nd7 <= ’0’;

        mult4a <= (others => ’0’);
        mult4b <= (others => ’0’);
        operation_nd8 <= ’0’;

        sub1a <= (others => ’0’);
        sub1b <= (others => ’0’);
        operation_nd9 <= ’0’;

        state <= One;

when others =>

        mult1a  <=      (others => ’0’);
        mult1b  <=      (others => ’0’);
        mult2a  <=      (others => ’0’);
        mult2b  <=      (others => ’0’);
        mult3a  <=      (others => ’0’);
        mult3b  <=      (others => ’0’);
        mult4a  <=      (others => ’0’);
        mult4b  <=      (others => ’0’);
        add1a   <=      (others => ’0’);
        add1b   <=      (others => ’0’);
        add2a   <=      (others => ’0’);
        add2b   <=      (others => ’0’);
        add3a   <=      (others => ’0’);
        add3b   <=      (others => ’0’);
        add4a   <=      (others => ’0’);
        add4b   <=      (others => ’0’);
        sub1a   <=      (others => ’0’);
        sub1b   <=      (others => ’0’);

        vresult <=      (others => ’0’);
        vX1     <=      (others => ’0’);
        vX2     <=      (others => ’0’);
        vX3     <=      (others => ’0’);
        vX4     <=      (others => ’0’);
        vKX     <=      (others => ’0’);
        vCX     <=      (others => ’0’);
        vRminusKX       <=      (others => ’0’);
        vSensorMinusCX  <=      (others => ’0’);
        vInter_add1     <=      (others => ’0’);
        vInter_add2     <=      (others => ’0’);
        vInter_add3     <=      (others => ’0’);
        vInter_add4     <=      (others => ’0’);
        vInter_misc1    <=      (others => ’0’);
        vInter_misc2    <=      (others => ’0’);
        DAC1out <=      (others => ’0’);
        DAC2out <=      (others => ’0’);

        operation_nd1   <=      ’0’;
        operation_nd2   <=      ’0’;
        operation_nd3   <=      ’0’;
        operation_nd4   <=      ’0’;
        operation_nd5   <=      ’0’;
        operation_nd6   <=      ’0’;
        operation_nd7   <=      ’0’;
        operation_nd8   <=      ’0’;
        operation_nd9   <=      ’0’;

        state <= One;

end case;

end if;

end process;

end Behavioral;
```

Acronyms

AC Alternating Current

AD Analog-to-Digital

ADC Analog-to-Digital Converter

AFM Atomic Force Microscope

AM Amplitude Modulation

CIC Cascaded Integrator-Comb

CPU Central Processing Unit

DA Digital-to-Analog

DAC Digital-to-Analog Converter

DC Direct Current

FEM Finite Element Method

FFT Fast Fourier Transform

FIB Focused Ion Beam

FIFO First In, First Out

FIR Finite Impulse Response

FM Frequency Modulation

FPGA Field Programmable Gate Array

IIR Infinite Impulse Response

IP Intellectual Property

LabVIEW Laboratory Virtual Instrumentation Engineering Workbench

LDPE Polyolefin Elastomer

LQE Linear Quadratic Estimator

LQG Linear Quadratic Gaussian

LQR Linear Quadratic Regulator

MATLAB Matrix Laboratory

MEMS Microelectromechanical Systems

NI National Instruments

PC Personal Computer

PECVD Plasma-Enhanced Chemical Vapor Deposition

PID Proportional Integral Differential

PLL Phase Locked Loop

PCB Printed Circuit Board

PS Polystyrene

RBS Random Binary Signal

RMS Root Mean Square

SEM Scanning Electron Microscope

SNR Signal-to-Noise Ratio

STM Scanning Tunneling Microscope

TEOS Tetraethyl Orthosilicate

THD Total Harmonic Distortion

UHV Ultra High Vacuum

USB Universal Serial Bus

VHDL VHSIC (Very High Speed Integrated Circuit) Hardware Description Language

Symbols

α_i	Eigenvalue of the i^{th} Eigenmode
a_0	External Damping
a_1	Internal Damping
A	Rectangular Cross Section
$\mathbf{A}$	State Transition Matrix
$\bar{\mathbf{A}}$	Model State Transition Matrix
A_i	Amplitude of the i^{th} Solution
$\mathbf{B}$	State Input Matrix
$\bar{\mathbf{B}}$	Model State Input Matrix
$\mathbf{C}$	State Output Matrix
$\bar{\mathbf{C}}$	Model State Output Matrix
D	Direct Feed-Through Factor
E	Modulus of Elasticity
$F_{act}(t)$	External Cantilever Actuation Force
f_d	Demodulator Internal Clock Rate
$F_{ts}(d)$	Tip-Sample Interaction Force
$\Gamma_i(x)$	Slope of the i^{th} Eigenmode
G	Signal Amplification of the Sensor Circuit
G_s	Shear Modulus
$G(s)$	Transfer Function, Laplace Transformed
H	Gain dependent on the Laser Sensor Configuration and Alignment
i	Mode Index for Addressing Individual Modes
I	Area Moment of Inertia

J	Count of Modes considered in the Model
κ	Shear Coefficient
K	Gain of system
$\mathbf{K}$	Controller Feedback Coefficient Vector
$k_{eff,i}$	Effective Spring Constant of the i^{th} vibrating Eigenmode
$k_{eq,i}$	Equivalent Spring Constant of the Cantilever in the i^{th} Eigenmode
k_s	Static Spring Constant of the Cantilever
k_{ts}	Effective Spring Constant of the Tip-Sample Interaction
l_p	Piezo-Resistive Sensor Length
L	Length of the Cantilever
$\mathbf{L}$	Estimator Feedback Coefficient Vector
$m_{eq,i}$	Equivalent Mass of the Cantilever in the i^{th} Eigenmode
$M_i(x)$	Moment of the i^{th} Eigenmode
m_r	Real Mass of the Cantilever
N	Gain at the input of the state space system for steady state error compensation
$\omega_{n,i}$	Natural Angular Frequency of the i^{th} Eigenmode
$\Phi_i(x)$	Mode Shape of i^{th} Eigenmode
$\varphi(\omega)$	Phase Shift of the i^{th} vibrating Eigenmode
π_l	Piezo-Resistive Coefficients
$\Psi_i(x)$	Strain of the i^{th} Eigenmode
$p_{i1,2}$	Poles of the i^{th} Eigenmode
$Q_{eff,i}$	Effective Q Factor of the i^{th} vibrating Eigenmode
Q_i	Q factor of the i^{th} Eigenmode
$Q_{i,des}$	Desired Q factor of the i^{th} Eigenmode
$\mathbf{q(t)}$	State Vector of the State-Space System
$q_i(t)$	i^{th} State in the State Vector of the State-Space System
$\dot{q}_i(t)$	Derivative of the i^{th} State in the State Vector of the State-Space System
$\mathbf{\dot{q}(t)}$	Differentiation of the State Vector of the State-Space System
$\mathbf{q_k}$	State vector at the discrete time Step k of the state-space system
$\mathbf{q_{k-1}}$	State vector one discrete time step before the current one

ρ	Mass Density of Specific Material
ΔR	Change of Resistance of Piezo-Resistive Sensor
R	Resistance of Piezo-Resistive Sensor
R_g	Radius of Gyration
$\sigma_i(x)$	Stress of the i^{th} Eigenmode
$\bar{\sigma}_i(x)$	Average Stress of the i^{th} Eigenmode
τ_i	Time Constant of the Cantilever Envelope Oscillation
t	Time Variable
T	Thickness of the Cantilever
$u(t)$	System Input Signal
$U(s)$	Laplace Transform of the Input of a System
v	Poisson Ratio
v_k	Measurement noise
V_{out}	Voltage Output of the Sensor Circuit
$\omega_{eff,i}$	Effective Natural Angular Frequency of the i^{th} vibrating Eigenmode
$\omega_{d,i}$	Damped Frequency of the i^{th} vibrating Eigenmode
$\omega_{n,i}$	Natural Frequency of the i^{th} Eigenmode
$\omega_{r,i}$	Resonance Frequency of the i^{th} vibrating Eigenmode
W	Width of the Cantilever
w_k	Process noise
ξ_i	Damping Ratio of the i^{th} Eigenmode
x	Coordinate Along the Length of the Cantilever
$y(t)$	System Output Signal
$y_i(t)$	Time Dependent Displacement
$Y(s)$	Laplace Transform of the Output of a System
$\hat{y}(t)$	Estimated System Output Signal
$z(x,t)$	Transversal Beam Displacement
Z_l	Lower Half of a Split Photodiode
Z_u	Upper Half of a Split Photodiode

List of Figures

List of Tables

Publications

Journals

(1) A. Schuh, I. S. Bozchalooi, I. W. Rangelow, and K. Youcef-Toumi. **Multi-eigenmode control for high material contrast in bimodal and higher harmonic atomic force microscopy**, Nanotechnology, vol. 26, no. 23, p. 235706, May 2015. DOI: 10.1088/0957-4484/26/23/235706

(2) A. Schuh, M. Hofer, T. Ivanov, and I. W. Rangelow. **Active microcantilevers for high material contrast in harmonic atomic force microscopy**. Journal of Microelectromechanical Systems, vol.24, no.5, pp.1622-1631, Oct. 2015. DOI: 10.1109/JMEMS.2015.2428677

(3) A. Ahmad, A. Schuh and I. W. Rangelow. **Adaptive afm scan speed control for high aspect ratio fast structure tracking**. Review of Scientific Instruments, vol. 85, p. 103706, 2014. DOI: 10.1063/1.4897141

(4) M. Kästner, Tzv. Ivanov, A. Schuh, A. Ahmad, T. Angelov, M. Budden, M. Hofer, A. Reum, S. Lenk, Y. Krivoshapkina, E.Guliyev, M. Holz, J-P. Zollner, and I.W. Rangelow. **Scanning probes in nanostructure fabrication**. Journal of Vacuum Science and Technology B 32, 06F101, 2014. DOI: 10.1116/1.4897500

(5) T. Schenkel, C.C. Lo, C. D. Weis, A. Schuh, A. Persaud and J. Bokor. **Critical issues in the formation of quantum computer test structures by ion implantation**. Nuclear Instruments and Methods in Physics Research Section B, 267 (8-9), 2563, 2009. DOI: 10.1016/j.nimb.2009.05.061

(6) C.D. Weis, A. Schuh, A. Batra, A. Persaud, I.W. Rangelow, J. Bokor, C.C. Lo, S. Cabrini, D. Olynick, S. Duhey, T. Schenkel. **Mapping of ion beam induced current changes in FinFETs**. Nuclear Instruments and Methods in Physics Research B 267, 2009, pp. 1222-1225. DOI: 10.1016/j.nimb.2009.01.019

(7) C.D. Weis, A. Schuh, A. Batra, A. Persaud, I.W. Rangelow, J. Bokor, C.C. Lo, S. Cabrini, E. Sideras-Haddad, G.D. Fuchs, R. Hanson, D.D. Awschalom and T. Schenkel. **Single atom**

doping for quantum device development in diamond and silicon. Journal of Vacuum Science and Technology B 26, 2596, 2008. DOI: 10.1116/1.2968614

Conference Proceedings

(1) A. Schuh, I. W. Rangelow, and K. Youcef-Toumi. **Control of First and Higher Transverse Eigenmodes of Active Atomic Force Microscope Cantilevers**. Submitted to the American Control Conference (ACC) 2016.

(2) A. Schuh, I. S. Bozchalooi, I. W. Rangelow, and K. Youcef-Toumi. **Estimator based multi-eigenmode control of cantilevers in multifrequency Atomic Force Microscopy**. In American Control Conference (ACC) 2015, pp.1905-1910, 1-3 July 2015. DOI: 10.1109/ACC.2015.7171011

(3) A. Schuh, A. Hegyi, A. Raghavan, A. Lochbaum, J, Schwartz, P. Kiesel. **High-resolution, high-frequency wavelength shift detection of optical signals with low-cost, compact readouts**. Proc. SPIE 9480, Fiber Optic Sensors and Applications XII, 94800B, June 3, 2015. DOI: 10.1117/12.2177478

(4) N. Vorbringer-Doroshovets, F. Balzer, E. Manske, M. Kästner, A. Schuh, J.-P. Zöllner, M. Hofer, E. Guliyev, A. Ahmad, Tzv. Ivanov and I.W. Rangelow. **0.1-nanometer resolution positioning stage for sub-10nm scanning probe lithography**. Advanced Lithography, Proc. SPIE - Int. Soc. Opt. Eng. 2013. DOI: 10.1117/12.2012324

(5) I.W. Rangelow, Tz. Ivanov, Y. Sarov, A. Schuh, A. Frank, H. Hartmann, J.-P. Zöllner, D. Olynick, V. Kalchenko. **Nanoprobe maskless lithography**. Proc. SPIE, 7637, 76370V-1-10, 2010. DOI: 10.1117/12.852265

Patents

(1) A. Schuh and K. Youcef-Toumi. **Localization and tracking system for mobile robots**. US 8818723 B2 (US 20140058667 A1, WO 2014035741 A1). On Google patents

(2) A. Ahmad, A. Schuh and I. W. Rangelow. **Method for High Speed Imaging of Sample Surfaces by Atomic Force Microscopy**. (Original Title: Verfahren zur Abbildung von Oberflaechen mittels eines Rasterkraftmikroskops mit hoher Geschwindigkeit.)
Filed with the Licensing Office of the Ilmenau University of Technology, Germany, on December 12, 2013. Submitted to the German Patent and Trade Mark Office (GPTO).

Reports

(1) A. Schuh, I. S. Bozchalooi, I. W. Rangelow, K. Youcef-Toumi. **Multi-Eigenmode Compensator for Multifrequency Atomic Force Microscopy**. Biannual Report 2013/2014, Institute of Micro- and Nanotechnologies, Ilmenau University of Technology.

(2) A. Schuh, I. S. Bozchalooi, I. W. Rangelow, K. Youcef-Toumi. **Control of Higher Cantilever Eigenmodes for High Speed Atomic Force Microscopy**. Biannual Report 2013/2014, Institute of Micro- and Nanotechnologies, Ilmenau University of Technology.

(3) A. Schuh, M. Hofer, T. Ivanov and I. W. Rangelow. **Harmonic Active Atomic Force Microscope Cantilevers for Improved Material Contrast**. Biannual Report 2013/2014, Institute of Micro- and Nanotechnologies, Ilmenau University of Technology.

(4) A. Schuh, K. Youcef-Toumi and I.W. Rangelow. **Active Q Control in Atomic Force Microscopy for Speed and Sensitivity Enhancement**. Biannual Report 2011/2012, Institute of Micro- and Nanotechnologies, Ilmenau University of Technology.

(5) M. Hofer, T. Angelov, L. Chervenkov, M. Kästner, A. Schuh, N. Nikolov and I.W. Rangelow. **Femto- to Atto-Gram Mass Sensor**. Biannual Report 2011/2012, Institute of Micro- and Nanotechnologies, Ilmenau University of Technology.

(6) T. Angelov, L. Chervenkov, M. Hofer, M. Kästner, A. Schuh, N. Nikolov, and I.W. Rangelow. **Ultra-Low Noise and High Gain Amplifier for High Frequency NEMS-Resonator with 2DEG-Read Out**. Biannual Report 2011/2012, Institute of Micro- and Nanotechnologies, Ilmenau University of Technology.

(7) A. Schuh, Y. Sarov, Tzv. Ivanov, I.W. Rangelow, C.D. Weis, A. Batra, A. Persaud, T. Schenkel. **Self-actuated Piezoresistive Cantilever based AFM for Single Ion Implantation**. In PRONANO- Proceedings of the Integrated Project on Massively Parallel Intelligent Cantilever Probe Platforms for Nanoscale Analysis and Synthesis (Ed. Th. Sulzbach, I.W. Rangelow), ISBN 978-386991-177-9, Verlagshaus Monsenstein und Vannerdat OHGMuenster (2010), 299-306.

(8) A. Schuh, C. D. Weis, A. Persaud, Y. Sarov, Tzv. Ivanov, T. Schenkel, I. W. Rangelow. **AFM Based Method for the Detection of Single Ion Hit Events in Field Effect Transistors**. Biannual Report 2009/2010, Institute of Micro- and Nanotechnologies, Ilmenau University of Technology.

(9) Y. Sarov, T. Ivanov, C.D. Weis, A. Schuh, I. W. Rangelow, A. Persaud, J. Bokor, T. Schenkel, J. Meijer, Biannual Report 2007/2008. **Tool for positioning of Atoms and Clusters**

with Nano-resolution. Institute of Micro- and Nanotechnologies, Ilmenau University of Technology.

Acknowledgments

First of all, I like to truly thank two of the most important and influential persons throughout my work: Prof. Ivo W. Rangelow and Prof. Kamal Youcef-Toumi. As my advisor at IUT, Ivo let me spend time away at MIT and family affairs. But he always welcomed me back in our group in Ilmenau. Kamal as my advisor at MIT has welcomed me in his group and let me stay for two years throughout my thesis. With both of them I did not only enjoy research related discussions, but also warm conversations about and advices for anything in life.

Being recognized on a second position, but certainly no less than anybody else, are my wife Linh and daughter Victoria. Both have had tremendous patience with me being away for most of the time. Linh has been a gorgeous mom, juggling between raising an active toddler and full time employment. It was not until the last year preceding the conclusion of this work that I was able to spend a lot more time with the two of them. In that time, in particular 3-year old Victoria has taught me a completely new meaning of patience that will certainly beneficial in any aspect of life.

Many thanks also go to my parents. In particular, I do wish my dad all the best for his recovery from a serious medical incident. May my mom have all the strength and patience to get both of them through this hard time.

I would also like to say many thanks to my colleagues and fellow students that were part of the successful completion of this work. Many of you have also been great friends. At IUT, this foremost applies to Manuel Hofer, Marcus Kästner, Tzvetan Ivanov, Ahmad Ahmad and Jens-Peter Zöllner, but also to Tihomir Angelov, Lazar Chervenkov, Tomas Hrasok, Marek Steffanson, Ute Wenzel, Steve Lenk, Elshad Guliyev, Konrad Nieradka and Alexander Reum. At MIT, it includes Iman Soltani Bozchalooi, Amith Somanath, Mauricio Gutierrez, Dimitris Chatzigeorgiou, Changrak Choi, Cynthia Walker-Panas, Dalei Wu, Audren Cloitre, Kwang Lim and Dan Burns.

Final thanks go to the German Academic Exchange Service (DAAD) that supported me with a six month fellowship and allowed me to start my two year journey at MIT.

Thank you, to all of you!

Affidavit

Ich versichere, dass ich die vorliegende Arbeit ohne unzulässige Hilfe Dritter und ohne Benutzung anderer als der angegebenen Hilfsmittel angefertigt habe. Die aus anderen Quellen direkt oder indirekt übernommenen Daten und Konzepte sind unter Angabe der Quelle gekennzeichnet.
Weitere Personen waren an der inhaltlich-materiellen Erstellung der vorliegenden Arbeit nicht beteiligt. Insbesondere habe ich hierfür nicht die entgeltliche Hilfe von Vermittlungs- bzw. Beratungsdiensten (Promotionsberater oder anderer Personen) in Anspruch genommen. Niemand hat von mir unmittelbar oder mittelbar geldwerte Leistungen für Arbeiten erhalten, die im Zusammenhang mit dem Inhalt der vorgelegten Dissertation stehen.
Die Arbeit wurde bisher weder im In- noch im Ausland in gleicher oder ähnlicher Form einer Prüfungsbehörde vorgelegt.
Ich bin darauf hingewiesen worden, dass die Unrichtigkeit der vorstehenden Erklärung als Täuschungsversuch bewertet wird und gemäß § 7 Abs. 10 der Promotionsordnung den Ab- bruch des Promotionsverfahrens zur Folge hat.

Ilmenau, den 30.06.2014

(Andreas Schuh)

I hereby declare that this submission is my own work and that, to the best of my knowledge and belief, it contains no material previously published or written by another person nor material which to a substantial extent has been accepted for the award of any other degree or diploma of the university or other institute of higher education, except where due acknowledgment has been made in the text.

Ilmenau, 06/30/2014

(Andreas Schuh)

Thesen

- AFM Cantilever können durch eine Regelschleife in ihren dynamischen Eigenschaften verändert werden - sowohl im Q Faktor als auch in der Frequenz.
- Der genutzte Regler kann mit einen Zustandsschätzer basierten Kompensator realisiert werden. Dieser erlaubt die Schätzung von nicht gemessenen Sensorgrösen, die jedoch für einen vollständigen Regeleinfluss auf die Resonanz nötig sind.
- Der Kompensator kann für jede modellierte Resonanz separat und gleichzeitig den Q Faktor und die Frequenz modifizieren.
- Der separat modifizierte Q Faktor in den ersten drei transversalen Eigenmoden kann enweder zum schnelleren oder kraftsensitiveren Abbilden genutzt werden.
- Das geschätzte Sensorsignal ist ein gefiltertes Signal, dass dem physikalischen Sensorsignal folgt. Durch das deutlich geringere Rauschen kann dieses Signal für eine alternative Amplitudendemodulation genutzt werden.
- Der Kompensator kann im Multi-Eigenmode betrieben werden und z.B. die ersten beiden transversalen Eigenmoden im Q Faktor modifizieren. Dies ist vorteilhaft, um jeweils die optimalen Bedingungen zum Topographie- und Materialeigenschaften-Abbilden zu erhalten. Ein verbesserter Materialkontrast kann in zwei populären Messmethoden (Bimodal und höhere Harmonische) wird dabei erreicht.
- Strukturelle Modifizierungen (Masse-Entnahme) des Cantilevers an geeigneten Stellen ermöglischt die Abstimmung von fundamentaler Frequenz und höher Harmonischen, um den Materialkonstrast zu verbessern.

Andreas Schuh E-mail: aschuh@mit.edu / andreas.schuh11@gmail.com

Education

Ilmenau University of Technology (IUT), Germany **04/2010 to 06/2014**

- Ph.D. in Electrical Engineering, Department of Micro- and Nanoelectronic Systems,
- In collaboration with the **Massachusetts Institute of Technology (MIT), Cambridge, MA,** **04/2010 to present**
  Mechatronics Research Laboratory, Department of Mechanical Engineering,
- Thesis: "Multi-Eigenmode Control for Improved Tracking Speed in Multifrequency Atomic Force Microscopy",
- Advisers: Prof. Dr. Ivo W. Rangelow (IUT) and Prof. Kamal Youcef-Toumi (MIT).

Ilmenau University of Technology, Germany **10/2006 - 02/2009**

- Master of Science (M. Sc.) in Electrical Engineering, specializing in Micro- and Nanoelectronic Systems,
- Thesis: "Detection and imaging of single ion impacts in field effect transistors",
  Research conducted at the **IBT, Lawrence Berkeley National Laboratory (LBNL), Berkeley, CA,**
- Honors degree: Master of Science, Grade 1.1 (on a scale of 1 to 4, with 1 being the highest),
- Advisers: Prof. Dr. Ivo W. Rangelow (IUT) and Dr. Thomas Schenkel (LBNL).

University of Applied Sciences Trier, Germany **10/2002 - 08/2006**

- Undergraduate studies in Electrical Engineering, specializing in Microelectronics,
- One term abroad at the **Dundalk Institute of Technology, Republic of Ireland,** **08/2004 - 01/2005**
- Thesis: "Development of a Mixed Software/Hardware Control Solution for Car Alternators",
- Degree: Graduate Engineer, Grade 1.5 ("Diplom-Ingenieur (FH)").

Experience

Palo Alto Research Center (PARC), Palo Alto, USA **01/2015 – Present**

Postdoctoral Researcher

System Sciences Lab / Electronic Materials and Devices Laboratory

- Improved Li-Ion battery sensing through integrated Fiber Bragg Grating based Fiber Optics towards more reliable State-of-Charge and State-of-Health estimation.

Ilmenau University of Technology, Germany **09/2012 – 10/2014**

Research Affiliate and Research Associate,

Department of Micro- and Nanoelectronic Systems, Prof. Dr. Ivo W. Rangelow (MNES)

- Continuation of my work at MIT in improved Atomic Force Microscope (AFM) image acquisition,
- Focused Ion Beam and FEA based topology optimization of fully integrated MEMS (AFM probes),
- Implementation of novel control algorithms into a prototype lithography AFM system using Simulink/VHDL,
- Preparation of research publications, patent submissions and dissertation.

Massachusetts Institute of Technology (MIT), Cambridge, MA **04/2010 - 08/2012**

Research Assistant and Visiting Student, Department of Mechanical Engineering, Prof. Kamal Youcef-Toumi

- Work on improved tracking speed and material contrast imaging of dynamic AFM cantilevers by means of control design, estimation, signal processing and system identification techniques,
- Work on a laser and imaging sensor based robot localization and tracking system, originally for the inspection

of cryogenic LNG/LPG storage tanks in Qatar that also led to a granted international patent.

Ilmenau University of Technology, Germany **03/2009 - 03/2010**
Research Associate, MNES

- Control and mechanical designs for AFM based nanometer lithographic applications, grant proposal writing.

Lawrence Berkeley National Laboratory (LBNL), Berkeley, CA **10/2007 - 10/2008**
Research Scholar, Quantum Computing Initiative at Accelerator and Fusion Research Division (AFRD)

- Research on single ion implantation into in field effect transistors and its automatic impact detection for the creation of future quantum computing devices.

Ilmenau University of Technology, Germany **11/2006 - 09/2007**
Research Assistant, MNES and Department of Micro- and Nanotechnology

- Involved in the creation of an AFM probe manufacturing laboratory,
- Involved in the development of High Electron Mobility Transistors by using high resolution electron beam lithography,
- MATLAB-GUI programming for AFM controllers.

Robert BOSCH GmbH, Reutlingen, Germany **03/2006 - 08/2006**
Internship and Thesis. Division of Automotive Electronics

- Hardware/software co-design controller implementation for car alternators,
  based on a Xilinx Virtex E FPGA (VHDL) and an ARM7 microprocessor (C language).

Skills

Programming Languages:	NI LabVIEW (G), C/C++, Visual C#, Assembler, Python, Basic, Environment: CodeWarrior IDE,
Hardware Description:	VHDL, NI LabVIEW FPGA, VisualElite,
Hardware Synthesis:	Xilinx ISE, Synopsys DesignCompiler,
Simulation Environments:	Comsol Multiphysics, Modelsim, Electronics Workbench/MultiSIM and other SPICE derivatives,
CAD Software:	Autodesk AutoCAD/Inventor,
Math Environments:	Matlab/Simulink, Scilab, Mathematica,
Layout-Design:	ISIS/ARES, Eagle,
Analytical Tools:	Atomic Force Microscopy, Dual Focused Ion Beam, Electron Beam Microscopy/Lithography,
General PC Software:	LaTeX, Microsoft Office, Origin, Inkscape.

Professional Review Service

Reviewer for the IEEE Industrial Electronics Society and IEEE Control Systems Society.
Proposal Reviewer for the U.S. Department of Energy.

Fellowships

German Academic Exchange Service (DAAD) fellowship for conducting research in the area of AFMs at the Massachusetts Institute of Technology under the supervision of Prof. Kamal Youcef-Toumi. **04/2010 - 10/2010**

Quantum Computing Initiative at the Accelerator and Fusion Research Division (AFRD) for conducting research on novel room temperature quantum computing devices. **10/2007 - 10/2008**

Workshops

German Academic Exchange Service, Bonn, Germany 10/2012
Project Management Workshop for Ph.D. graduates.

Kristianstad University, Sweden, Alice-Project for Embedded Systems, 09/2005
Team Based control system design project with inverted pendulums.

Core Courses in

MEMS Micromachining, (Semiconductor) Physics, Control System Design, (Digital) Signal Processing, Image Processing, Hardware Description, Programming, Electronics, Mechanics, Statistics, Mathematics.

Languages

German:	Native proficiency,
English:	Full professional proficiency.

Honors

M. Sc. degree with distinction for high GPA and top of the class graduation. 04/2009